Temporal and Spatial Patterns of the Interannual Variability of Stratospheric Ozone and Dynamics

Thesis by

Charles D. Camp

In Partial Fulfillment of the Requirements

for the Degree of

Doctor of Philosophy

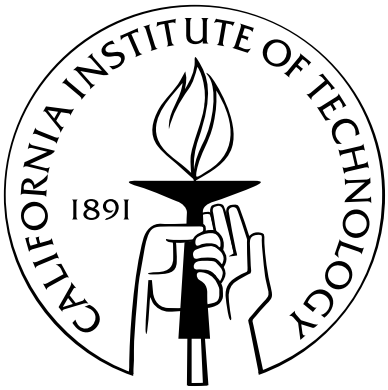

California Institute of Technology

Pasadena, California

2004

(Defended May 20, 2004)

Acknowledgements

I would like to thank the many people without whom this thesis would not have been possible. Foremost is my advisor, Yuk Yung, whom I thank for his insightful guidance and generous support. I am indebted to Michael Cross for his mentorship. I would also like to thank Tapio Schneider and Andy Ingersoll for their advice and aid.

I would like to thank many graduate students, postdocs and staff for all the enjoyable times and intriguing discussions. Chris Walker, Dave Noone, Xianglei Huang, Shane Byrne, Sarah Stewart, Mark Roulston, Xun Jiang, Ron Henderson, Muruhan Rathinam, Moira Regelson, Donal Gallagher, Russina Sgoureva, Chris Parkinson, Mao-Chang Liang, Ben Lane, Claire Newman, Run-Lie Shia, thank you. I would particularly like to thank David Hill, Beth Howard and Zhiming Kuang for all of the many conversations and for their invaluable support.

I must thank Mike Black for all his help and Shawn Ewald and Ian McEwan for all the discussions, technical and otherwise.

I am extremely grateful to two of my teachers, Sylvia Bonnell and Munzer Afifi, for helping to put my feet on this path many years ago.

To my family, Anita, Ann, Nabil, Tarecq, Shirley, and Janet, thank you for all the love, encouragement and advice. This truly would have been impossible without

you.

Finally, to Ali, thank you for reminding me of what is truly important in life.

Abstract

This dissertation is a collection of empirical and modeling studies focusing on the interannual variability (IAV) of stratospheric ozone and the dynamics associated with that variability. Empirical analyses of the IAV of total column ozone in the tropics and midlatitudes are performed using the Merged Ozone Data (MOD) set. MOD combines the monthly mean column abundances collected by the Total Ozone Mapping Spectrometer and the Solar Backscatter Ultraviolet instruments, provides a nearly continuous record from late 1978 to present on a 2D grid. The first four EOFs from principal component analyses of MOD capture over 93% (82%) of the variance of the tropical (midlatitude) IAV. These analyses display structures attributable to the quasi-biennial oscillation (QBO), with influence from a decadal oscillation, an interaction between the QBO and an annual cycle (QBO-AB), and ENSO. Similar decompositions occur for dynamical fields from the NCEP/NCAR reanalysis. Using these analyses, we found possible connections between the deduced patterns in ozone and the climate variables. For comparison to the observations, a 2D chemistry and transport model (CTM) was used to simulate the ozone IAV. The NCEP/Department of Energy (DOE) Reanalysis 2 data are used to derive a monthly mean meridional circulation from 1979 to 2002 which is then used to drive the Caltech/JPL 2D CTM,

allowing for an investigation of the impact of dynamics on the interannual variability (IAV) of the total column ozone for all years for which the MOD is available. The 2D CTM provides realistic simulations of the seasonal and IAV of ozone in the tropics, reasonable agreement in the NH midlatitudes but poor agreement in the SH midlatitudes. The influence of the QBO and QBO-AB are well represented in the simulation. A 71-year record of column ozone from Arosa, Switzerland is analyzed using singular spectrum analysis (SSA). The SSA decomposition separates the signals from the seasonal cycle, QBO, QBO-AB, and decadal oscillations. A 3.5-year oscillation is also discovered. A nonlinear trend is extracted and nonstationary behavior of some of the oscillations is found. Finally, a connection between fluctuations in stratospheric ozone and in tropospheric methane is observed and modeled.

Contents

Acknowledgements **iii**

Abstract **v**

1 Overview **1**

2 Temporal and Spatial Patterns of the Interannual Variability of Total Ozone in the Tropics **3**

2.1 Introduction 3

2.2 Datasets and Indices 5

2.3 Methodology 7

2.4 Ozone EOFs 10

2.4.1 Merged Ozone Data (MOD) EOFs 10

2.4.2 TOMS EOFs 12

2.5 Analysis of the Ozone Decomposition 14

2.5.1 QBO and Decadal 14

2.5.2 Separating the QBO and Decadal Signals 16

2.5.3 QBO-Annual Beat 19

2.5.4 ENSO 20

2.6 Analysis of NCEP/NCAR Data 22

2.6.1 Layer Thickness EOFs 23

2.6.2 100 hPa Surface EOFs 25

2.7 Conclusions 27

3 Interannual Variability of the Midlatitude Stratospheric Ozone: Observations and Modeling 44

3.1 Introduction 44

3.2 Analysis of the Merged Ozone Dataset 49

3.2.1 Climatology 49

3.2.2 PCA of MOD 50

3.3 Simulating Ozone Transport in a 2D Chemical Transport Model . . . 54

3.3.1 NCEP-2 Derived Transport Fields 54

3.3.1.1 Stream Function 54

3.3.1.2 Isentropic Mixing Coefficient 59

3.3.2 IAV of the Stream Function 60

3.3.3 Simulated Total Column Ozone 62

3.3.3.1 Climatology 64

3.3.3.2 IAV 66

3.4 Conclusions 69

4 A Singular Spectrum Analysis of the 71-Year Record of Total Column Ozone at Arosa, Switzerland 106

4.1 Introduction 106

4.2 Singular Spectrum Analysis 107

4.3 Analysis of Arosa Total Column Ozone 110

4.3.1 Climatology and Spectral Analysis 110

4.3.2 Decomposition Using Singular Spectrum Analysis 111

4.4 Regression of SSA Components on NCEP Geopotential Heights . . . 113

4.5 Dependence on Window Length 116

4.6 Nonstationary Behavior in the IAV of ATCO 118

4.7 Discussion 119

5 The Sensitivity of Tropospheric Methane to the Interannual Variability in Stratospheric Ozone 149

5.1 Introduction 149

5.2 Sensitivity to Interannual Fluctuations 152

5.3 Simulating Interannual Fluctuations 157

5.4 Discussion 158

A Response of the Methane Evolution Equation to Various Forcings 167

A.1 Impulse Response 168

A.2 Constant Forcing 168

A.3 Single Period Oscillatory Forcing 169

A.4 Multiple Period Oscillatory Forcing 170

List of Figures

2.1 Standard deviations of the detrended, deseasonalized ozone time series from the Merged Ozone Dataset. 32

2.2 Cumulative variance as a function of number of EOFs. 33

2.3 Spatial patterns for the first four MOD EOFs. 34

2.4 PC time series (left column) and spectra (right column) for the first four MOD EOFs. PCs (solid lines) are shown along with an appropriate index (dotted line). (a,b) PC1 and QBO index. (c,d) PC2 and inverted Solar Flux. (e,f) PC3. (g,h) PC4 and SOI. 35

2.5 Spatial patterns for the fourth TOMS EOF. 36

2.6 PC time series (a) and spectrum (b) for the fourth TOMS EOF. PC4 (solid) is compared to the SOI (dotted). 36

2.7 Comparisons of filtered PCs of the MOD EOFs (solid) to appropriate indices (dotted). (a) Bandpass A filtered PC1 and QBO index. (b) Lowpass C filtered PC1 and Solar Flux. (c) Bandpass A filtered PC2 and QBO index. (d) Lowpass C filtered PC2 and inverted Solar Flux. 37

2.8 (a) Zonal averages of MOD EOF1 (solid line) and EOF2 (dashed line). (b) Weighted sum (solid line) and difference (dashed) of the MOD EOF1 and EOF2 zonal averages. 37

2.9 Leading EOFs from the filtered MOD analyses. (a) EOF1 of the Bandpass B filtered MOD (MOD-Band). (b) EOF1 of the Lowpass B filtered MOD (MOD-Low). 38

2.10 PC time series (a) and spectrum (b) for the third EOF from the Bandstop A filtered MOD data (MOD-Notch). 38

2.11 Spatial patterns for the first four EOFs from the NCEP/NCAR reanalysis 30 hPa to 100 hPa layer thickness (NCEP-Layer). 39

2.12 PC time series (left column) and spectra (right column) for the first four NCEP-Layer EOFs. PCs (solid lines) are shown along with an appropriate index (dotted lines). (a,b) PC1 and Solar Flux. (c,d) PC2 and QBO index. (e,f) PC3 and SOI. (g,h) PC4. 40

2.13 Comparisons of filtered PCs of the NCEP-Layer EOFs to appropriate indices. (a) Bandpass A filtered PC1 and QBO index. (b) Lowpass C filtered PC1 and Solar Flux. (c) Bandpass A filtered PC2 and QBO index. (d) Lowpass C filtered PC2 and inverted Solar Flux. 41

2.14 (a) Zonal averages of NCEP-Layer EOF1 (solid line) and EOF2 (dashed line). (b) Weighted sum (solid line) and difference (dashed) of the NCEP-Layer EOF1 and EOF2 zonal averages. 41

2.15 Spatial patterns for the first two EOFs from the NCEP/NCAR reanalysis 100 hPa geopotential height data (NCEP-100). 42

2.16 PC time series (left column) and spectra (right column) for the first two NCEP-100 EOFs. PCs (solid lines) are shown along with the appropriate index (dotted line). (a,b) PC1 and Solar Flux. (c,d) PC2 and inverted SOI. 42

2.17 Comparisons of filtered PCs of the NCEP-100 EOFs to appropriate indices. (a) Bandpass A filtered PC1 and inverted SOI. (b) Lowpass C filtered PC1 and Solar Flux. (c) Bandpass A filtered PC2 and inverted SOI. (d) Lowpass C filtered PC2 and inverted Solar Flux. 43

3.1 Nov. 1978–Dec. 2002 mean of MOD. Units are DU. 72

3.2 Monthly means for MOD. Units are DU. (a) 1979–2002 Jan. mean. (b) 1979–2002 Mar. mean. (c) 1979–2002 May mean. (d) 1979–2002 Jul. mean. (e) 1979–2002 Sep. mean. (f) 1979–2002 Nov. mean. 73

3.3 Nov. 1978–Dec. 2002 linear trend for MOD. Units are DU / decade. . 74

3.4 Standard deviation of the deseasonalized and detrended MOD. Units are DU. 75

3.5 Relative and cumulative relative variance from the PCA of MOD. (a) Cumulative relative variance. (b) Relative variance. 76

3.6 First 4 EOFs from PCA for MOD. (a) EOF1, (b) EOF2, (c) EOF3, (d) EOF4. 77

3.7 First four PC time series and associated PSD from PCA for MOD. PC time series (solid) shown with appropriate index (dotted). (a) PC1 and QBO index. (b) PSD of PC1, (c) PC2, (d) PSD of PC2, (e) PC3 and Solar Flux, (f) PSD of PC3, (g) PC4 and SOI, (h) PSD of PC4. . . . 78

3.8 (a) 1979–2002 mean of the isentropic mass stream function interpolated to pressure surfaces. Units are $10^9\,\mathrm{kg/\,s}$. (b) 1979–2002 mean of the isentropic velocity stream function interpolated to pressure surfaces. Units are $\mathrm{m}^2/\,\mathrm{s}$. 79

3.9 Mean seasonal cycle of the isentropic mass stream function. Units are $10^9\,\mathrm{kg/\,s}$. (a) 1979–2002 Jan. mean. (b) 1979–2002 Apr. mean. (c) 1979–2002 Jul. mean. (d) 1979–2002 Oct. mean. 80

3.10 Linear trends of the isentropic mass stream function. Units are $10^9\,\mathrm{kg/\,s/}$ decade. (a) Trend fit to entire dataset (all months). (b) Trend fit to Jan. only. (c) Trend fit to Jul. only. 81

3.11 (a) 1979–2002 mean of the mean residual circulation stream function scaled by density. Units are $10^9\,\mathrm{kg/\,s}$. (b) 1979–2002 mean of the mean residual circulation stream function. Units are $\mathrm{m}^2/\,\mathrm{s}$. 82

3.12 Isentropic mixing coefficient, K_{yy}, interpolated to pressure surfaces. Units are $10^5\,\mathrm{m}^2/\,\mathrm{s}$. (a) Jan. 1985 (b) Apr. 1985 (c) Jul. 1985 (d) Oct. 1985 83

3.13 Relative and cumulative relative variance for PCA analysis of the isentropic velocity stream function (a) Cumulative relative variance. (b) Relative variance. 84

3.14 First EOF of the isentropic velocity stream function, associated PC time series and its PSD. (a) EOF1; units are m^2/s. (b) PC1 time series (solid). Inverted QBO index (dotted). (c) PSD of PC1. 85

3.15 Second EOF of the isentropic velocity stream function, associated PC time series and PSD. (a) EOF2; units are m^2/s. (b) PC2 time series (solid). Constructed QBO-AB index (dotted). (c) PSD of PC2. 86

3.16 Third EOF of the isentropic velocity stream function, associated PC time series and PSD. (a) EOF3; units are m^2/s. (b) PC3 time series (solid). QBO index (dotted). (c) PSD of PC3. 87

3.17 1979–2002 mean column ozone abundances for 2D CTM simulated ozone (solid) and zonally averaged MOD (dotted) 88

3.18 1979–2002 mean column ozone abundances for individual months; 2D CTM simulated ozone (solid) and zonally averaged MOD (dotted) (a) 1979–2002 Jan. mean. (b) 1979–2002 Apr. mean. (c) 1979–2002 Jul. mean. (d) 1979–2002 Oct. mean. 89

3.19 Seasonal cycles in northern latitudes; 2D CTM simulated ozone (solid) and zonally averaged MOD (dotted) (a) 55°N, (b) 45°N, (c) 35°N, (d) 25°N, (e) 15°N, (f) 5°N, ... 90

3.20 Seasonal cycles in southern latitudes; 2D CTM simulated ozone (solid) and zonally averaged MOD (dotted) (a) 5°S, (b) 15°S, (c) 25°S, (d) 35°S, (e) 45°S, (f) 55°S, ... 91

3.21 Slope of the fitted linear trend for 1979–2002; 2D CTM simulated ozone (solid) and zonally averaged MOD (dotted) 92

3.22 Slope of the fitted linear trend for various months during the period 1979–2002. 2D CTM simulated ozone (solid) and zonally averaged MOD (dotted) (a) 1979–2002 Jan. mean (b) 1979–2002 Apr. mean (c) 1979–2002 Jul. mean (d) 1979–2002 Oct. mean 93

3.23 Lowpass filtered, deseasonalized and detrended ozone anomalies for the northern midlatitudes; 2D CTM simulated ozone (solid) and zonally averaged MOD (dotted) (a) 55°N, (b) 45°N, (c) 35°N. 94

3.24 Lowpass filtered, deseasonalized and detrended ozone anomalies for the northern subtropics and tropics; 2D CTM simulated ozone (solid) and zonally averaged MOD (dotted) (a) 25°N, (b) 15°N, (c) 5°N, ... 95

3.25 Lowpass filtered, deseasonalized and detrended ozone anomalies for the southern subtropics and tropics; 2D CTM simulated ozone (solid) and zonally averaged MOD (dotted) (a) 5°S, (b) 15°S, (c) 25°S, ... 96

3.26 Lowpass filtered, deseasonalized and detrended ozone anomalies for the southern midlatitudes; 2D CTM simulated ozone (solid) and zonally averaged MOD (dotted) (a) 35°S, (b) 45°S, (c) 55°S, ... 97

3.27 Relative and cumulative relative variance for PCA analysis of the 2D CTM simulated ozone. (a) Cumulative relative variance. (b) Relative variance. 98

3.28 First EOF of the 2D CTM simulated ozone, associated PC time series and PSD. (a) EOF1. (b) PC1 time series (solid). QBO index (dotted). (c) PSD of PC1. 99

3.29 Second EOF of the 2D CTM simulated ozone, associated PC time series and PSD. (a) EOF2. (b) PC2 time series. (c) PSD of PC2. 100

3.30 Third EOF of the 2D CTM simulated ozone, associated PC time series and PSD. (a) EOF3. (b) PC3 time series (solid). QBO index (dotted). (c) PSD of PC3. 101

3.31 Relative and cumulative relative variance for PCA analysis of zonally averaged MOD. (a) Cumulative relative variance. (b) Relative variance. 102

3.32 First EOF of zonally averaged MOD, associated PC time series and PSD. (a) EOF1. (b) PC1 time series (solid). QBO index (dotted). (c) PSD of PC1. 103

3.33 Second EOF of zonally averaged MOD, associated PC time series and PSD. (a) EOF2. (b) PC2 time series (solid). (c) PSD of PC2. 104

3.34 Third EOF of zonally averaged MOD, associated PC time series and PSD. (a) EOF3. (b) PC3 time series (solid). (c) PSD of PC3. 105

4.1 **(a)** Arosa total column ozone (ATCO) with $O(2)$ polynomial trend. **(b)** Deseasonalized, detrended ATCO. **(c)** Mean seasonal cycle of ATCO. **(d)** PSD of deseasonalized, detrended ATCO. Vertical (dotted) lines mark periods of 11 yr., 3.5 yr., 28 mo., 20 mo., and 1 yr. 122

4.2 **(a)** MEM spectra for ATCO of order 120 (solid), 140 (dotted), and 160 (dashed). Vertical (dotted) lines denote same periods as in Figure 4.1 **(b)** Adaptively weighted MTM spectrum for ATCO. Estimated red-noise background and associated 90%, 95%, and 99% significance levels are shown. The bandwidth parameter was set to $p = 2$ and $K = 3$ tapers were used. 123

4.3 Eigenvalue spectrum for the M270 SSA analysis of ATCO. 124

4.4 Leading pairs of EOFs for the M270 SSA analysis of ATCO; Solid (dotted) line denotes first (second) member of each pair. **(a)** (1,2), **(b)** (3,4), **(c)** (5,6), **(d)** (7,8), **(e)** (9,10), **(f)** (11,12), **(g)** (13,14), **(h)** (15) unpaired. **(i)** (16,17), **(j)** (18,19). 125

4.5 Leading pairs of PCs for the M270 SSA analysis of ATCO, **(a)** (1,2), **(b)** (3,4), **(c)** (5,6), **(d)** (7,8), **(e)** (9,10), **(f)** (11,12), **(g)** (13,14), **(h)** (15) unpaired. **(i)** (16,17), **(j)** (18,19). 128

4.6 Sum of the leading pairs of RCs for the M270 SSA analysis of ATCO, **(a)** (1+2), **(b)** (3+4), **(c)** (5+6), **(d)** (7+8), **(e)** (9+10), **(f)** (11+12), **(g)** (13+14), **(h)** (15) unpaired. **(i)** (16+17), **(j)** (18+19). 131

4.7 PSDs of the RCs in the previous figure; **(a)** (1+2), **(b)** (3+4), **(c)** (5+6), **(d)** (7+8), **(e)** (9+10), **(f)** (11+12), **(g)** (13+14), **(h)** (15) unpaired, **(i)** (16+17), **(j)** (18+19). 134

4.8 **(a)** Partial reconstruction (solid) of ATCO time series (dotted) based on first 20 EOFs of the M270 SSA analysis. **(b)** PSDs of the partial reconstruction (solid) and raw ATCO (dotted). 136

4.9 **(a)** Regression coefficient for the regression of the M270 3.5-year component (RCs 7+8) onto the NCEP 100 hPa geopotential height. **(b)** *t*-statistic associated with the regression coefficient. 137

4.10 **(a)** Regression coefficient for the regression of the M270 3.5-year component (RCs 7+8) onto the NCEP 30 hPa geopotential height. **(b)** *t*-statistic associated with the regression coefficient. 138

4.11 **(a)** Regression coefficient for the regression of the M270 decadal component (RCs 9+10) onto the NCEP 100 hPa geopotential height. **(b)** *t*-statistic associated with the regression coefficient. 139

4.12 **(a)** Regression coefficient for the regression of the M270 QBO component (RCs 11+12) onto the NCEP 30 hPa geopotential height. **(b)** *t*-statistic associated with the regression coefficient. 140

4.13 **(a)** Regression coefficient for the regression of the M270 QBO-AB component (RCs 13+14) onto the NCEP 30 hPa geopotential height. **(b)** *t*-statistic associated with the regression coefficient. 141

4.14 Comparison of various reconstructed IAV oscillations (solid curves), based on pairs of M270 EOFs, to appropriate indices (dotted). (a) M270 3.5-year oscillation (RCs 7+8) and leading oscillation of a SSA analysis of the PNA, (b) M270 decadal oscillation (RCs 9+10) and anomalous sunspot number, (c) M270 QBO oscillation and the 30 hPa Singapore wind, (d) M270 QBO-AB oscillation and a QBO-AB index. 142

4.15 Eigenvalue spectra for M155 and M85 SSA analyses of ATCO. (a) M155 (b) M85. 143

4.16 Comparison of the 3.5-year oscillations found in SSA analyses of ATCO for various window lengths. **(a)** sum of paired RCs (7,8) from the M155 (solid) and M270 (dotted) analyses. **(b)** sum of paired RCs (5,6) from the M85 analysis. 144

4.17 Comparison of the trends found in SSA analyses of ATCO for various window lengths plotted against the original ATCO (black line): $M =$ 270 (red), 155 (green), and 85 (blue). 145

4.18 Comparison of the annual cycle found in SSA analyses of ATCO for various window lengths **(a)** $M = 270$, **(b)** $M = 85$, **(c)** $M = 12$. . . . 146

4.19 Power spectral estimates of 30 year segments of the deseasonalized, detrended ATCO. Segments begin every 5 years staring in 1933. Vertical dotted lines mark periods of 11 years, 3.5 years, 28 months and 20 months. 147

5.1 (a) Fractional change in ozone column abundance from the merged SBUV/TOMS dataset. (b) Spectrum of the ozone data. The solid line is the filtered data or spectrum and the dotted line is the unfiltered data or spectrum. 162

5.2 **(a)** Fractional change in methane abundance from the NOAA-CMDL flask monthly means database. **(b)** Spectrum of the methane data. The solid line is the filtered data or spectrum and the dotted line is the unfiltered data or spectrum. 163

5.3 Estimates of the delay of the methane response to the ozone forcing. **(a)** Cross correlation of the changes in ozone and methane abundances for the 1984–1998 period. The delay can be estimated by the lag corresponding to the maximum cross correlation. **(b)** Plot of $G(L)$ from Equation (A.16). The delay can be estimated by the lag corresponding to the first positive root. 164

5.4 Paired ozone-methane changes (with a 6 month delay). The sensitivity, α_{CH_4}, is the slope of the least squares linear fit (solid line) to the paired data. Data between Apr. 1984 and Dec. 1991 are denoted by +'s. Data between Jan. 1992 and Dec. 1998 are denoted by $\diamond$'s. Least square linear fits are shown for the data prior to 1992 (dotted line) and the data for 1992 on (dashed line). 165

5.5 **(a)** Comparison of the filtered methane data (solid line) to filtered ozone data (dotted line). The ozone data has been shifted up 6 months and its amplitude has been multiplied by the sensitivity, α_{CH_4}. **(b)** Comparison of the filtered methane data to the simulated methane response (dotted line). 166

List of Tables

2.1 Frequency Filters 30

2.2 Correlations between TOMS and MOD PCs and Various Indices 30

2.3 Correlations between NCEP/NCAR Reanalysis PCs and Various Indices 31

3.1 Correlations between MOD PCs and Various Indices 71

3.2 Correlations (Lag = 0) and Maximum Cross Correlations of the Stream Function PCs with Various Indices. The numbers in parentheses denote significance levels. Units of lag are month. Positive (negative) lags correspond to the PC time series leading (trailing) the indices. 71

3.3 Correlations between 2D Model Ozone and Zonal MOD. 72

4.1 Clustered eigenvalues and the periods of the associated oscillations for three SSA analyses. Clusters which satisfy a same-frequency test are shown in parentheses. 121

5.1 **Calculated sensitivity, α_{CH_4}, of the methane response to ozone fluctuations.** The sensitivity is estimated by the slope of the linear fit to the paired ozone and methane data, as shown in Figure 5.4. Values are shown for the entire time domain and for a partition of the time domain. Values for the intercepts of the linear fits are also given. . . . 161

5.2 **Correlations between the methane observations, $(\mathbf{CH_4})_\mathbf{d}$, and the ozone observations, $\mathbf{O_3}$, and the simulated methane response, $(\mathbf{CH_4})_\mathbf{s}$.** The coefficient of determination (R^2), associated Fisher Z significance and estimated degrees of freedom are also shown. 161

5.3 **Sensitivity, $\alpha_\mathbf{X}$, of tropospheric chemical species X to stratospheric ozone changes for the period 1979–1994.** The values reported here correspond to the relative change in global tropospheric annual average levels in X (%) resulting from a 1% decrease in total column ozone; the assumed scenarios are discussed in the cited publications. The type of model used is indicated in parentheses. Note that the values of Granier *et al.* (1996) correspond to the 1990–1994 period. The calculations indicated as Granier-1997 correspond to the 1979–1994 period and have been obtained using an updated version of the model used by Granier *et al.* (1996). 161

Chapter 1

Overview

This dissertation is a collection of empirical and odeling studies focusing on the interannual variability (IAV) of stratospheric ozone and the dynamics associated with that variability.

Chapter 2[1] studies the IAV of the tropical total ozone column as seen in satellite observations. A principal component analysis is used to determine the dominant patterns of variability. Results are then compared to dynamical fields from the National Centers for Environmental Prediction (NCEP)/ National Center for Atmospheric Research (NCAR) reanalysis in order to connect physical processes to the observed modes of variability.

Chapter 3[2] extends the tropical analysis into the midlatitudes. In addition, ozone IAV is simulated using a two-dimensional chemical transport model driven by a monthly mean meridional circulation derived from the NCEP/NCAR reanaly-

[1]Chapter 2 has appeared as "Temporal and spatial patterns of the interannual variability of total ozone in the tropics" in *J. Geophy. Res.*, **108(D20)** (2003), 4643, doi:10.1029/2001JD001504 (co-authored with Mark S. Roulston and Yuk L. Yung). It is reproduced in this dissertation with permission of the publisher.

[2]Portions of Chapter 3 are to appear as "QBO and QBO-annual beat in the tropical total column ozone: A two-dimensional model simulation" in *J. Geophy. Res.*, (2004), doi:10.129/2003JD004377 (co-authored with Xun Jiang, Run-Lie Shia, David Noone, Christopher Walker, and Yuk L. Yung). It is reproduced in this dissertation with permission of the publisher.

sis. Simulated ozone results are compared to satellite observations of ozone. I would like to acknowledge Xun Jiang and Run-Lie Shia for their work in deriving the stream function and running the 2D model.

Chapter 4 is a singular spectrum analysis (SSA) of a 71-year record of column ozone from Arosa, Switzerland. This long continuous record allows a detailed study of the IAV to be performed and the SSA technique allows intermittent, anharmonic oscillations and nonlinear trends to be extracted.

Chapter 5[3] is an investigation of a mechanism by which IAV variability in stratospheric ozone affects concentrations of tropospheric methane. This is an unusual mode of stratospheric-tropospheric interaction, in which UV radiation to couple stratospheric dynamics to tropospheric chemistry.

[3]Chapter 5 and Appendix A appeared as "The sensitivity of troposheric methane to the interannual variability in stratopsheric ozone" in *Chemosphere — Global Change Science*, **3** (2001), 147-156 (co-authored with Mark S. Roulston, Albert F. C. Haldemann, and Yuk L. Yung). It is reproduced in this dissertation with permission of the publisher.

Chapter 2

Temporal and Spatial Patterns of the Interannual Variability of Total Ozone in the Tropics

2.1 Introduction

The total column abundance of ozone in the atmosphere represents an intricate interaction between chemical and dynamical processes (see, for example, *Brasseur et al.* (1999)). A primary motivation for studying the interannual variability (IAV) of total ozone is to separate anthropogenic perturbations of the ozone layer from natural variability (see, for example, *WMO* (1999)). The latter imposes "noise" on the system that makes the detection of ozone depletion and its attribution to anthropogenic forcing more difficult. In addition, the IAV offers insights into the subtle coupling between chemistry and dynamics that are important for determining the abundance and distribution of ozone, as well as providing opportunities to test the sensitivity of models to external and internal forcing.

An extensive global dataset is currently available for studying IAV of ozone. The Total Ozone Mapping Spectrometer (TOMS) instrument on the Nimbus 7 space-

craft measured the spatial distribution of total ozone from 1978 until 1993 (*Herman et al.*, 1991). By scanning across the track of the satellite, TOMS obtained data between successive satellite orbital tracks. Daily TOMS gridded ozone data of Version 7 (*McPeters et al.*, 1996) (on a $1^\circ \times 1.25^\circ$ grid in latitude and longitude) are available from 1979 to 1992. The data were extended to 2000 (on a $5^\circ \times 10^\circ$ grid) in the the Merged Ozone Datasets (MOD), which combine the monthly mean column abundances of the of TOMS instruments on Nimbus 7 and Earth Probe with additional data from the Solar Backscatter Ultraviolet (SBUV and SBUV/2) instruments on Nimbus 7, NOAA 9, NOAA 11 and NOAA 14.

Previous studies have fruitfully mined the rich TOMS dataset. Using globally averaged TOMS data, *Herman et al.* (1991) detected the ozone depletion trend, quasi-biennial oscillation (QBO) and a possible 11-year solar cycle variation. Using zonally averaged TOMS data, *Tung and Yang* (1994a,b) studied the propagation of QBO effects from the tropics to the midlatitudes, and the interaction between the QBO and the annual cycle, giving rise to 20-month and 8.6-month oscillations. *Shiotani* (1992) studied the zonal variability of ozone in the tropics related to the El Niño-Southern Oscillation (ENSO) and *Kayano* (1997) carried out an empirical orthogonal function (EOF) study of the relation between total ozone and ENSO.

However, we notice the curious omission of a *simultaneous* decomposition of the TOMS data to reveal all spatial and temporal patterns in the tropics. This paper attempts to fill this gap in our analysis of total ozone.

The analysis was restricted to the tropics because the midlatitudes demonstrate

more variability than the tropics. This can be seen in Figure 2.1, which shows the standard deviations for the time series at each grid point of the detrended, deseasonalized Merged Ozone Data. (Details of this dataset and its processing are described in the following section.) The inclusion of data from higher latitudes in the analysis would result in EOF patterns dominated by midlatitude signals. Therefore, the tropical patterns would be much harder to isolate and analyze.

In Section 2.2, the datasets and indices used are described. In Section 2.3, the EOF technique is briefly discussed. The results of the EOF analysis of the ozone data are shown in Section 2.4. Comparisons of this analysis to physical processes are discussed in Section 2.5. In Section 2.6, an EOF analysis of the NCEP/NCAR data is shown and compared to the ozone results. Section 2.7 contains conclusions and final remarks.

2.2 Datasets and Indices

For this study, we have used two datasets for monthly mean column ozone abundances: Nimbus 7 TOMS (*McPeters et al.*, 1996) and the Merged Ozone Data (MOD) as described in the NASA website,

http://code916.gsfc.nasa.gov/Data_services/merged/mod_data.public.html.

For both datasets, we have restricted our analysis to a tropical band from 25°S to 25°N. To lower the computational load of the EOF analysis, the TOMS data has been rebinned from its original 1°×1.25° grid to a 2°×7.5° grid. The MOD data is on a 5°×10° grid. We have used the TOMS data from Nov. 1978 to Apr. 1993 and the

MOD data from Nov. 1978 to Dec. 2000.

Data from the National Centers for Environmental Prediction and National Center for Atmospheric Research (NCEP/NCAR) reanalysis were also analyzed (*Kalnay et al.*, 1996). To match the analyses performed on the ozone datasets, we restricted the EOF analysis of the NCEP/NCAR fields to the 25°S to 25°N tropical band. The data were also rebinned from the original 2.5°×2.5° grid to a 2°×7.5° grid. Cubic spline interpolation was used to refine the latitude spacing. The EOF analysis was performed on data from Jan. 1979 to Sept. 1999.

All datasets were detrended by removing the linear long-term trends from the time series of each grid point; the linear trends were determined by a least squares fit. Seasonal cycles for each time series were also removed; cycles were determined by taking averages for each month independently. Missing months were replaced by cubic spline interpolation in time. To isolate interannual variability from higher-frequency oscillations, further filtering was performed spectrally. The spectral filter applied was a convolution of a step function with a Hanning window chosen to obtain a full signal from periods above 15 months and no signal from periods below 12.5 months; see *Press et al.* (1992, Chap.13). The details of this filter, Lowpass A, and other similarly constructed filters used in this study are shown in Table 2.1.

Various indices were used to help identify the processes seen in the EOF analyses. For a QBO index, we used the QBO Zonal Wind Index, 1953–September 2001. For our time interval, this index uses the 30 hPa zonal wind measured above Singapore (1°N, 104°E). Further details can be found in *Naujokat* (1986), *Marquardt* (1997) and

Marquardt and Naujokat (1997). For an ENSO index, we used the SOI: Standardized Sea Level Pressure Anomaly time series described in the International Research Institute for Climate Prediction (IRI) web site:
http://ingrid.ldgo.columbia.edu/SOURCES/.Indices/.soi/ .dataset_documentation.html.
For a solar cycle index, we used the Adjusted Monthly Solar Flux: 2800 MHz Series C time series, described on the NOAA web site:
http://spidr.ngdc.noaa.gov/spidr/help/solar_main.htm#flux.
Linear detrending and lowpass filtering, using the Lowpass A filter, were performed on all indices.

For presentation purposes only, the data for all color figures have been bilinearly interpolated to a much finer spatial resolution.

2.3 Methodology

Given a multivariate dataset consisting of measurements from S stations taken simultaneously at T times, the EOFs are found by determining the eigenvectors of the covariance matrix, $\mathbf{C}$, of the dataset constructed from the T measurement vectors, $\mathbf{x}_t$ (*i.e.* the state of the system at time t) (*Preisendorfer*, 1988). If $\mathbf{X}$ is the matrix given by $\mathbf{X} = [\mathbf{X}_t]^*$ $(T \times S)$ and the temporal means of the data from each station have been removed, then the covariance matrix is given by

$$\mathbf{C} = \frac{1}{T}\mathbf{X}^*\mathbf{X} \qquad (S \times S) \tag{2.1}$$

The covariance matrix is a real symmetric positive-semidefinite matrix and can therefore be written as

$$\mathbf{C} = \mathbf{Q}\mathbf{\Lambda}\mathbf{Q}^* \tag{2.2}$$

where $\mathbf{\Lambda}$ is a diagonal matrix whose elements are the S real, nonnegative eigenvalues, λ, and $\mathbf{Q}$ is a orthogonal matrix whose columns are the S orthonormal eigenvectors, $\mathbf{e}$. These eigenvectors are the EOFs and form a new basis with which the original data can be represented,

$$\mathbf{X} = \mathbf{P}\mathbf{Q}^* = \sum \mathbf{p}\mathbf{e}^* \qquad (T \times S) \tag{2.3}$$

$\mathbf{P}$ is a $(T \times S)$ matrix whose columns, $\mathbf{p}$, are the S principal component time series (PCs) determined by projecting the original dataset onto the associated EOFs,

$$\mathbf{p} = \mathbf{X}\mathbf{e} \tag{2.4}$$

Combining equations (2.1),(2.2) and (2.3), we can see that

$$\mathbf{\Lambda} = \frac{1}{T}\mathbf{P}^*\mathbf{P} \tag{2.5}$$

Since $\mathbf{\Lambda}$ is diagonal, the PCs ($\mathbf{p}$) are mutually orthogonal and the eigenvalues (λ) are equal to their variances. In the context of this study, the EOFs can be considered two-dimensional spatial standing waves while the associated PCs are the time-dependent amplitudes of their oscillations. The associated eigenvalues are the variances cap-

tured by each EOF. When sorted by decreasing λ, the leading n eigenvectors (EOFs) describe more variance than any other n vectors.

It is clear from Equation 2.3 that an arbitrary scaling factor can be applied to the EOFs, if it is simultaneously removed from the associated PC. One convention is to normalize the EOFs, $\|\mathbf{e}\| = 1$; then the variance of the associated PCs will be equal to the associated eigenvalues. However, to present our results more clearly, we wanted the EOF patterns to have dimensional units. Therefore we have multiplied the EOFs (and divided the PCs) by the square root of their associated eigenvalue, *i.e.*, the standard deviation of the conventional PC. Therefore our PCs have been normalized to have unity standard deviation, while the EOFs display typical values of the amplitude of oscillation at each grid point. The peak-to-trough amplitudes of the oscillations at any grid point can be recovered by taking the product of the EOF value and the peak-to-trough amplitude of the associated PC time series.

Significance statistics for correlations between time series, such as PCs and indices, were generated by a Monte Carlo (bootstrap) method (*Press et al.*, 1992, chap. 15). Three thousand isospectral surrogate time series (same power spectrum, randomized phases) were generated for each comparison to create a distribution of correlations. This distribution was transformed into an approximately normal distribution by the Fisher transformation (*Devore*, 1982). The significance level of the actual (transformed) correlation within the transformed-correlation distribution was then determined.

2.4 Ozone EOFs

EOF analyses were performed on the [25°S, 25°N] latitude band of the detrended, deseasonalized MOD and TOMS datasets. The patterns found in the decomposition of MOD are quite robust; analyses performed on other latitude bands have very similar patterns and symmetries. The TOMS analysis has the same features as the MOD analysis; however, they appear in different combinations within the first few EOFs than they do in the MOD analysis. The relationship between the derived spatial patterns, their associated time series and physical processes will be discussed in Section 2.5.

2.4.1 Merged Ozone Data (MOD) EOFs

The first four EOFs of MOD together account for more than 93% of the variance, as shown by the solid line in Figure 2.2. The spatial patterns associated with these EOFs are shown in Figure 2.3. The associated PC time series and their Fourier spectra are shown in Figure 2.4. Each PC is shown in comparison to an appropriate index.

The first EOF (MOD EOF1) captures 42% of the variance of MOD. It is basically a meridional arc showing zonal uniformity and symmetry about the equator. It oscillates about nodes at latitudes approximately 15° off the equator. The values shown range from a high of 7.0 Dobson units (DU) on the equator to a low of -2.8 DU at the northern boundary. The associated PC time series (MOD PC1), given in Figure 2.4a, shows the amplitude of the oscillation of this EOF in MOD. A maximum peak-to-trough amplitude of approximately 28 DU occurs in the equatorial Pacific.

The spectrum of the PC, Figure 2.4b, shows a dominant peak at 28 months with a secondary decadal signal. There are additional peaks at approximately 18 months and 4 years. Figure 2.4a shows the PC (solid line) compared to the QBO index (dotted line).

A quick comment about the fine-scale features of the EOFs: While the maximum of MOD EOF1 actually appears to occur a couple of degrees south of the equator, we are reluctant to subscribe any significance to this asymmetry (as well as to other fine-scale behavior in this and following EOF patterns). Since MOD has 5° latitude bins, we can only say that the maximum occurs between 2.5°N and 2.5°S. Furthermore, the fine-scale features are not robust between analyses, whereas the qualitative nature is.

The second EOF (MOD EOF2) is similar to MOD EOF1 in that it is basically a zonally uniform and equatorially symmetric meridional arc, albeit with somewhat more zonal structure than MOD EOF1. It captures 33% of the variance of MOD. However, the pattern is almost entirely negative, barely breaking zero only at the equator. The maximum of 0.9 DU lies on the equator and the minimum of −6.4 DU at the northern boundary. It is thus very similar to EOF1 except for a DC shift (*i.e.*, a spatially constant offset). The associated PC (MOD PC2)is shown in Figure 2.4c. The spectrum of the PC, Figure 2.4d, has the same two primary peaks, 28 months and decadal, but the decadal is clearly dominant.

The third EOF (MOD EOF3), capturing 15% of the variance, is a tilted plane oscillating about the equator. The pattern is still roughly zonally uniform, but it is now antisymmetric about the equator. Values range from 3.5 DU in the north to

−4.1 DU in the south. The spectrum of the associated PC, shown in Figure 2.4f, has a single dominant peak at 21 months.

The fourth EOF (MOD EOF4), capturing less than 4% of the variance, is the first occurrence of a pattern with strong zonal structure. Roughly symmetric about the equator, the EOF is a standing wave oscillating about nodes in the western and eastern Pacific. Values range from 2.1 DU in the central Pacific to −3.1 DU over Indonesia. The spectrum of the associated PC, Figure 2.4h, is fairly broad with its highest peak at a period of 4 years and substantial power in periods greater than 5 years.

Analyses performed on MOD for [20°S, 20°N] and [30°S, 30°N] latitude bands (not shown) display very similar results to the analysis of [25°S, 25°N] band of MOD described above.

2.4.2 TOMS EOFs

The EOF decomposition of the TOMS dataset displays the same features as described above for the MOD analysis, albeit in a different combination. The TOMS dataset has a finer spatial resolution than MOD, but a shorter time series. Therefore the EOFs show more detail, but the PCs are in general noisier and the spectra less resolved. In particular, with only 14 years of data, all correlations with decadal signals must be treated with great caution.

The first four EOFs capture over 94% of the variance of TOMS with basically the same individual contributions as in the MOD decomposition; see Figure 2.2. The

first three TOMS EOFs and PCs (not shown) contain the same basic structures as the equivalent MOD EOFs and PCs, but in a different combination than that seen in the MOD analysis. TOMS EOF1 shows the meridional arc and its associated spectrum shows the 28-month peak. TOMS EOF2 shows a combination of a tilted plane and a DC shift with its spectrum dominated by a broad low-frequency band (7–10+ years) and a secondary peak at 20 months. TOMS EOF3 shows a tilted plane (its node slightly offset from the equator) and a dominant 20-month peak with a secondary low-frequency signal. These are the same features that appear in the first three MOD EOFs and PCs, but they have been shuffled somewhat. In the TOMS decomposition, the DC shift and decadal components are combined with the tilted plane and 20-month signals in the second and third EOFs/PCs, as opposed to being combined with the meridional arc and 28-month signals as occurs in the first and second EOFs/PCs of the MOD analysis. This conflation of signals is discussed in detail in Section 2.5.2.

Like MOD EOF4, the fourth TOMS EOF (Figure 2.5) is the first appearance of a pattern with a primarily longitudinal oscillation; however, it has a somewhat different structure. Both EOFs show rough equatorial symmetry and a zonal oscillation with nodes in the central and western Pacific. But in TOMS EOF4, there is a double-ridged symmetric structure with ridges at 12°N,S and maxima thereof at 150°W; this structure was not present at the lower spatial resolution of MOD EOF4, which exhibited a maximum near the equator at 150°W. Furthermore, TOMS PC4, Figure 2.6a, has a much cleaner spectrum, Figure 2.6b, than its MOD counterpart, Figure

2.4h, despite coming from a shorter dataset.

2.5 Analysis of the Ozone Decomposition

The patterns seen in both the MOD and TOMS EOF decompositions can be closely tied to dynamical processes in the atmosphere. Most of the structure in the first four EOFs of both datasets can be attributed to three physical processes: the QBO, the interaction between the QBO and annual cycles, and ENSO. There is also substantial contribution from a process (or multiple processes) fluctuating on decadal time scales. With the exception of the decadal behavior and (to a much lesser degree) ENSO, the EOF analyses separate these processes into distinct EOFs. The correlations between indices for the physical processes and the PCs of both MOD and TOMS are listed in Table 2.2.

2.5.1 QBO and Decadal

Ignoring for the moment the decadal signal, the dominant pattern seen in the first two EOFs of both datasets is the meridional arc structure oscillating with a period of 28 months. These are the spatial and temporal characteristics of the effect of the QBO on the ozone. Ozone is primarily created in the tropics of the middle stratosphere and carried poleward by the Brewer-Dobson circulation. This zonal mean meridional circulation is slow compared to the mean zonal wind. Therefore the spatial patterns of tracer transport associated with it should be zonally uniform to first order. During its westerly (easterly) phase, the QBO diminishes (enhances) the

Brewer-Dobson circulation (*Plumb and Bell*, 1982; *Baldwin et al.*, 2001). Therefore the tropical column ozone will increase (decrease) while the opposite will occur at higher latitudes. The phase change of this effect occurs at approximately 12° north and south of the equator (*Tung and Yang*, 1994a). The patterns of both EOFs are roughly characteristic of the QBO, but the nodes of the EOFs appear to occur at the wrong latitudes. Furthermore, the appearance of two very similar EOFs and the conflation of the QBO and decadal signals obscures the connection to either process. These points will be revisited later in Section 2.5.2.

The source of the decadal signal is an area of active research. One strong candidate is the decadal variation in the solar flux (*Chandra and McPeters*, 1994; *Shindell et al.*, 1999). An increase in insolation leads to an increase in net ozone production. However, it has been demonstrated that this cannot account for all of the amplitude of the decadal variation (*WMO*, 1999). Furthermore, the solar cycle appears to have a more complicated relationship with some of the other processes involved. For example, the length of the positive and negative phases of the QBO may be affected by the solar cycle (*Salby and Callaghan*, 2000).

For better comparison to the QBO and Solar Flux indices, MOD PC1 and PC2 were filtered to isolate the two signals. The Bandpass A filter (Table 2.1) was used to remove the decadal contribution. The filtered PCs are compared to the QBO index in Figures 2.7a,c. The Lowpass C filter was used to remove the QBO contribution. Figures 2.7b,d show the results in comparison to the Solar Flux index. These indicate that MOD PC1 has a positive correlation with both the QBO and Solar Flux while

MOD PC2 has a positive correlation with the QBO but a negative correlation with the Solar Flux.

2.5.2 Separating the QBO and Decadal Signals

The conflation of decadal and QBO signals in the first two EOFs and the appearance of similar patterns in the two orthogonal EOFs need further examination. It is unclear from the original EOF analysis whether the decadal signal is independent of the QBO time scale signal or if it is a low-frequency variation in the higher-frequency signal.

Since both EOFs are roughly zonally uniform, it is simpler to explore the zonal averages of the EOFs, shown in Figure 2.8a. MOD EOF2 (dashed line) is basically a constant shift of MOD EOF1. Recalling the filtered PCs, Figures 2.7a–d, both MOD EOF1 and EOF2 are positively correlated with the QBO index. Therefore, on QBO time scales, EOF1 and EOF2 oscillate in phase. But EOF2 is inversely correlated to the Solar Flux, while EOF1 is positively correlated, so on decadal time scales they oscillate a half period out of phase. Therefore the QBO contribution is the weighted sum of the two EOFs, while the decadal contribution is the weighted difference. The weights for the sum can be determined by finding the standard deviation of the Bandpass A filtered PCs. They roughly represent the portion of the amplitude of the oscillation of each EOF attributable to QBO time scales. The weights for the difference can be determined by finding the standard deviation of the Lowpass C filtered PCs and represent the portion attributable to decadal time scales. The weighted sum (solid line) and difference (dashed line) of the zonal averages calculated

in the manner are shown in Figure 2.8b. This suggests that, for the combination of the first two EOFs, the QBO time scale signal is a meridional arc with nodes at approximately 11° off the equator, while the decadal signal is roughly a flat plane with no nodes. Thus, by separating the QBO and the decadal contributions, we have recovered the expected structure for the QBO signal and identified one for the decadal variability.

The same procedure can be performed with the full EOFs instead of the zonal averages and an associated time series can be found by projecting the original data onto these constructed patterns. However, these patterns and time series will no longer be mutually orthogonal.

A more rigorous way to separate the decadal and QBO time scale signals is to filter the data for the desired frequencies *prior* to performing the EOF analysis. It should however be noted that disadvantages of this method include the loss of the ability to examine long-term fluctuations of shorter time scale features and the possible distortion of highly nonsinusoidal signals when narrow-bandwidth Fourier filtering is applied. These caveats notwithstanding, this procedure is a useful confirmation of the previous linear combination method. This procedure was performed using the Bandpass B and Lowpass B filters described in Table 2.1. The leading EOFs of the resulting analyses are shown in Figure 2.3. These EOFs are very similar to those found by the linear recombinations of the full (2D) MOD EOF1 and EOF2 (data not shown).

The first two EOFs of the Bandpass B filtered MOD (MOD-Band), capturing

81% of the variance of the filtered dataset, display patterns associated with the QBO without the interference from any decadal process(es). Obvious signs of ENSO are also removed, although higher harmonics of ENSO's fundamental period may still be present. These harmonics are discussed later in more depth.

The first EOF, Figure 2.9a, captures 61% of the variance. It shows the QBO pattern with nodes at approximately 12° off the equator. Values range from 6.3 DU at the equator to −4.8 DU at the northern boundary. The associated PC (data not shown) correlates well with the QBO index; see Table 2.2. Its spectrum is very similar to the portion of the MOD PC1 spectrum contained between periods of 1 to 3 years; see Figure 2.4b. The second EOF (data not shown) captures 20% of the variance. It shows a tilted plane pattern similar to that of MOD EOF3, Figure 2.3c. This pattern is characteristic of the QBO-annual beat, described later in this section. Values are similar, ranging from 3.6 DU in the north to −2.8 DU in the south, and there a little more longitudinal structure. The spectrum of the associated PC shows a clean peak at 21 months, again similar to MOD PC3, Figure 2.4f.

The first EOF of the Lowpass B filtered MOD (MOD-Low), Figure 2.9b, captures over 76% of the variance of the filtered data. It is roughly a flat plane with no nodes; values are strictly positive, ranging from 4.0 DU to 2.0 DU. This DC component seems to be a consistent feature of the patterns associated with decadal variability. The associated PC correlates well with the Solar Flux index; see Table 2.2. Its spectrum shows a strong decadal peak and a weaker broad peak at 3.5–4.5 year periods. This is probably due to ENSO and is the likely source of much of the longitudinal variability

of this EOF. The decadal signal can be separated from the ENSO signal by a tighter filter, *e.g.* the Lowpass C filter. However, this restrictive a filter would leave very few degrees of freedom in the resulting time series, so the resulting EOF analysis might not be very robust.

2.5.3 QBO-Annual Beat

The third MOD EOF displays a tilted plane oscillating about a node at the equator with a period of 21 months. These are spatial and temporal characteristics of the interaction between the QBO and annual cycles. The modulation of the annual meridional transport by the tropical QBO results in the creation of two beat oscillations with frequencies equal to the sum and difference of the QBO and annual frequencies, *i.e.*, at periods of 21 and 8.4 months (*Tung and Yang*, 1994a; *Baldwin et al.*, 2001). While this process is primarily an extratropical one, its effects can be seen inside the [25°S, 25°N] band of this study. However, the interaction between the QBO and any annual cycle (*e.g.* the annual cycle in ozone production) has the potential to create identical beat frequencies. Modeling work to determine the correct phase of the beat oscillations as well as their amplitudes may help determine which annual cycle is responsible for the beat frequency seen here.

Since the data for these analyses have been lowpass filtered for periods above 15 months, only the 21-month beat appears in these EOFs. To determine if the high-frequency beat can be resolved, we redid the EOF analysis of the MOD data using Bandstop Filter A (MOD-Notch) instead of Lowpass Filter A. In this analysis, only

periods between 15 and 9.5 months were damped or removed, in order to remove the shoulders of the annual cycle peak that remained after the mean annual cycle was removed. The resulting EOFs were nearly identical to those found in the analysis of the lowpass filtered MOD except that the percentage of the variability explained by the first four EOFs dropped by about 10%. This is not due to a decrease in the absolute variance explained, but rather to the approximately 10% increase in total variance of the dataset caused by the presence of the high-frequency signals. The PC of the third EOF, shown along with its spectrum in Figure 2.10, contains the signal of both the 21-month and 8.4-month beat interactions.

In the TOMS analysis, both PC2 and PC3 display the characteristic 20-month frequency of the QBO-annual beat, but they also have a decadal component. The spatial structures are tilted planes offset from each other by a DC shift. This is analogous to the conflation of QBO and decadal seen in the MOD analysis and they can be separated in a similar manner.

2.5.4 ENSO

The fourth EOFs of the MOD and TOMS sets display a zonal wavenumber-1 oscillation with extrema in the central Pacific and near Indonesia. The spectra show peaks at periods around 4–5 years, but there is a broad range of frequencies with substantial power. This is strongly suggestive of the spatial and temporal characteristics of the (highly nonsinusoidal) ENSO process. Comparisons to the SOI index confirm that these EOFs are dominated by ENSO. The noisiness of the EOF and PC in MOD can

be at least partially attributed to the low spatial resolution. A much cleaner ENSO signal is seen in the TOMS dataset EOFs. The TOMS EOF4 has the characteristic bimodal structure in the central Pacific and the spectrum of TOMS PC4, Figure 2.6b, clearly shows the set of harmonic frequencies of the fundamental 56-month frequency (*Jiang et al.*, 1995; *Ghil and Robertson*, 2000). The presence of the bimodal structure in the TOMS EOF4 means that only processes with such structure, such as ENSO, will strongly project onto this EOF. Therefore the resulting PC has a cleaner signal and spectrum. For the ENSO signal, the increased spatial resolution of the TOMS data has thus overcome the limitations inherent in its shorter time series.

One possible source of the ENSO signal in ozone is the induced variation in tropospheric ozone due to changes in western Pacific convection patterns and to biomass burning. Another possible source is the induced variation in the tropopause height. During El Niño years, *i.e.*, negative SOI, increased convection in the central Pacific raises the tropopause height. This, in turn, causes a decrease in total column ozone. A vertical perturbation in the tropopause in the tropics generally coincides with a vertical perturbation in an isentropic surface. The relatively rapid movement of air along an isentropic surface mixes air at the higher elevation of the perturbation with the surrounding lower air. Since the ozone concentration generally increases with height near the tropopause, this mixing lowers the ozone concentration at the perturbation while raising the concentration in the surrounding air. This is a similar mechanism to that proposed in *Salby and Callaghan* (1993) for ozone variations on synoptic time scales. During La Niña years, *i.e.*, positive SOI, the opposite will occur, causing a

relative increase in total column ozone over the central Pacific.

ENSO probably has a projection on to the first MOD EOF as well. It is the likely source of the 4–5 year period fluctuation seen in the MOD PC1, Figure 2.4a–b. Furthermore, the double peak at ∼16 months is consistent with ENSO's ∼16-month 2nd harmonic. The signal of the first harmonic of ENSO, at ∼2–2.5 years, would be obscured by the dominant QBO peak. Since the structure of this oscillation is zonally uniform, it would correspond to the overall warming of the tropics that occurs during El Niño years. This effect on the ozone column is most likely due to tropopause height variations rather than biomass burning, since the latter has a large longitudinal variation.

2.6 Analysis of NCEP/NCAR Data

For comparison to structures in dynamical variables, similar analyses were performed on various fields from the NCEP/NCAR reanalysis product. To examine the behavior near the tropopause, we performed an EOF decomposition on the geopotential height of the 100 hPa pressure surface (NCEP-100). To examine the behavior in the stratosphere, we performed an EOF analysis on the thickness of the layer determined by differencing the geopotential heights of the 30 hPa and 100 hPa pressure surfaces (NCEP-Layer). The 30 hPa level is near the region of maximum ozone density within the column. Ozone is the principal absorber of solar UV radiation in the stratosphere (*Goody and Yung*, 1989). An increase in ozone concentration would result in an increase in the stratospheric heating rate, and hence the temperature. Near 100 hPa,

the temperature is dynamically controlled and is expected to be insensitive to ozone heating. However, near 30 hPa the temperature is radiatively controlled. Therefore, increases (decreases) in the ozone of the lower stratosphere will induce thermal expansion (contraction) of the lower stratosphere. The results, particularly for the NCEP-Layer analysis, are probably caused by a combination of the direct effect of the physical processes on the dynamical variables and an indirect effect using chemical species such as ozone as an intermediary.

2.6.1 Layer Thickness EOFs

The first four EOFs of the NCEP-Layer data capture over 97% of the variance. They show roughly the same basic structures seen in the ozone analyses, except that patterns of the third and fourth NCEP-Layer EOFs correspond to the fourth and third ozone EOFs, respectively. Furthermore, with its finer spatial resolution, NCEP EOF3 displays a bimodal structure closer to that of TOMS EOF4, rather than to the equatorially centered structure of MOD EOF4. The spatial patterns are shown in Figure 2.11, associated PC time series and spectra in Figure 2.12 and correlations in Table 2.3.

As in the ozone analyses, the first two EOFs (capturing 79% and 14% of the variance, respectively) show the meridional arc structure associated with the QBO. However, there is a strong spatial DC shift in the first EOF, Figure 2.11a. It is strictly positive with values ranging from 34 meters on the equator in the central Pacific to 17 meters on the north and south boundaries. There is also substantially more zonal

variation than was seen in the first EOFs of the ozone data. The second EOF, Figure 2.11b, is the more standard shape with nodes occurring at an average of ∼11° off the equator. The spectrum of the first PC, Figure 2.12b, shows peaks at decadal and QBO periods but is in general noisier than the comparable spectrum from MOD PC1.

Figure 2.13 shows the results of Bandpass A and Lowpass C filtering on NCEP-Layer PC1 and PC2. As in the ozone EOFs, NCEP-Layer PC1 and PC2 are positively correlated with each other on QBO time scales and inversely correlated on decadal time scales. Zonal averages and their weighted sum and difference are shown in Figure 2.14. The QBO time scale behavior is a meridional arc, with a maximum of the equator of 37 m, while the decadal time scale behavior is relatively flat. However, unlike the ozone results, the QBO structure does not recover the ∼12° nodes seen in the ozone analysis; it is almost entirely positive with a node at ∼22°S and not quite reaching zero by the northern boundary at 25°N. It is not clear if this spatial DC shift on QBO time scales is a real physical behavior, an artifact of the NCEP/NCAR reanalysis data or an artifact of the EOF analysis. It is possible that later EOFs could compensate for this shift, although the decreasing amplitudes of subsequent EOF eigenvalues make this rather unlikely.

The ENSO and QBO-annual beat patterns appear in the NCEP-Layer analysis in opposite order to that of the ozone analyses. The third NCEP-Layer EOF, Figure 2.11c, captures 3% of the variance and shows the zonal oscillation associated with ENSO while the fourth, Figure 2.11d, captures 1.5% of the variance and shows the

tilted plane of the QBO-annual beat. Compared to MOD EOF3, there is substantially more zonal variation in NCEP-Layer EOF4. This can be primarily ascribed to the small percentage of variability that it captures; it is much closer to the background noise level.

We can investigate the relative importance of ozone fluctuations in the NCEP-Layer results by making a rough calculation of the expected amplitude of the thermal expansion caused by solar absorption. An approximate estimate based on radiative equilibrium yields 1°K increase for every 10 DU increase in ozone column; see Figures 14 and 15 of *McElroy et al.* (1974). A change in the NCEP/NCAR reanalysis geopotential height of about 10 m corresponds to a 0.3°K change. The latter change can be caused by an increase of 3 DU in ozone column. We see a 37 m change in the NCEP-Layer results (see Figure 2.14b) corresponding to a 7 DU change in the MOD results, Figure 2.8b. Therefore ozone heating is a important source of the variability seen in the NCEP-Layer data, but other processes such as dynamically forced heating are likely to play a comparable role.

2.6.2 100 hPa Surface EOFs

To examine behavior near the tropopause, an EOF decomposition was performed on the NCEP/NCAR reanalysis 100 hPa geopotential height field (NCEP-100). Spatial patterns from the first two EOFs are shown in Figure 2.15, associated PC time series in Figure 2.16 and correlations in Table 2.3. The first EOF, by itself, captures over 89% of the variance. The spatial pattern, Figure 2.15a, consists of a large zonal

oscillation and a meridional arc superimposed upon a relatively flat plane. Note that the values of the EOF are all positive, ranging from a maximum of 31 m to a minimum of 8 m. The second EOF, capturing less than 5% of the variance, has a similar pattern without the spatial DC shift. Both PCs show evidence of ENSO and decadal oscillations.

Bandpass filter A and Lowpass filter C were applied to the PCs to separate these effects. The resulting time series, along with appropriate indices, are shown in Figure 2.17. They show that NCEP-100 PC1 and PC2 oscillate with opposite phases on decadal time scales but in phase on shorter time scales. This is analogous to the conflation of decadal and QBO signals seen in the MOD analyses. The second EOF enhances the internal structure of the first EOF on the faster time scale, while suppressing it on the decadal time scale. Therefore, the decadal behavior (correlated with Solar Flux) contains less of the zonal and meridional variability; it is dominated by the DC component. The zonal and meridional variability occur primarily on the shorter time scales (inversely correlated with SOI). However, as in the NCEP-Layer analysis, a substantial spatial DC shift at shorter time scales still remains.

Comparing the ENSO-related patterns of these results to those found in the MOD analysis, we can see that NCEP-100 PC1 and PC2 have an inverse correlation with the SOI, while MOD PC4 has a positive correlation (Figure 2.7g). Therefore, for the variations associated with ENSO, the 100 hPa geopotential height and the column ozone anomaly are inversely correlated. This is consistent with the explanation given in Section 2.5.4. A rough estimate of the expected change in the ozone column caused

by these fluctuations in tropopause height can be made. *Stephenson and Royer* (1995) reported about 1 DU increase for every 5 m decrease in the 200 hPa geopotential height. Scaling from their result, we estimate that a 10 m change in geopotential height could cause about 2 DU change in column ozone. This is consistent with our MOD and NCEP-100 results if we compare the relative fluctuations within the NCEP/NCAR reanalysis EOFs, but cannot account for the lack of response to the DC component of NCEP-100 EOF1.

Comparing the patterns associated with decadal variation from the MOD and NCEP-100 analyses, we find a different behavior. Both datasets display a positive correlation with solar flux; therefore, the 100 hPa geopotential height and the column ozone anomaly are positively correlated for the tropical latitudes studied. This is consistent with the model results from *Shindell et al.* (1999) and *Hood* (1997). A possible component of this difference in behavior may be the difference in the patterns associated with decadal and ENSO oscillations. The ENSO pattern has relatively steep gradients, while decadal pattern is primarily a flat DC oscillation. Therefore, little tilting of isentropic surfaces is expected on decadal time scales; therefore, the mechanism described for the ENSO-related variability would not be invoked.

2.7 Conclusions

We have shown the spatial-temporal patterns of tropical column ozone variability on interannual time scales. To our knowledge, this is the first time longitudinal, latitudinal and temporal behavior has been simultaneously examined. Spatial patterns

relating to the fluctuations of the QBO, QBO-annual beat and ENSO have been identified and decadal oscillations examined. The structure of these patterns appears in the ozone record quite robustly (with a reshuffling of the components in the TOMS analysis) and in the NCEP/NCAR reanalysis fields as well, albeit with less fidelity.

We have been able to distinguish the meridional shape of the QBO, *i.e.*, the meridional arc, from the relatively flat plane oscillating on decadal time scales. The decadal fluctuations in ozone oscillate in phase with the 11-year solar cycle but the shortness of the ozone record precludes the confirmation of the connection.

Three oscillations associated with the QBO have been identified: the standard 28-month cycle and the 20-month and 8.6-month QBO-annual beats. The equatorially asymmetric spatial pattern of the QBO-annual beat has been isolated from the symmetric one of the 28-month cycle. Both patterns show the expected zonal uniformity, and the meridional phase transition of the QBO signal at $\sim 12^\circ$ off the equator has been recovered as well. A time series relating to the QBO-annual beat has been determined thereby allowing questions of the phase of this oscillation to be addressed in later work.

The effect of ENSO on the ozone column has also been identified. It is a testament to the precision of the TOMS and MOD datasets that such a small signal, $\sim 1\%$ of total column ozone, is seen so clearly. A mechanism linking the column ozone abundance to the ENSO cycle through the variation of tropopause height has been proposed, but separation of this process from the effects of tropospheric ozone variations induced by ENSO is beyond the scope of this study.

This work constitutes a preliminary study of each of these processes, particularly for the decadal signal. We have primarily focused on matching the phase and periods of the signals, while discussing the qualitative nature of the spatial patterns. Future work should include quantitative studies of the amplitudes of the oscillations and comparisons to modeling studies. The extension of this analysis to higher latitudes is also desirable.

Table 2.1: Frequency Filters

Filter Name	Period Ranges (mo.)	
	Passed	Stopped
Lowpass A	(15, max)	(0, 12.5)
Lowpass B	(40.5, max)	(0, 34.5)
Lowpass C	(72, max)	(0, 50)
Bandpass A	(15, 72)	(0, 12.5) & (96, max)
Bandpass B	(15, 34.5)	(0, 12.5) & (40.5, max)
Bandstop A	(0, 9.5) & (12.5, max)	(11.5, 12.5)

Table 2.2: Correlations between TOMS and MOD PCs and Various Indices

PC #	Filter	Index	Corr.	Sig. (%)
		MOD PCs		
1	(none)	Solar Flux	0.26	84.3
	Lowpass C		0.80	91.4
	(none)	QBO	0.80	99.91
	Bandpass A		0.84	99.91
2	(none)	Solar Flux	-0.73	96.3
	Lowpass C		-0.87	94.2
	(none)	QBO	0.31	94.0
	Bandpass A		0.48	95.4
4	(none)	SOI	0.71	99.995
	Bandpass A		0.80	99.9998
		MOD-Band PCs		
1	(none)	QBO	0.84	99.8
		MOD-Low PCs		
1	(none)	Solar Flux	0.84	95.8
		TOMS PCs		
1	(none)	QBO	0.88	98.7
2	(none)	Solar Flux	0.80	99.6
	Lowpass C		0.95	99.91
3	(none)	Solar Flux	-0.25	93.6
	Lowpass C		-0.61	95.9
4	(none)	SOI	0.76	99.90

Table 2.3: Correlations between NCEP/NCAR Reanalysis PCs and Various Indices

PC #	Filter	Index	Corr.	Sig. (%)
		NCEP-Layer PCs		
1	(none)	Solar Flux	0.43	84.6
	Lowpass C		0.60	84.5
	(none)	QBO	0.20	86.8
	Bandpass A		0.30	88.4
2	(none)	Solar Flux	-0.15	92.3
	Lowpass C		-0.50	84.1
	(none)	QBO	0.92	99.997
	Bandpass A		0.94	99.9993
3	(none)	SOI	0.82	99.9999
		NCEP-100 PCs		
1	(none)	Solar Flux	0.22	83.5
	Lowpass C		0.66	91.6
	(none)	SOI	-0.43	96.7
	Bandpass A		-0.54	99.2
2	(none)	Solar Flux	-0.29	77.9
	Lowpass C		-0.40	75.2
	(none)	SOI	-0.72	99.997
	Bandpass A		-0.70	99.99

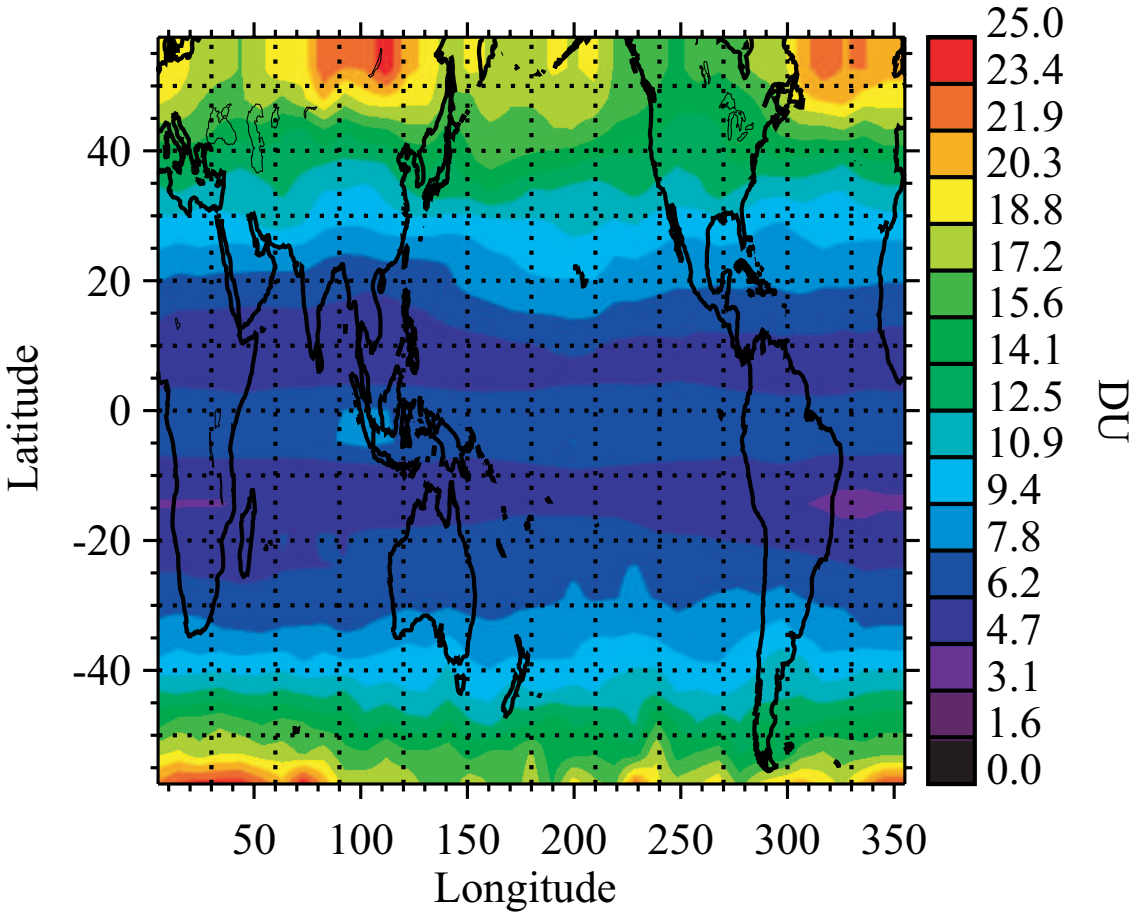

Figure 2.1: Standard deviations of the detrended, deseasonalized ozone time series from the Merged Ozone Dataset.

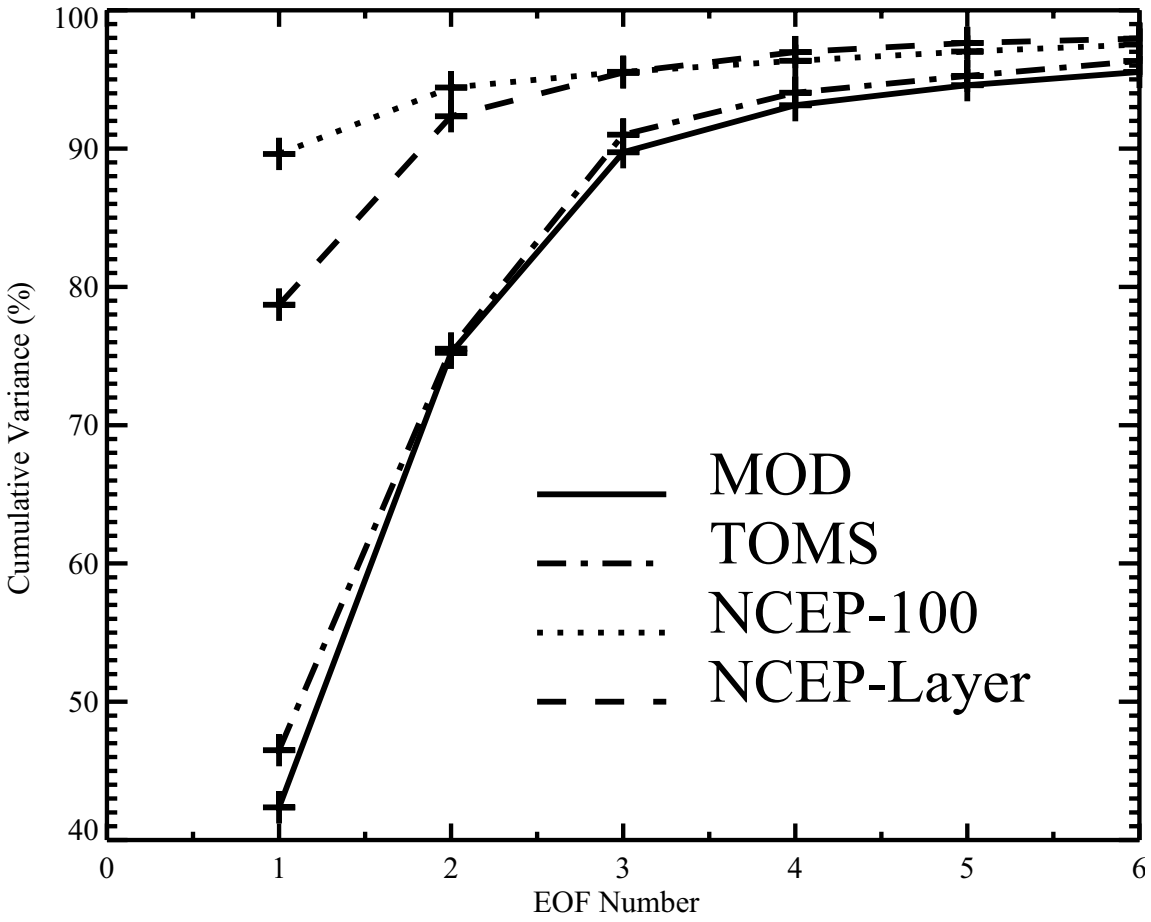

Figure 2.2: Cumulative variance as a function of number of EOFs.

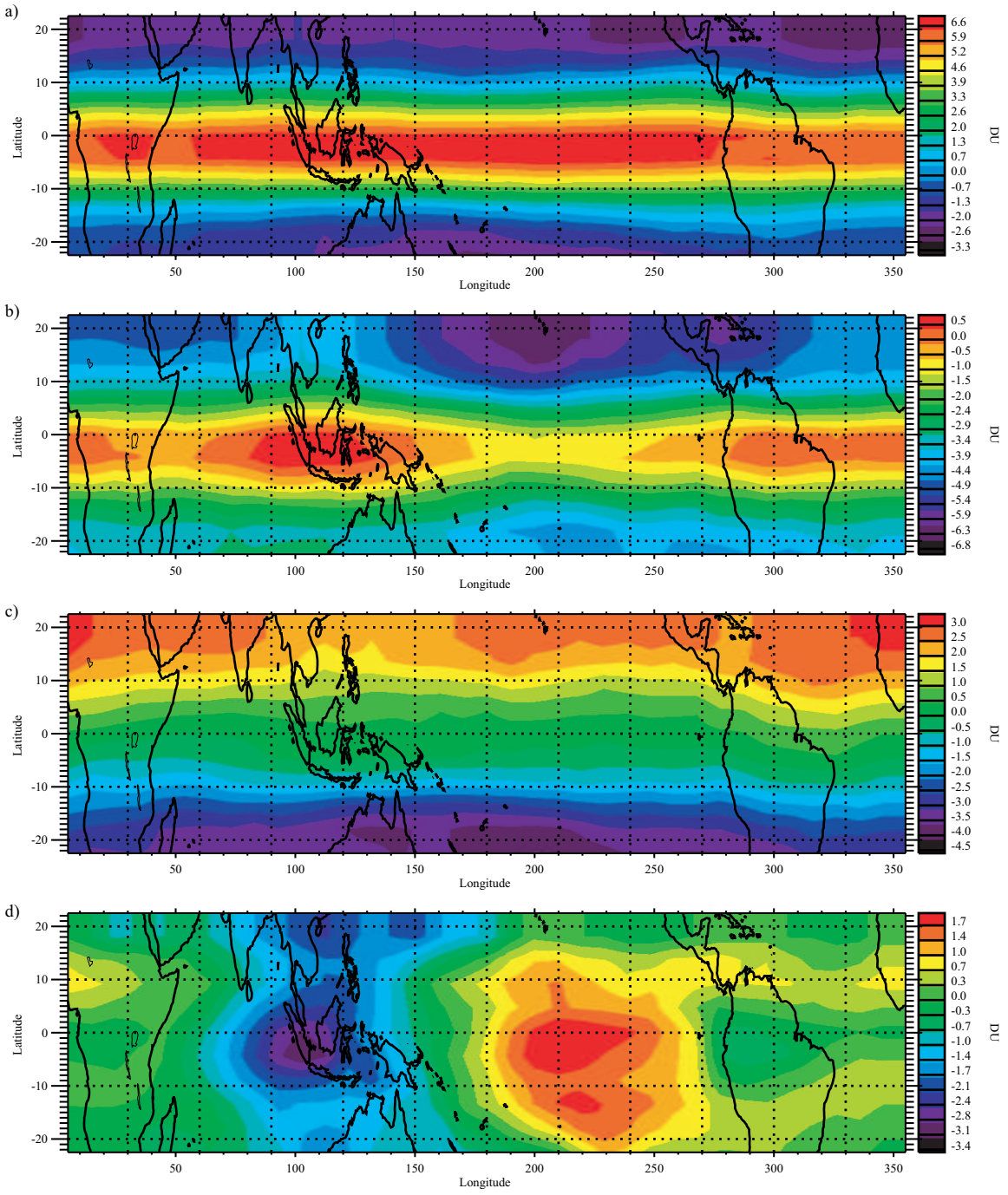

Figure 2.3: Spatial patterns for the first four MOD EOFs.

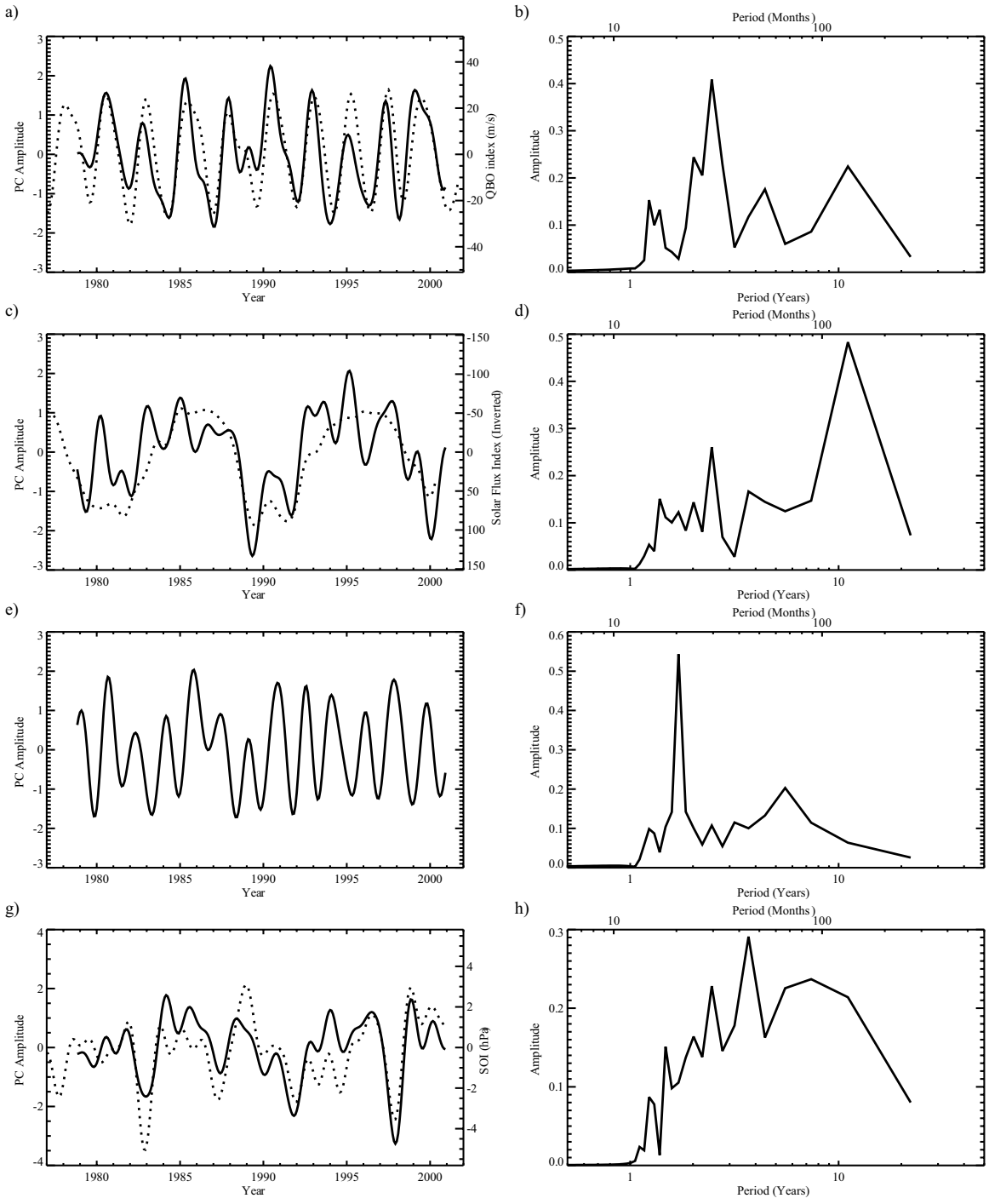

Figure 2.4: PC time series (left column) and spectra (right column) for the first four MOD EOFs. PCs (solid lines) are shown along with an appropriate index (dotted line). (a,b) PC1 and QBO index. (c,d) PC2 and inverted Solar Flux. (e,f) PC3. (g,h) PC4 and SOI.

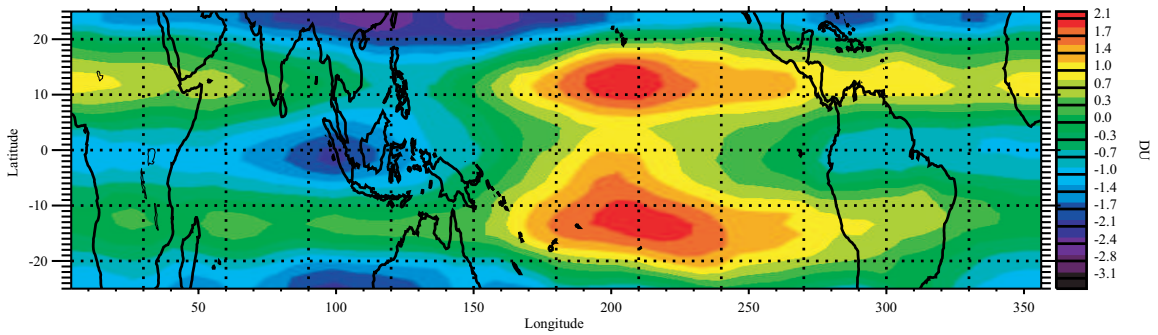

Figure 2.5: Spatial patterns for the fourth TOMS EOF.

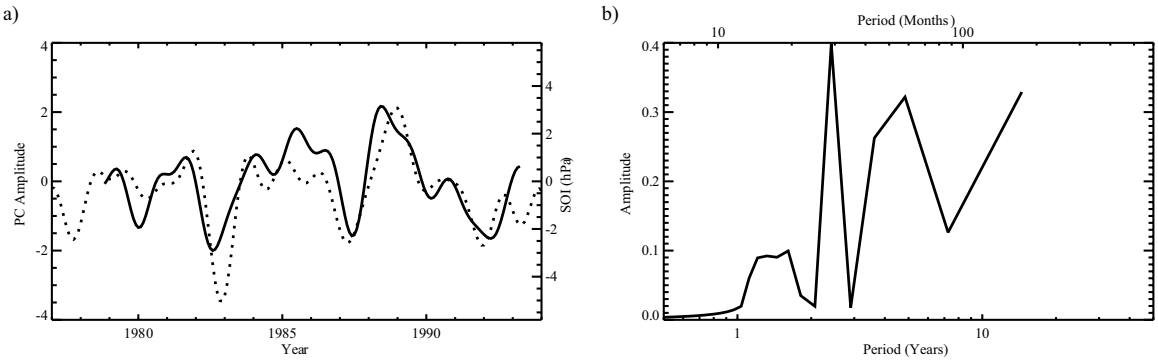

Figure 2.6: PC time series (a) and spectrum (b) for the fourth TOMS EOF. PC4 (solid) is compared to the SOI (dotted).

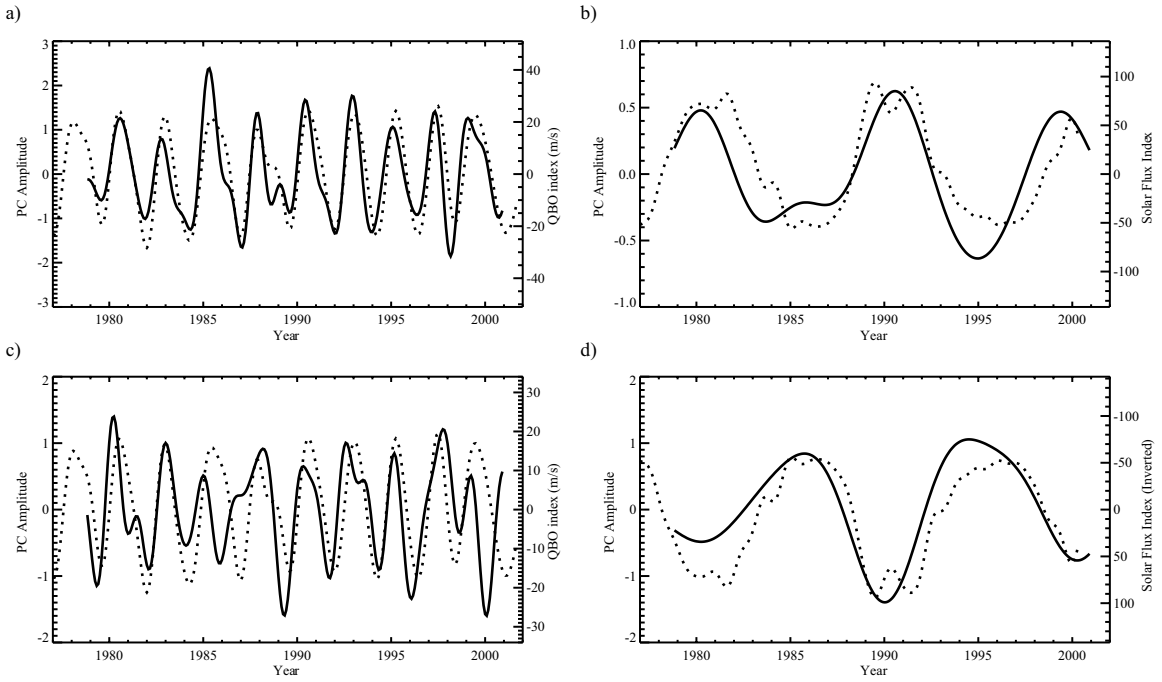

Figure 2.7: Comparisons of filtered PCs of the MOD EOFs (solid) to appropriate indices (dotted). (a) Bandpass A filtered PC1 and QBO index. (b) Lowpass C filtered PC1 and Solar Flux. (c) Bandpass A filtered PC2 and QBO index. (d) Lowpass C filtered PC2 and inverted Solar Flux.

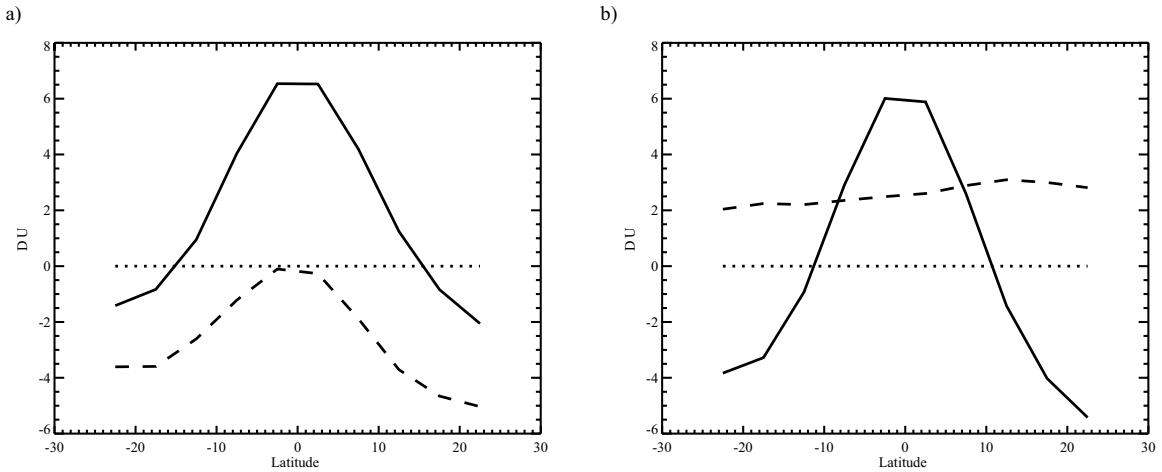

Figure 2.8: (a) Zonal averages of MOD EOF1 (solid line) and EOF2 (dashed line). (b) Weighted sum (solid line) and difference (dashed) of the MOD EOF1 and EOF2 zonal averages.

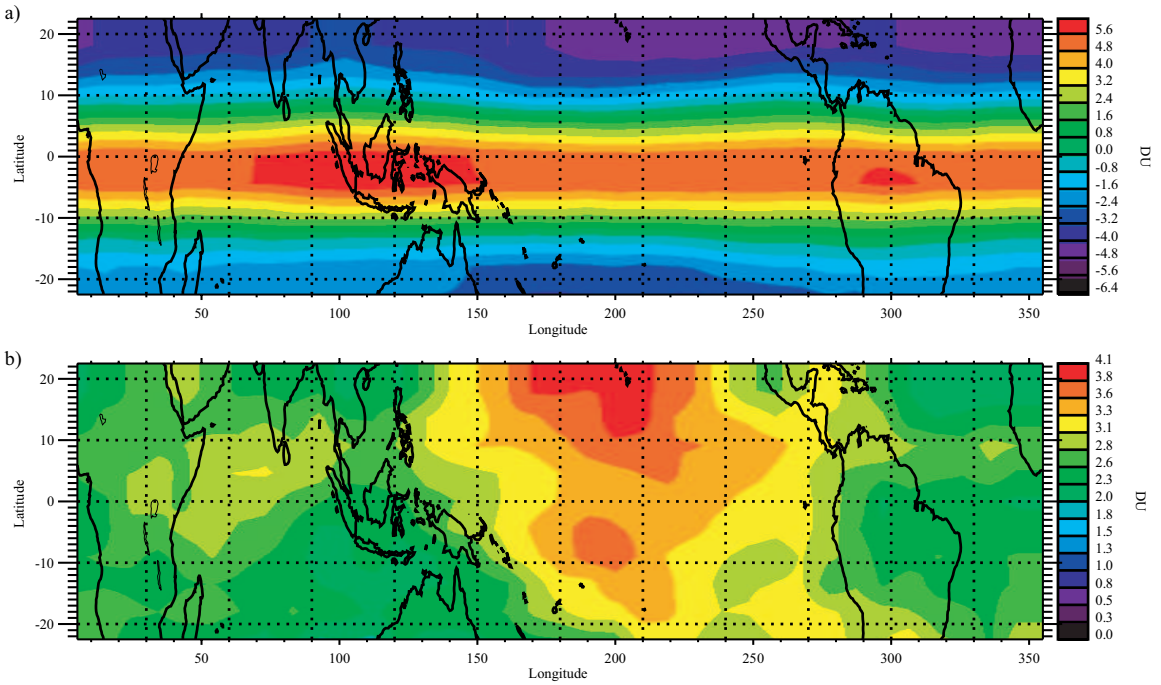

Figure 2.9: Leading EOFs from the filtered MOD analyses. (a) EOF1 of the Bandpass B filtered MOD (MOD-Band). (b) EOF1 of the Lowpass B filtered MOD (MOD-Low).

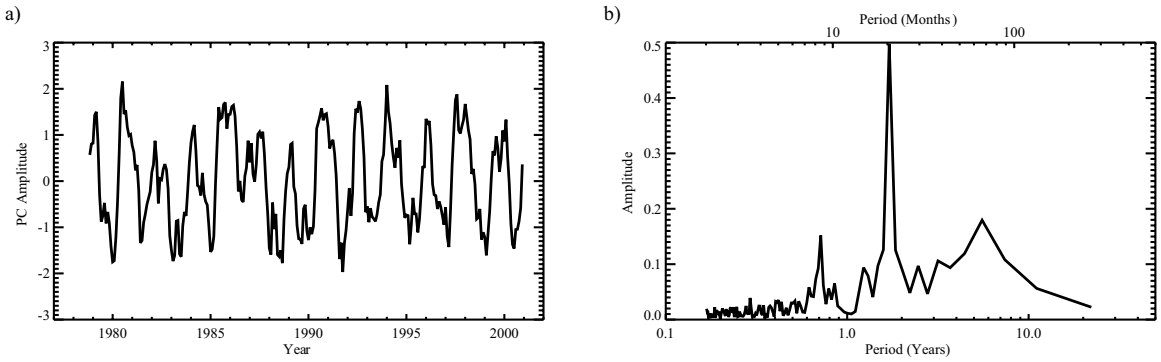

Figure 2.10: PC time series (a) and spectrum (b) for the third EOF from the Bandstop A filtered MOD data (MOD-Notch).

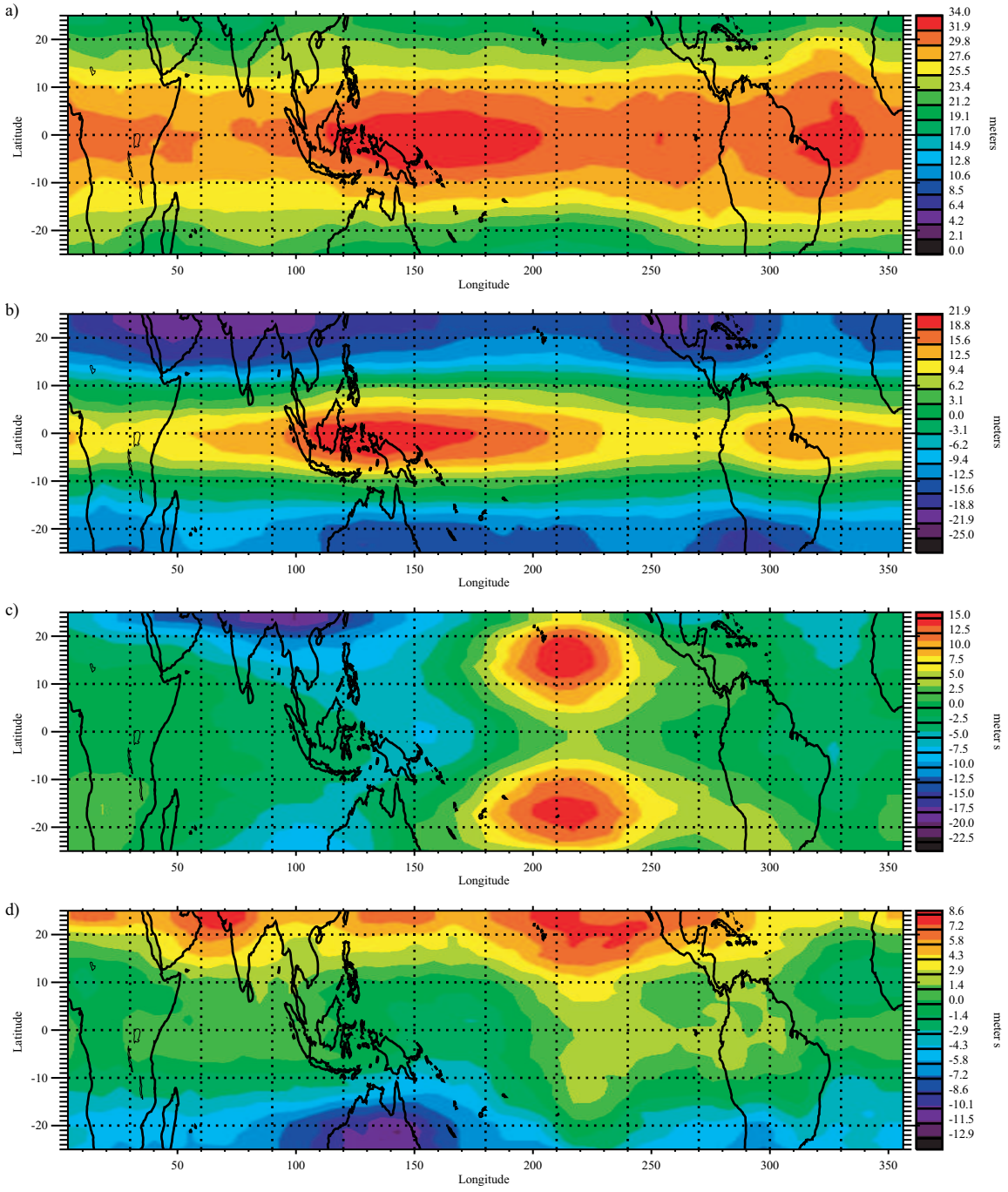

Figure 2.11: Spatial patterns for the first four EOFs from the NCEP/NCAR reanalysis 30 hPa to 100 hPa layer thickness (NCEP-Layer).

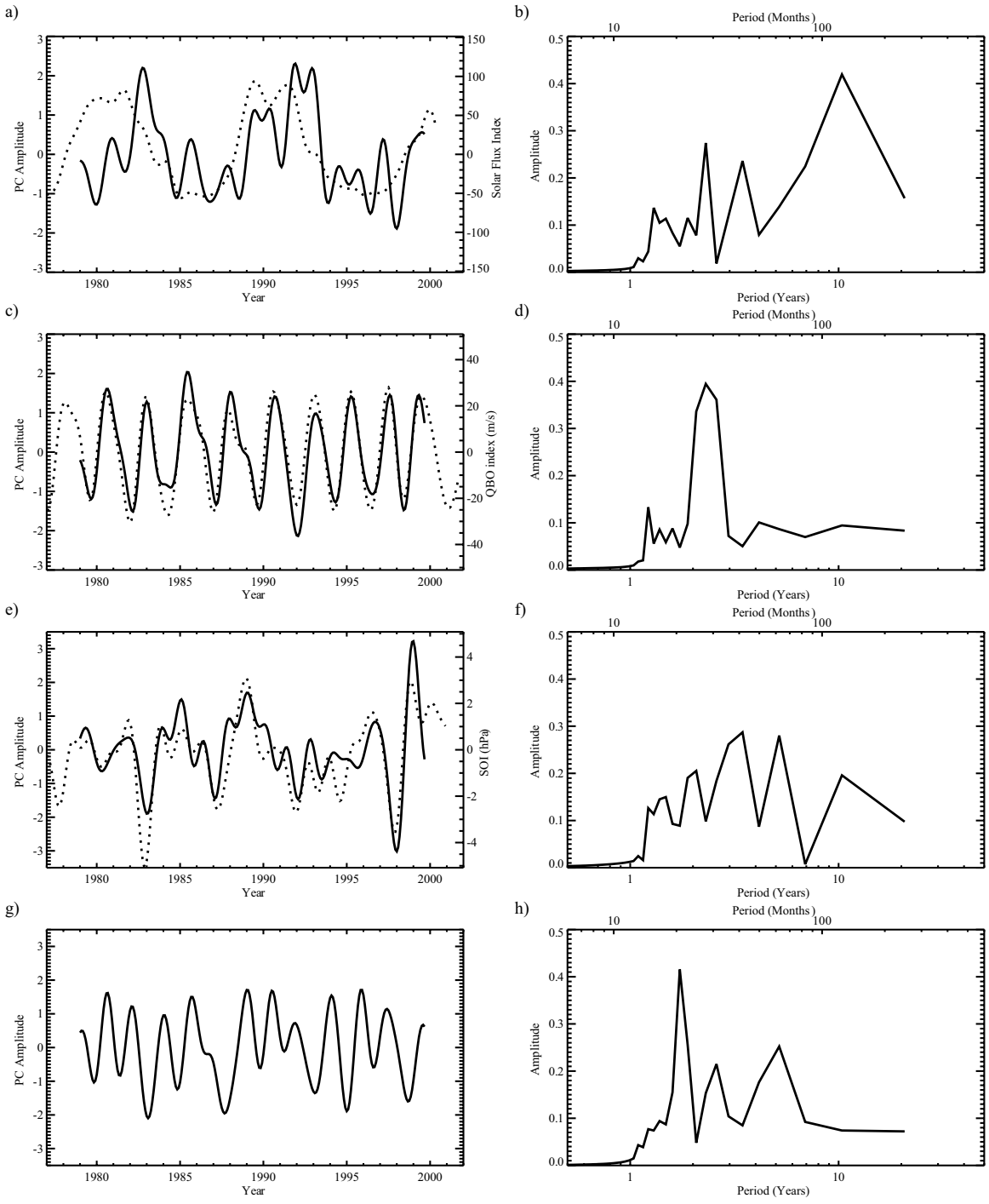

Figure 2.12: PC time series (left column) and spectra (right column) for the first four NCEP-Layer EOFs. PCs (solid lines) are shown along with an appropriate index (dotted lines). (a,b) PC1 and Solar Flux. (c,d) PC2 and QBO index. (e,f) PC3 and SOI. (g,h) PC4.

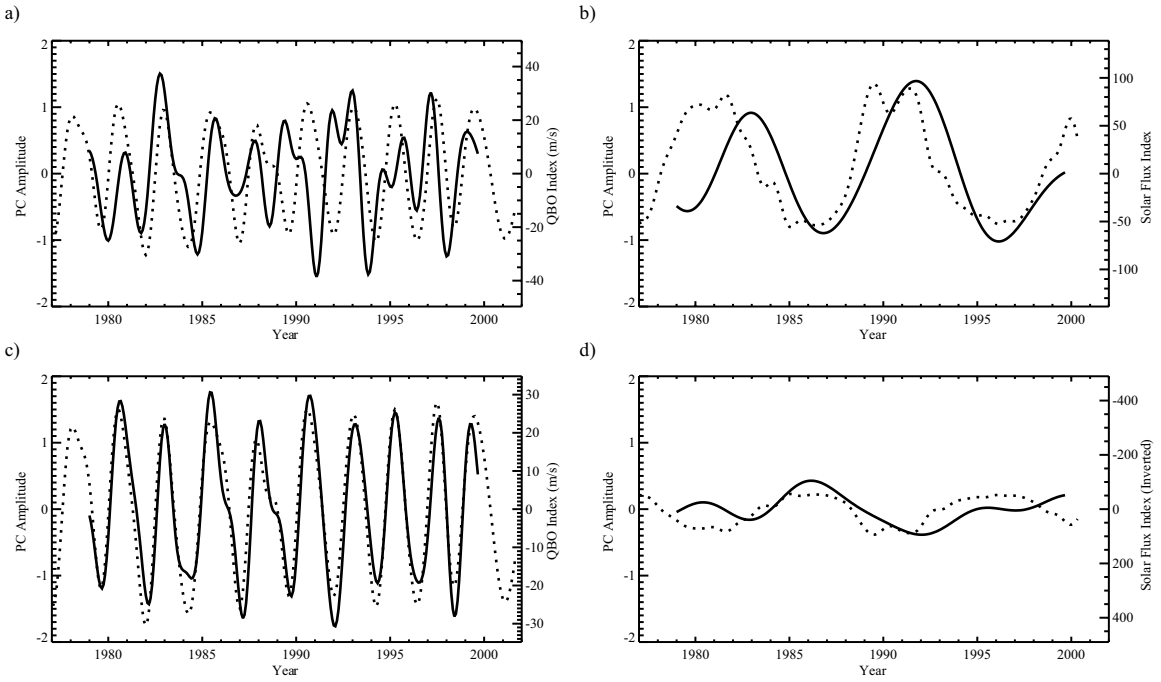

Figure 2.13: Comparisons of filtered PCs of the NCEP-Layer EOFs to appropriate indices. (a) Bandpass A filtered PC1 and QBO index. (b) Lowpass C filtered PC1 and Solar Flux. (c) Bandpass A filtered PC2 and QBO index. (d) Lowpass C filtered PC2 and inverted Solar Flux.

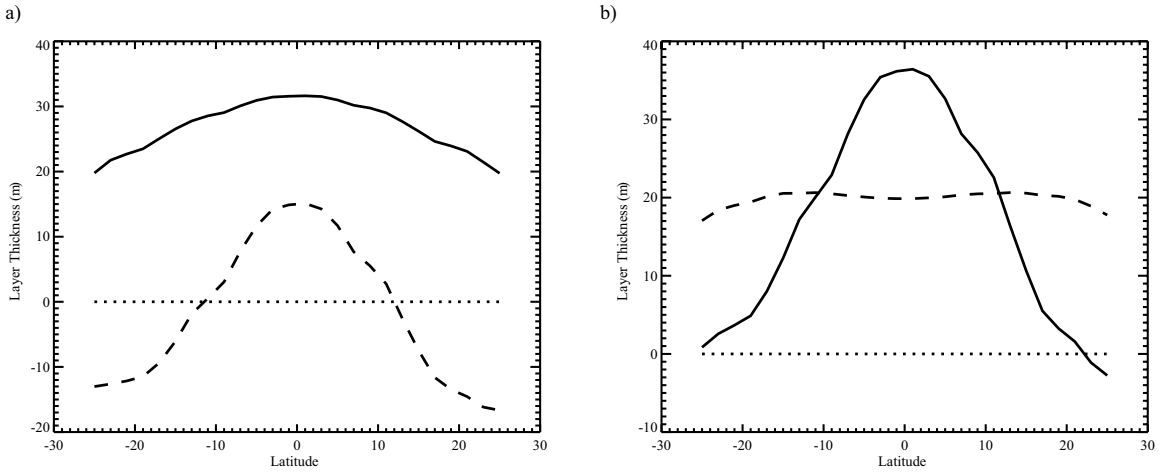

Figure 2.14: (a) Zonal averages of NCEP-Layer EOF1 (solid line) and EOF2 (dashed line). (b) Weighted sum (solid line) and difference (dashed) of the NCEP-Layer EOF1 and EOF2 zonal averages.

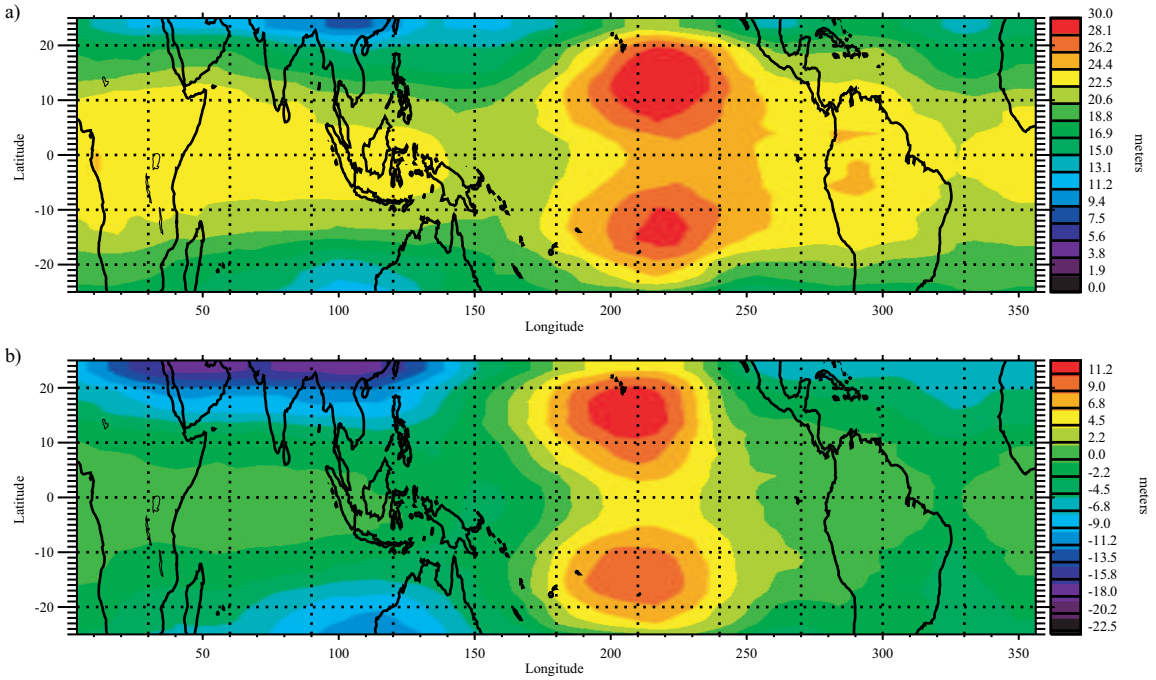

Figure 2.15: Spatial patterns for the first two EOFs from the NCEP/NCAR reanalysis 100 hPa geopotential height data (NCEP-100).

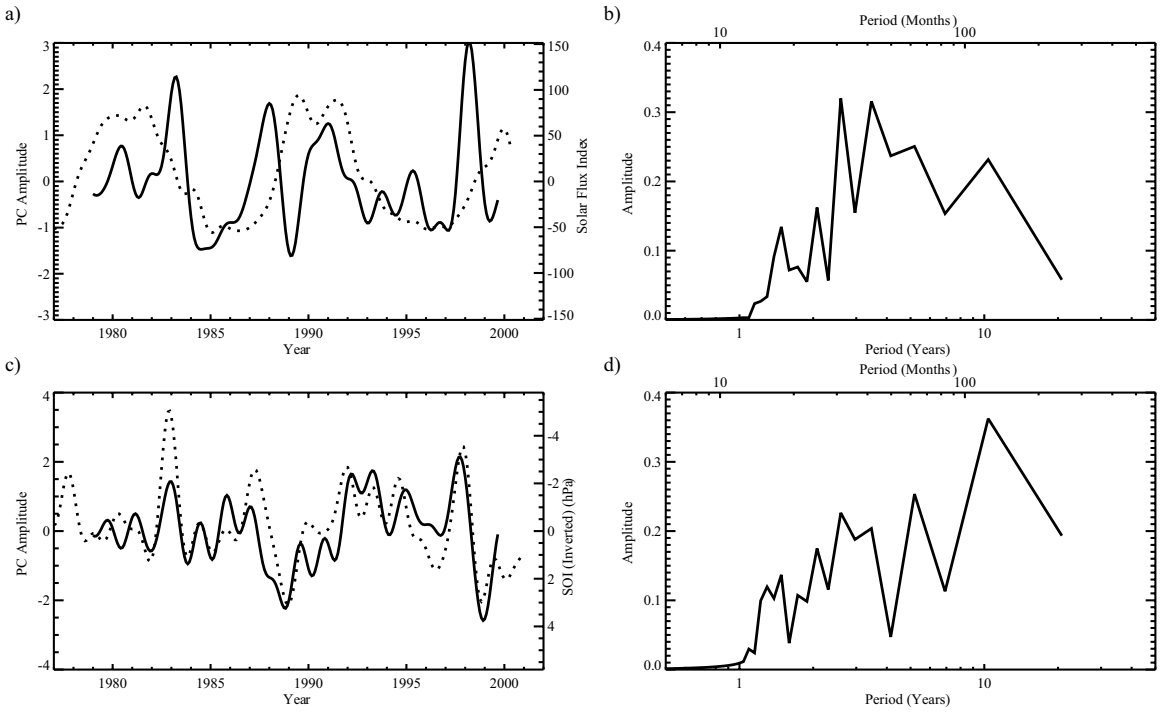

Figure 2.16: PC time series (left column) and spectra (right column) for the first two NCEP-100 EOFs. PCs (solid lines) are shown along with the appropriate index (dotted line). (a,b) PC1 and Solar Flux. (c,d) PC2 and inverted SOI.

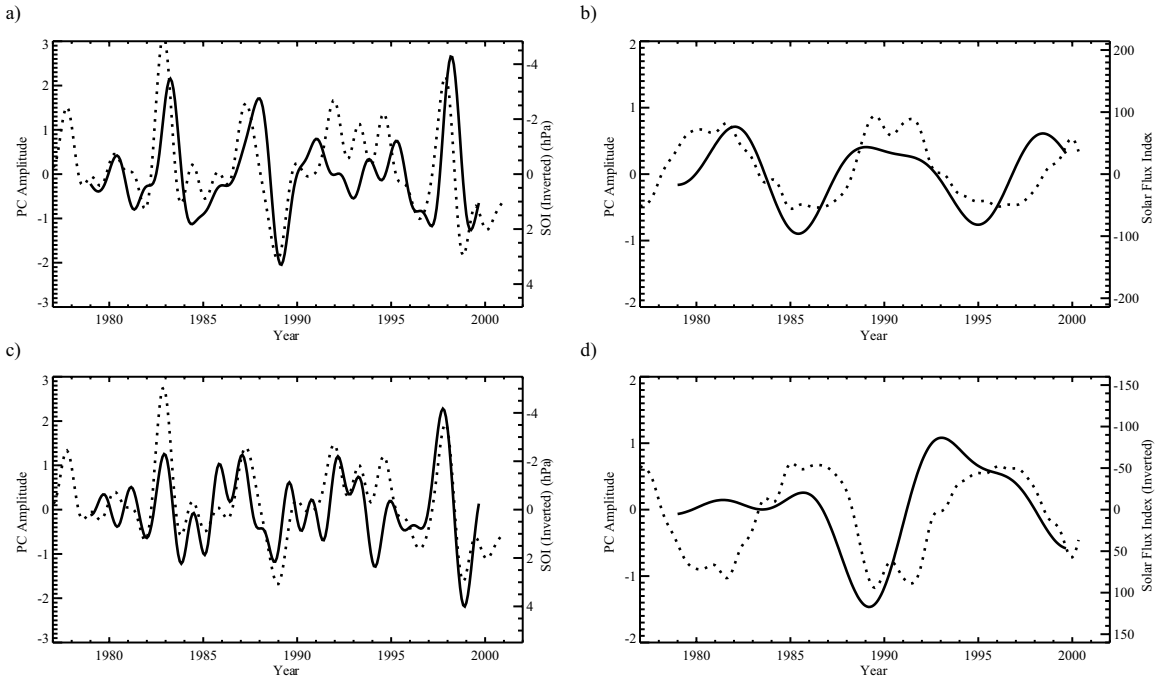

Figure 2.17: Comparisons of filtered PCs of the NCEP-100 EOFs to appropriate indices. (a) Bandpass A filtered PC1 and inverted SOI. (b) Lowpass C filtered PC1 and Solar Flux. (c) Bandpass A filtered PC2 and inverted SOI. (d) Lowpass C filtered PC2 and inverted Solar Flux.

Chapter 3

Interannual Variability of the Midlatitude Stratospheric Ozone: Observations and Modeling

3.1 Introduction

One of the major goals of upper atmosphere research is to observe the expected recovery of the ozone layer that results from the regulation of chlorofluorcarbons (CFCs) and other ozone-depleting substances by the Montreal Protocol (*Austin et al.*, 2000; *WMO*, 2003, chap. 4). Before the Montreal Protocol was implemented, the average rate of ozone depletion between 60°S and 60°N was about 2% per decade. The derivation of this loss rate was more reliable in the Southern Hemisphere (SH), where it was dominated by the occurrence of the Antarctic Ozone Hole in the austral spring. The signal was smaller in the Northern Hemisphere (NH) and subject to interference by a large seasonal cycle (5%) and an uncertain interannual variability (IAV) of about 2% (*WMO*, 2003, chap.4). Indeed, a substantial fraction of the observed ozone depletion may be attributed to the natural IAV in atmospheric dynamics (*Hood et al.*, 1997; *Fusco and Salby*, 1999; *Hadjinicolaou et al.*, 2002). The question of what fraction of

the change is chemical versus dynamical has never been satisfactorily resolved. The unambiguous detection of the expected recovery would be even more difficult because of the slow rate of decay of CFCs. *Stevermer and Weatherhead* (2001) estimated that it might take 15–35 years to detect this gradual recovery in the total column ozone, even under the best of circumstances. Therefore, a better characterization of the IAV of ozone is urgently needed.

Shiotani (1992) found signals associated with the quasi-biennial oscillation (QBO) and the El Niño-Southern Oscillation (ENSO) in the total column ozone derived from the Total Ozone Mapping Spectrometer (TOMS) from 1979 to 1989. Using the merged ozone dataset (MOD), which combined the monthly mean column abundances collected by the TOMS (*McPeters et al.*, 1996) and the Solar Backscatter Ultraviolet (SBUV and SBUV/2) instruments, *Camp et al.* (2003) carried out a principal component analysis (PCA) of the temporal and spatial patterns of the IAV of the total column ozone in the tropics from late 1979 to 2000 on a $5^\circ \times 10^\circ$ latitude-longitude grid; see Chapter 2. This work was a complete analysis of tropical ozone data, simultaneously examining the longitudinal, latitudinal and temporal patterns. The first four empirical orthogonal functions (EOFs) of their study captured over 93% of the variance of the detrended and deseasonalized data on interannual time scales. The leading two EOFs, respectively accounting for 42% and 33% of the variance, displayed structures attributable to the QBO, with influence from a decadal oscillation (most likely the solar cycle). The third EOF (15% of the variance) represented an interaction between the QBO and an annual cycle (QBO-AB). The fourth EOF (3% of

the variance) was related to the ENSO. In this chapter, we will extend the analysis performed in *Camp et al.* (2003) to the midlatitudes. Then we will present a two-dimensional model of the ozone transport based on a representation of the meridional circulation by an isentropic mass stream function.

The mechanism by which the QBO modulates ozone column abundance in the tropical stratosphere is well known (*Plumb and Bell*, 1982; *Baldwin et al.*, 2001). When the QBO is in the westerly (easterly) phase, there is descending (upwelling) anomalous motion in the tropical stratosphere and upwelling (descending) anomalous motion in the subtropical stratosphere. This results in more (less) ozone at the equator in the westerly (easterly) QBO phase (*Tung and Yang*, 1994a; *Randel and Cobb*, 1994). The QBO period varies from about 22 to 32 months, with a mean of approximately 28 months. The interaction of the annual cycle with the QBO will thus produce two cycles with periods of approximately 20 and 8.6 months (*Tung and Yang*, 1994a). These periods were first found in the total column ozone data obtained by TOMS in the tropics and extratropics (*Tung and Yang*, 1994a,b).

Several idealized numerical models have been developed to study the influence of QBO on the ozone. Using a mechanistic model, *Hasebe* (1994) found that the phase of the ozone QBO approached that of the temperature QBO. *Politowicz and Hitchman* (1997) introduced an analytic forcing of the stratospheric QBO in a two-dimensional (2D) middle atmosphere model in three different ways. They used a different amplification factor for each method, seeking good agreement with the observed QBO in the column ozone, and found that the diabatic forcing method was

better than wave-driving or thermal-nudging. Similarly, using an equatorial wave forcing parameterization, *Jones et al.* (1998) successfully generated a QBO with a period of about 28 months. The induced circulation in their model was stronger in the winter hemisphere. Further analysis of the *Jones et al.* (1998) model (*Jiang et al.,* 2004, manuscript in preparation) reveals the existence of the QBO-AB signal at about 20 months. However, the *Jones et al.* (1998) model is idealized and cannot simulate the IAV of the observed ozone.

Kinnersley and Tung (1999) used an interactive stratospheric model by relaxing the equatorial zonal wind to the observed Singapore zonal wind. Their model simulates the observed ozone anomaly satisfactorily. However, there appears to be some underestimation of the equatorial QBO amplitude in the ozone column.

Fleming et al. (2002) used meteorological data from the United Kingdom Meteorological Office (UKMO) model and constituent data from the Upper Atmospheric Research Satellite (UARS) to calculate yearly zonal mean dynamical fields, which they then used to drive the NASA/Goddard Space Flight Center 2D chemistry and transport model. This model provided a good simulation of the IAV of the total column ozone from 1993 to 2000. However, like that of *Kinnersley and Tung* (1999), it also underestimated the QBO amplitudes at the equator, which is partially because the UKMO temperatures underestimated the QBO amplitude by at least 40% (*Randel et al.*, 1999). *Fleming et al.* (2002) also calculated the total column ozone by increasing the QBO amplitude in the UKMO temperatures by 40%; however, the result still underestimated the QBO signal in MOD by nearly a factor of 2.

Pawson and Fiorino (1998a) and *Pawson and Fiorino* (1998b) studied the annual cycle and the QBO in the reanalysis product from the National Centers for Environmental Prediction (NCEP)/ National Center for Atmospheric Research (NCAR) and in the 40 Years Re-analysis from the European Centre for Medium-Range Weather Forecasts (ECMWF), hereafter denoted NCEP-1 and ERA-40, respectively. They found high correlations between the zonal winds of each reanalysis and the observations. The northward velocities from NCEP-1 showed a more realistic structure than those from ERA-40. *Randel et al.* (2000) found that the signatures of the QBO and ENSO events were strong in the 1957–1997 NCEP-1 tropopause statistics.

Using monthly mean meridional circulation to drive the Caltech/JPL 2D chemical transport model (CTM), we carry out the first realistic simulation of the ozone QBO and QBO-AB from 1979 to 2002, coincident with the MOD record. The mean meridional circulation is derived from the NCEP/DOE AMIP-II Reanalysis, hereafter denoted NCEP-2. This data is provided by the NOAA-CIRES Climate Diagnostics Center. We then apply PCA to the simulated ozone calculated by the 2-D CTM. The model ozone results for QBO and QBO-AB are compared to the signals obtained by *Camp et al.* (2003) from the MOD observations.

3.2 Analysis of the Merged Ozone Dataset

3.2.1 Climatology

The MOD dataset is described in Section 2.2. For the analyses in this chapter, the dataset used is unchanged except that we are using data from Nov. 1978 to Dec. 2002.

Stratospheric ozone is primarily created in the upper tropical and subtropical stratosphere. It is then advected to higher latitudes by the Brewer-Dobson circulation (BDC). Figure 3.1 displays the overall mean of MOD. Values range from lows around 250–260 DU in the tropics to highs around 300–340 DU at 60°S and 350–380 DU at 60°N. The tropical depletion and high-latitude enrichment is a result of the BDC.

The BDC is predominantly a winter-hemisphere phenomenon. Evidence of this can be clearly seen in Figure 3.2, which shows the mean seasonal cycle for MOD. At the beginning of the Northern fall, there is very little poleward advection in the NH. Therefore the meridional gradient of ozone is small; see Figure 3.2e. As the season progresses into winter, the northern cell of the BDC increases in strength, and a buildup of ozone in the northern latitudes is seen. Peak values of more than 450 DU at 60°N are seen in February to March. In spring, the meridional circulation declines, and ozone abundances relax throughout the spring and summer. A similar circulation occurs in the SH, in sync with the SH seasons. But a maximum of only $\sim$ 400 DU is seen at 60°S in September to October, since the SH cell of the BDC is weaker than the NH cell.

Figure 3.3 shows the linear trend fit to MOD. Very weak trends are seen in the tropics, with strong negative trends seen in the higher latitudes, particularly in the SH.

The variability of the deseasonalized ozone varies greatly with latitude, as shown in Figure 3.4. The tropics are relatively quiescent, with standard deviations of 5–8 DU. The midlatitudes are much more active, with standard deviations rising to over 20 DU in the higher latitudes.

3.2.2 PCA of MOD

The IAV of the tropical ozone was analyzed in Chapter 2. In order to extend our understanding to the midlatitudes, we performed a similar PCA for MOD between 45°S and 45°N. The results of this analysis are shown in Figures 3.5–3.7.

The first 4 EOFs together explain 82% of the variance, see Figure 3.5, and are dominated by the same four signals seen in the tropics: QBO, QBO-AB, ENSO, and decadal.

Figure 3.6 shows the first four EOFs from the PCA. The first EOF (Figure 3.6a), capturing 40% of the variance, is zonally uniform and roughly equatorially symmetric. The associated PC time series and its power spectral density (PSD) are shown in Figures 3.7a and 3.7b, respectively. All PSDs in this chapter are calculated by Welch's method for power spectrum estimation; Fourier spectra for three half-length segments with 50% overlap are averaged, with a Hamming window applied to each segment prior to determining its spectrum (*Press et al.*, 1992, chap.13). The PSD shows a

broad peak centered at 28 months, indicative of the ozone QBO. This high-frequency shoulder of this peak is consistent with the QBO-AB period of 20 mo. The time series is plotted against the QBO index, with which it shows a correlation of 0.57 (see Table 3.1). There is also a significant negative correlation with the solar flux index.

Table 3.1 shows all of the significant correlations between the leading PCs of the MOD PCA and various indices. Correlations between filtered PCs and indices are also shown; the filters used are described in Section 2.2 and Table 2.1. Significance statistics were generated by the following Monte Carlo method (*Press et al.*, 1992, chap.15): A distribution of correlations was generated by determining the correlations of three thousand isospectral surrogate time series with the relevant indices. This distribution was transformed into an approximately normal distribution by the Fisher transformation (*Devore*, 1982). The significance level of the actual correlation within the normal distribution was then determined. A small numerical value of the significance level denotes a statistical high significance.

The second EOF (Figure 3.6b), capturing 20% of the variance, is antisymmetric about the equator, showing zonal symmetry except at the higher latitudes. The PSD of its associated PC time series (Figure 3.7d) shows a sharp spike at 20 months, indicative of the QBO-AB. It also shows weak correlations with the solar flux and QBO indices (Table 3.1).

The third EOF (Figure 3.6c), capturing 18% of the variance, shows a pattern with many similarities to EOF1, but with DC shift (higher ozone levels throughout). The PSD of the associated PC time series (Figure 3.7f) shows a sharp peak at the

28-month period indicative of the QBO, and broad power on decadal time scales. It shows strong correlations with both the solar flux and QBO indices. The PC time series is shown plotted against the solar flux index in Figure 3.7e.

The fourth EOF (Figure 3.6d), capturing only 4.6% of the variance, is the first pattern to strongly break the zonal symmetry, particularly in the tropics. It is dominated by a pair of positive anomalies in the central subtropical Pacific and a negative anomaly over Indonesia. The PSD of the associated time series (Figure 3.7h) is broad, with significant power on time scales ranging from 5 years to annual. Both the spatial pattern and the spectral features are indicative of an ENSO process, and the time series (Figure 3.7g) shows a very significant correlation with the ENSO index.

The dominant features captured are the same as those seen in the tropical analysis (see Chapter 2) However, the QBO signal dominating the first EOF has a distinctly larger amplitude in the northern high latitudes than in the southern. This is primarily caused by the hemispheric asymmetry in the BDC; the northern cell of the BDC is stronger than the southern cell. Since the QBO's modulation of the BDC is a dominant feature of the meridional transport of ozone, this hemispheric asymmetry is seen in the ozone QBO as well. Furthermore, since EOF1 has some hemispheric asymmetry, the inherently hemispherically antisymmetric QBO-AB pattern is no longer orthogonal to the QBO pattern. Therefore, the first EOF actually mixes the patterns associated with the QBO and QBO-AB processes. This mixing is why the PSD for PC1 (Figure 3.7b) shows a broad peak that encompasses both the 28-month QBO period and the 20-month QBO-AB period.

Comparing the midlatitude analysis to the tropical analysis, see 2.4.1, we can see that the QBO-AB gains in prominence since higher latitudes with stronger seasonal cycles are included. The pattern associated with the QBO-AB thus appears as the second EOF in this analysis, rather than the third EOF as in Chapter 2. The zonal symmetry seen in the tropics and subtropics is interrupted by wave-like synoptic-scale patterns at the higher latitudes.

The third midlatitude EOF behaves much like the second EOF of the tropical analysis, showing behaviors associated with decadal variability and with the QBO. As in the tropical analysis, the fourth EOF shows a very clear signature indicative of ENSO.

The extension of the PCA analysis from the tropics into the midlatitudes has further muddied the interpretability of the output. In the tropical analysis, the signals associated with the QBO and decadal variability did not separate into distinct EOFs, but were distributed between EOFs 1 and 2 (see Section 2.5.2 for details). In the midlatitude analysis, this conflation of signals is even more pronounced, as now three processes (QBO, QBO-AB, and decadal) are conflated amongst the first three EOFs. Furthermore, new physical processes are coming into play in the higher latitudes ($> 30^\circ$ latitude). This is evident in the synoptic-scale structures seen at these latitudes in all four EOFs.

In a PCA analysis extending from 60°S to 60°N (not shown), these problems, plus the overall growth in variability with latitude, render the analysis very difficult to interpret.

3.3 Simulating Ozone Transport in a 2D Chemical Transport Model

3.3.1 NCEP-2 Derived Transport Fields

3.3.1.1 Stream Function

NCEP-2 4-times-daily spectral coefficients are used to calculate the monthly mean meridional circulations from 1979 to 2002, using the method of *Johnson* (1989). This method uses zonal averaging on isentropes to separate the diabatic circulation from the reversible adiabatic motions. Recently, the same method was used by *Bartels et al.* (1998) to study the Ertel's potential vorticity flux in the upper troposphere and lower stratosphere. *Held and Schneider* (1999) also applied this method to study the near-surface branch of the overturning mass transport circulation in the troposphere.

The core of this method is the representation of the mean meridional mass transport by an isentropic stream function. Following the notation of *Andrews et al.* (1987, chap.3), the continuity equation in isentropic coordinates can be written as

$$\frac{\partial \sigma}{\partial t} + \frac{1}{a\cos\phi}\left\{\frac{\partial(\sigma u)}{\partial \lambda} + \frac{\partial(\sigma v\cos\phi)}{\partial \phi} + \frac{\partial(\sigma Q)}{\partial \theta}\right\} = 0 \tag{3.1}$$

where a denotes the radius of the Earth; λ, ϕ, and θ denote longitude, latitude and potential temperature, respectively; u and v denote the zonal and meridional velocities, respectively; $\sigma = -g^{-1}\partial_\theta p$ is the isentropic density; p is the pressure and $Q = \frac{D\theta}{Dt}$ is the diabatic heating, which is equivalent to the isentropic vertical velocity.

Applying a zonal average to Equation 3.1, we get

$$\frac{\partial \overline{\sigma}}{\partial t} + \frac{1}{a\cos\phi}\frac{\partial(\overline{\sigma v}\cos\phi)}{\partial \phi} + \frac{\partial\left(\overline{\sigma Q}\right)}{\partial \theta} = 0 \tag{3.2}$$

where $\overline{(\cdot)}$ denotes the zonal average; $(\cdot)' = (\cdot) - \overline{(\cdot)}$ denotes the deviation from the zonal average, $\overline{\sigma v}$ is the meridional mass flux and $\overline{\sigma Q}$ is the vertical mass flux. If we also take a sufficiently long temporal average, *e.g.,* 1 month, we can neglect the first term of Equation 3.2, leaving

$$\frac{\partial[\overline{\sigma v}]\cos\phi}{\partial \phi} + \frac{\partial\left[\,\overline{\sigma Q}\,\right]}{\partial \theta} = 0 \tag{3.3}$$

where $[(\cdot)]$ denotes the temporal average. Now we can define the isentropic mass stream function, $\Psi_\theta\,(\phi, \theta, t)$, such that

$$[\overline{\sigma v}] = -\frac{1}{2\pi a\cos\phi}\frac{\partial \Psi_\theta}{\partial \theta} \tag{3.4}$$

$$\left[\,\overline{\sigma Q}\,\right] = \frac{1}{2\pi a}\frac{\partial \Psi_\theta}{\partial \phi} \tag{3.5}$$

In this model, the isentropic mass stream function, Ψ_θ, is determined from the NCEP-2 spectral coefficients. These coefficients are available on 28 sigma levels with T62 (triangular wavenumber truncation at 62) resolution in the horizontal (*Kalnay et al.*, 1996; *Kistler et al.*, 2001). On pressure surfaces, the three-dimensional (3D)

meridional mass flux, $\psi_p(\lambda, \phi, p, t)$, is determined by

$$\psi_p(\lambda, \phi, p, t) = \frac{2\pi a \cos\phi}{g} \int_0^p v(\lambda, \phi, p', t)\, dp' \tag{3.6}$$

where p is the pressure. Then we interpolate this field onto isentropic surfaces, $\psi_p(\lambda, \phi, p, t) \rightarrow \psi_\theta(\lambda, \phi, \theta, t)$, using a mass-conserving linear interpolation scheme (*Juckes et al.*, 1994). The 2D isentropic mass stream function is then derived by zonal and temporal averaging,

$$\Psi_\theta(\phi, \theta, t) = \left[\, \overline{\psi_\theta} \,\right] \tag{3.7}$$

Finally, we interpolate Ψ_θ back to the pressure coordinates and scale by the density to produce the pressure-surface velocity stream function, $\Psi_p(\phi, p, t)$, needed to drive the 2D CTM.

Figure 3.8a shows the 1979–2002 mean of the isentropic mass stream function,Ψ_θ. Figure 3.8b shows the mean for the velocity stream function, Ψ_p. In both hemispheres, air is drawn upward and poleward from the tropical lower stratosphere and pushed downward into the extratropical troposphere by wave-induced forces (*Holton et al.*, 1995). This circulation is important for the transportation of ozone and other trace species in the stratosphere. The NH circulation is roughly 50% larger that the SH circulation. This hemispheric asymmetry in the circulation is consistent with the stratospheric wave activity being stronger in the NH than in the SH.

The seasonal variation is also captured well by this stream function; see Figure 3.9.

The NH stream function is strong during the NH winter, when the temperature gradient and wave activity are large. The stream function weakens during the spring and summer, when the temperature gradient and wave activity decrease. In the fall, the stream function strengthens again. As a result, the transport of ozone to the northern polar region is stronger in the NH fall and winter than during the NH summer and spring. For the SH circulation and ozone transport, a similar seasonal pattern occurs in sync with the SH seasons, albeit with a smaller amplitude. It is important to note that the northern cell of BDC in January extends deeper into to the northern latitudes, ∼60–70°N, than the southern cell in July extends into the southern latitudes, ∼50–60°S. This is consistent with observations that southern polar night vortex is stronger (and therefore colder) than the northern polar night vortex. The polar night vortices are maintained above radiative equilibrium temperatures primarily by the compressional heating associated with the downwelling branch of the winter cell of the BDC. Since the southern cell during July is weaker than the northern cell during January, less heat is transported to the southern vortex than to the northern vortex.

Linear trends fit to the stream function in January show an ∼ 2% decline per decade in the strength of the northern cell BDC during northern winter over the 24 years of the study; see Figure 3.10b. During the NH winter, both the northern and the southern cells are shifting southward. The southern cell of the BDC in July (southern winter) shows no trend in the maximum strength at 30°S, (Figure 3.10c). However, the southern cell is reaching increasing deeper into the southern latitudes during the SH winter as evidenced by the negative trends seen between 40°S and 70°S.

No previous results for the isentropic mass stream function in the stratosphere have been published, so we compare our results with the mass stream function computed in pressure coordinates shown in *Shia et al.* (1989, Fig. 2). The structures of these stream functions generally agree. The annual mean flux through the tropopause in the *Shia et al.* (1989) model is $9.3 \times 10^9\,\mathrm{kg/s}$, which is consistent with $^{14}\mathrm{C}$ data. The analogous flux through the 400 K isentropic surface, which is close to the tropical tropopause, is $14 \times 10^9\,\mathrm{kg/s}$, in good agreement with that in *Shia et al.* (1989).

In previous studies, the meridional circulation has usually been computed from net radiative heating rates using a diagnostic stream function model (*e.g., Ko et al., 1985)*. However, these studies have tended to exaggerate the tropical vertical transport through the tropopause, and have therefore underestimated the tropical total column ozone and overestimated the column ozone in the extratropics (*Kinnersley and Tung*, 1999; *Fleming et al.*, 2002).

For comparison, the stratospheric transformed Eulerian mean (TEM) circulation calculated from the residual velocity derived from the NCEP-2 meridional wind and temperature fields is shown in Figure 3.11. This circulation displays spurious counter-rotating cells in the polar stratosphere that cause an unphysical transport of ozone. This error may be caused by poor quality data in the NCEP-2 temperature and wind fields in the polar stratosphere. Alternatively, the calculation depends on the strong cancellation between the eddy heat flux convergence and the adiabatic cooling; the diabatic heating term is the small residual of this cancellation (*Andrews et al.*, 1987). This may cause numerical problems or amplify noise in the data. In this study, we

adopt the computed isentropic mass stream function, Ψ_θ, which is a closer approximation to the Lagrangian motion than the residual mean meridional circulation.

3.3.1.2 Isentropic Mixing Coefficient

In the lower stratosphere zonal mean transport mainly takes the form of advection by the mean diabatic circulation in the meridional plane and eddy mixing approximately along isentropic surfaces (*Malhman et al.*, 1984; *Tung*, 1984). The isentropic mixing coefficient, K_{yy}, can be related to the Eliassen-Palm flux divergence (*Tung*, 1986; *Yang et al.*, 1990). It is defined by

$$K_{yy} = -\overline{\hat{P}\hat{v}}^* \left(\frac{\partial \overline{P}^*}{\partial y} \right)^{-1} \tag{3.8}$$

where $P = \sigma^{-1}(\zeta + f)$ is Ertel's potential vorticity, ζ is the relative vorticity, and f is the planetary vorticity; $y = a\phi$ is the meridional coordinate. $\overline{(\cdot)}^* = \overline{(\sigma\cdot)}/\overline{\sigma}$ denotes the mass-weighted zonal average and $\hat{(\cdot)} = (\cdot) - \overline{(\cdot)}^*$ denotes the deviation from the mass-weighted zonal average.

K_{yy} values are interpolated from the isentropic surfaces to the pressure surfaces for use in the 2D CTM. For surfaces between 15 and 35 km, the values are calculated from the vorticity, divergence and temperature fields of NCEP-2 for the years from 1979 to 2002. Above 35 km and below 15 km, the values are from *Fleming et al.* (2002); these values consist of a climatological seasonal cycle with no IAV. Figure 3.12 shows the K_{yy} field on the pressure surfaces in January, April, July and October of 1985. K_{yy} values are large in the midlatitudes, on the order of $10^6\,\mathrm{m}^2/\mathrm{s}$, and small in the high

latitudes and tropics, on the order of $10^5\,\mathrm{m}^2/\,\mathrm{s}$. Since wave activity is larger in the NH than in the SH, K_{yy} values are larger in the NH. There are some negative values calculated from the NCEP-2 dataset where $\partial_y \overline{P}^*$ changes sign, an indication of either noise in the data or local baroclinic or barotropic instability (*Yang et al.*, 1990). For this study, negative values of were set to zero to avoid numerical instability.

3.3.2 IAV of the Stream Function

In order to study the IAV of the pressure-surface velocity stream function, ψ_p, used to drive the 2D CTM, we define a stream function anomaly in the following manner. First, the time series for each grid point is decomposed as

$$\psi_p\,(t) = \psi_p^a\,(t) + (\alpha + \beta t) + \psi_p'\,(t) \tag{3.9}$$

where ψ_p^a is the mean annual cycle determined by evaluating the mean value for each month independently. The next two terms constitute a linear trend determined by a least squares fit to the deseasonalized data. To isolate the IAV from higher frequency oscillations, a spectral filter is applied to the anomaly, ψ_p'; the filter is constructed as the convolution of a step function with a Hanning window and chosen to obtain a full signal from periods above 15 months and no signal from periods below 12.5 months. PCA is then performed on the filtered stream function anomaly. The details of the methodology are explained in *Camp et al.* (2003); see Chapter 2.

The first three EOFs from this analysis, along with the associated principal component (PC) time series and their PSDs, are shown in Figures 3.14, 3.15, and 3.16.

These three EOFs account for 95% of the total variance of the filtered stream function anomaly; see Figure 3.13. The correlations (lag = 0) and maximum cross correlations, along with corresponding significance levels, between the PCs of the stream function and the relevant indices are given in Table 3.2.

The first EOF, Figure 3.14a, captures over 70% of the variance and represents an oscillation in the strength of BDC caused by the QBO. During the westerly (easterly) phase of the QBO, the BDC is weakened (strengthened). The associated principal component time series, PC1, is plotted in Figure 3.14b against the inverted 30 hPa QBO index (the zonal average of the 30 hPa zonal wind at the equator computed from the NCEP-2). The PSD of PC1, Figure 3.14c, shows the 28-month period characteristic of the QBO. PC1 leads the 30 hPa QBO index by 4 months (derived from the maximum cross correlation position), which, since the QBO is characterized by a downward propagation, is consistent with the occurrence of the maximum of the stream function anomaly variation above the 30 hPa level. A secondary 20-month period oscillation is also evident. The modulation of the annual cycle of the BDC by the QBO results in the creation of two oscillations with frequencies equal to the difference and sum of the QBO and annual frequencies, *i.e.,* at periods of 20 and 8.6 months (*Tung and Yang*, 1994a). Only the 20-month signal is evident, since the spectral filtering destroys the signal from the higher frequency. Variations in QBO captured by the EOF are distinctly asymmetric about the equator (3.14a); the amplitude of variations in the northern lobe is greater than that in the southern lobe by more than a factor of three. To our knowledge, this is the first time that an

asymmetric QBO circulation has been found in the stream function derived from the NCEP-2 data.

The second EOF, Figure 3.15a, capturing about 18% of the variance, represents a smaller variation in just the southern cell of the circulation. It oscillates with the 20-month period characteristic of the QBO-AB. The pattern of the 20-month signal is thus a linear combination of EOF1, containing the entire northern cell variability and some of the southern cell variability, and EOF2, containing the remaining southern variability. In Figure 3.15b, PC2 is shown against a constructed index for the QBO-AB (PC3 of the EOF results for the zonal mean MOD; see Section 4 for details). PC2 correlates well with the QBO-AB (see Table 3.2).

The third EOF, Figure 3.16a, capturing about 6% of the variance, represents an oscillation in the height of the upwelling branch of the Hadley cell at the equator. Like that of PC1, the PSD of PC3 is dominated by a 28-month signal with a secondary 20-month signal. In Figure 3.16b, PC3 is shown along with the 30 hPa QBO index. PC3 lags the 30 hPa QBO index by 3 months, which is consistent with the occurrence of the center of the stream function anomaly variation below the 30 hPa level.

3.3.3 Simulated Total Column Ozone

The Caltech/JPL 2D CTM is a zonally averaged model for trace species in the terrestrial troposphere and middle atmosphere (see *Shia et al.* (1989) and Appendix A in *Morgan et al.* (2004) for details). The model has 18 latitude boxes, equally spaced from pole to pole, and 40 layers, equally spaced in log(p) from the surface to the

upper boundary at 0.01 mb. Transport in the model is by the stream function and calculated from NCEP-2 datasets. The values for K_{zz} are taken from *Summers et al.* (1997); they are only important in the mesosphere and troposphere. The model includes all the gas phase chemistry in the NASA recommendations for stratospheric modeling (*DeMore et al.*, 1997). There is no heterogeneous chemistry. The numerical method used for solving the continuity equation in the model is the Prather scheme (*Prather*, 1986; *Shia et al.*, 1990). The model was run from 1975 to 2002, where the stream function and mixing coefficients for the first four years are derived from NCEP-1 data fields. The stream function and eddy mixing coefficients from 1979 to 2002 are calculated from NCEP-2. *Huesmann and Hitchman* (2001, 2003) and *Pawson and Fiorino* (1999) show that there exists a large discontinuity in the NCEP-1 data coincident with the incorporation of the TOVS satellite data beginning in 1979. Therefore, we only use the 1975–1978 period as spin-up time for the 2D CTM; all results are based on the 1979–2002 period.

To examine the IAV of the simulated ozone, time series for the ozone anomalies are calculated by first removing the mean seasonal cycle from the simulated ozone time series for each latitude; then a linear trend is fit to the deseasonalized time series; finally, a lowpass filter (described in Section 2.2) is applied to isolate the IAV from the intra-annual variability. For comparison, a similar analysis is performed on the zonally averaged MOD observations. Data from the 24 years spanning Jan. 1979 to Dec. 2002 is used for both datasets.

3.3.3.1 Climatology

The climatology of total column ozone in these 24 years from zonal average of the MOD observations and the model results are compared in Figures 3.17–3.22. The climatology of total column ozone in these 24 years from zonal average of the MOD observations (*McPeters et al.*, 1996) and the model results are compared in Figures 3.17–3.22. In general, the model simulates the tropics and northern midlatitude ozone reasonably well, but has large discrepancies in the extratropical SH. In agreement with observations, mean column abundances are lower in the tropics than in the midlatitudes or polar regions; see Figure 3.17. The model underestimates the total column abundance by approximately 10–20 DU at all latitudes. This underestimation is most likely caused by the simple parameterization of the height of the tropopause. In the model, pressure levels defined as being in the troposphere are connected by parameterized vertical mixing, K_{zz}, to fixed low ozone mixing ratios at the surface, thereby creating a tropospheric sink for ozone. Therefore, an overestimation of the height of the tropopause in the model will reduce the total column ozone abundance, because the lowest part of the stratosphere is erroneously coupled to the tropospheric sink. This effect could be ameliorated by a finer vertical resolution near the tropopause, an adjustment of the K_{zz} values to weaken the vertical mixing at appropriate pressure levels, and/or a conversion of the model to isentropic surfaces, which better represent a natural boundary between troposphere and stratosphere.

The meridional circulation of the winter hemisphere is stronger that that of the summer; see Figure 3.9. Consequently, ozone accumulates in the extratropics during

winter and spring. The simulated ozone captures this behavior, as shown in Figure 3.18. During the northern winter, Figure 3.18a, the simulation successfully captures the northward transport of ozone by the winter cell of the BDC. The model correctly predicts the latitude of the minimum column abundance at 15°N and has a reasonably good match to the gradient of the meridional profile between 15°N and 55°N. On the other hand, the gradient of the simulated ozone values in the southern latitudes (southern summer) is larger than the observed gradient, suggesting that the summer cell of the BDC may be exaggerated in the model, although the lack of heterogeneous chemistry in the winter poles or the aforementioned tropopause height error may also be factors. A similar pattern is seen in the southern winter, Figure 3.18c; the simulation has a good match to the observed gradient in the south but has an exaggerated gradient in the north.

During the northern spring, Figure 3.18b, there is a large accumulation of ozone in the high latitudes of the NH. This is consistent with the known reach of the northern BDC cell into the polar region during winter, thereby building up the ozone concentration throughout the winter season. Conversely, in the SH, the maximum abundances characteristically occur between 50°S and 60°S. This is consistent with the known exclusion of the southern cell of the BDC from the south polar region, even during the southern winter and spring (see Figures 3.18c and 3.18d). Since there is no heterogeneous chemistry in the model, the destruction of ozone during the polar spring of both hemispheres is not simulated.

In the northern latitudes and tropics, the seasonal cycles match fairly well, Figure

3.19, although the simulated summer values in the extratropics are larger than the observations (once the overall 10–20 DU shift is accounted for). This may be due to an overly large summer circulation as described above. Furthermore, there is a 1–2 month phase shift between the observed and simulated ozone. The discrepancies in the between the simulated and observed seasonal cycles of the southern latitudes are much more pronounced for the southern latitudes, Figure 3.20. The cycles are as much as 4–5 months out of phase. The origin of this phase shift is uncertain at this time; it may be due to the tropopause height error described above if that error is seasonally dependent or it may be an indication of problems in the NCEP-2 stratospheric dynamic fields used to construct the driving stream function. The NCEP-2 meridional wind field may not be realistic in the high latitudes of the SH because there are relatively few radiosonde measurements.

The linear trends in the simulated ozone match the observed trends fairly well in the tropics and northern midlatitudes; see Figures 3.21 and 3.22. However, the decline of ozone abundances in the southern latitudes seen in the observations is not captured in the simulation. This may be due to the lack of heterogeneous chemistry, which causes a much larger loss of ozone in the SH than in the NH. However, discrepancies in the southern circulation or tropopause height may also play a role.

3.3.3.2 IAV

Correlation coefficients between the simulated and observed anomaly time series are shown in Table 3.3. In the northern latitudes, Figures 3.23 and 3.24, the anomaly time series are reasonable well correlated, showing a transition from a QBO-dominated

signal in the tropics to a QBO-AB dominated signal in the higher latitudes. The node in the ozone QBO occurs near 15°N; this is the cause of the low correlation value seen there. The simulated ozone at 5°N shows that the simulated ozone QBO is substantially larger than the observed ozone QBO in the tropics. This exaggerated QBO signal is present at most latitudes.

In the southern latitudes, the simulated and observed anomaly time series have weaker correlation than their northern counterparts. However, they are still significant up to 35°S. Below 35°S, the time series decorrelate; at 45°S, they are only weakly correlated and at 55°S, they are statistically uncorrelated.

Fleming et al. (2002) first successfully calculated the residual mean meridional stream function using data from UKMO GCM and UARS observations. Their results for the total column ozone are a good simulation of MOD from 1993 to 2000. However, their model underestimates the tropical total column ozone. Our model also underestimates the total column ozone; conversely, it somewhat overestimates the tropical ozone anomaly.

In order to further study the simulated ozone IAV, we compared PCA analyses of the simulated ozone and of the zonally averaged MOD. Both datasets were deseasonalized, detrended and lowpass filtered at 15 mo. prior to performing the PCAs. The results of the PCA of the simulated data are shown in Figures 3.27–3.30. The first three EOFs of the PCA for the simulated ozone capture 89% of the IAV; see Figure 3.27. The first EOF (Figure 3.28), capturing 66% of the IAV, shows a slightly asymmetric QBO signal. The second EOF (Figure 3.29), capturing 16% of the IAV, is

dominated by a QBO-AB signal. However, the pattern is distorted from the expected tilted plane by a tropical bulge reminiscent of a QBO pattern. The third EOF (Figure 3.30), capturing 7.5% of the IAV, shows strong signals of both QBO and QBO-AB.

The results of the PCA of the observed ozone are shown in Figures 3.31–3.34. The first three EOFs of the PCA for the observed ozone capture 81% of the IAV; see Figure 3.31. The first EOF (Figure 3.32), capturing 43% of the IAV, shows a very asymmetric signal with significant contributions from both the QBO and QBO-AB. The second EOF (Figure 3.33), capturing 24% of the IAV, is dominated by a QBO-AB signal. The third EOF (Figure 3.30), capturing 14% of the IAV, shows strong symmetric signals associated with the QBO.

Comparing these analyses, we can see that the three leading EOFS of both are dominated by the same two signals, the QBO and the QBO-AB. Between them, they account for comparable amounts of the total IAV. However, the distribution of the variance amongst the three modes is substantially different in the two analyses. In the observed ozone, there is comparable variability associated with the QBO and QBO-AB and asymmetry of the QBO at higher latitudes allows the two signals to strongly project onto each other creating a leading EOF that contains a substantial contribution from both. The next two EOFs account for much of the remaining variance associated with the QBO and QBO-AB signals, respectively. In the simulated ozone, the excessive variability associated with the QBO skews the first EOF towards a QBO pattern. It is now the third mode which has significant contributions from both processes. Reducing the variability in the simulation associated with the

QBO would probably result in a better agreement between the PCA analyses of the simulated and observed ozone.

3.4 Conclusions

A PCA of the 45°S – 45°N latitude band of MOD for the years 1979 to 2002 results in a concise representation of the IAV of the total column ozone abundances. The first four modes capture 82% of the IAV, and reflect the spatial and temporal patterns of the QBO, QBO-AB, ENSO, and decadal fluctuations, albeit with substantial conflation of these processes amongst the leading PCA modes. However, attempting to extend the PCA analysis to a 60°S–60°N latitude band does not result in a comparably useful representation. Even more conflation of the processes occurs; furthermore, the prominent synoptic-scale variability present at higher latitudes projects strongly onto all of the leading EOFs.

We also use the Caltech/JPL 2D CTM, driven by an isentropic mass stream function derived from NCEP-2, to study the IAV of ozone related to the QBO and QBO-AB in the tropics and midlatitudes from 1979 to 2002. The use of the isentropic mass stream function shows great promise. This study successfully simulates the IAV associated with the QBO and QBO-AB of ozone between 40°S and 60°N, although the amplitude of the QBO signal is exaggerated. Curiously, the model's representation of the IAV in this region is better than its representation of the climatology. While the tropical and northern linear trend are reasonable, none of the southern trends in the simulation show the expected decline in ozone column abundances. The

severest discrepancies occur in the mean seasonal cycle; the northern seasonal cycles are underestimated and slightly out of phase, while the southern seasonal cycles are almost 180° out of phase. Since the 2D meridional stream function cannot capture the longitudinal variation of the ENSO signal, no clear ENSO signal is expected or found in the simulated total column ozone results. The decadal signal in the simulation is substantially weaker than that observed. Since the model does not incorporate fluctuations in ozone production associated with the solar flux variability, some decrease, $\sim 50\%$, in decadal variability is expected.

These results point to many ways to improve the simulation of the ozone IAV. A better parameterization of the tropopause is needed. Some ways to achieve this include a finer vertical resolution (particularly near the tropopause), using isentropic rather pressure coordinates and an improvement vertical mixing (convection) parameterization. This may greatly help the simulation in the tropics and midlatitudes. However, to simulate polar behavior and to capture the variability associated with zonally asymmetric patterns such as ENSO, the North Atlantic Oscillation or other perturbations of the tropopause, a three-dimensional model is necessary.

Table 3.1: Correlations between MOD PCs and Various Indices

PC #	Filter	Index	Corr.	Sig. Level
1	(none)	Solar Flux	-0.49	.01
	Lowpass C		-0.86	.006
	(none)	QBO	0.57	.03
	Bandpass A		0.67	.02
2	(none)	Solar Flux	-0.31	.01
	Lowpass C		-0.70	.02
	(none)	QBO	0.35	.03
	Bandpass A		0.37	.04
3	(none)	Solar Flux	0.61	.03
	Lowpass C		0.82	.02
	(none)	QBO	0.43	.03
	Bandpass A		0.58	.03
4	(none)	SOI	0.60	.0005
	Bandpass A		0.61	.0004

Table 3.2: Correlations (Lag = 0) and Maximum Cross Correlations of the Stream Function PCs with Various Indices. The numbers in parentheses denote significance levels. Units of lag are month. Positive (negative) lags correspond to the PC time series leading (trailing) the indices.

PC#	Index	Corr. (Sig.)	Max. Cross Corr.	Lag (mo.)
1	QBO	-0.46 (.13)	-0.82 (0.004)	4 mo.
2	QBO-AB	0.52 (.03)	0.65 (0.004)	2 mo.
3	QBO	-0.58 (.07)	-0.81 (0.007)	-3 mo.

Table 3.3: Correlations between 2D Model Ozone and Zonal MOD.

Latitude	Corr.	R^2	Sig.
55.0	0.48	0.23	0.01
45.0	0.62	0.39	0.001
35.0	0.67	0.44	5.e-05
25.0	0.72	0.52	5.e-05
15.0	0.39	0.13	0.005
5.0	0.74	0.55	0.005
-5.0	0.72	0.52	0.01
-15.0	0.40	0.16	0.05
-25.0	0.53	0.29	0.005
-35.0	0.48	0.23	0.005
-45.0	0.37	0.14	0.02
-55.0	0.13	0.016	> 0.1

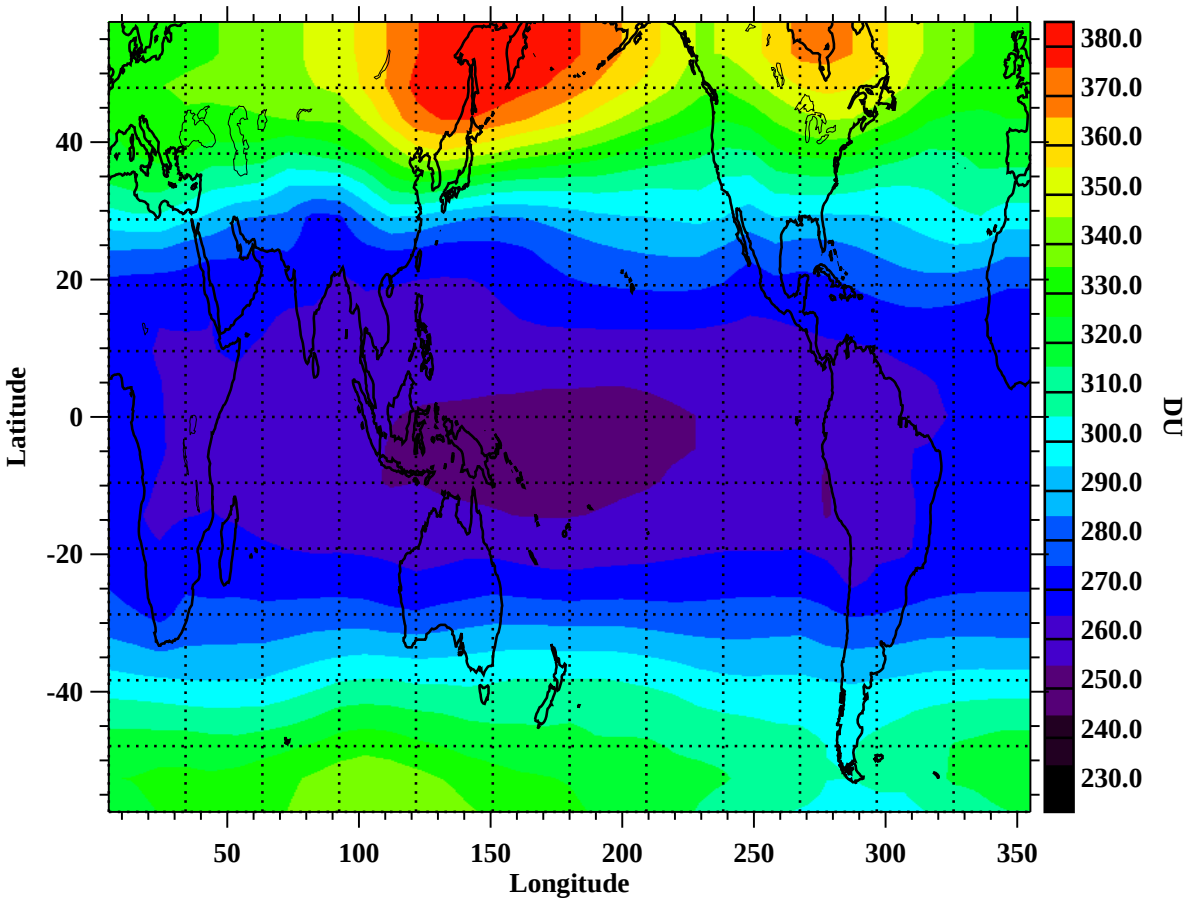

Figure 3.1: Nov. 1978–Dec. 2002 mean of MOD. Units are DU.

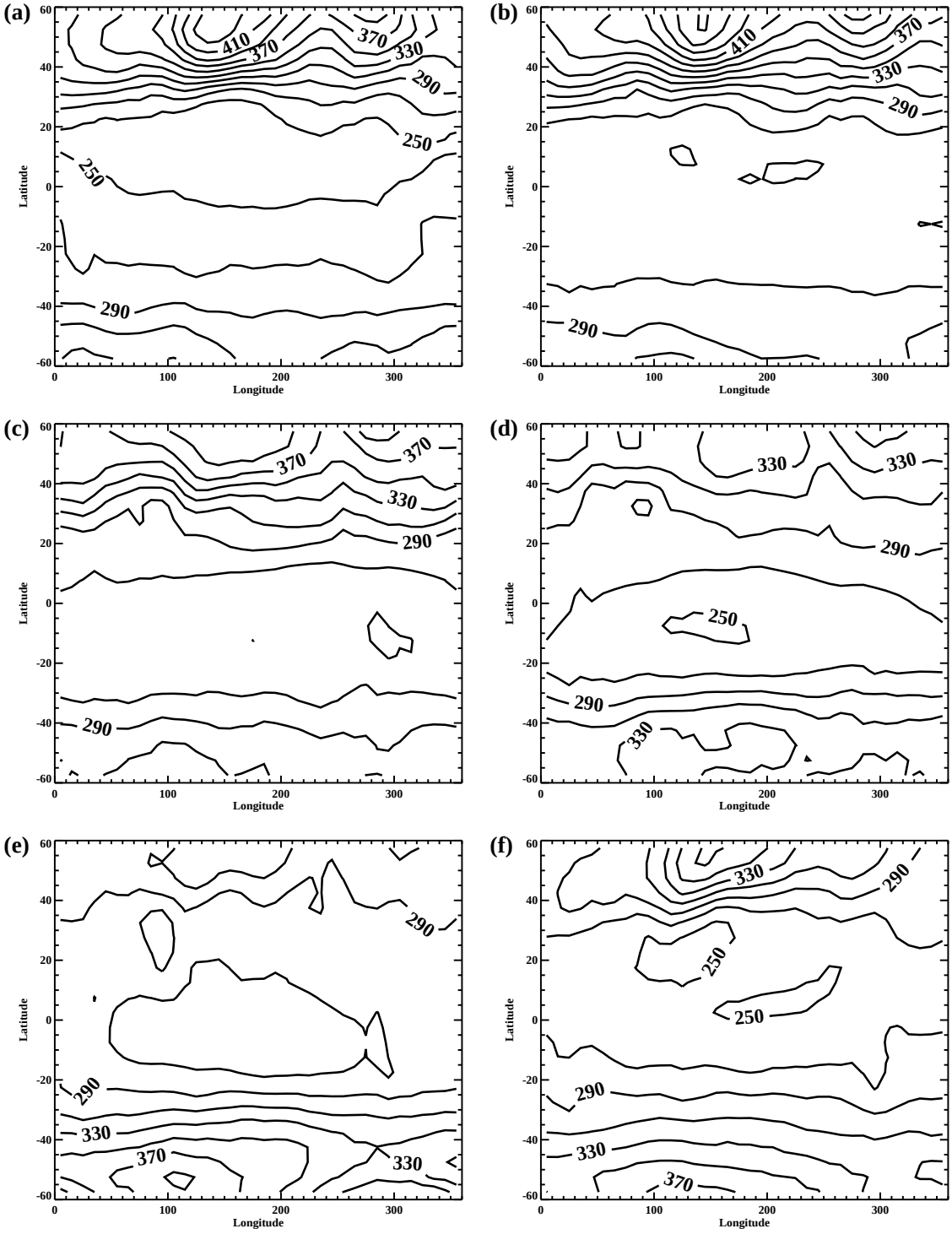

Figure 3.2: Monthly means for MOD. Units are DU. (a) 1979–2002 Jan. mean. (b) 1979–2002 Mar. mean. (c) 1979–2002 May mean. (d) 1979–2002 Jul. mean. (e) 1979–2002 Sep. mean. (f) 1979–2002 Nov. mean.

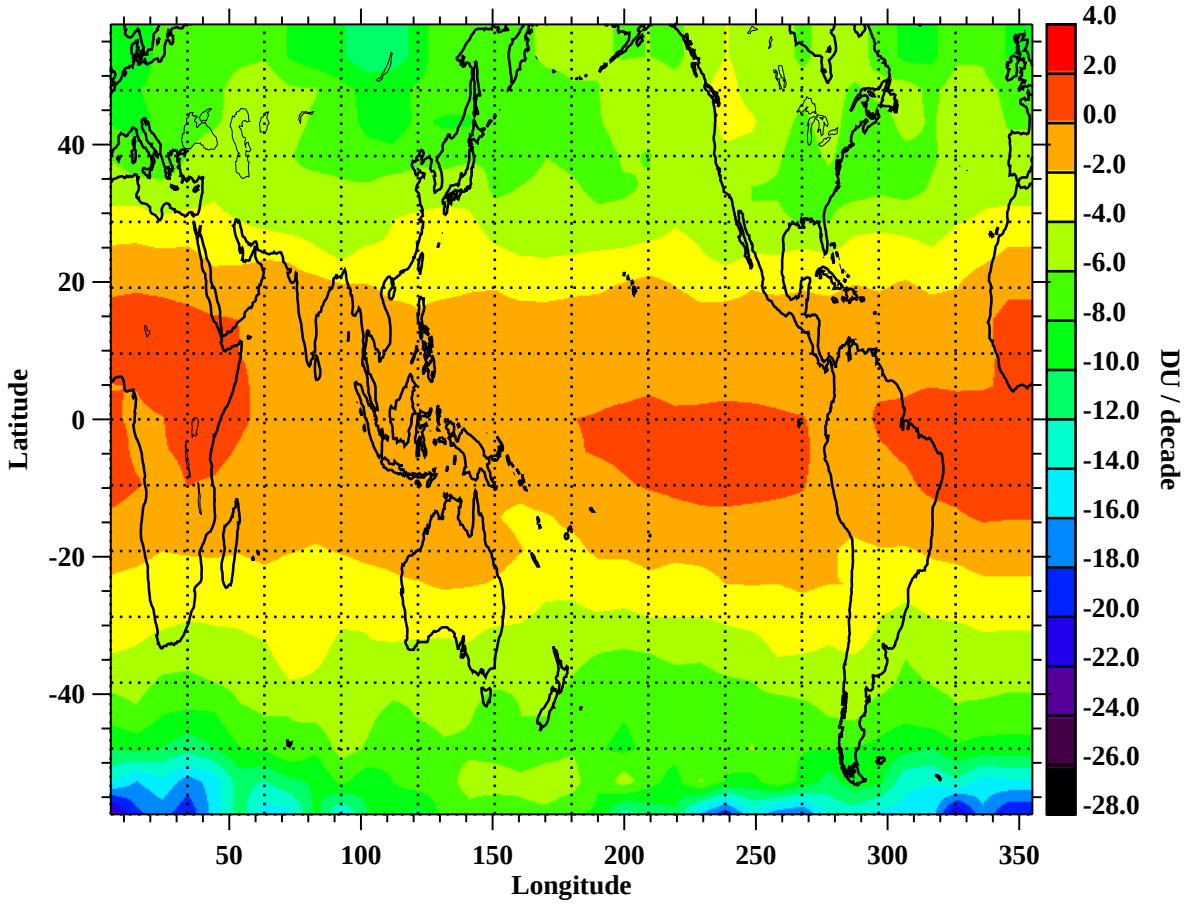

Figure 3.3: Nov. 1978–Dec. 2002 linear trend for MOD. Units are DU / decade.

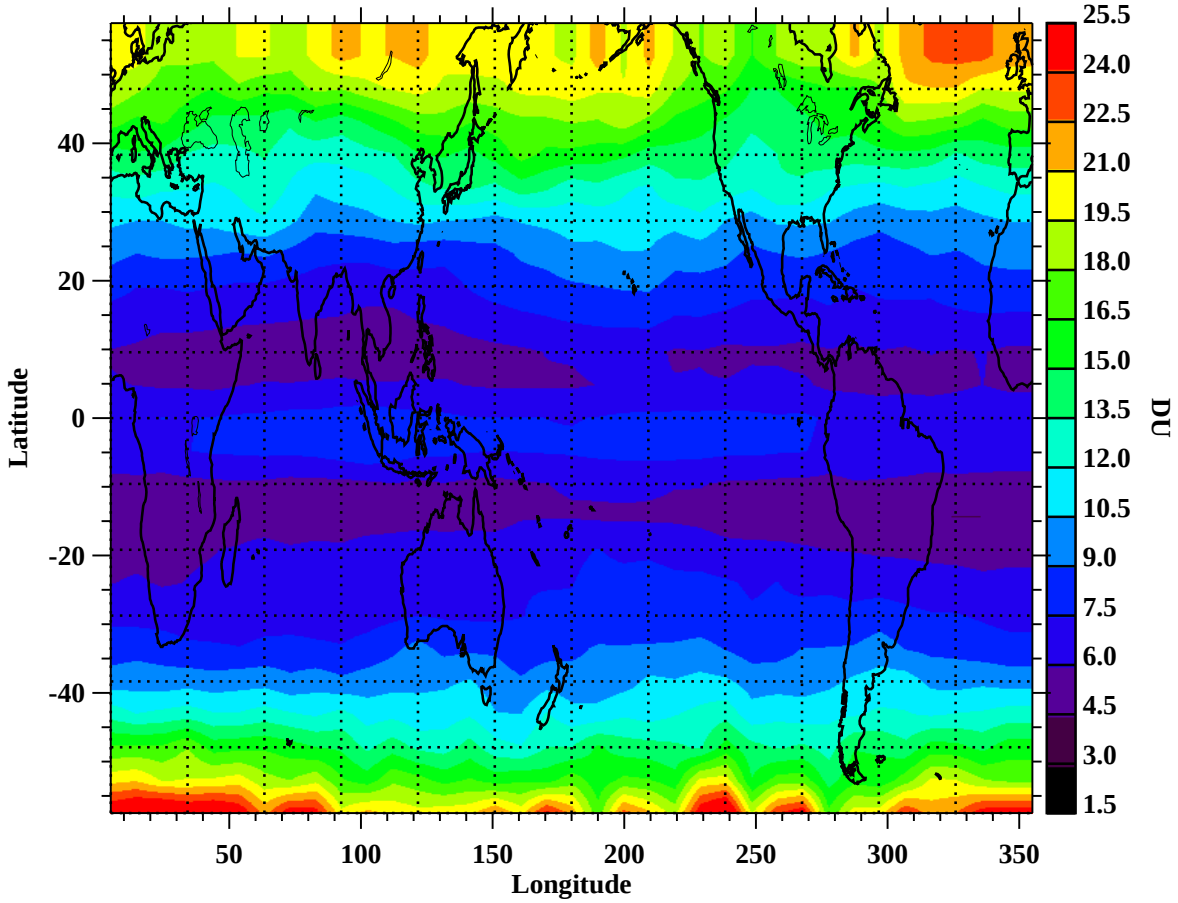

Figure 3.4: Standard deviation of the deseasonalized and detrended MOD. Units are DU.

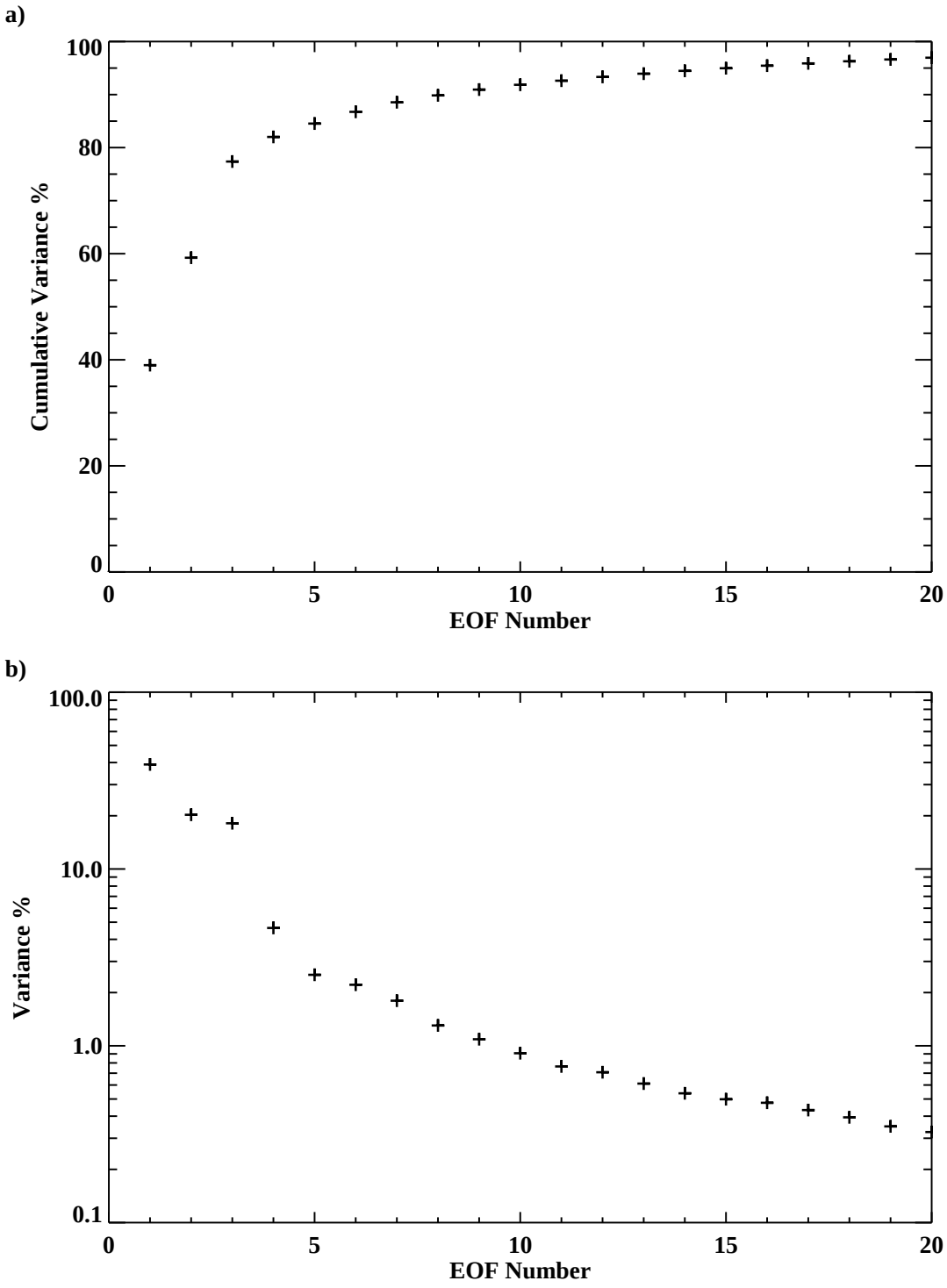

Figure 3.5: Relative and cumulative relative variance from the PCA of MOD. (a) Cumulative relative variance. (b) Relative variance.

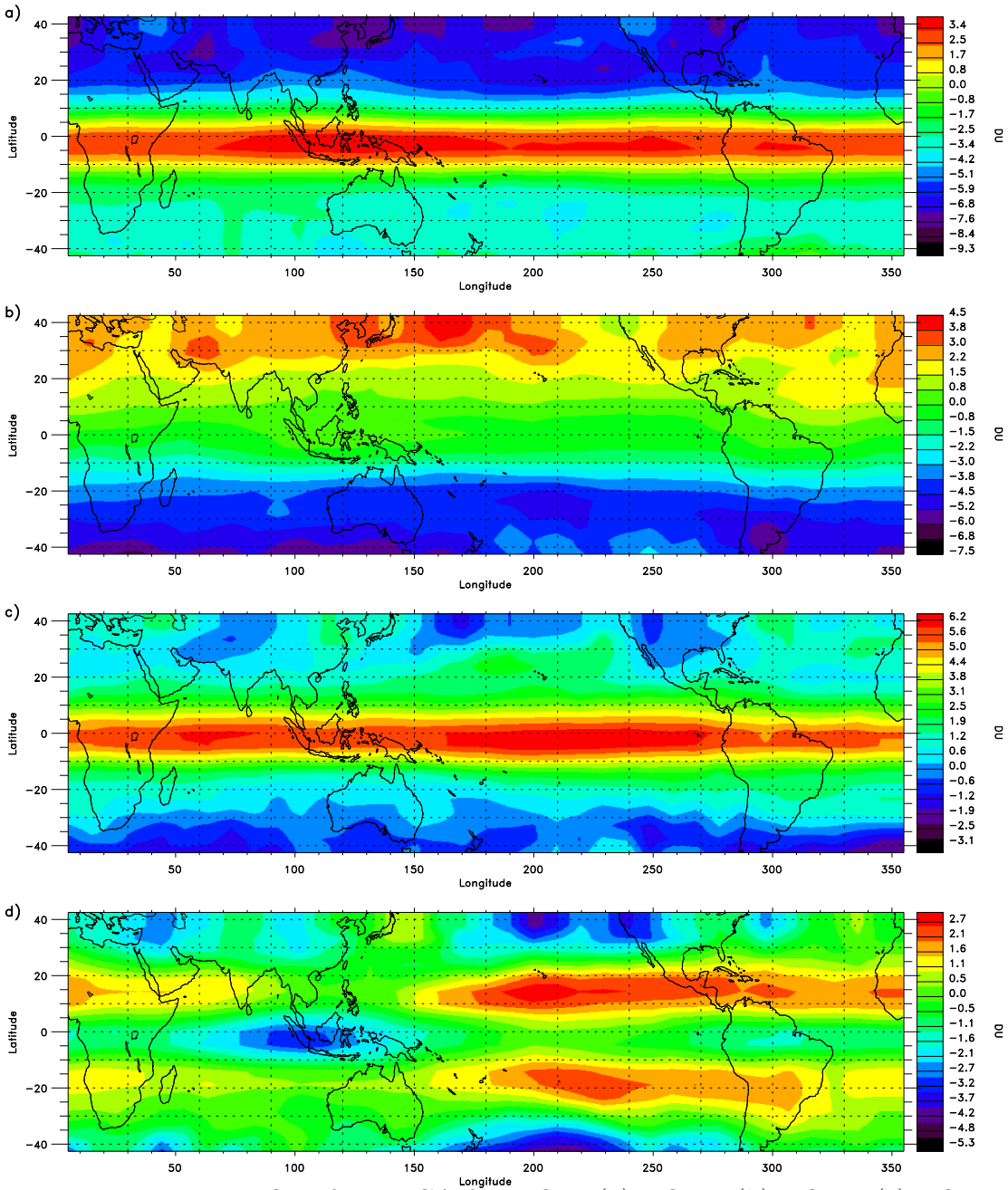

Figure 3.6: First 4 EOFs from PCA for MOD. (a) EOF1, (b) EOF2, (c) EOF3, (d) EOF4.

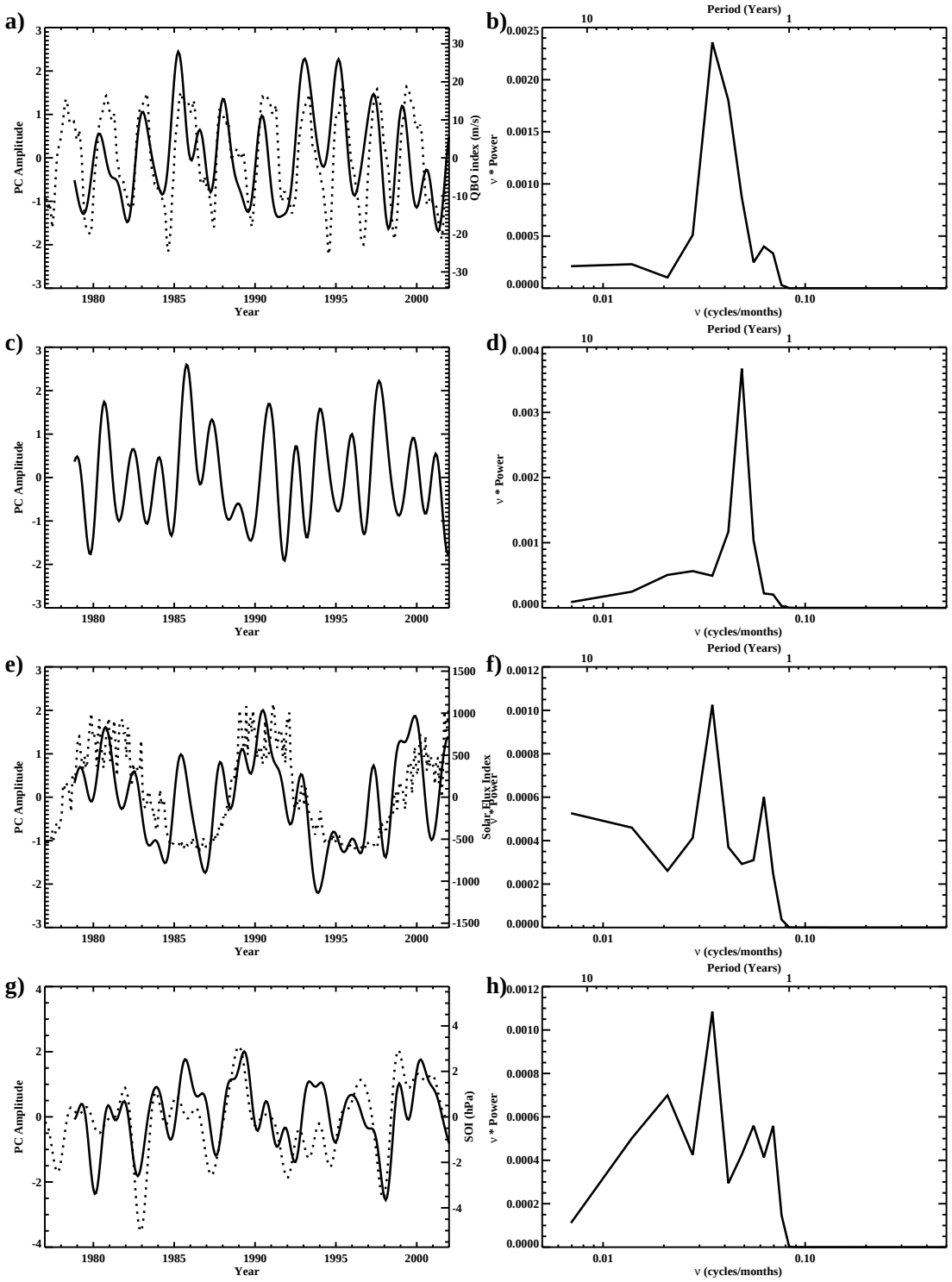

Figure 3.7: First four PC time series and associated PSD from PCA for MOD. PC time series (solid) shown with appropriate index (dotted). (a) PC1 and QBO index. (b) PSD of PC1, (c) PC2, (d) PSD of PC2, (e) PC3 and Solar Flux, (f) PSD of PC3, (g) PC4 and SOI, (h) PSD of PC4.

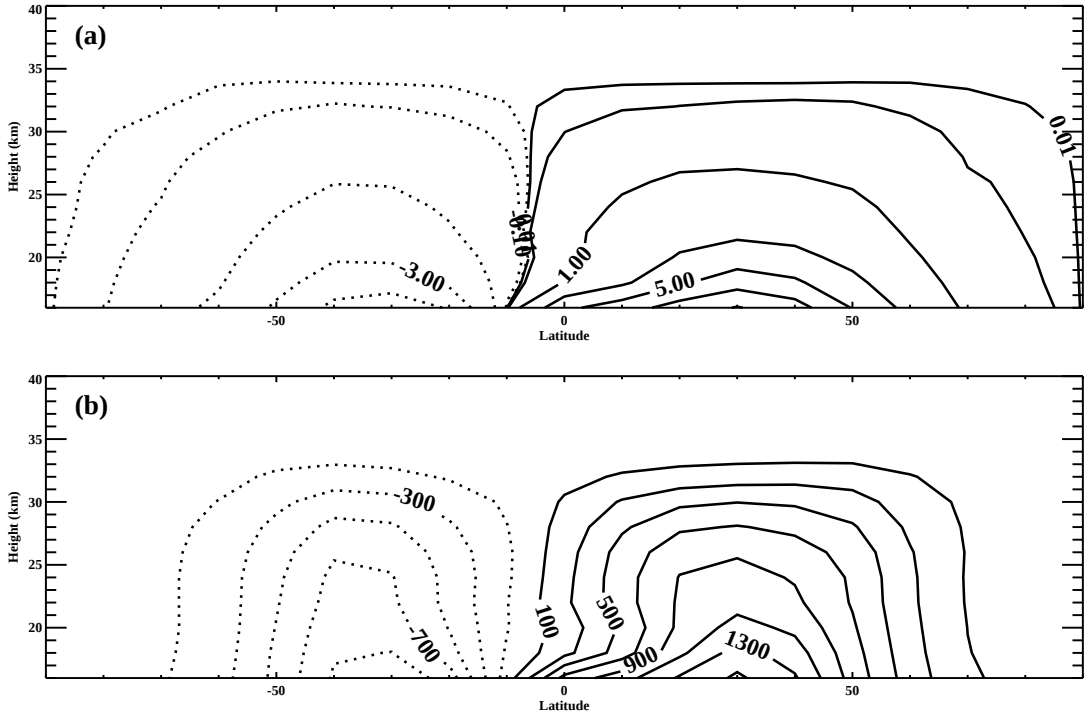

Figure 3.8: (a) 1979–2002 mean of the isentropic mass stream function interpolated to pressure surfaces. Units are $10^9\,\mathrm{kg/\,s}$. (b) 1979–2002 mean of the isentropic velocity stream function interpolated to pressure surfaces. Units are $\mathrm{m}^2/\,\mathrm{s}$.

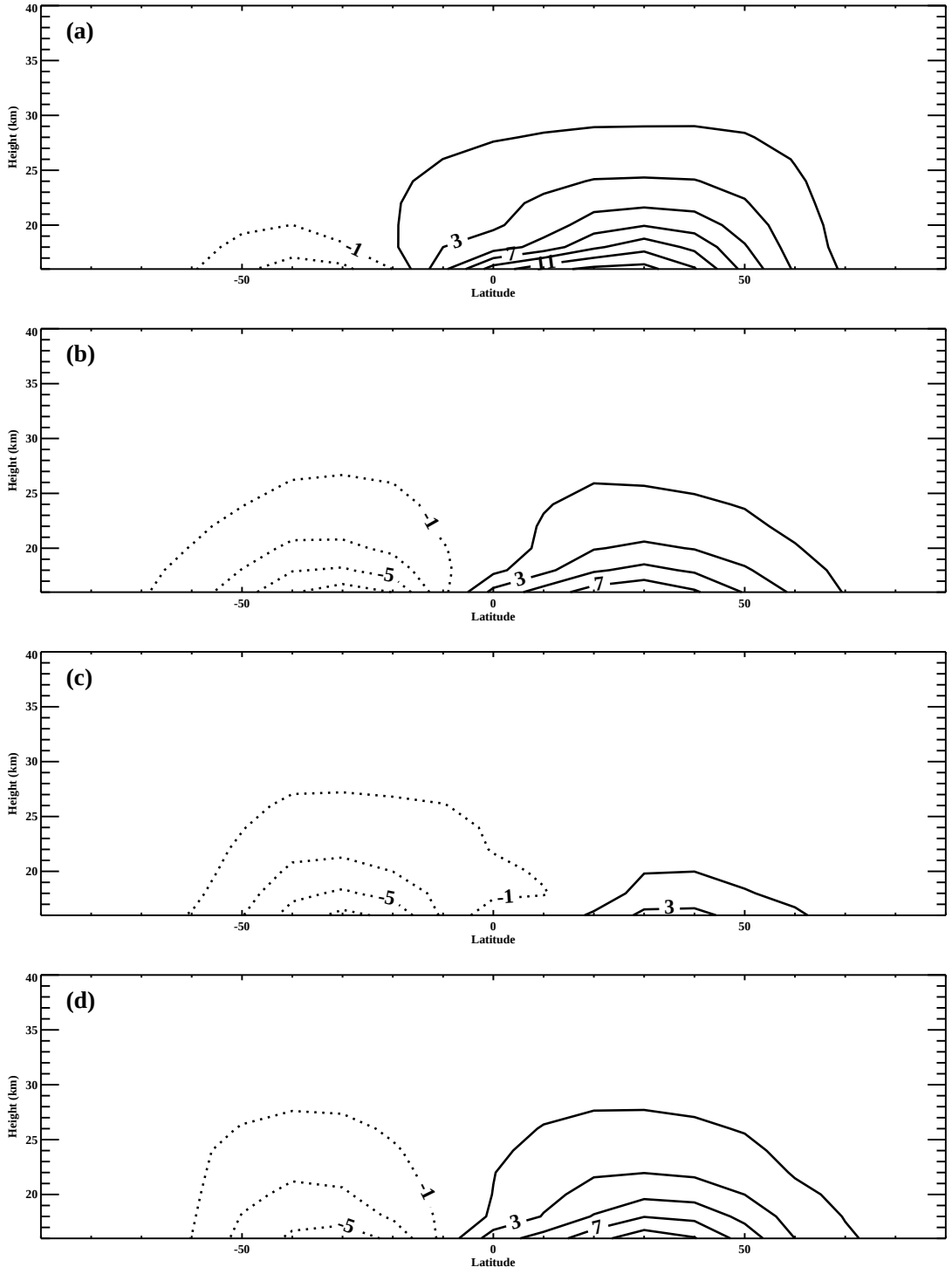

Figure 3.9: Mean seasonal cycle of the isentropic mass stream function. Units are $10^9\,\mathrm{kg/\,s}$. (a) 1979–2002 Jan. mean. (b) 1979–2002 Apr. mean. (c) 1979–2002 Jul. mean. (d) 1979–2002 Oct. mean.

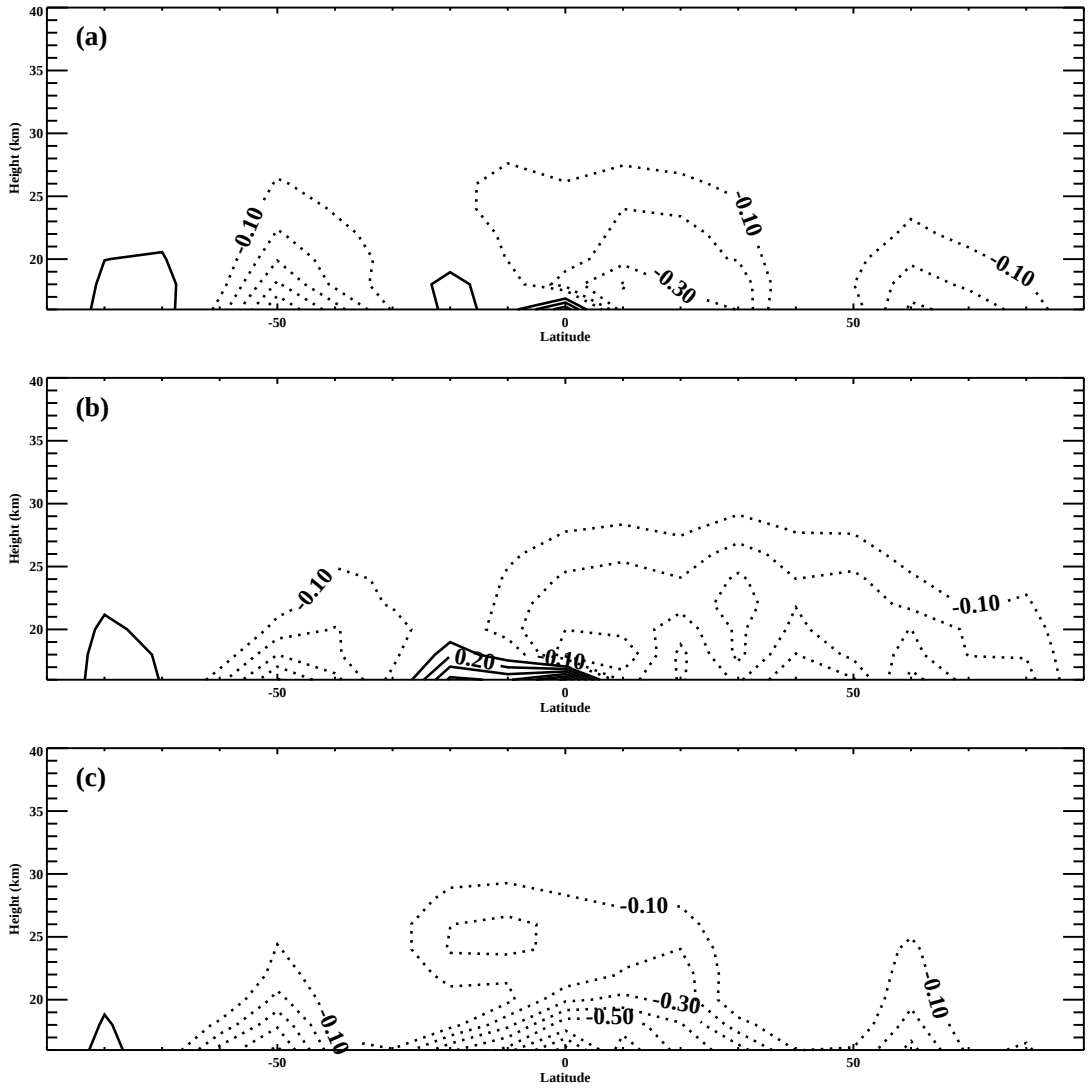

Figure 3.10: Linear trends of the isentropic mass stream function. Units are $10^9\,\mathrm{kg/\,s/\,decade}$. (a) Trend fit to entire dataset (all months). (b) Trend fit to Jan. only. (c) Trend fit to Jul. only.

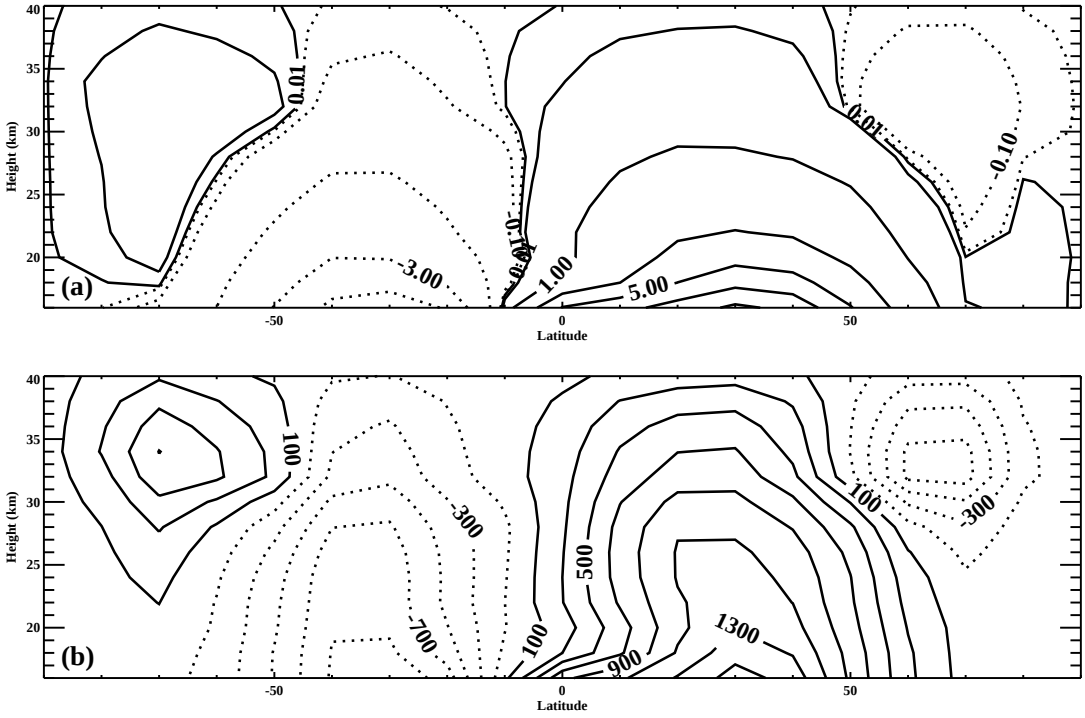

Figure 3.11: (a) 1979–2002 mean of the mean residual circulation stream function scaled by density. Units are $10^9\,\mathrm{kg/\,s}$. (b) 1979–2002 mean of the mean residual circulation stream function. Units are $\mathrm{m}^2/\,\mathrm{s}$.

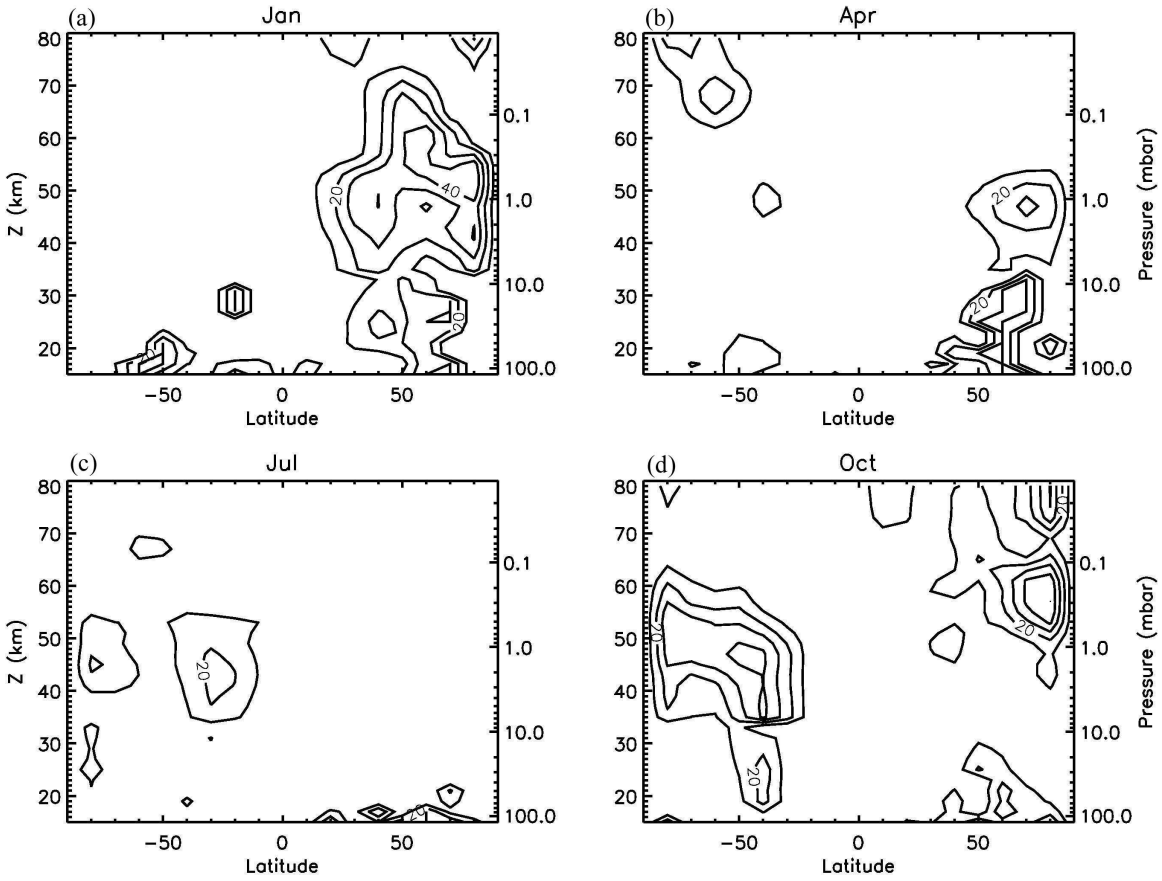

Figure 3.12: Isentropic mixing coefficient, K_{yy}, interpolated to pressure surfaces. Units are $10^5\,\mathrm{m}^2/\,\mathrm{s}$. (a) Jan. 1985 (b) Apr. 1985 (c) Jul. 1985 (d) Oct. 1985

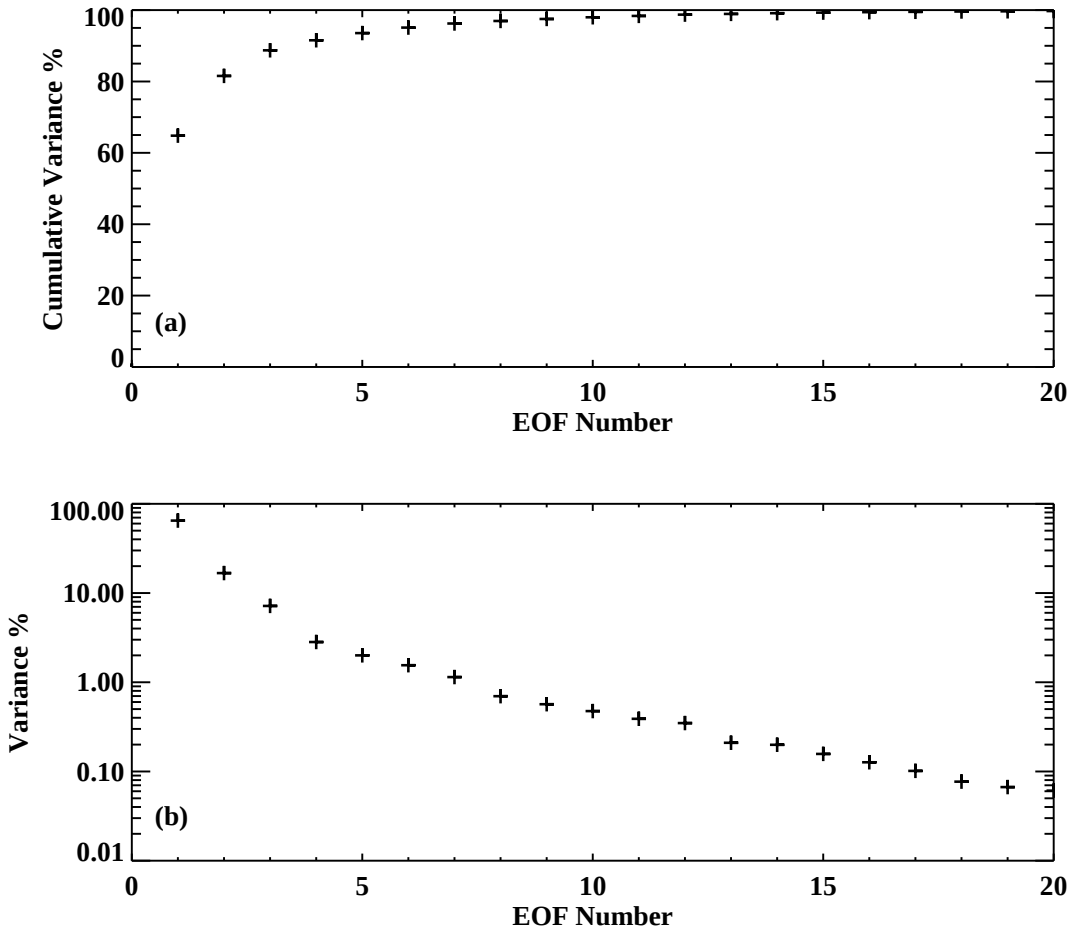

Figure 3.13: Relative and cumulative relative variance for PCA analysis of the isentropic velocity stream function (a) Cumulative relative variance. (b) Relative variance.

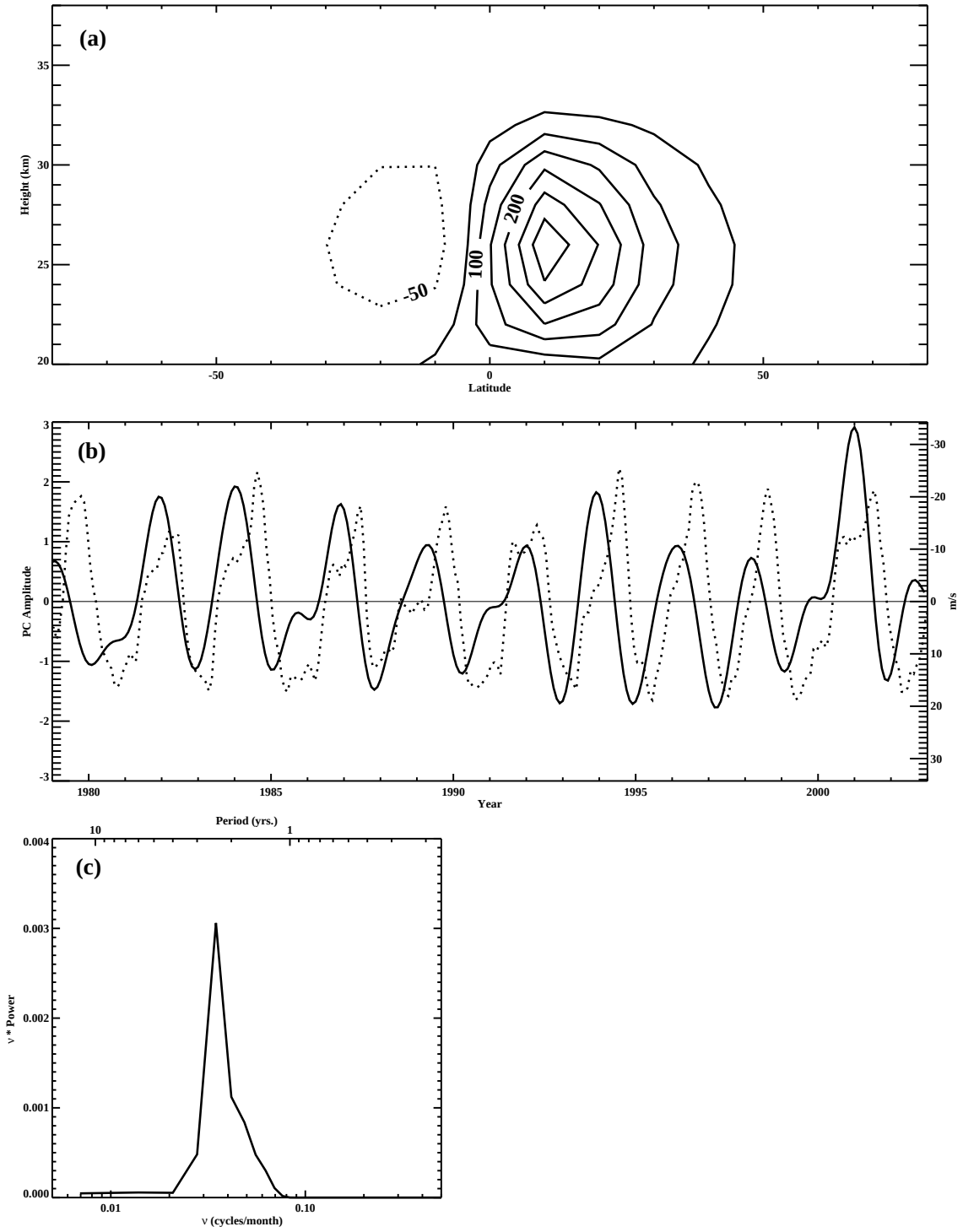

Figure 3.14: First EOF of the isentropic velocity stream function, associated PC time series and its PSD. (a) EOF1; units are m^2/s. (b) PC1 time series (solid). Inverted QBO index (dotted). (c) PSD of PC1.

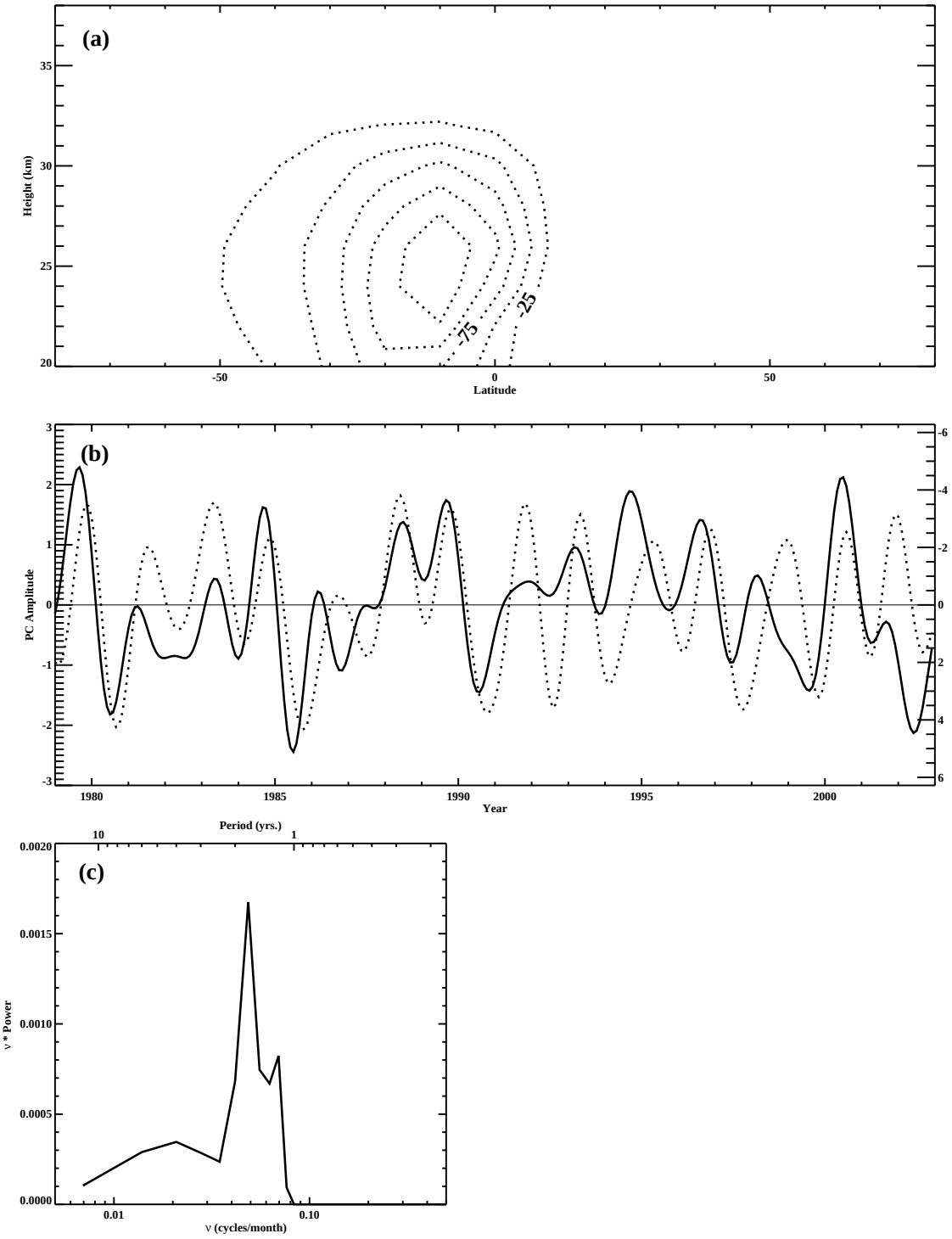

Figure 3.15: Second EOF of the isentropic velocity stream function, associated PC time series and PSD. (a) EOF2; units are m^2/s. (b) PC2 time series (solid). Constructed QBO-AB index (dotted). (c) PSD of PC2.

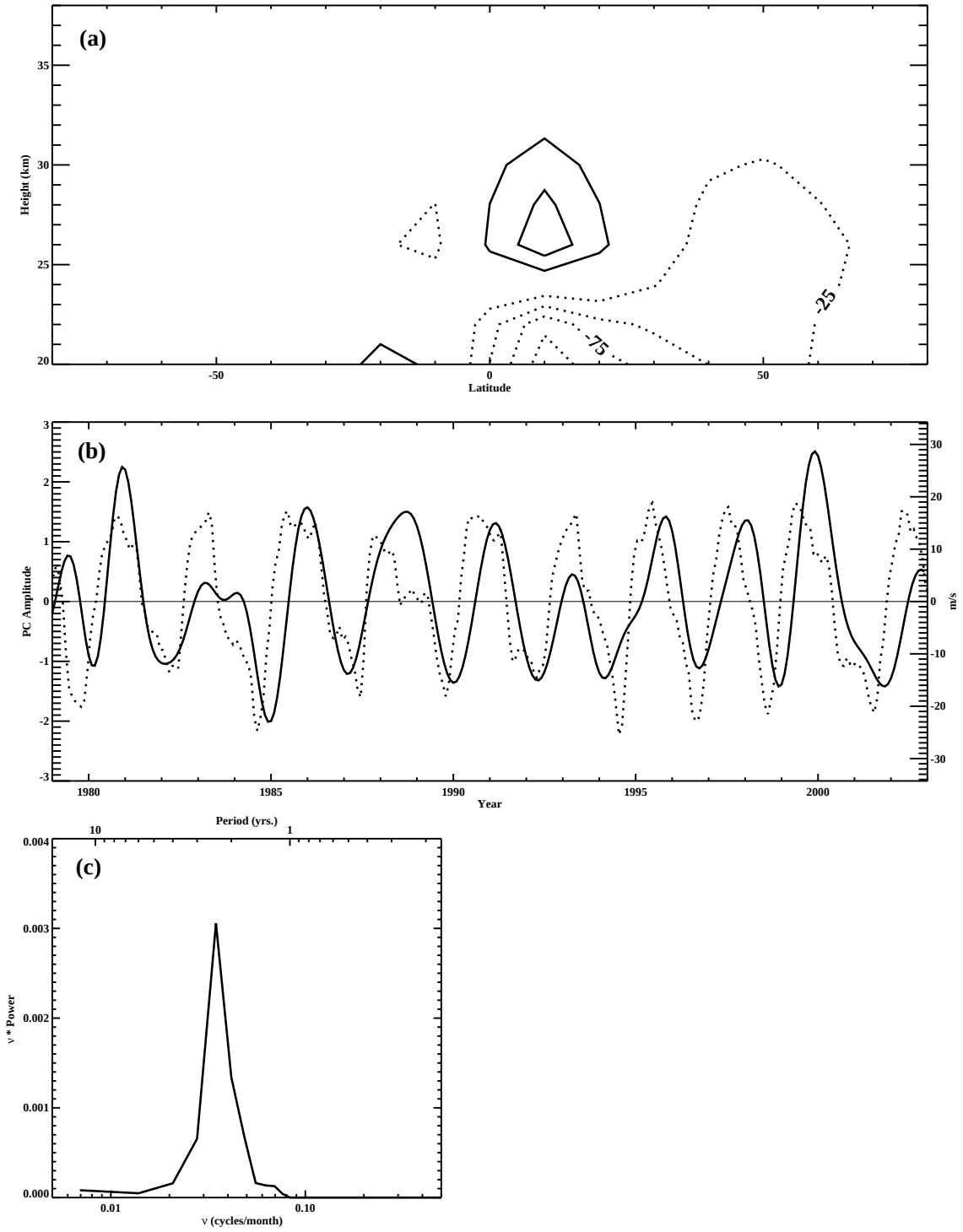

Figure 3.16: Third EOF of the isentropic velocity stream function, associated PC time series and PSD. (a) EOF3; units are m^2/s. (b) PC3 time series (solid). QBO index (dotted). (c) PSD of PC3.

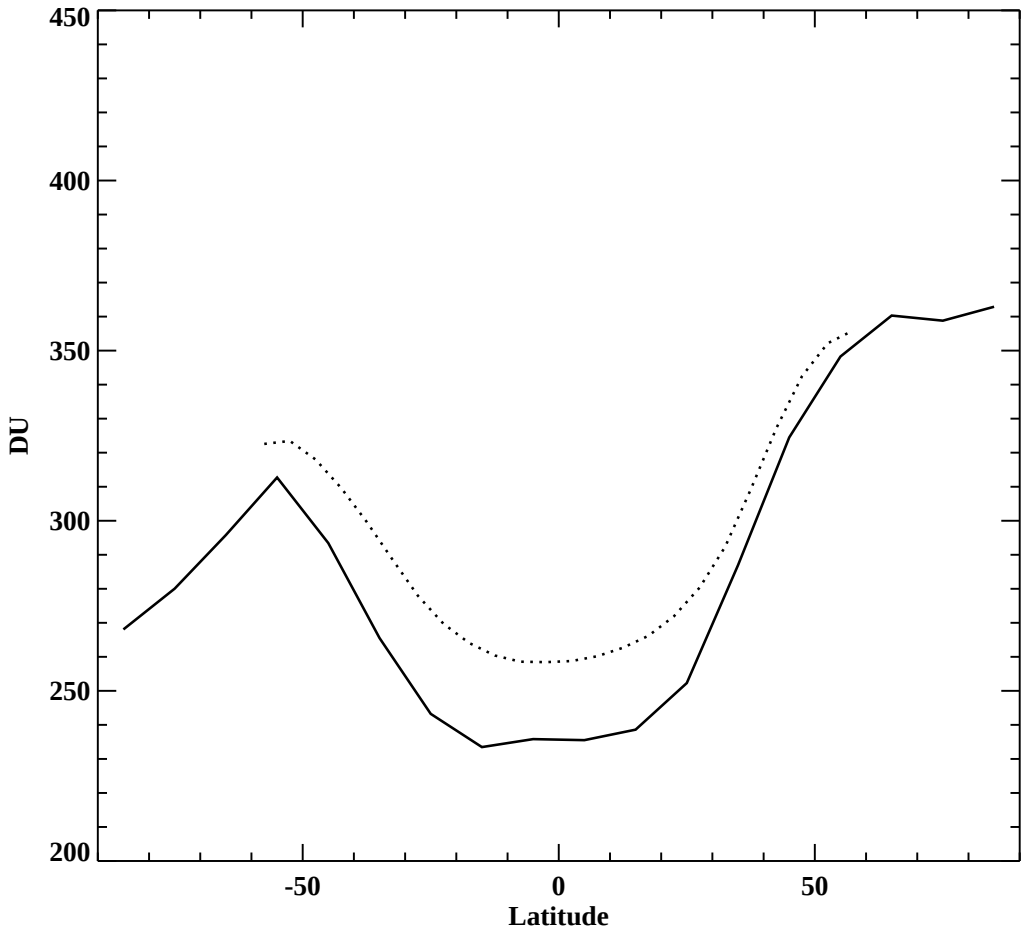

Figure 3.17: 1979–2002 mean column ozone abundances for 2D CTM simulated ozone (solid) and zonally averaged MOD (dotted)

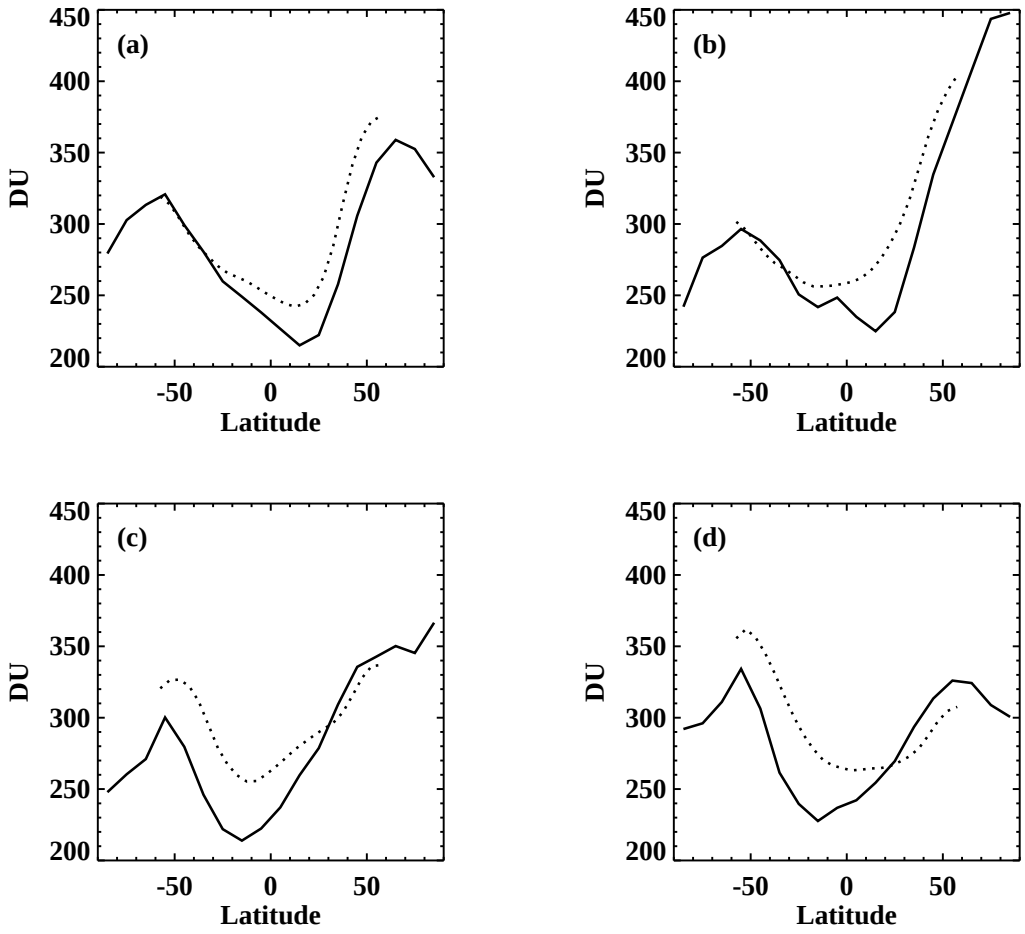

Figure 3.18: 1979–2002 mean column ozone abundances for individual months; 2D CTM simulated ozone (solid) and zonally averaged MOD (dotted) (a) 1979–2002 Jan. mean. (b) 1979–2002 Apr. mean. (c) 1979–2002 Jul. mean. (d) 1979–2002 Oct. mean.

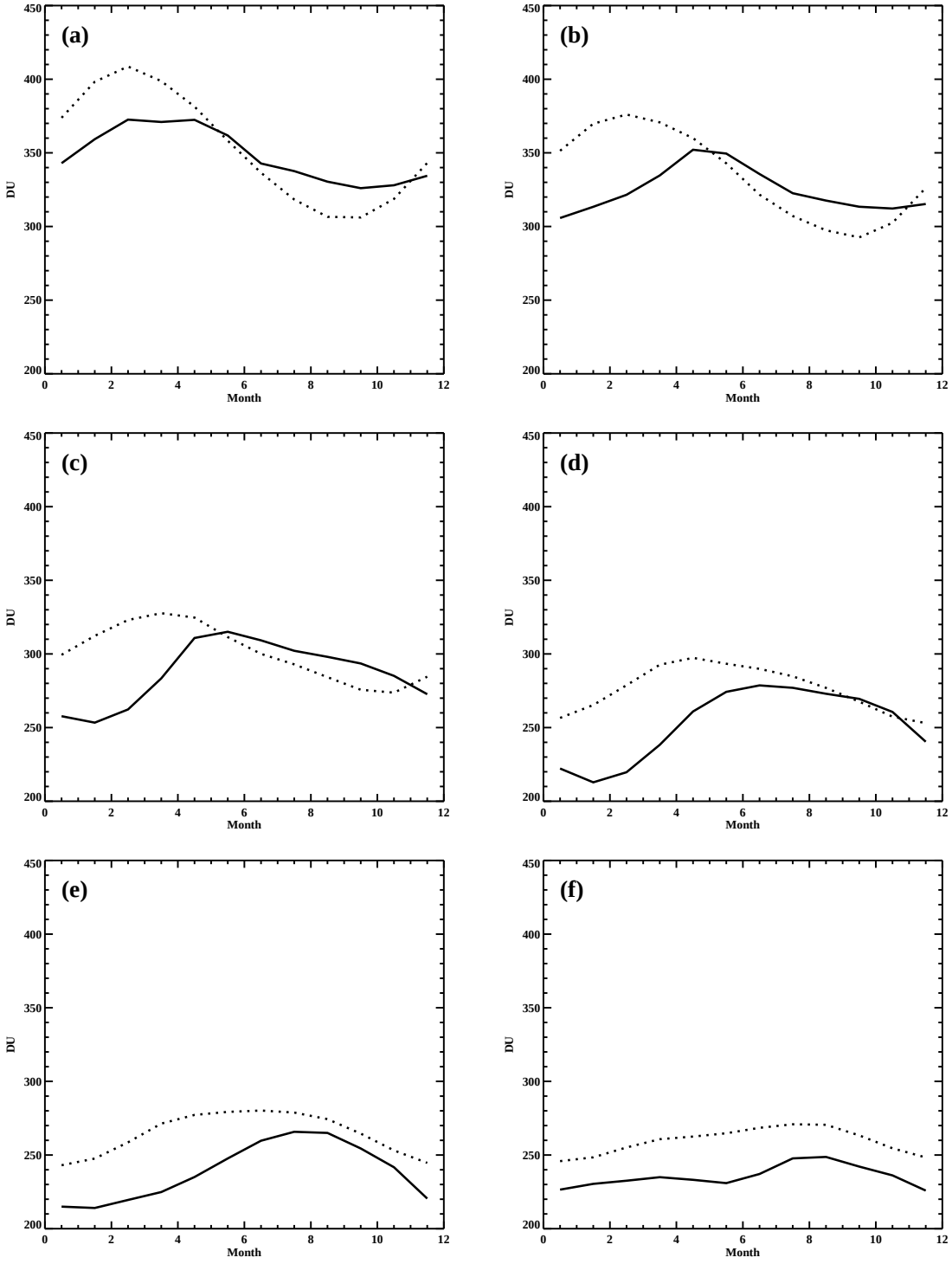

Figure 3.19: Seasonal cycles in northern latitudes; 2D CTM simulated ozone (solid) and zonally averaged MOD (dotted) (a) 55°N, (b) 45°N, (c) 35°N, (d) 25°N, (e) 15°N, (f) 5°N,

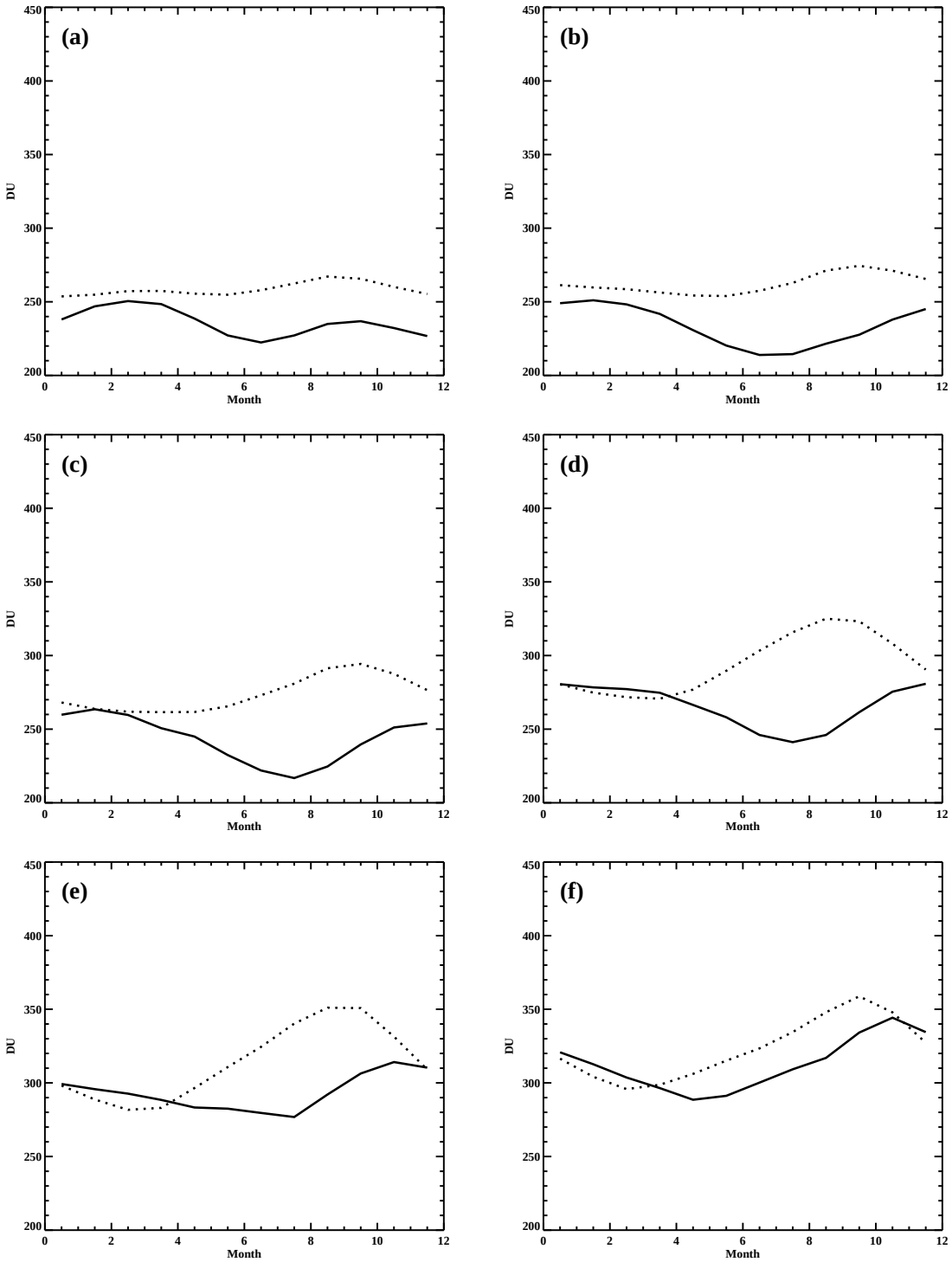

Figure 3.20: Seasonal cycles in southern latitudes; 2D CTM simulated ozone (solid) and zonally averaged MOD (dotted) (a) 5°S, (b) 15°S, (c) 25°S, (d) 35°S, (e) 45°S, (f) 55°S,

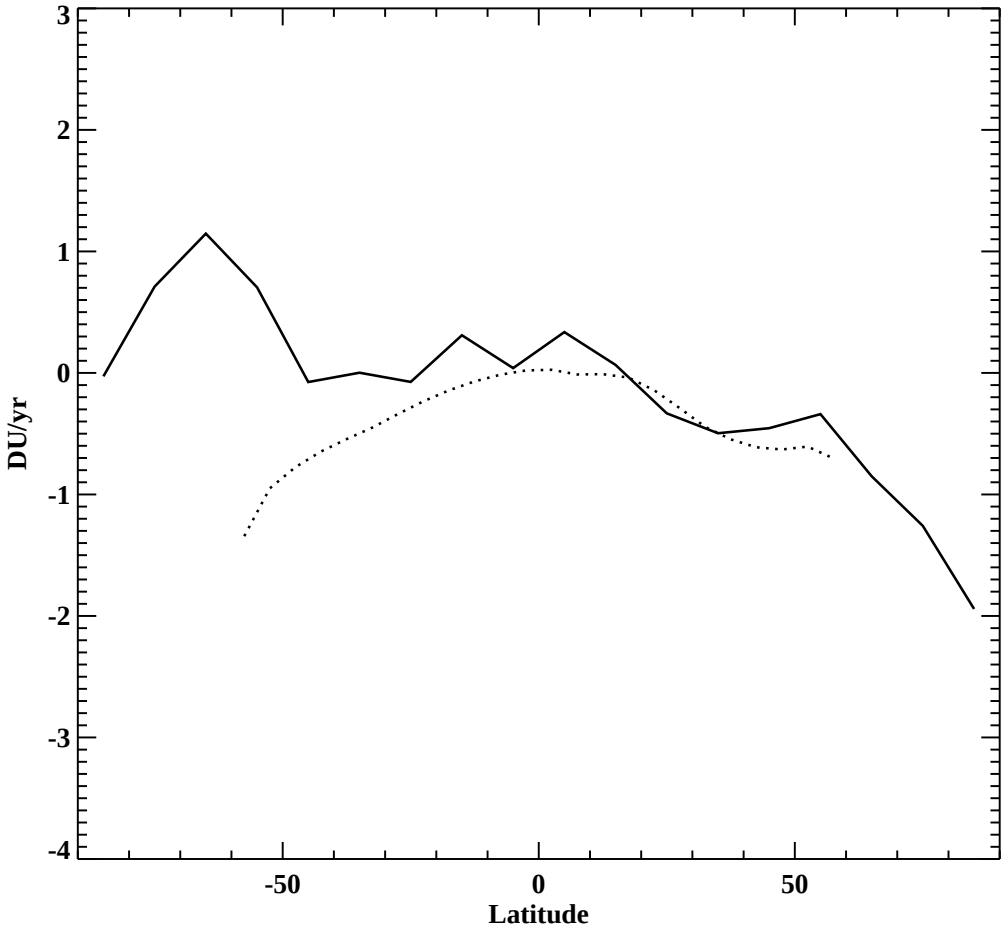

Figure 3.21: Slope of the fitted linear trend for 1979–2002; 2D CTM simulated ozone (solid) and zonally averaged MOD (dotted)

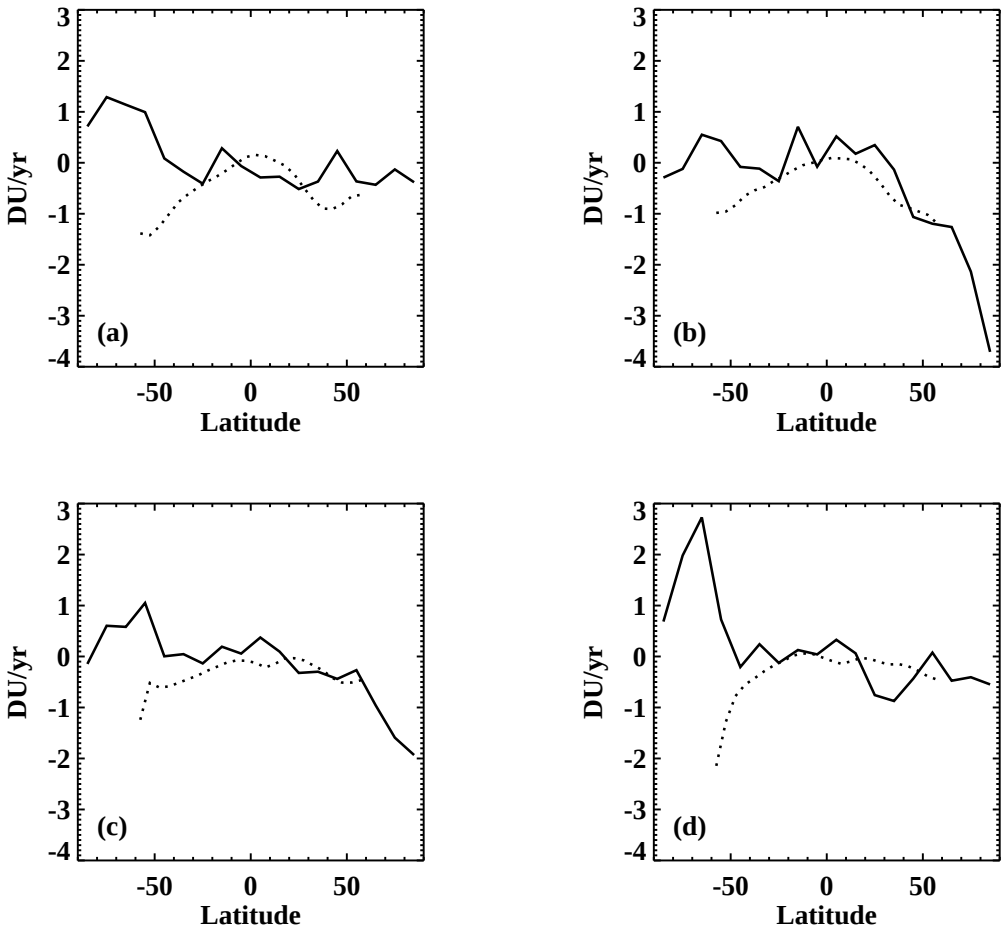

Figure 3.22: Slope of the fitted linear trend for various months during the period 1979–2002. 2D CTM simulated ozone (solid) and zonally averaged MOD (dotted) (a) 1979–2002 Jan. mean (b) 1979–2002 Apr. mean (c) 1979–2002 Jul. mean (d) 1979–2002 Oct. mean

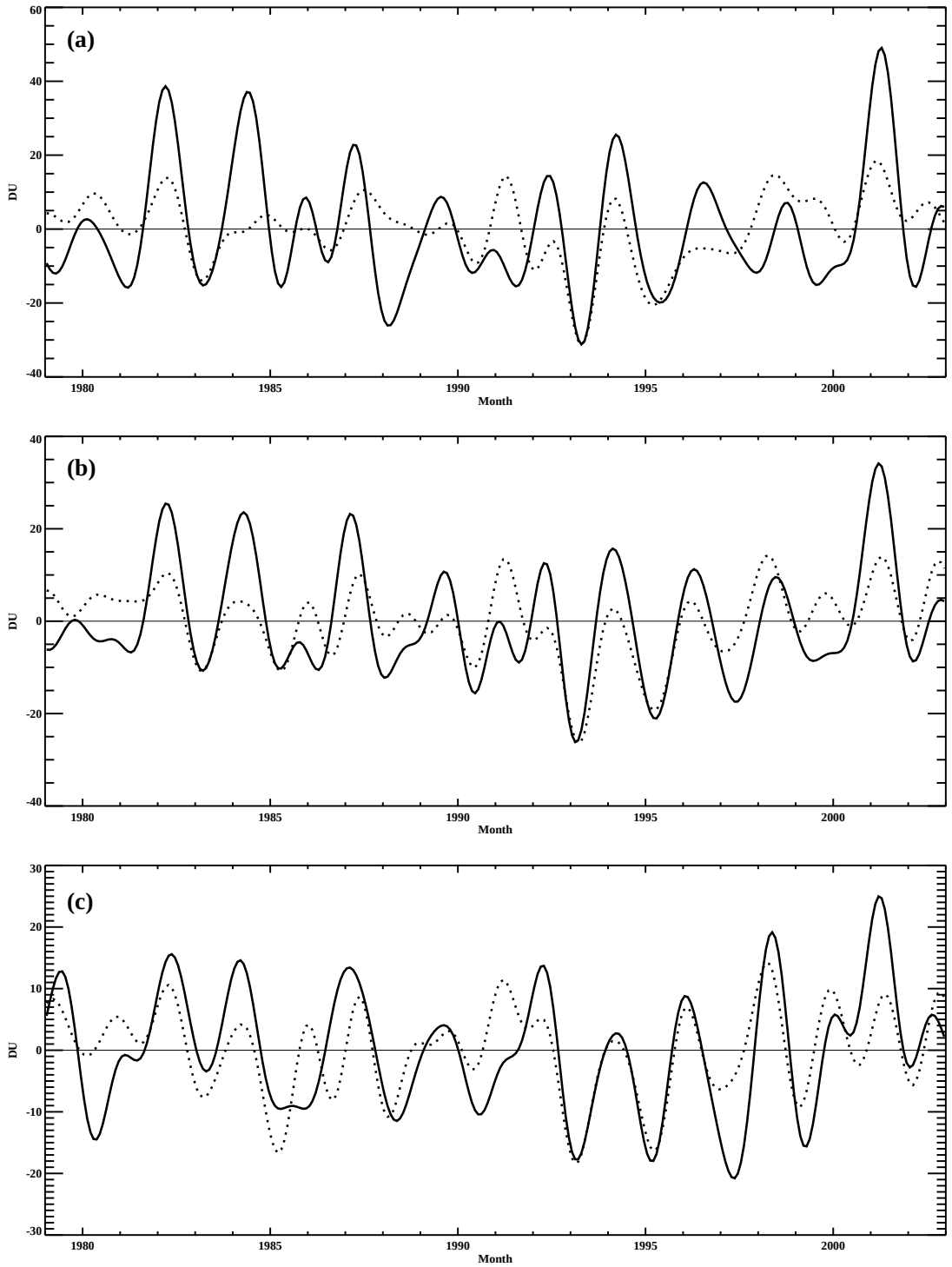

Figure 3.23: Lowpass filtered, deseasonalized and detrended ozone anomalies for the northern midlatitudes; 2D CTM simulated ozone (solid) and zonally averaged MOD (dotted) (a) 55°N, (b) 45°N, (c) 35°N.

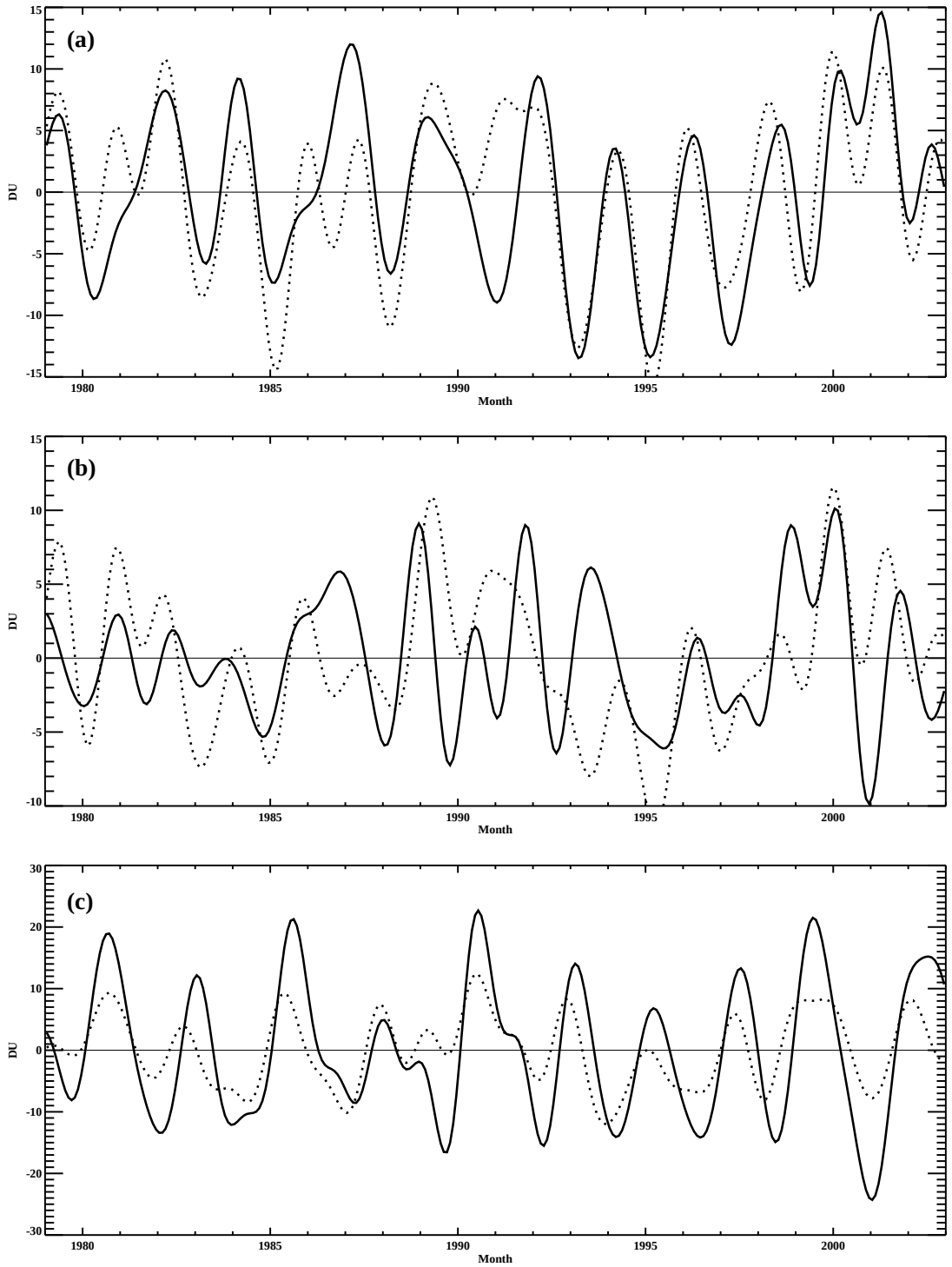

Figure 3.24: Lowpass filtered, deseasonalized and detrended ozone anomalies for the northern subtropics and tropics; 2D CTM simulated ozone (solid) and zonally averaged MOD (dotted) (a) 25°N, (b) 15°N, (c) 5°N,

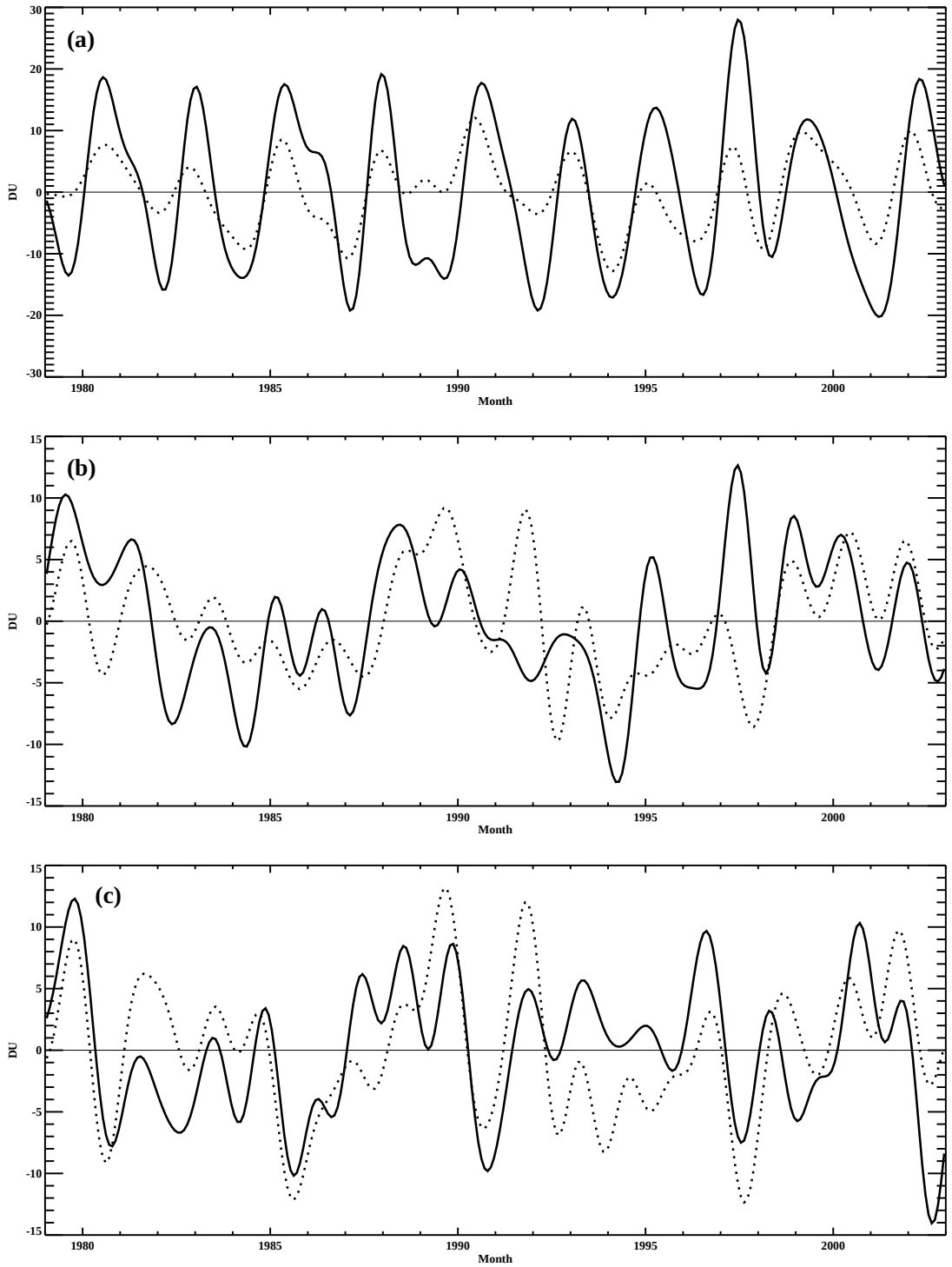

Figure 3.25: Lowpass filtered, deseasonalized and detrended ozone anomalies for the southern subtropics and tropics; 2D CTM simulated ozone (solid) and zonally averaged MOD (dotted) (a) 5°S, (b) 15°S, (c) 25°S,

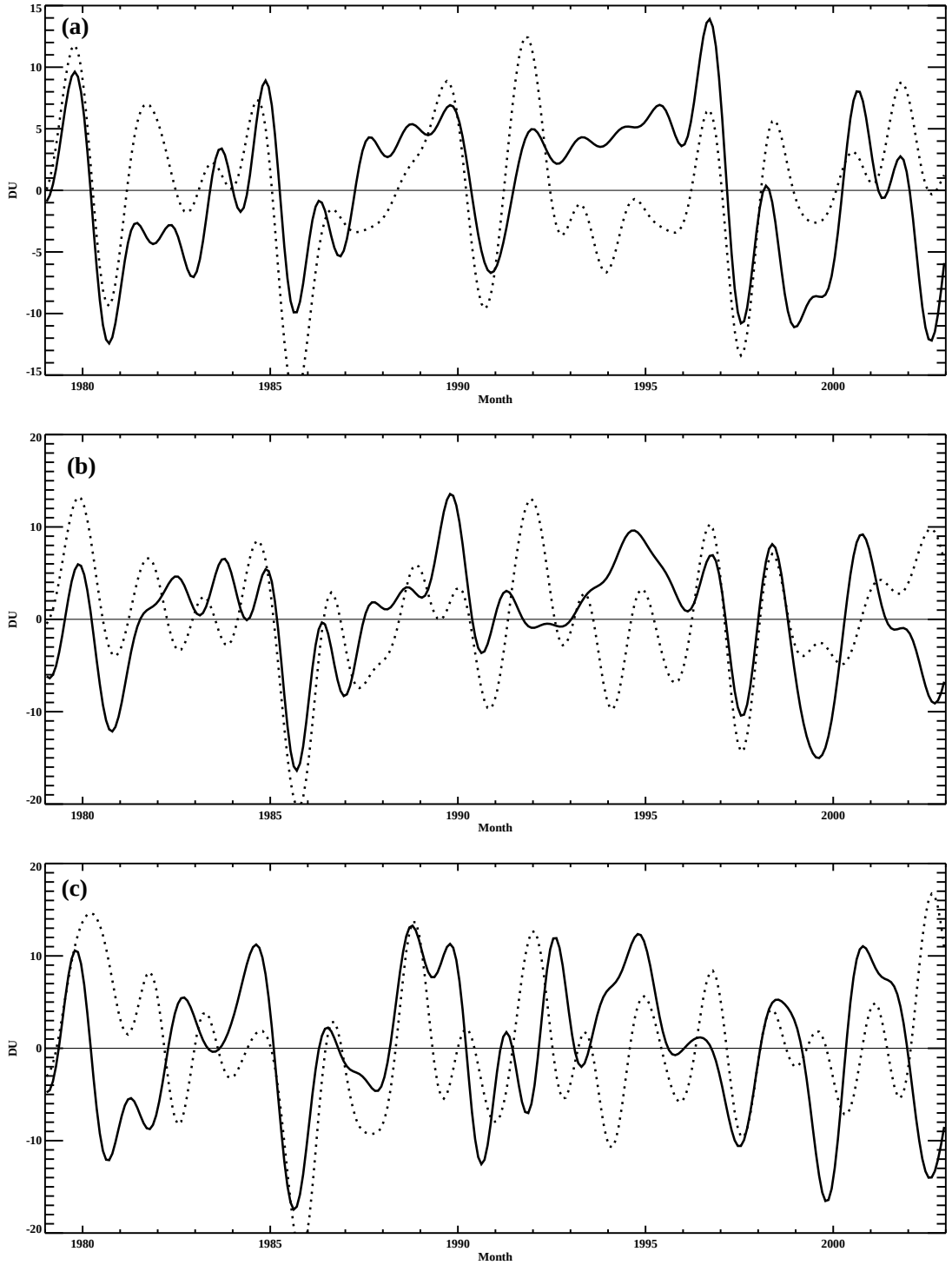

Figure 3.26: Lowpass filtered, deseasonalized and detrended ozone anomalies for the southern midlatitudes; 2D CTM simulated ozone (solid) and zonally averaged MOD (dotted) (a) 35°S, (b) 45°S, (c) 55°S,

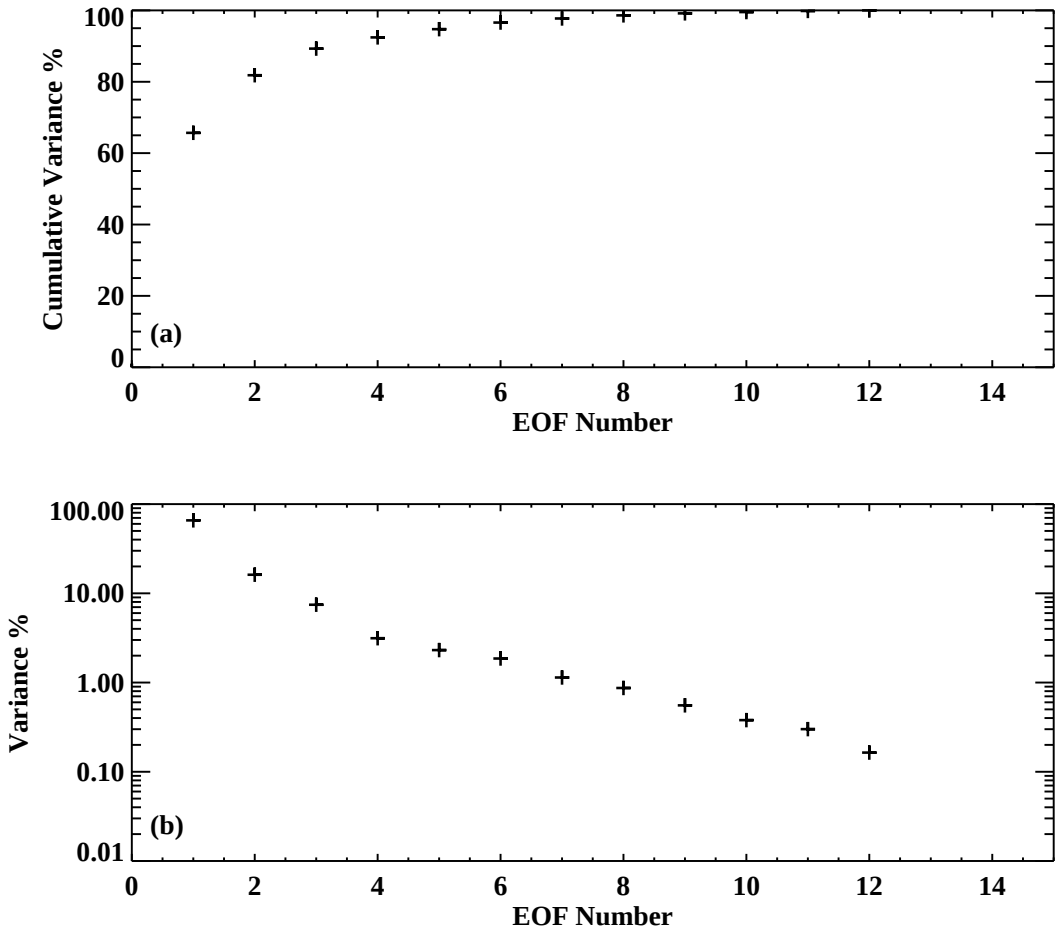

Figure 3.27: Relative and cumulative relative variance for PCA analysis of the 2D CTM simulated ozone. (a) Cumulative relative variance. (b) Relative variance.

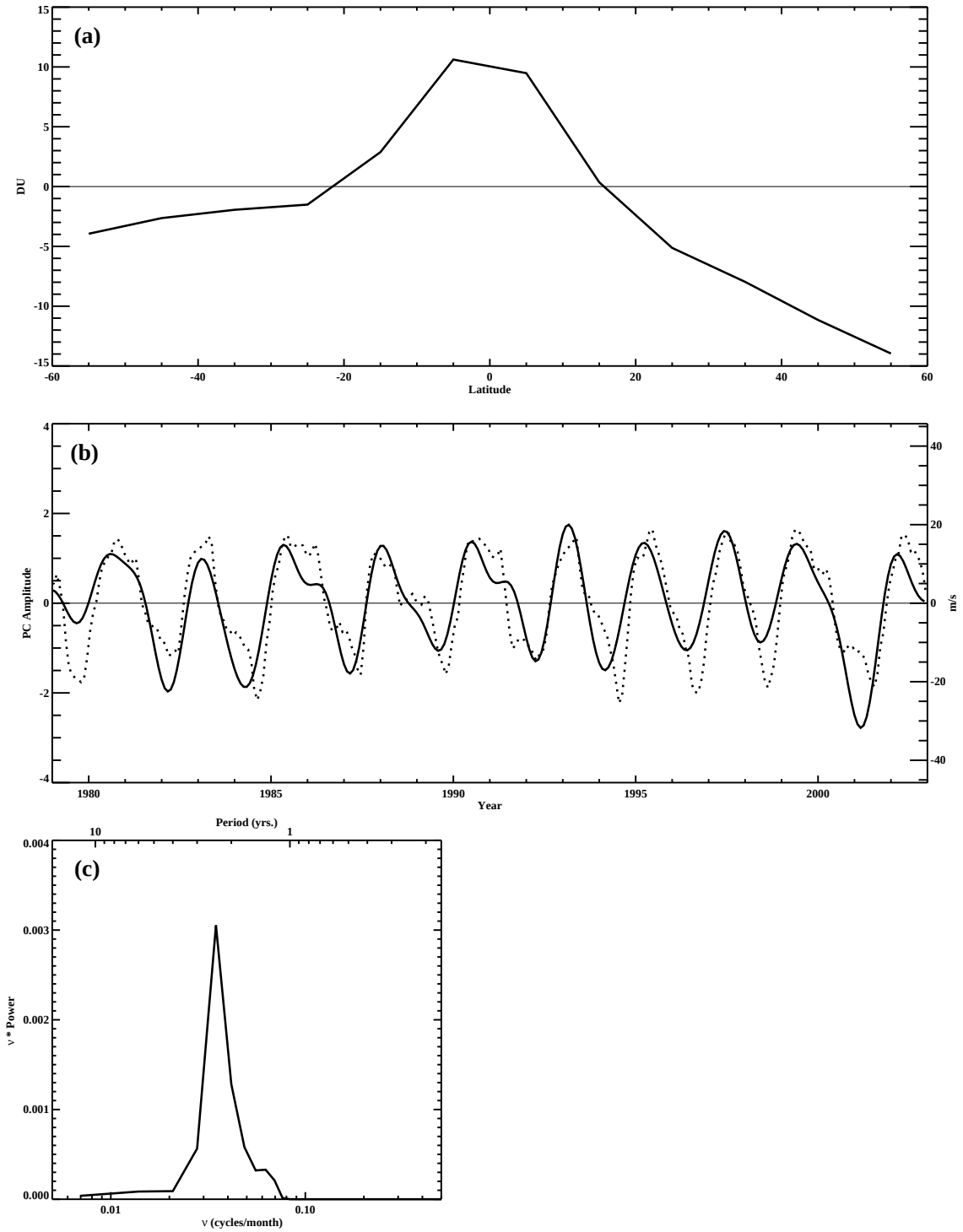

Figure 3.28: First EOF of the 2D CTM simulated ozone, associated PC time series and PSD. (a) EOF1. (b) PC1 time series (solid). QBO index (dotted). (c) PSD of PC1.

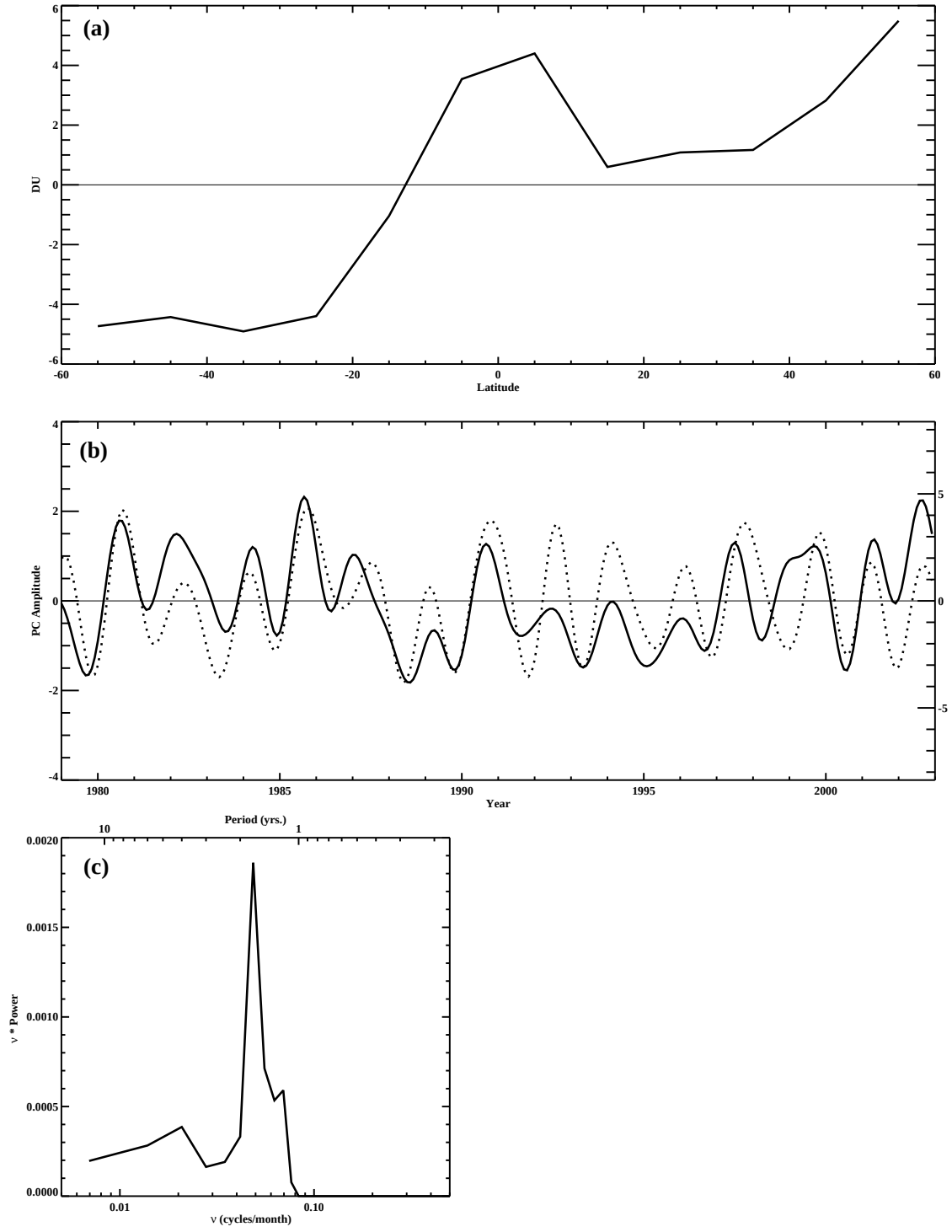

Figure 3.29: Second EOF of the 2D CTM simulated ozone, associated PC time series and PSD. (a) EOF2. (b) PC2 time series. (c) PSD of PC2.

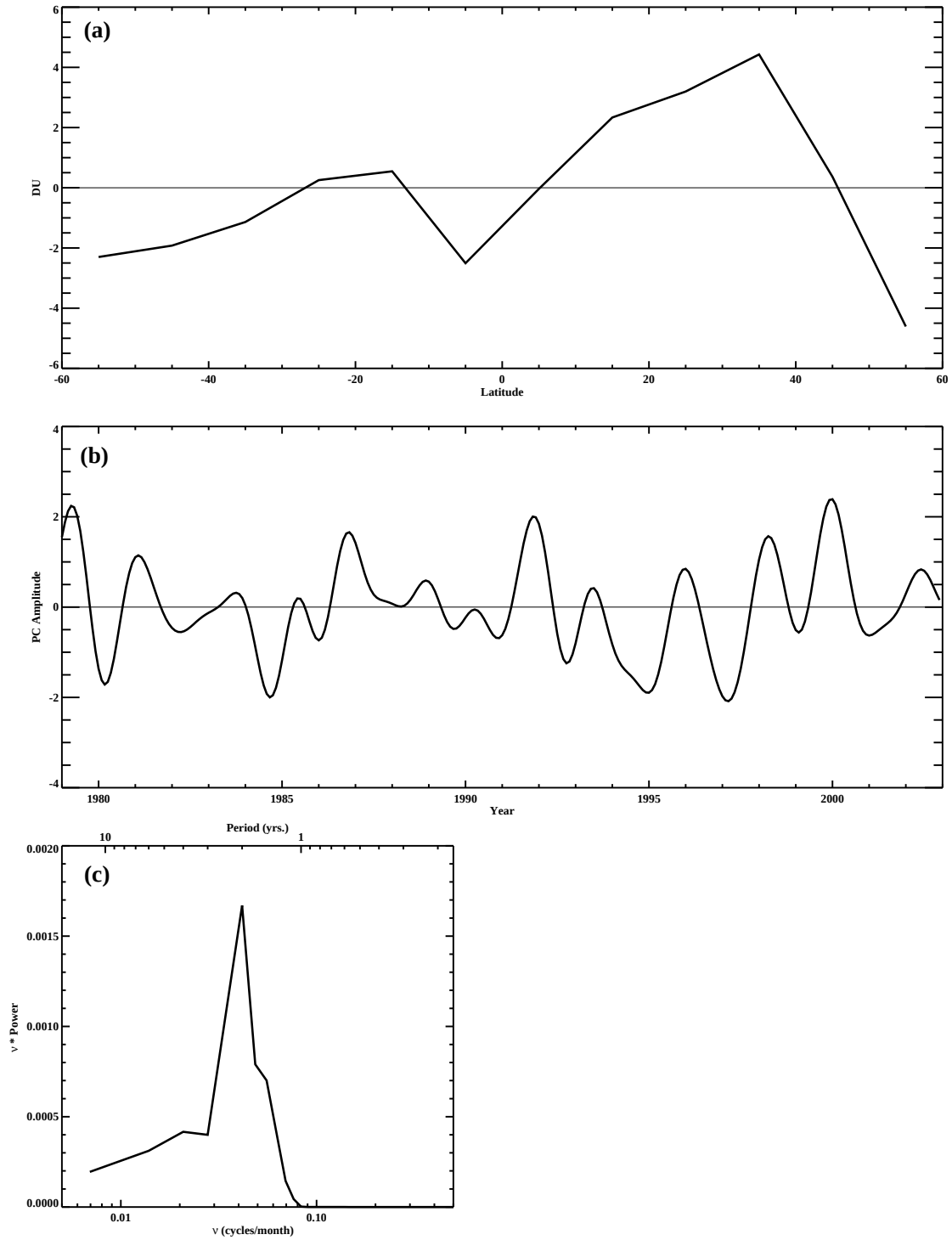

Figure 3.30: Third EOF of the 2D CTM simulated ozone, associated PC time series and PSD. (a) EOF3. (b) PC3 time series (solid). QBO index (dotted). (c) PSD of PC3.

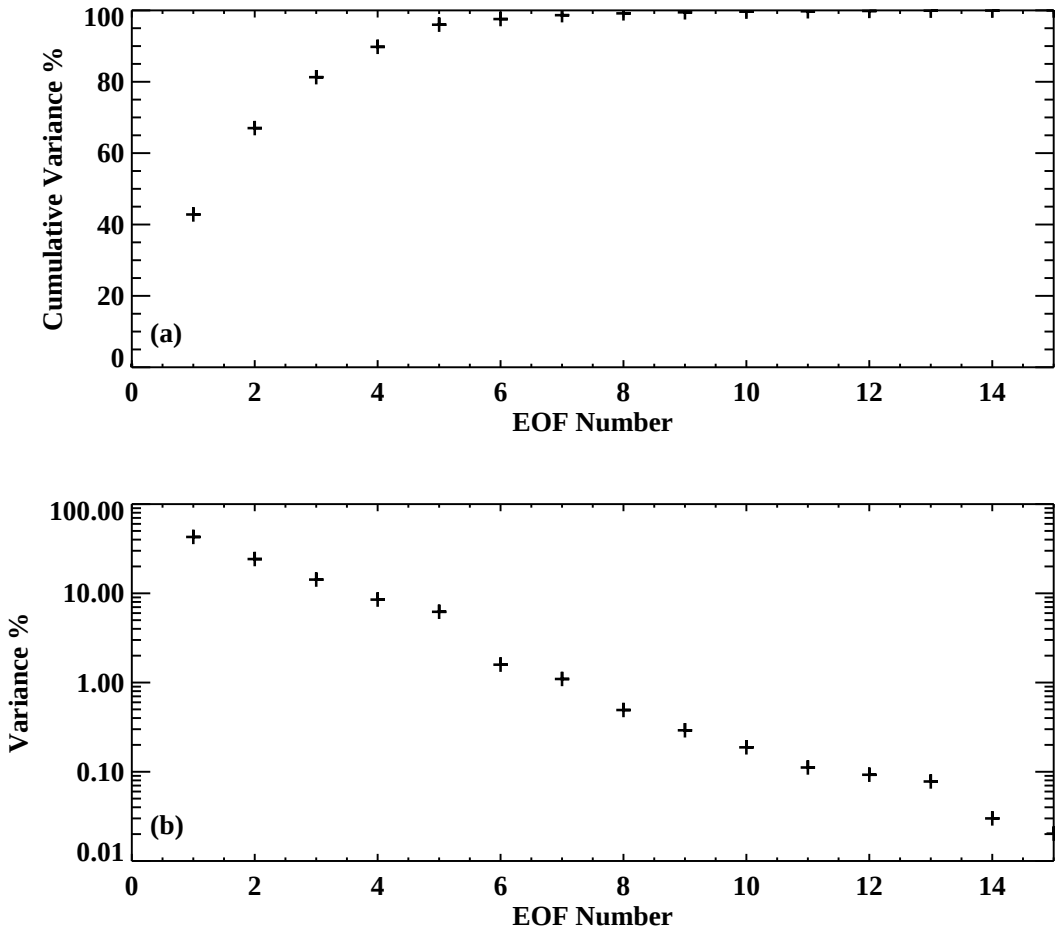

Figure 3.31: Relative and cumulative relative variance for PCA analysis of zonally averaged MOD. (a) Cumulative relative variance. (b) Relative variance.

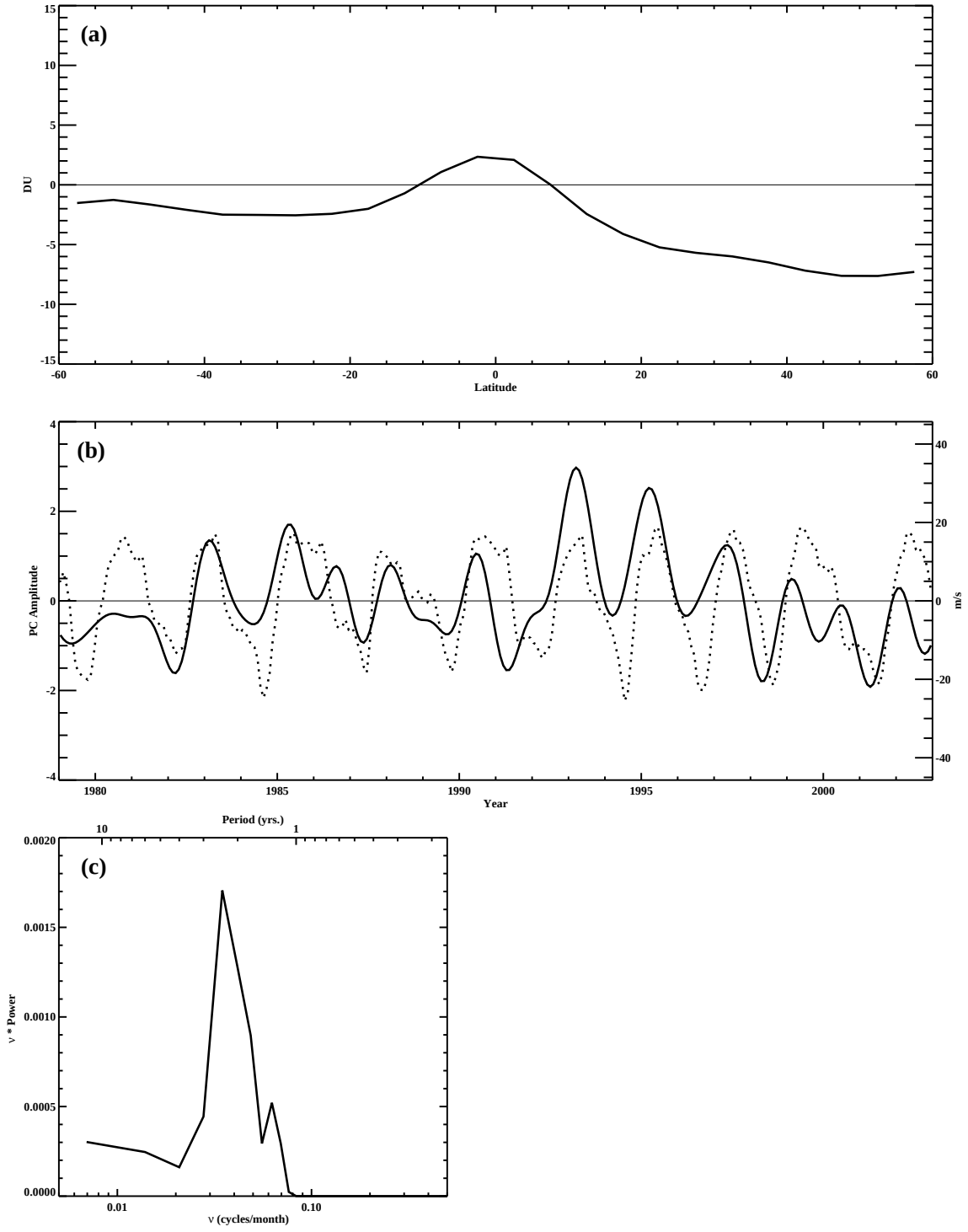

Figure 3.32: First EOF of zonally averaged MOD, associated PC time series and PSD. (a) EOF1. (b) PC1 time series (solid). QBO index (dotted). (c) PSD of PC1.

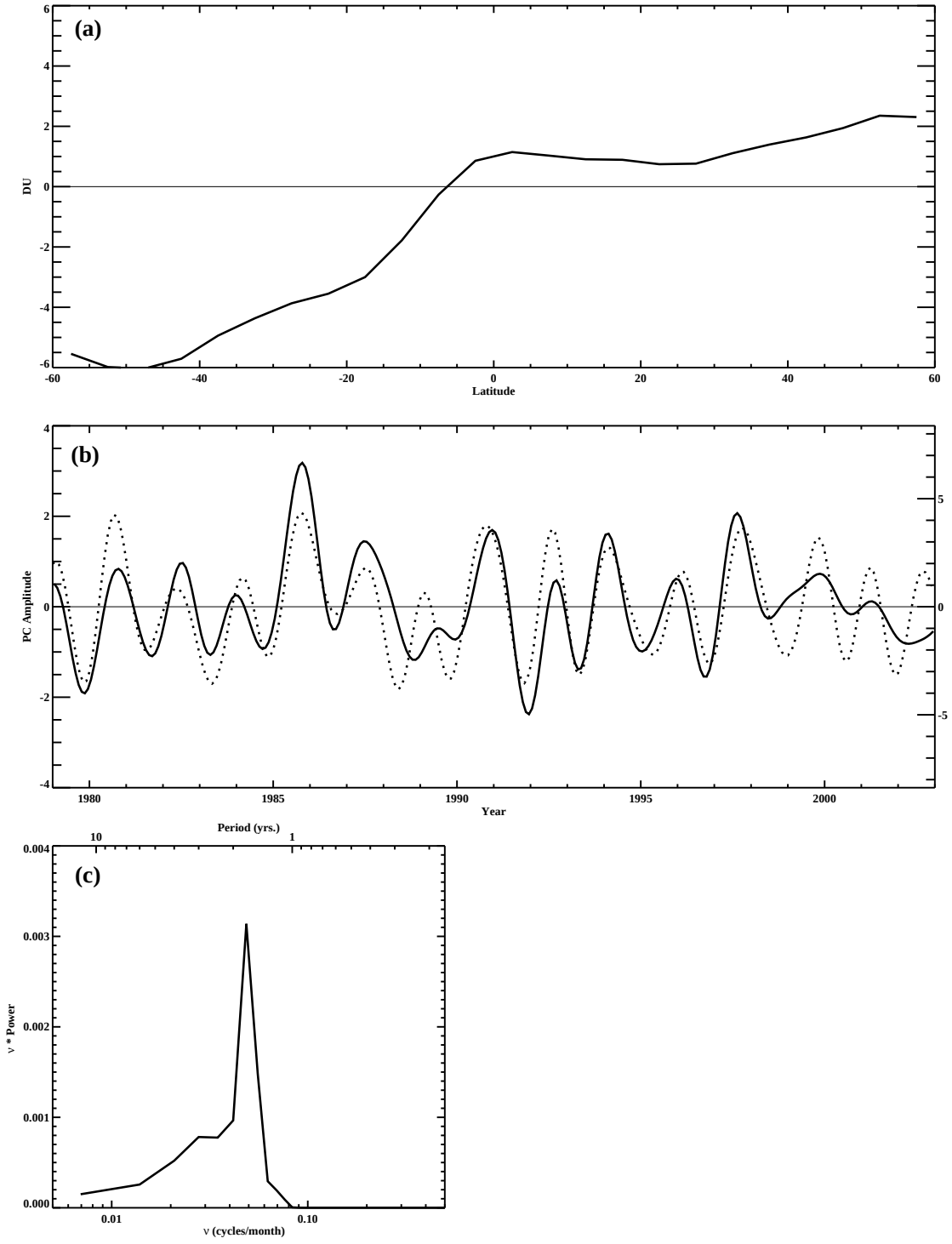

Figure 3.33: Second EOF of zonally averaged MOD, associated PC time series and PSD. (a) EOF2. (b) PC2 time series (solid). (c) PSD of PC2.

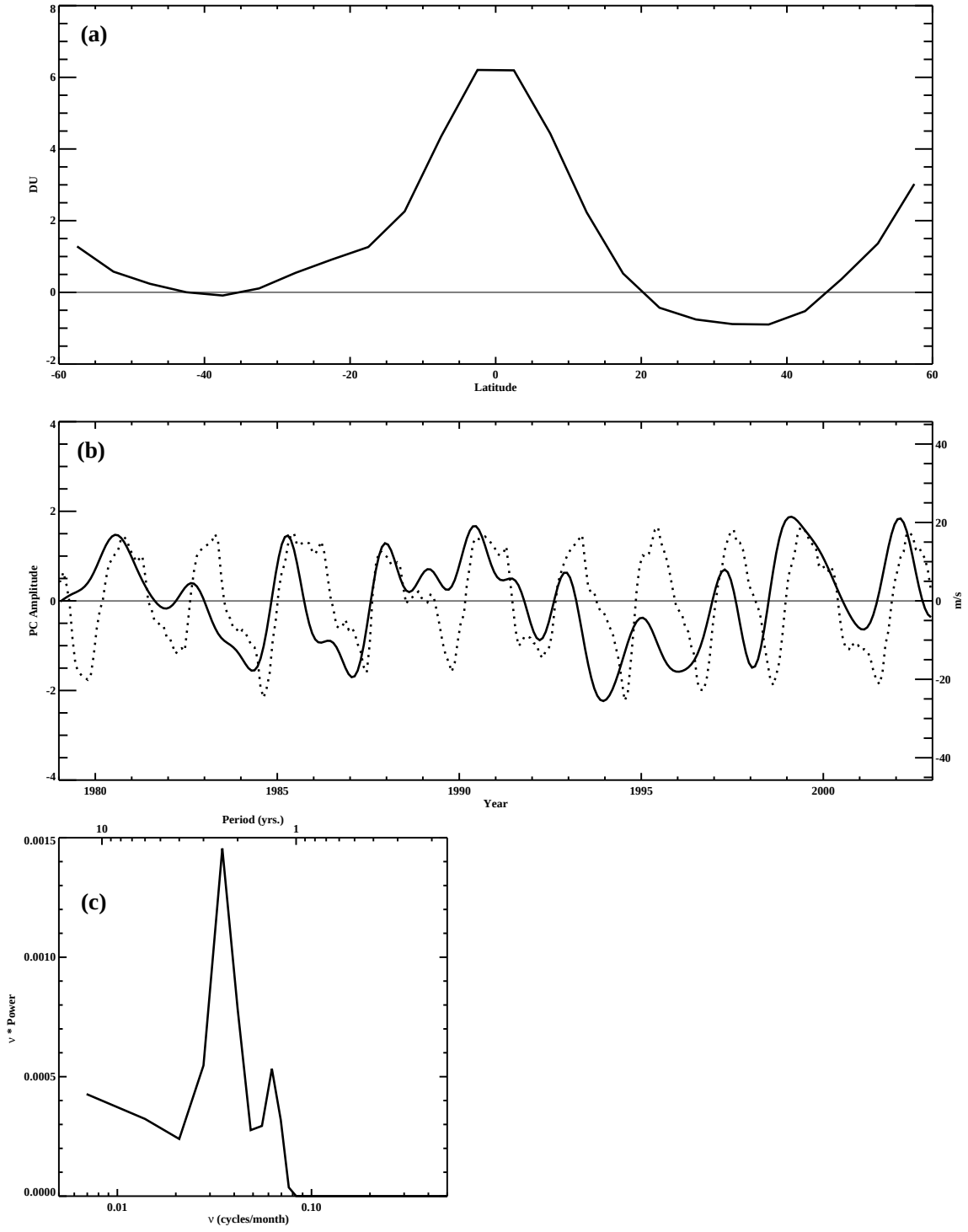

Figure 3.34: Third EOF of zonally averaged MOD, associated PC time series and PSD. (a) EOF3. (b) PC3 time series (solid). (c) PSD of PC3.

Chapter 4

A Singular Spectrum Analysis of the 71-Year Record of Total Column Ozone at Arosa, Switzerland

4.1 Introduction

The over-70-year record, beginning in 1926, of total ozone column abundances measured at Arosa, Switzerland ("Arosa Total Column Ozone," or ATCO) is the longest sequence of measurements of the monthly mean total column ozone in existence. This record was recently homogenized by *Staehelin et al.* (1998b) and now provides a unique resource for the study of the long-term trends and interannual variability (IAV) of ozone (*Staehelin et al.*, 1998a; *Brönnimann et al.*, 2000). In this study, we use the nearly continuous portion of the record from Aug. 1931–Dec. 2002.

In Section 4.2, we describe the singular spectrum analysis (SSA) technique used to analyze the IAV of ATCO. The climatology of ATCO and the results of the SSA analysis are examined in Section 4.3. Comparisons to dynamical fields from the

National Centers for Environmental Prediction (NCEP)/ National Center for Atmospheric Research (NCAR) reanalysis are shown in Section 4.4. In Section 4.5, we examine the robustness of the SSA analysis to changes in the embedding dimension. Finally, Section 4.6 examines nonstationary behavior in ATCO.

4.2 Singular Spectrum Analysis

Singular spectrum analysis (SSA) is a powerful technique for the investigation of oscillatory and trend behavior in short, noisy time series (*Vautard et al.*, 1992; *Ghil et al.*, 2002). It allows the decomposition of a time series into trend, oscillatory and noise components where the trends can be nonlinear and the oscillations can be anharmonic and both amplitude- and phase-modulated.

SSA is based on the eigenfunction expansion of the lagged-covariance matrix of the time series studied. The original time series, $\{x(t), 1 \leq i \leq N\}$, is embedded in a higher-dimensional space by constructing a multichannel time series consisting of lagged copies of $x(t)$,

$$\mathbf{X}(t) = (\mathbf{x}(t), \mathbf{x}(t+1), \cdots, \mathbf{x}(t+M-1)), \qquad 1 \leq t \leq N' \tag{4.1}$$

where M is the embedding dimension, or window length, chosen by the user and $N' = N - M + 1$. The covariance matrix can be estimated by a Toeplitz matrix,

$\mathbf{C}_x\,(M \times M)$, whose elements are

$$c_{ij} = \frac{1}{N - |i-j|} \sum_{t=1}^{N-|i-j|} x\,(t)\,x\,(t + |i-j|)\,. \tag{4.2}$$

A principal component analysis (PCA) is then performed on C_x, resulting in the decomposition of the *augmented* time series into

$$\mathbf{X} = \mathbf{A}\mathbf{E}^T = \sum_{k=0}^{M-1} \mathbf{a}_k \mathbf{e}_k^T \qquad (N' \times M) \tag{4.3}$$

where $\mathbf{e}_k = e_k\,(j)\,, 1 \leq j \leq M$ is the k^{th} eigenfunction or empirical orthogonal function (EOF), ordered by decreasing eigenvalue, and $\mathbf{a}_k = a_k\,(t)\,, 1 \leq t \leq N'$ is the corresponding principal component (PC) time series determined by projecting the time series onto each EOF:

$$a_k\,(t) = \sum_{j=1}^{M} x(t+j-1) e_k\,(j) \qquad 1 \leq t \leq N'. \tag{4.4}$$

By construction, EOFs are always symmetric or antisymmetric about the midpoint of the window, $M/2$. Oscillatory behavior in the original time series will be represented by a pair of nearly equal eigenvalues and the associated EOFs and PCs will be in quadrature. Dominant trend components are also isolated. *Ghil et al.* (2002) discusses various tests for the existence of oscillations and trends in the data.

The PCs do not provide a unique expansion of the original time series into a sum of different components, so a set of reconstructed components (RCs) is defined that

will allow such a decomposition; see *Vautard et al.* (1992) for details. For each EOF, we define the associated RC by

$$r_k(t) = \frac{1}{t}\sum_{j=1}^{t} a_k(t-j)\, e_k(j) \qquad 1 \le t \le M-1 \tag{4.5}$$

$$r_k(t) = \frac{1}{M}\sum_{j=1}^{M} a_k(t-j)\, e_k(j) \qquad M \le t \le N' \tag{4.6}$$

$$r_k(t) = \frac{1}{N-t+1}\sum_{j=t-N+M}^{M} a_k(t-j)\, e_k(j) \qquad N'+1 \le t \le N. \tag{4.7}$$

These RCs provide the unique decomposition of the original time series, $x = \sum_{k=1}^{M} r_k$, that is closest, in the least-squares sense, to the PCA decomposition of augmented time series, $\mathbf{X}$. The RCs preserve phase, except possibly for edge effects near the ends of the series. Note that there is no phase shift for the entire time domain if the sum of the paired RCs associated with the paired eigenvalues of an oscillation are considered. Furthermore, the paired RCs can correctly locate any amplitude modulation (intermittency) in the oscillation.

The choice of the window length, M, is crucial to the analysis. There exists a general trade-off between spectral resolution and the fidelity of the intermittency or amplitude modulation of the signal. If M is too short, signals with nearby periods may conflate into a single mode. Furthermore, SSA can only resolve periods $\le M$. Choosing a larger M can improve the isolation of different signals into SSA components. However, if M is too large, a signal with a broad range of periods may be split into several components with neighboring frequencies. Furthermore, if the signal is intermittent, spells of oscillation will be smoothed out. The rule-of-thumb

suggested by *Vautard et al.* (1992) is that a window length of M is usually successful at analyzing periods in the range $(M/5, M)$.

4.3 Analysis of Arosa Total Column Ozone

4.3.1 Climatology and Spectral Analysis

The ATCO was deseasonalized by removing the mean for each individual month. A second-order polynomial trend was fit to the deseasonalized data. Figures 4.1a–c respectively show the ATCO itself, with fitted trend; the deseasonalized, detrended time series; and the mean seasonal cycle. Also shown, Figure 4.1d, is an estimate of the power spectral density (PSD) of the deseasonalized, detrended time series calculated using Welch's method (*Press et al.*, 1992). PSD estimates were also calculated by applying the maximum entropy method (MEM) and the multitaper method (MTM) to the original ATCO (*Burg*, 1978; *Ghil et al.*, 2002); see Figures 4.2a and 4.2b, respectively. Similar low-frequency features are seen in all three PSDs. The IAV is dominated by an ∼3.5 year signal and a broad decadal signal. There are significant signals with periods of 20–22 months, 28–30 months, and 5–6 years.

The 28–30 month peak can be ascribed to the QBO, and the 20–22 month peak to the QBO-AB; see Section 2.5.3. The 3.5 and 5–6 year signals, however, are of unclear origin. While these signals fall in the same range of periods as the ENSO signal seen in the tropical ozone (see Section 2.5.4); they cannot be directly ascribed to ENSO. ENSO's primary effect on the total column ozone is via perturbations in the tropical

tropopause height, and this effect is localized to the tropics. It is possible that these signals are still related to ENSO, but only if the effects of ENSO are transported to the midlatitudes by another mechanism.

4.3.2 Decomposition Using Singular Spectrum Analysis

In order to isolate the various signals present in ATCO, an initial SSA was performed utilizing a window length of $M = 270$ months, hereafter denoted M270. This value for M was chosen because the associated SSA isolates all the major signals of ATCO from the annual to decadal time scales. Shorter window lengths did not separate the decadal variability from other modes. The use of such a long window length implies that excessive smoothing is likely to occur for signals below 4–5 years. However, this analysis provides a good starting place for the study of the IAV in ATCO. The effect of varying window lengths is explored in greater detail in Section 4.5.

The eigenvalue spectrum for the M270 analysis is shown in Figure 4.3; the EOFs in Figure 4.4; the PCs in Figure 4.5; the RCs in Figure 4.6; and the power spectral estimates of RCs in Figure 4.7. The eigenvalue spectrum, Figure 4.3, shows a steep descent in the first ∼20 eigenvalues. Seven oscillatory pairs were found with peak periods similar to those seen in the ATCO spectral estimates (see Figures 4.1d and 4.2), *i.e.,* 12 months (pair 1-2), 6 months (pair 5-6), ∼3.5 years (pair 7-8), ∼28 months (pair 11-12), ∼20–22 months (pair 13-14), ∼5 years (pair 16-17), and ∼6 years (pair 18-19). The associated paired EOFs, Figure 4.4, and paired PCs, Figure 4.5, are clearly in quadrature. The sums of the associated RCs, Figure 4.6, show clean

oscillations (see spectral estimates in Figure 4.7) with varying degrees of amplitude modulation. The separation of the broad 5–6 year spectral band seen in the ATCO spectrum, Figure 4.2, into distinct 5 and 6 year components is probably an artifact of the long window length chosen. Analyses performed with shorter window lengths (not shown) do not show this separation. The long window length is also responsible for the excessive smoothing seen in the signals with shorter periods; this will be examined in more detail later.

Two components, No. 9 and 10, are associated with decadal variability but did not satisfy the test of oscillatory behavior. While the associated EOFs and PCs, Figures 4.4e and 4.5e respectively, do appear to be roughly in quadrature for the decadal variability, the details of the two components are quite different. Furthermore, there is a large degree of variability amongst the 5 realizations of the decadal period seen in each of the PCs. The EOFs from an analysis with a longer window would average over more realizations of the decadal period, creating smoother PCs and possibly passing the oscillation tests. However, the $M = 270$ window length used is already close to the maximum recommended length, $N/3 = 857/3 = \sim 286$. The sum of the associated RCs, Figure 4.6e, and its spectral estimate, Figure 4.7e, show a reasonably regular oscillation with a broad spectral peak centered at 9 years.

Two components corresponding to the trend, No. 3 and 4, were identified. EOF3 and EOF4, Figure 4.4b, are primarily a constant and linear trend for the window. The reconstructed trend from these two components, Figure 4.6b, shows a nonlinear structure.

There is one unpaired eigenvalue (No. 15) that is dominated by multidecadal variability. It is dominated by a period equal to the window length and is not robust with changes in M, suggesting that it is artifactual.

The reconstructed time series based on the first 20 EOFs, *i.e.,* the sum of RCs 1–20, captures 89% of the variability of ATCO. Comparisons of the raw ATCO and reconstructed time series along with their spectra are shown in Figure 4.8.

4.4 Regression of SSA Components on NCEP Geopotential Heights

To investigate the potential physical processes associated with the dominant interannual signals seen in the SSA decomposition of ATCO, we performed linear regressions of the 30 hPa and 100 hPa geopotential heights from the NCEP/NCAR reanalysis product (NCEP1) using as predictors the four RC pairs associated with ∼3.5 year, ∼28 month, 20–22 month and decadal signals (Figure 4.6d–g) plus a linear trend. The regressions were performed for the interval from 1958 to 2002. The mean seasonal cycles of the NCEP1 fields were removed prior to performing the regressions. The 100 hPa level was chosen as a rough approximation of the tropopause height, whereas the 30 hPa level is approximately the height of the maximum ozone concentration in the column and is representative of stratospheric variability. Selected regression coefficients and their associated t-statistics are shown in Figures 4.9–4.13. The ∼3.5 year oscillation (pair 7-8), Figure 4.6d, shows significant correlations with the NCEP

geopotential height at both the 100 hPa and 30 hPa levels, Figures 4.9 and 4.10 respectively. Regression coefficients, β_k, are shown in the upper plot of both figures; t-statistic, defined by $t_k = |\beta_k / \mathrm{se}\,(\beta_k)|$, are shown in the lower plot. The regression of the 100 hPa geopotential height, shows a strong and highly significant correlation between the tropical tropopause height and the ∼3.5 year component. Furthermore, the bimodal pattern seen in central/eastern Pacific is very evocative of the tropopause variability associated with ENSO.

One mechanism for the northward transport of the ENSO signal to midlatitudes is the Pacific-North American (PNA) oscillation. The leading RC of a SSA analysis of the PNA, using $M = 85$, is a ∼3.5 year oscillation; see Figure 4.14a. This figure also compares the 3.5-year ATCO and PNA oscillations, showing that they are in good agreement from the late 1960s to 2003. However, they are completely out of phase for the earlier decades, late 1940s to mid 1960s. This change in behavior will be discussed further in Section 4.6. There is also a strong correlation on both levels with polar variability, albeit not as significant as the tropical correlations. This is a feature common to many of the regressions coefficients. The primary pattern of polar variability in the northern hemisphere is the Northern Annular Mode (NAM); see *Thompson and Wallace* (2000). The NAM time series at various pressure levels have large variances and red-noise spectra with power in most bands. Therefore, while many time series will have large correlations with polar geopotential heights, they may only be weakly significant.

The sum of the decadal RCs (9-10), Figure 4.6e, shows reasonably significant

correlations with the NCEP1 100 hPa geopotential height throughout the tropics and midlatitudes, Figure 4.11. There is no pattern of significant correlations in the 30 hPa regression correlations (not shown). This is consistent with the decadal variability seen in the analysis of the tropical merged ozone data; see Section 2.5.2. A comparison of the ATCO decadal oscillation to the sunspot cycle is shown in Figure 4.14b. The two time series do not correlate well over the entire record; the ATCO signal is clearly at a higher frequency than the solar variability.

Regression coefficients for the 30 hPa geopotential height onto the ∼28 month (Figure 4.5f) and 20–22 month (Figure 4.5g) ATCO oscillations show spatial patterns associated with the QBO and the QBO annual beat (QBO-AB), respectively; see Figures 4.12 and 4.13. The zonally symmetric patterns seen in the tropics and lower midlatitudes are consistent with the QBO and QBO-AB patterns seen in MOD; see Section 2.5. Neither oscillation has a pattern of significant correlations at the 100 hPa level (not shown). The ∼28 month ATCO oscillation and an index for the QBO are in good agreement from the early 1970s through 2002; see Figure 4.14c. However the two time series are clearly uncorrelated in the preceding decades. Furthermore, there is a strong amplitude modulation occurring throughout the ATCO oscillation; the QBO signal in ATCO almost vanishes in the 1940s and early 1950s. A comparison between the 20–22 month ATCO oscillation and a constructed index for the QBO-AB shows good agreement from 1958 through 2002; see Figure 4.14d.

4.5 Dependence on Window Length

The choice of the window length, M, can have a large impact on the results of the SSA analysis. The very large M used in the analysis described above has allowed many clearly defined oscillations to be separated into distinct components, but has provided an overly smooth representation of the behavior of these oscillations. Furthermore, the split of the broad spectral band seen at 5–6 years into distinct 5 and 6 year oscillations is probably an artifact of the large M.

To investigate the dependence of the SSA decomposition on window length, two additional SSA analyses were performed with window lengths of 155 and 85 months, denoted M155 and M85 respectively. The eigenfunction spectra for these analyses are shown in Figure 4.15. The paired eigenvalues representing oscillations are listed in Table 4.1. As the window length shrinks, fewer eigenvalues stay above the noise floor and previously separated oscillations start to combine in some eigenvalue pairs. *E.g.,* in the M85 analysis, the 3.5-year and 5–6 year signals coalesce into one pair (5,6). The variance associated with the combined signals is larger than the variance associated with the 6-month signal so the order of the 6-month and 3.5-year signals is reversed. In the M155 analysis, a cluster of three eigenvalues is found; the sum of the three associated RCs displays two oscillatory signals.

The sums of the paired RCs associated with the 3.5-year oscillation from the three SSA analyses are compared in Figure 4.16. The (7,8) pairs from the M155 and M270 analyses show similar clean 3.5-year oscillations with a modulating amplitude that decays during the 1970s and 1980s. The (5,6) pair from the M85 analysis shows the

conflation of the 3.5-year signal with the 5–6 year signal. The decay in amplitude during the 1970s and 1980s is still evident.

The trend and seasonal cycle are robustly represented in the three analyses, modulo smoothing. The trend components, constructed by the sum of RCs 3 and 4, are shown with the full time series in Figure 4.17. They all show a roughly flat trend centered at approximately 330 DU from the 1930s until the mid-1970s, a decline of ∼20 DU from the mid-1970s to the late 1990s, and a slight increase thereafter. This is consistent with the modeling results of *Austin et al.* (2000). Since the M85 analysis does not resolve decadal variability, there is a decadal oscillation in the M85 trend component.

The reconstructed seasonal cycles — defined as the sum of the paired RCs associated with the annual and 6-month oscillations — for the M270 and M85 analyses are shown in Figures 4.18a and 4.18b, respectively. The amplitude of the M270 seasonal cycle is relatively constant at ∼45 DU from the 1930s until the early 1970s; its amplitude then declines by approximately 15%, reaching a minimum of ∼38 DU in the late 1990s to early 2000s. The M85 seasonal cycle shows a similar behavior but with some additional low frequency variability in the amplitude of the cycle. In this case, the decline is closer to 20% and the minimum of ∼43 DU is more tightly localized to the late 1990s. These M270 and M85 seasonal cycles can be thought of as the 22.5-year and 7-year mean seasonal cycles. For comparison, the seasonal cycle reconstructed from a SSA analysis with window length $M = 12$ months, denoted M12, is shown in Figure 4.18c. Since the M12 analysis isolates no IAV, the M12 seasonal cycle shows

the annually varying seasonal cycle, *i.e.,* the seasonal cycle as modulated by IAV signals such as the QBO.

4.6 Nonstationary Behavior in the IAV of ATCO

The preceding analyses display many indications of qualitative changes over time in the relative importance of the various signals in ATCO. Both the trend and the amplitude of seasonal cycle show a decline starting sometime around 1970 (Figures 4.17 and 4.18), the 3.5-year oscillation displays a reduced amplitude in the 1970s to 1980s (Figure 4.16), and the oscillation associated with the QBO practically vanishes in the early decades of ATCO (Figure 4.6f). The seasonal cycle and trend have been robustly characterized by the SSA analyses, as shown in the previous section. To further examine the intermittency of the IAV of ATCO, a coarse spectrogram was calculated by determining the spectral estimates of 30-year segments of the deseasonalized, detrended ATCO. The results are shown in Figure 4.19. These spectra show clear transitions in the structure of the IAV. While there consistently is power in the 20–22 month range associated with the QBO-AB, there is no power near the QBO frequency, ∼28 months, for the first five intervals, 1933–1962 to 1953–1982; see Figures 4.19a–e. Starting with the sixth segment, 1958–1987, the QBO signal grows until it dominates the IAV by the final segment, 1973–2002; see Figures 4.19f–i. On the other hand, the signal associated the 3.5-year oscillation is more significant in the earlier segments. In the first two segments, 1933–1962 and 1938–1967, the signal of a 3.5-year oscillation would be obscured by the broad band of power that ranges

over time scales from 3.5 years to decadal. This spectral band may be caused by the anomalously high values seen in ATCO during the three years from 1940–1943 (*Brönnimann et al.*, 2004); see Figure 4.17. Starting with the third interval, 1943–1972, the 3.5-year signal becomes the dominant mode of IAV in ATCO during the next 3 segments. In the seventh segment, 1977–1992, there is little significant power at 3.5 years. The signal recovers during the final two segments. The behavior of IAV demonstrated by these spectra is consistent with the behavior seen in the SSA components associated with the QBO, QBO-AB and 3.5-year oscillations.

4.7 Discussion

SSA has proven to be a powerful tool for investigating the IAV and trend of the ATCO record. A robust nonlinear trend was determined showing little change in the mean state until about 1970 followed by a decline of ∼20 DU or ∼6%. Similarly, the amplitude of the seasonal cycle remained relatively steady at ∼45 DU until the early 1970's, then declined by 15–20% by the late 1990's. Both the trend and amplitude of the seasonal cycle show possible indications of recovery after 2000, but the potential for edge effects in the analyses preclude this from being a robust result.

Several oscillatory signals were also seen. Firstly, oscillations attributable to the QBO and QBO-AB were identified. While the QBO-AB appears to have a relatively steady signal in the ATCO, the QBO signal nearly vanishes from the first decades of the record. It is not clear from this analysis whether this is an isolated anomaly of the Arosa record or if there has been a substantial change in the interaction between

the QBO and the Brewer-Dobson circulation. Secondly, a decadal oscillation was also identified but was poorly characterized by the SSA analyses. The data record appears to be too short for SSA to be cleanly isolated the decadal signal. Finally, a strong 3.5-year signal was isolated. Like the QBO signal, its amplitude varies greatly throughout the Arosa record. It is dominant in the early decades, weakening during the 1970s and 1980s, and then recovering in the 1990s. However, unlike the QBO, QBO-AB and decadal signals, this 3.5-year signal does not have an obvious tropical counterpart. Preliminary investigations into the source of this oscillation suggest possible connections to ENSO — possibly via the PNA teleconnection — and to the polar NAM.

To continue to study the mid- to high-latitude IAV of total ozone, we can use appropriately chosen SSA analyses to better isolate each individual signal, both within the entire Arosa record and within partitions of it. It would be useful to apply this analysis to another long northern hemisphere record to distinguish those features that are generally characteristic of midlatitude IAV from those that are peculiar to the Arosa record. Finally, a multichannel SSA can be applied to the two-dimensional Merged Ozone Dataset since classical PCA is not proving to be informative.

Table 4.1: Clustered eigenvalues and the periods of the associated oscillations for three SSA analyses. Clusters which satisfy a same-frequency test are shown in parentheses.

$M = 270$		$M = 155$		$M = 85$	
k	period(s)	k	period(s)	k	period(s)
(1,2)	12 mo.	(1,2)	12 mo.	(1,2)	12 mo.
3,4	trend	3,4	trend	3,4	trend
(5,6)	6 mo.	(5,6)	6 mo.	(5,6)	3.5 yr. & 5–6 yr.
(7,8)	3.5 yr.	(7,8)	3.5 yr.	(7,8)	6 mo.
9,10	decadal	(9,10)	decadal	(9,10)	21 mo. & 28 mo. & 3.5 yr
(11,12)	28 mo.	(11,12)	28 mo.	(12,13)	21 mo.
(13,14)	21 mo.	(13,14,15)	21 mo. + 5–6 yr.		
(16,17)	5 yr.				
(18,19)	6 yr.				

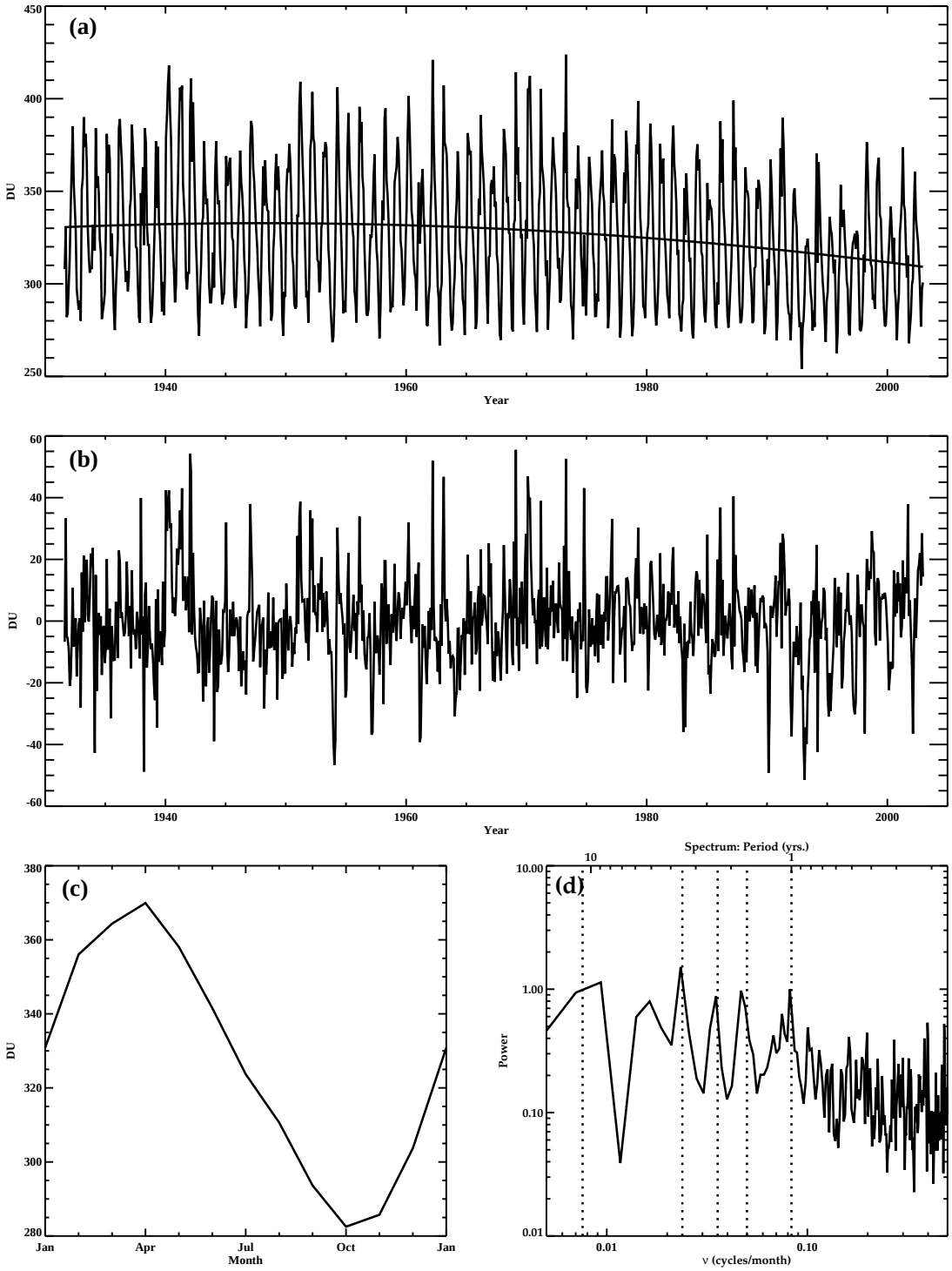

Figure 4.1: **(a)** Arosa total column ozone (ATCO) with $O\,(2)$ polynomial trend. **(b)** Deseasonalized, detrended ATCO. **(c)** Mean seasonal cycle of ATCO. **(d)** PSD of deseasonalized, detrended ATCO. Vertical (dotted) lines mark periods of 11 yr., 3.5 yr., 28 mo., 20 mo., and 1 yr.

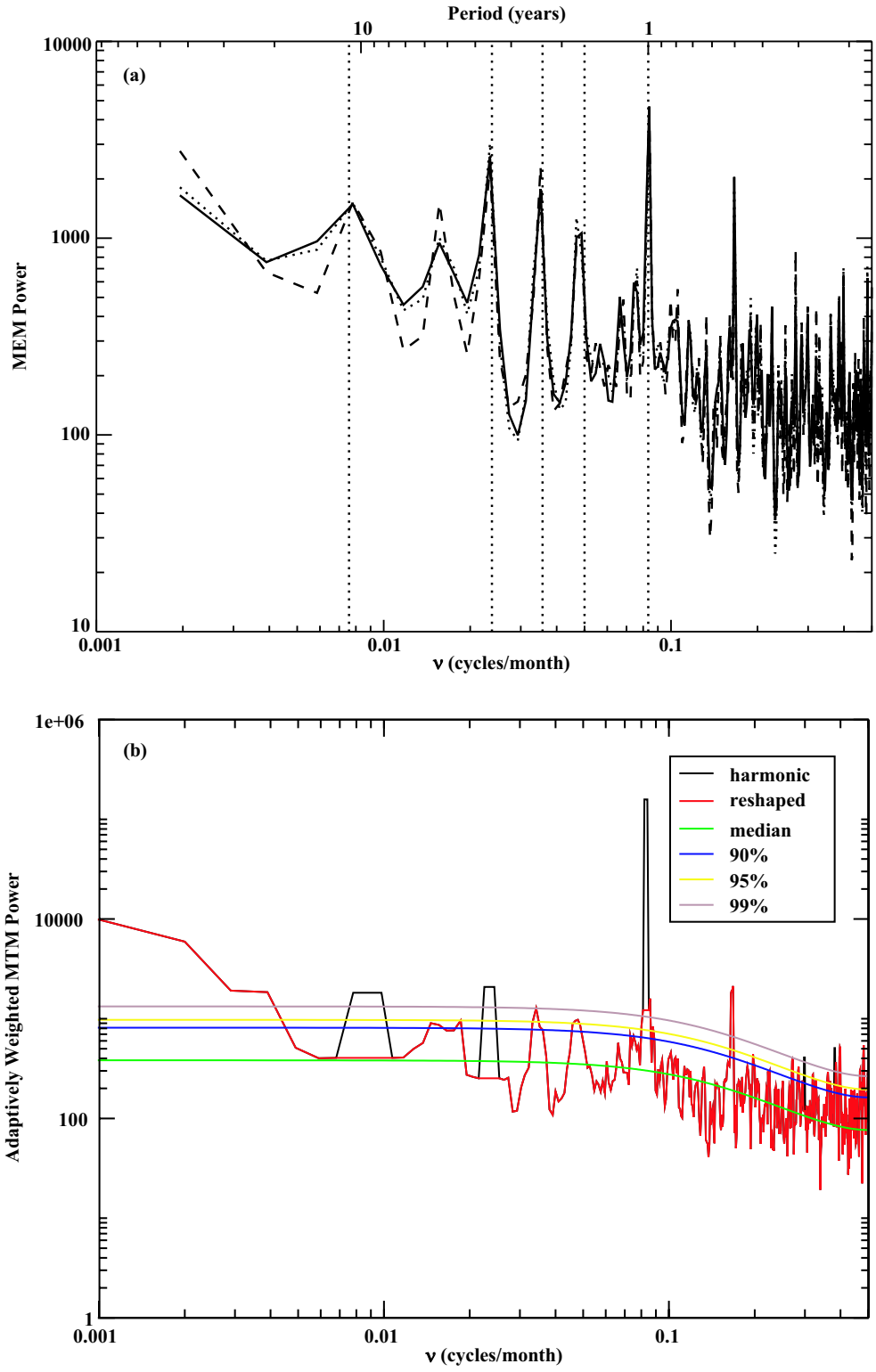

Figure 4.2: **(a)** MEM spectra for ATCO of order 120 (solid), 140 (dotted), and 160 (dashed). Vertical (dotted) lines denote same periods as in Figure 4.1 **(b)** Adaptively weighted MTM spectrum for ATCO. Estimated red-noise background and associated 90%, 95%, and 99% significance levels are shown. The bandwidth parameter was set to $p = 2$ and $K = 3$ tapers were used.

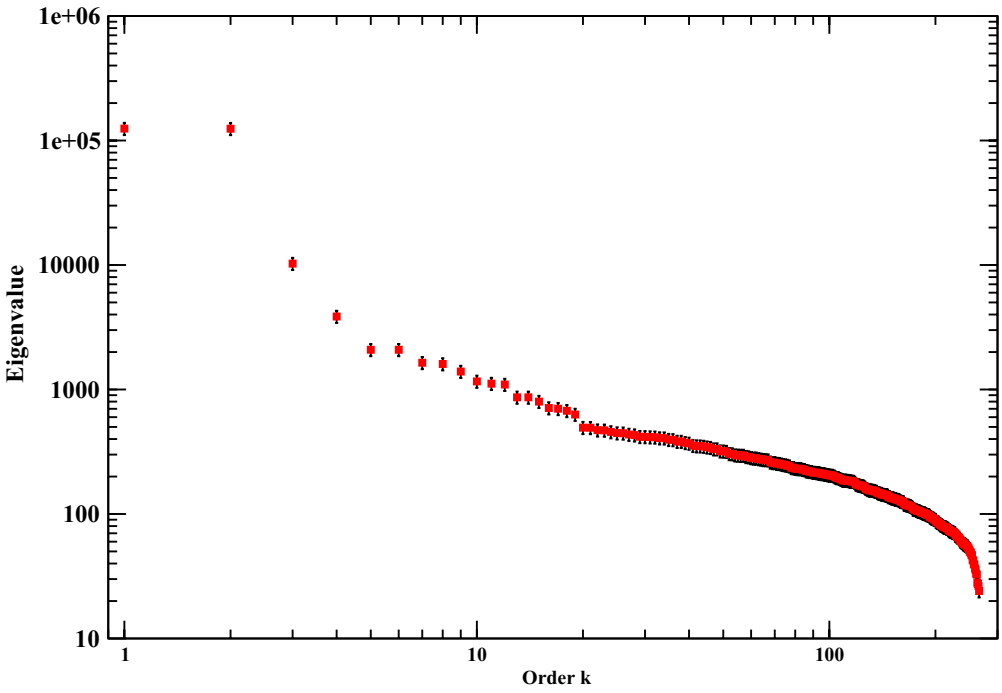

Figure 4.3: Eigenvalue spectrum for the M270 SSA analysis of ATCO.

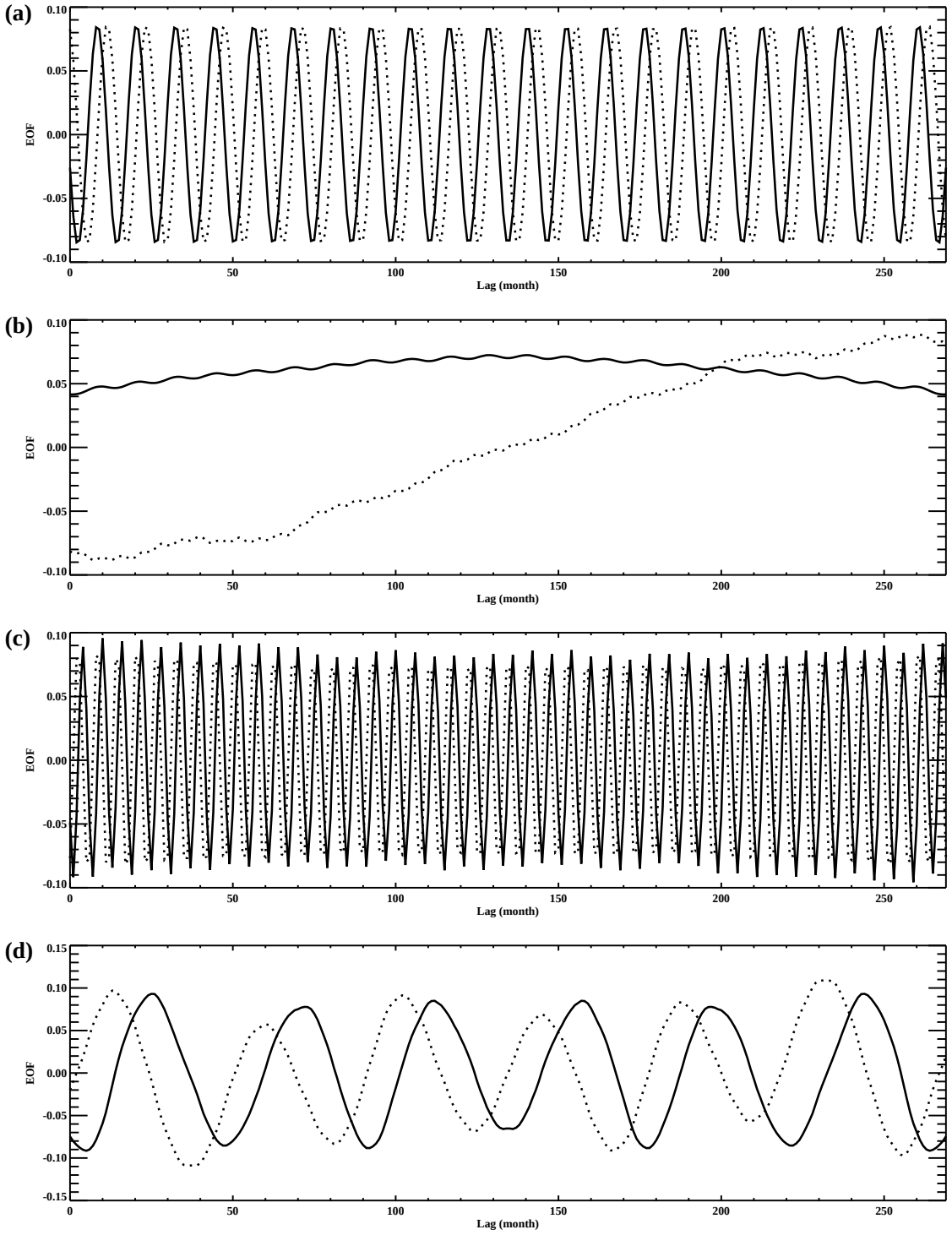

Figure 4.4: Leading pairs of EOFs for the M270 SSA analysis of ATCO; Solid (dotted) line denotes first (second) member of each pair. **(a)** (1,2), **(b)** (3,4), **(c)** (5,6), **(d)** (7,8), **(e)** (9,10), **(f)** (11,12), **(g)** (13,14), **(h)** (15) unpaired. **(i)** (16,17), **(j)** (18,19).

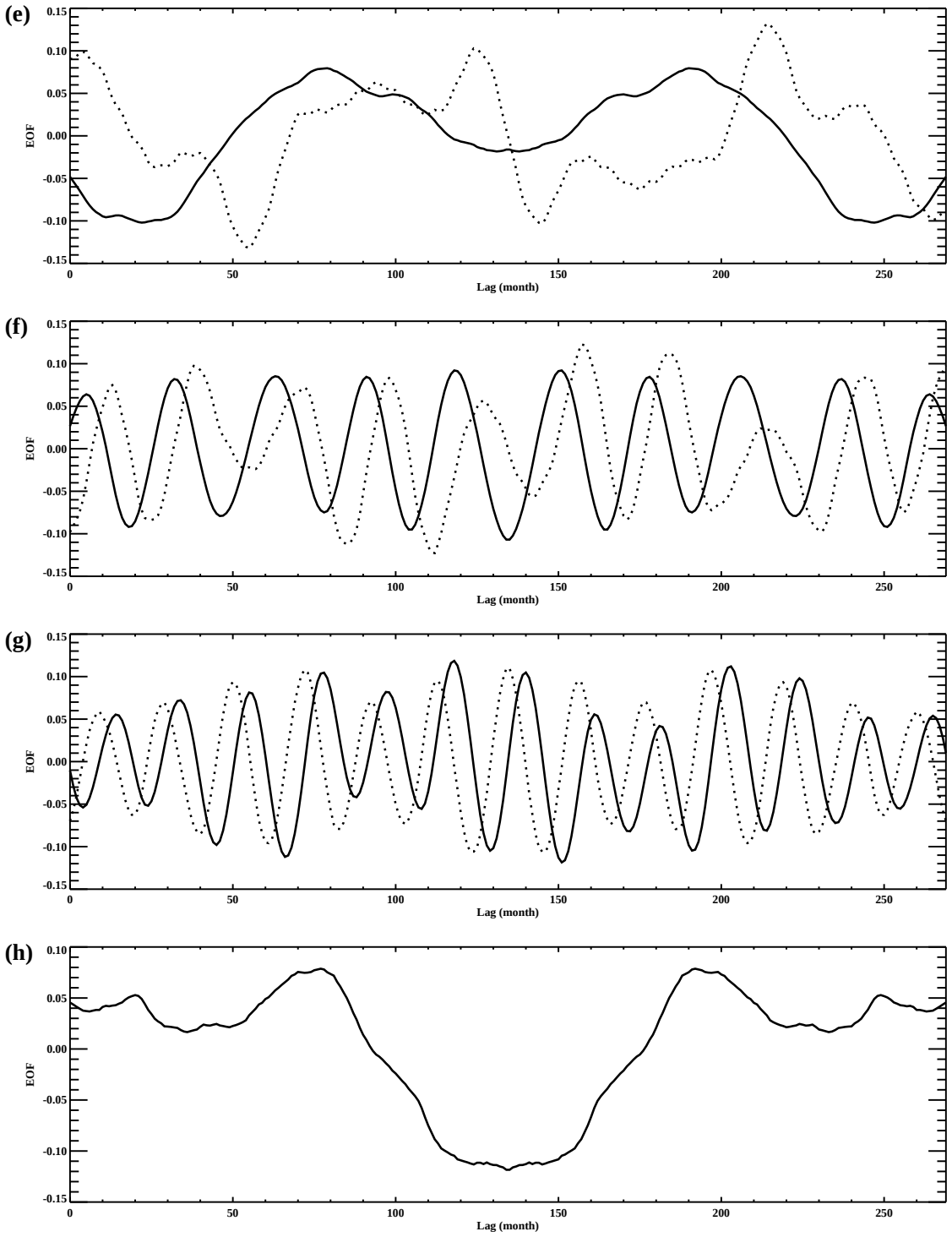

Figure 4.4 cont.; Leading EOFs: **(e)** (9,10), **(f)** (11,12), **(g)** (13,14), **(h)** (15) unpaired.

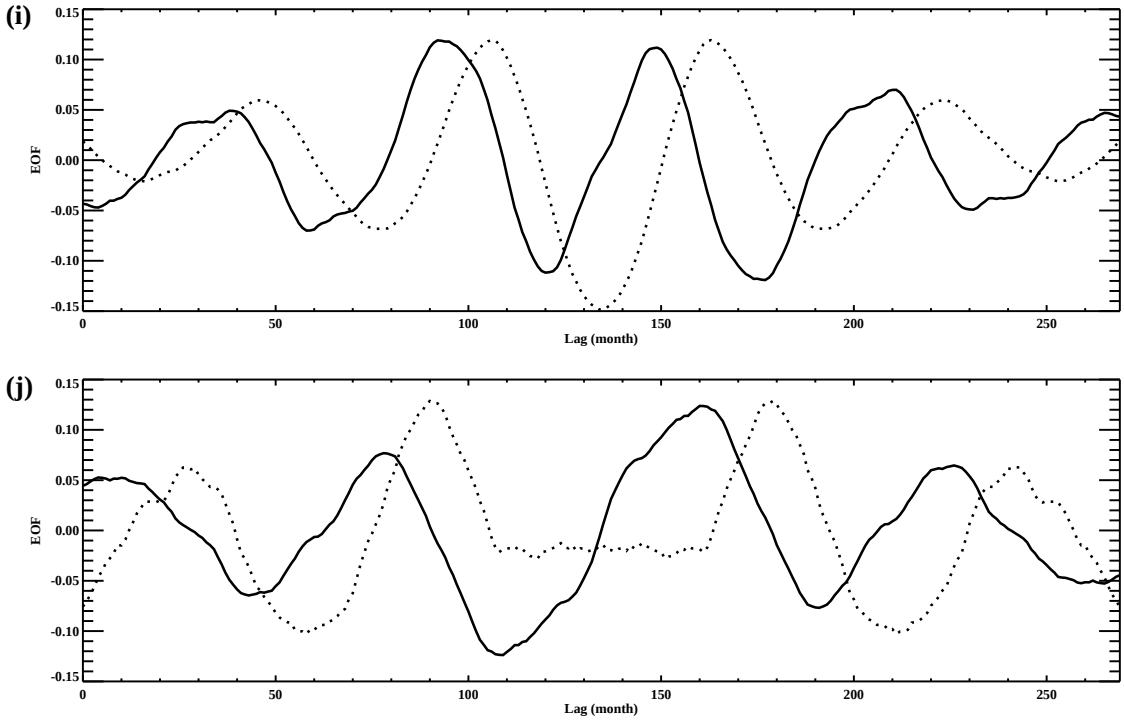

Figure 4.4 cont.; Leading EOFs: **(i)** (16,17), **(j)** (18,19).

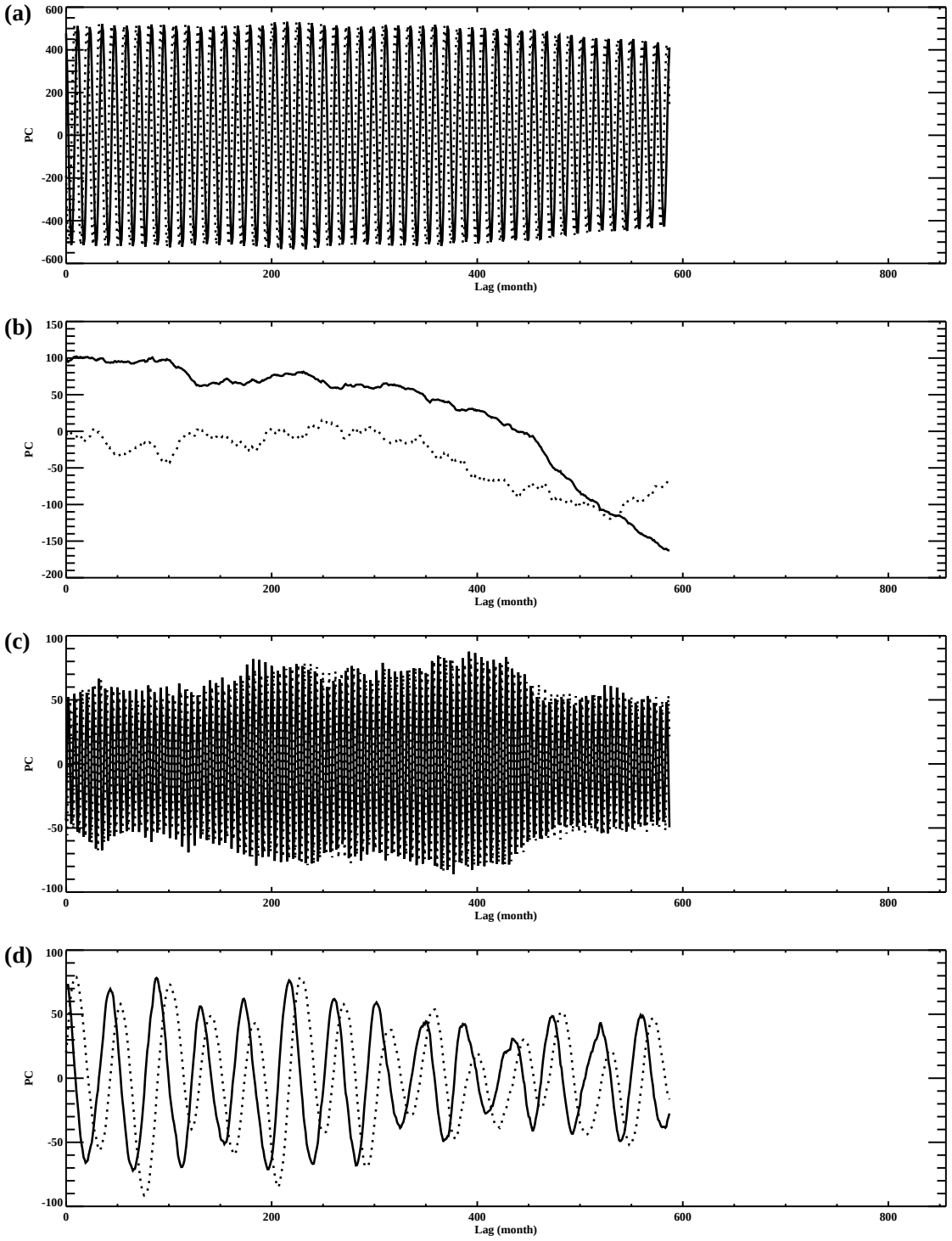

Figure 4.5: Leading pairs of PCs for the M270 SSA analysis of ATCO, **(a)** (1,2), **(b)** (3,4), **(c)** (5,6), **(d)** (7,8), **(e)** (9,10), **(f)** (11,12), **(g)** (13,14), **(h)** (15) unpaired. **(i)** (16,17), **(j)** (18,19).

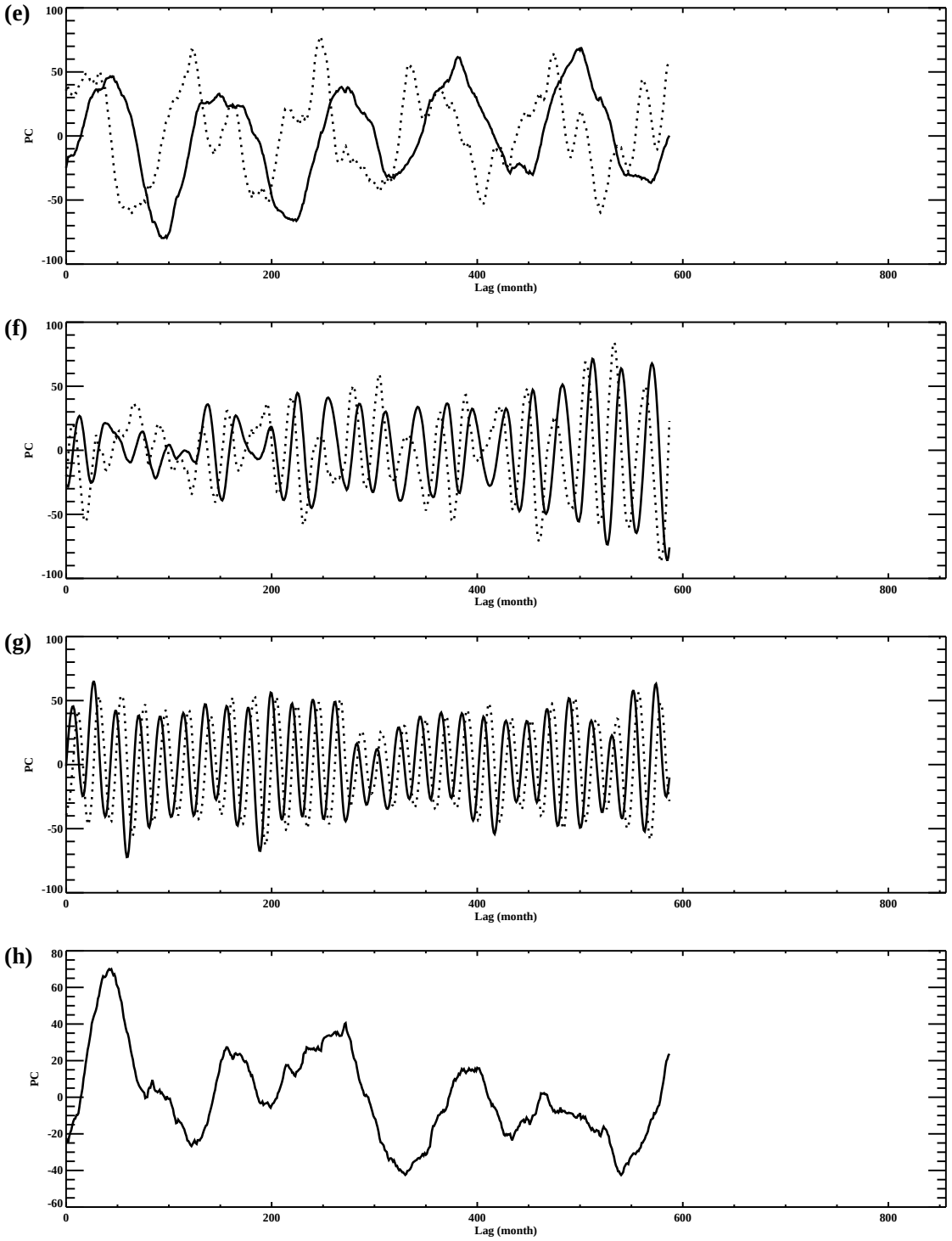

Figure 4.5 cont.; Leading PCs: **(e)** (9,10), **(f)** (11,12), **(g)** (13,14), **(h)** (15) unpaired.

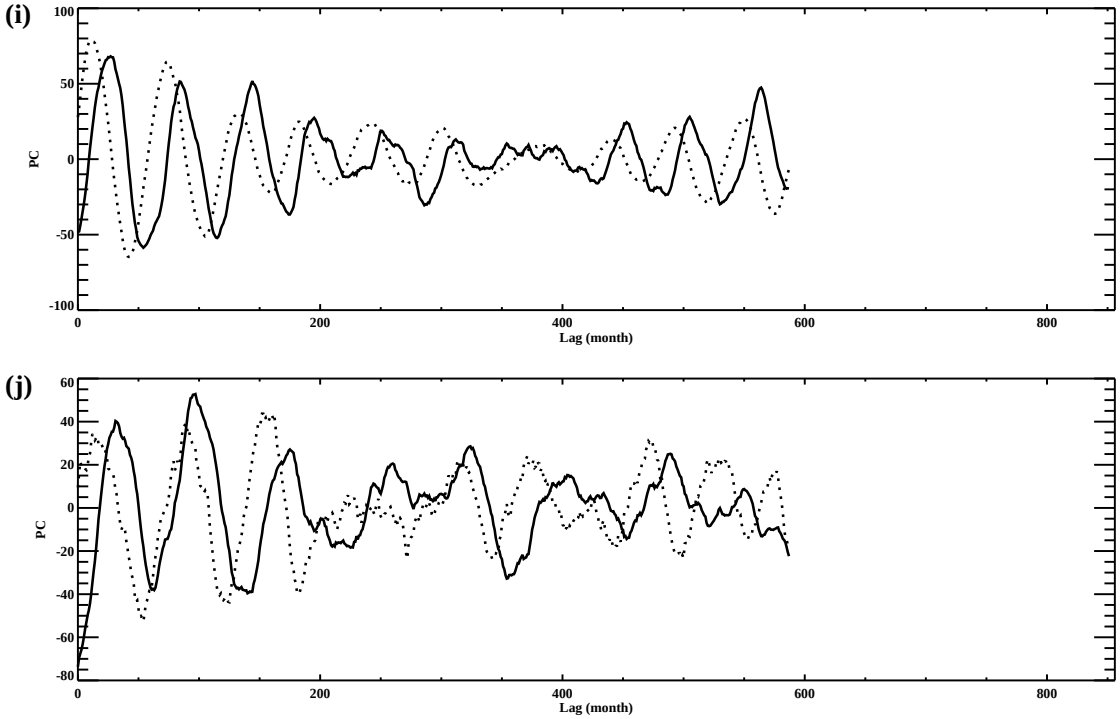

Figure 4.5 cont.; Leading PCs: **(i)** (16,17), **(j)** (18,19).

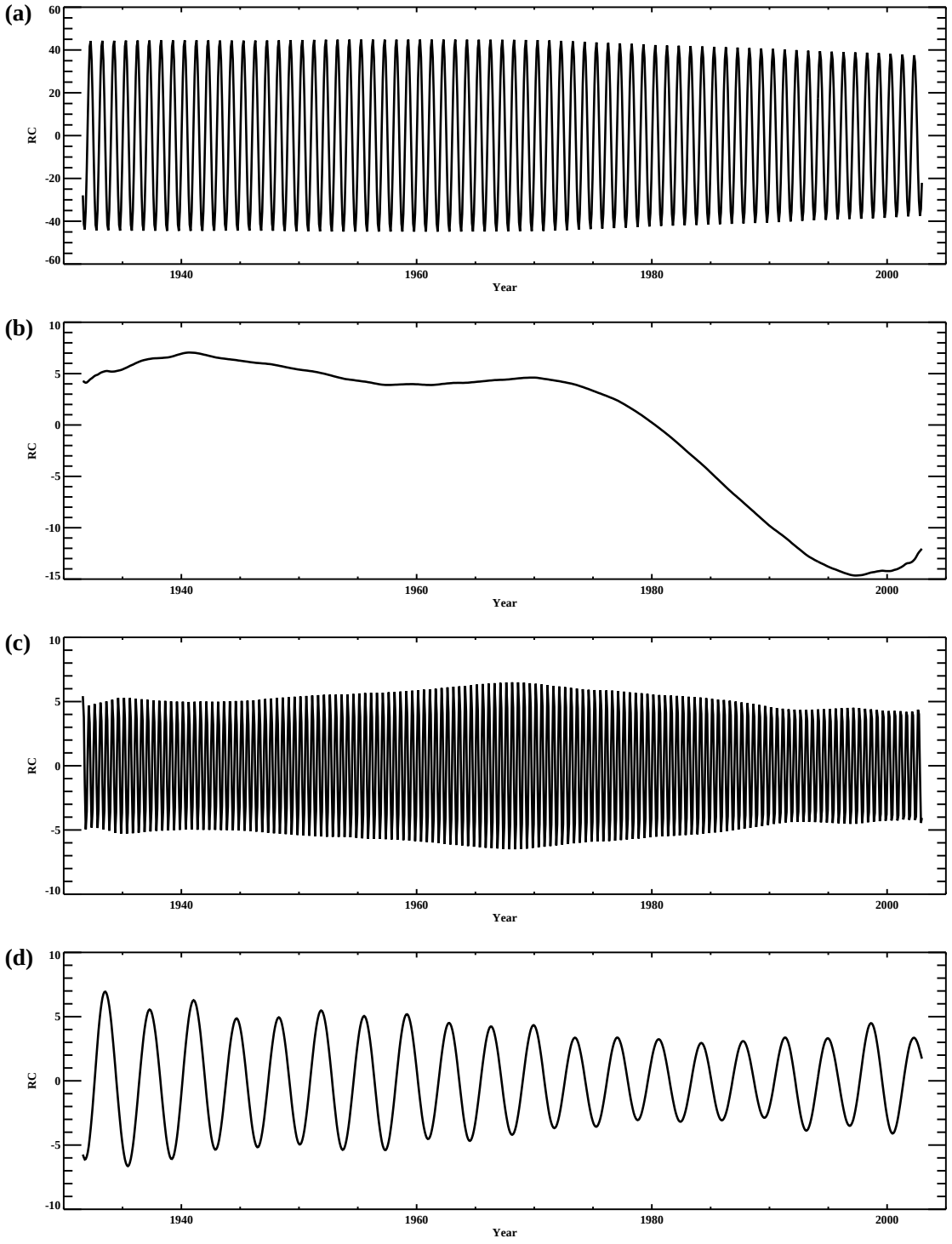

Figure 4.6: Sum of the leading pairs of RCs for the M270 SSA analysis of ATCO, **(a)** (1+2), **(b)** (3+4), **(c)** (5+6), **(d)** (7+8), **(e)** (9+10), **(f)** (11+12), **(g)** (13+14), **(h)** (15) unpaired. **(i)** (16+17), **(j)** (18+19).

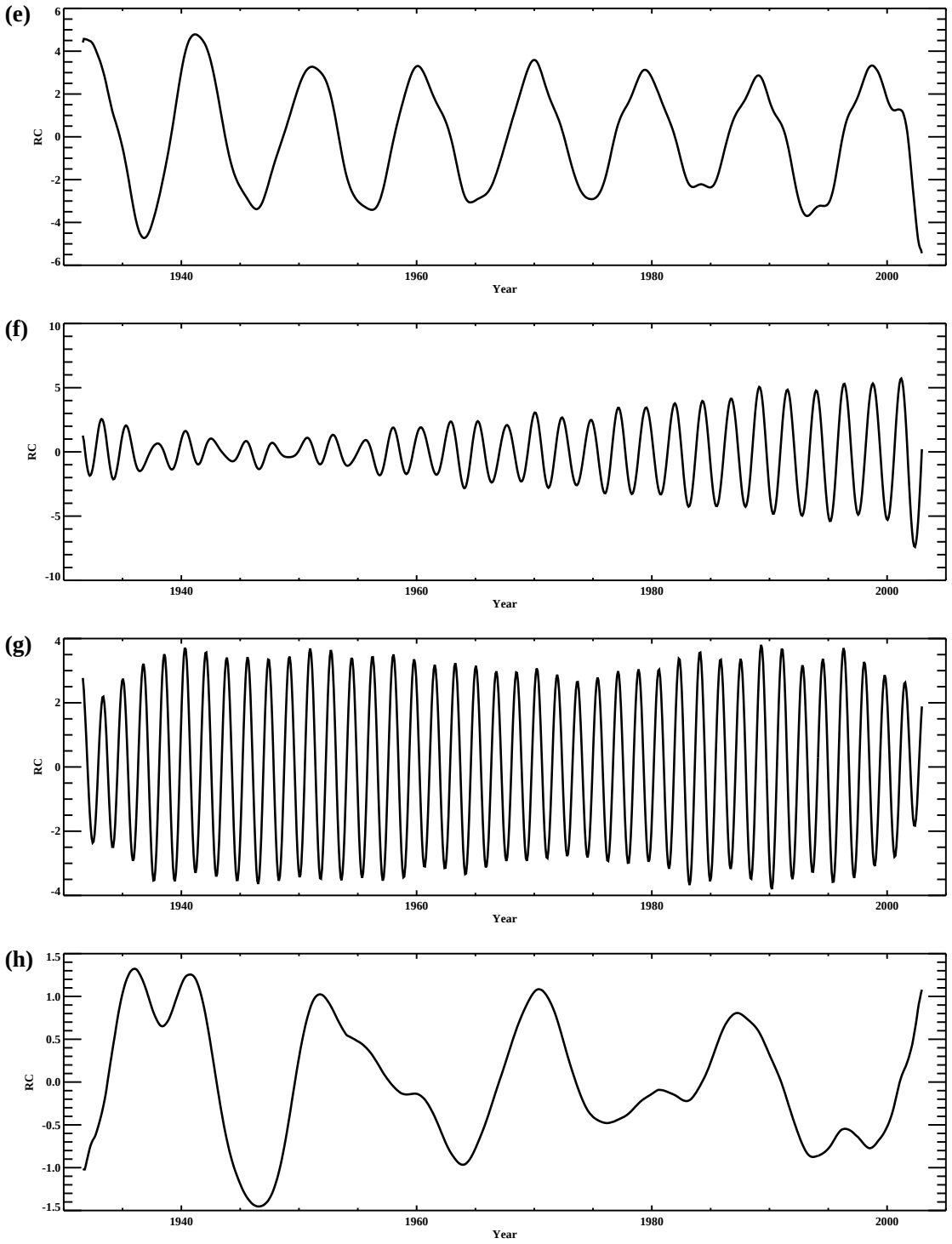

Figure 4.6 cont.; Leading RCs: **(e)** (9+10), **(f)** (11+12), **(g)** (13+14), **(h)** (15) unpaired.

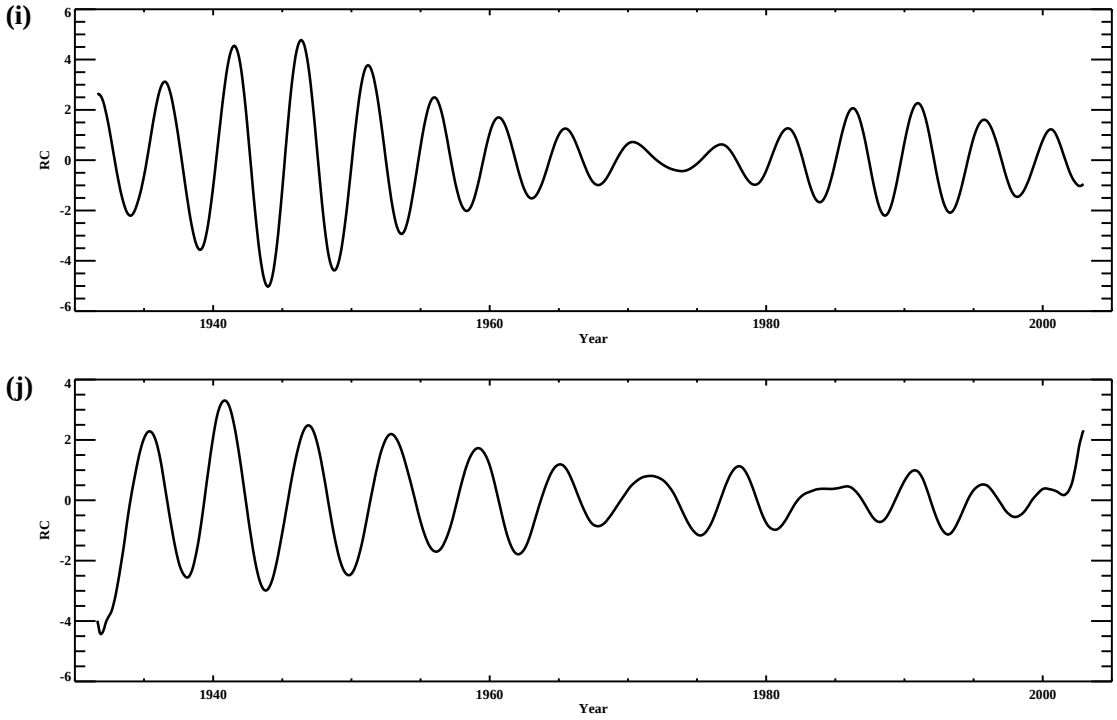

Figure 4.6 cont.; Leading RCs: **(i)** (16+17), **(j)** (18+19).

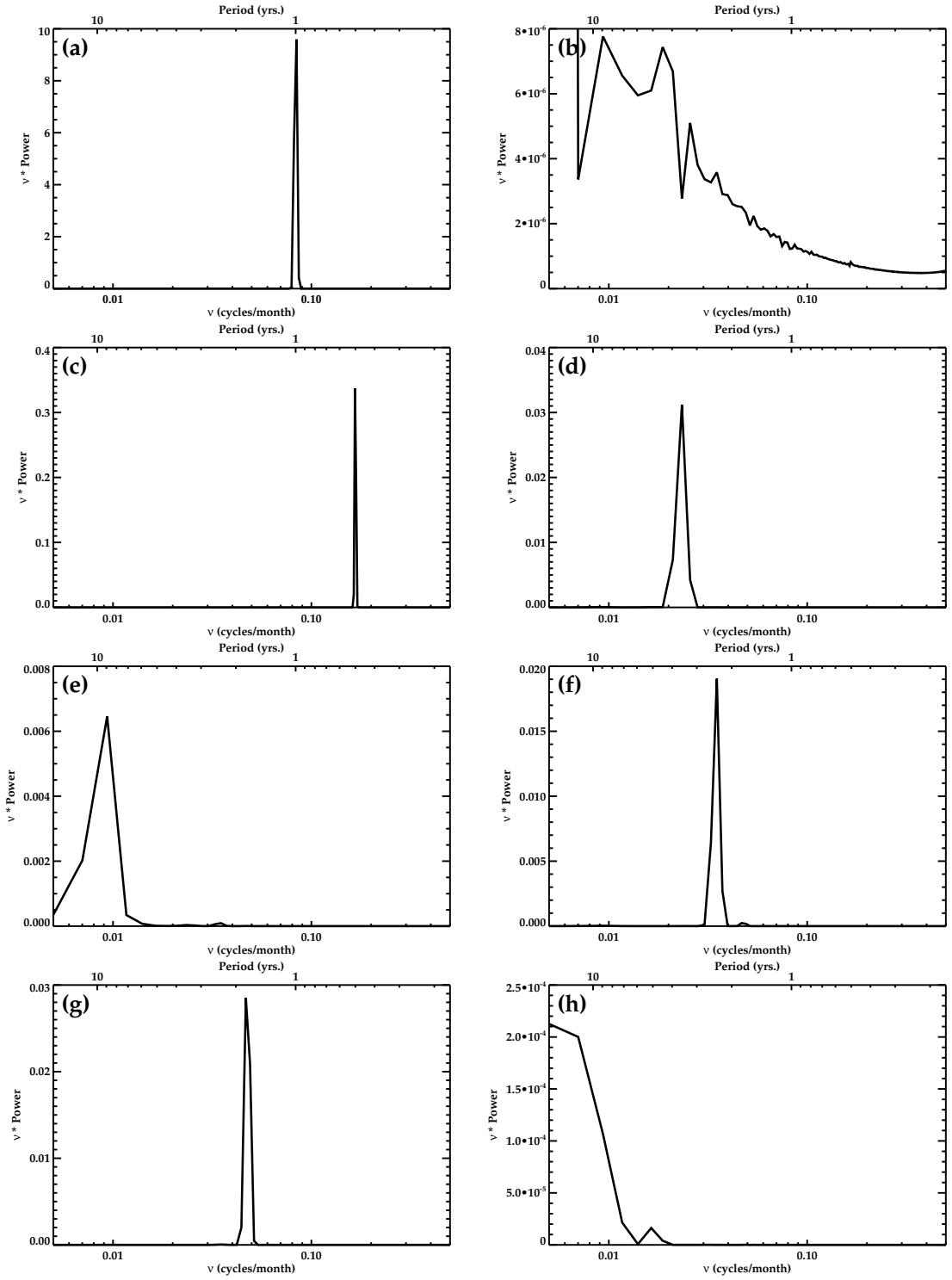

Figure 4.7: PSDs of the RCs in the previous figure; **(a)** (1+2), **(b)** (3+4), **(c)** (5+6), **(d)** (7+8), **(e)** (9+10), **(f)** (11+12), **(g)** (13+14), **(h)** (15) unpaired, **(i)** (16+17), **(j)** (18+19).

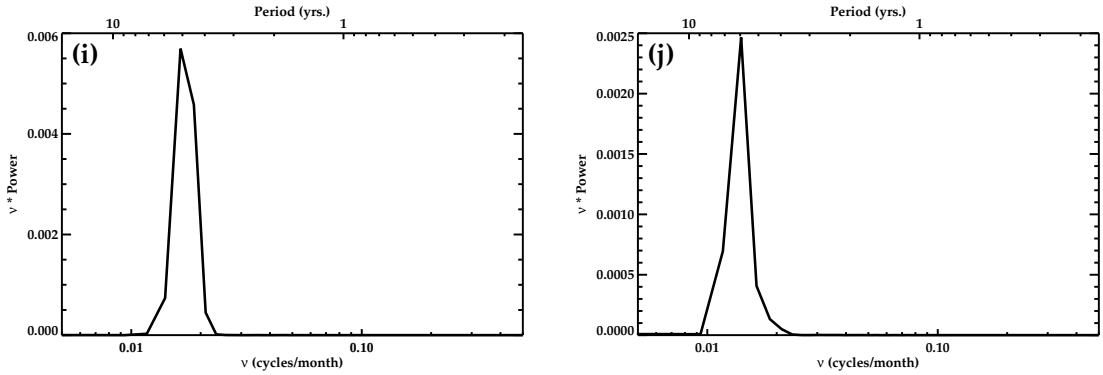

Figure 4.7 cont.; Leading RCs: **(i)** (16+17), **(j)** (18+19).

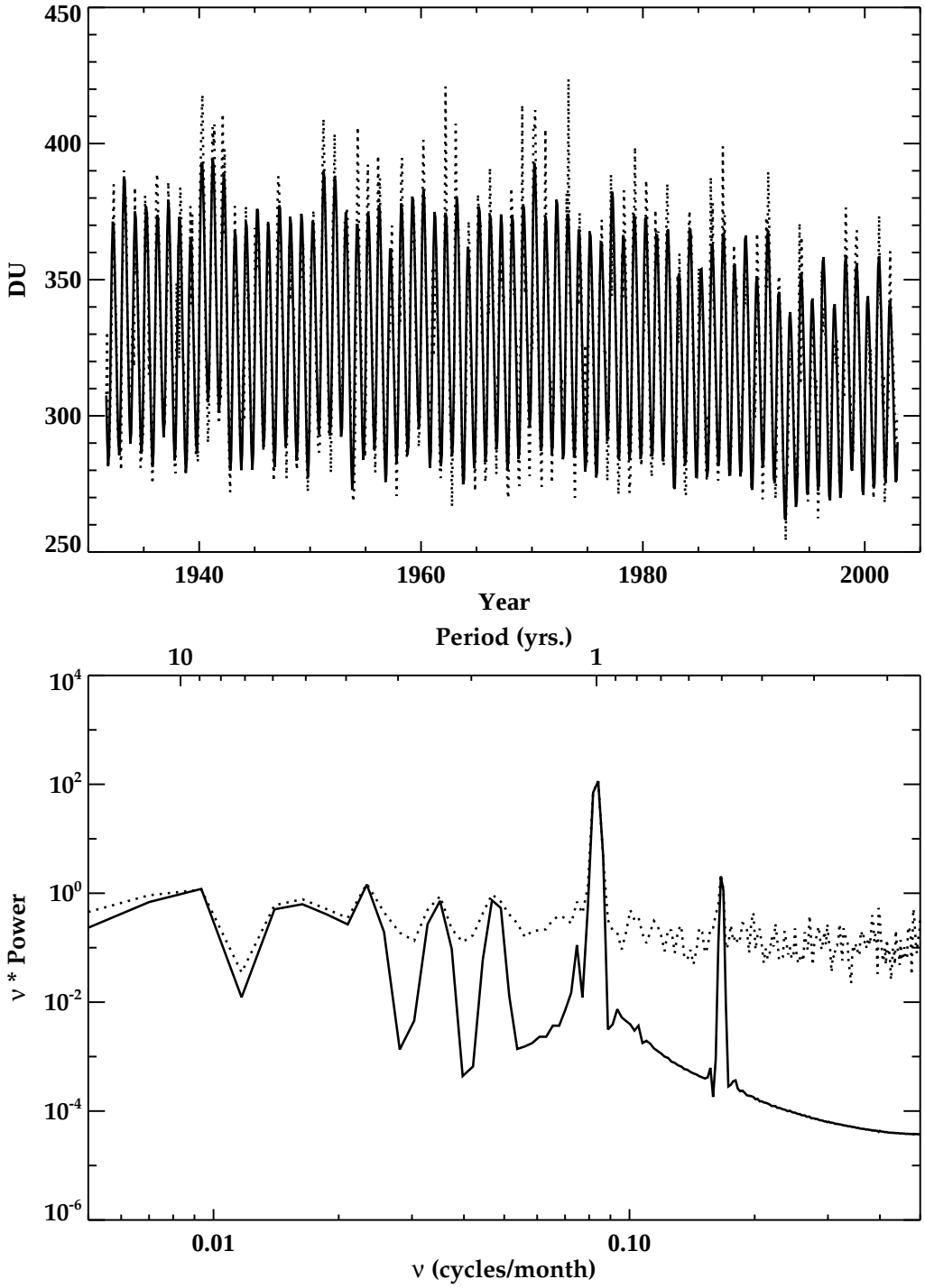

Figure 4.8: **(a)** Partial reconstruction (solid) of ATCO time series (dotted) based on first 20 EOFs of the M270 SSA analysis. **(b)** PSDs of the partial reconstruction (solid) and raw ATCO (dotted).

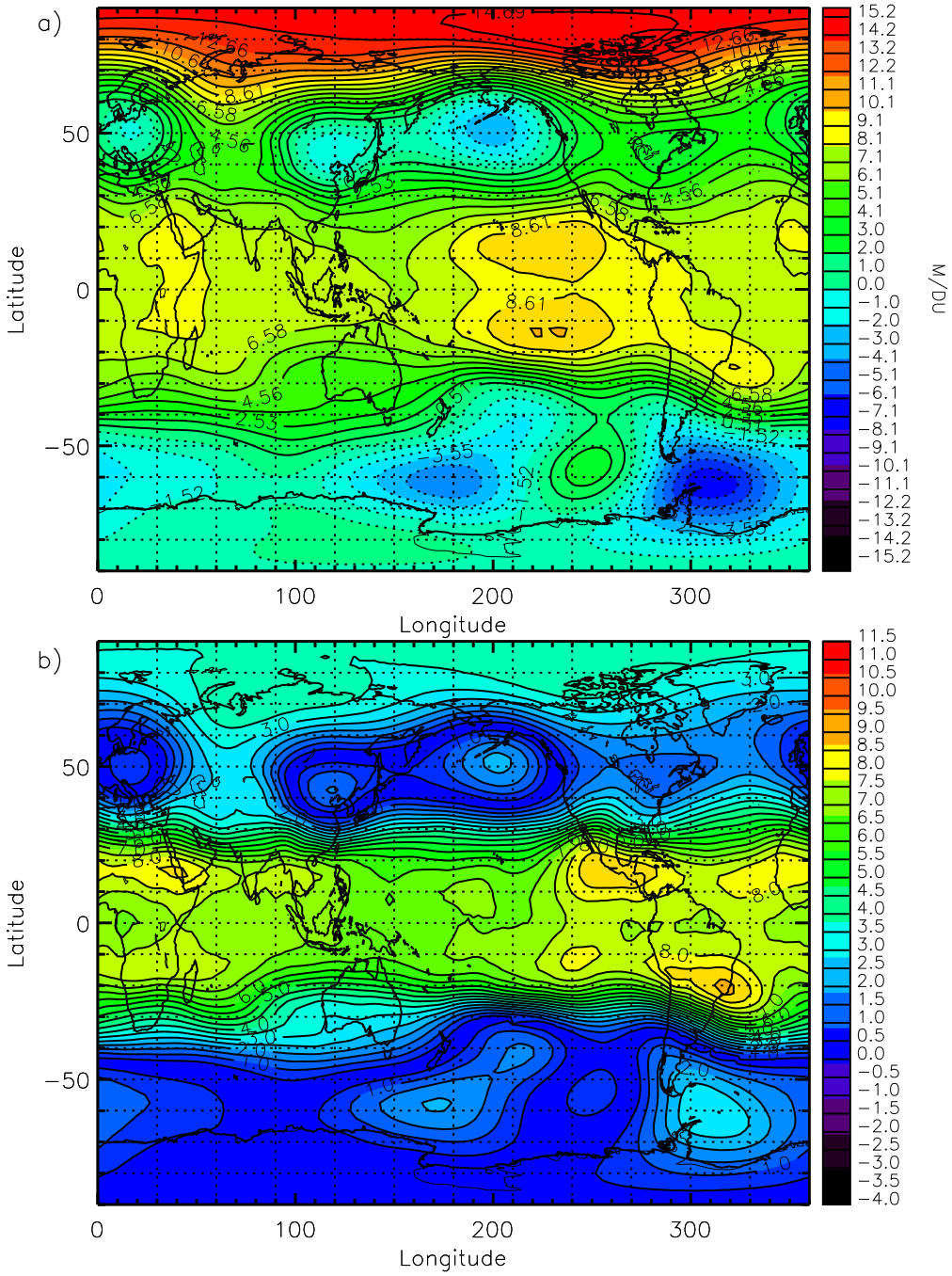

Figure 4.9: **(a)** Regression coefficient for the regression of the M270 3.5-year component (RCs 7+8) onto the NCEP 100 hPa geopotential height. **(b)** t-statistic associated with the regression coefficient.

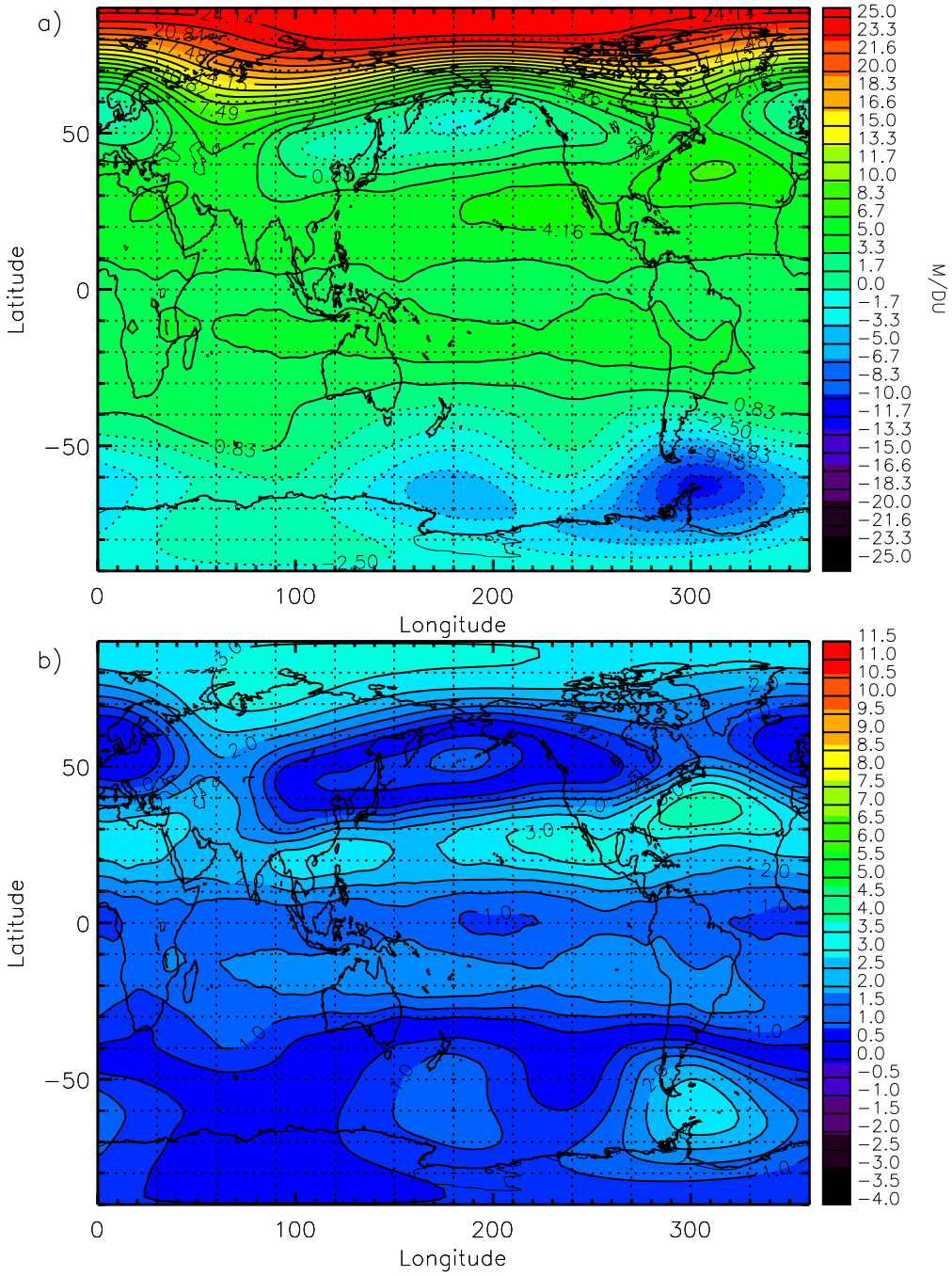

Figure 4.10: **(a)** Regression coefficient for the regression of the M270 3.5-year component (RCs 7+8) onto the NCEP 30 hPa geopotential height. **(b)** t-statistic associated with the regression coefficient.

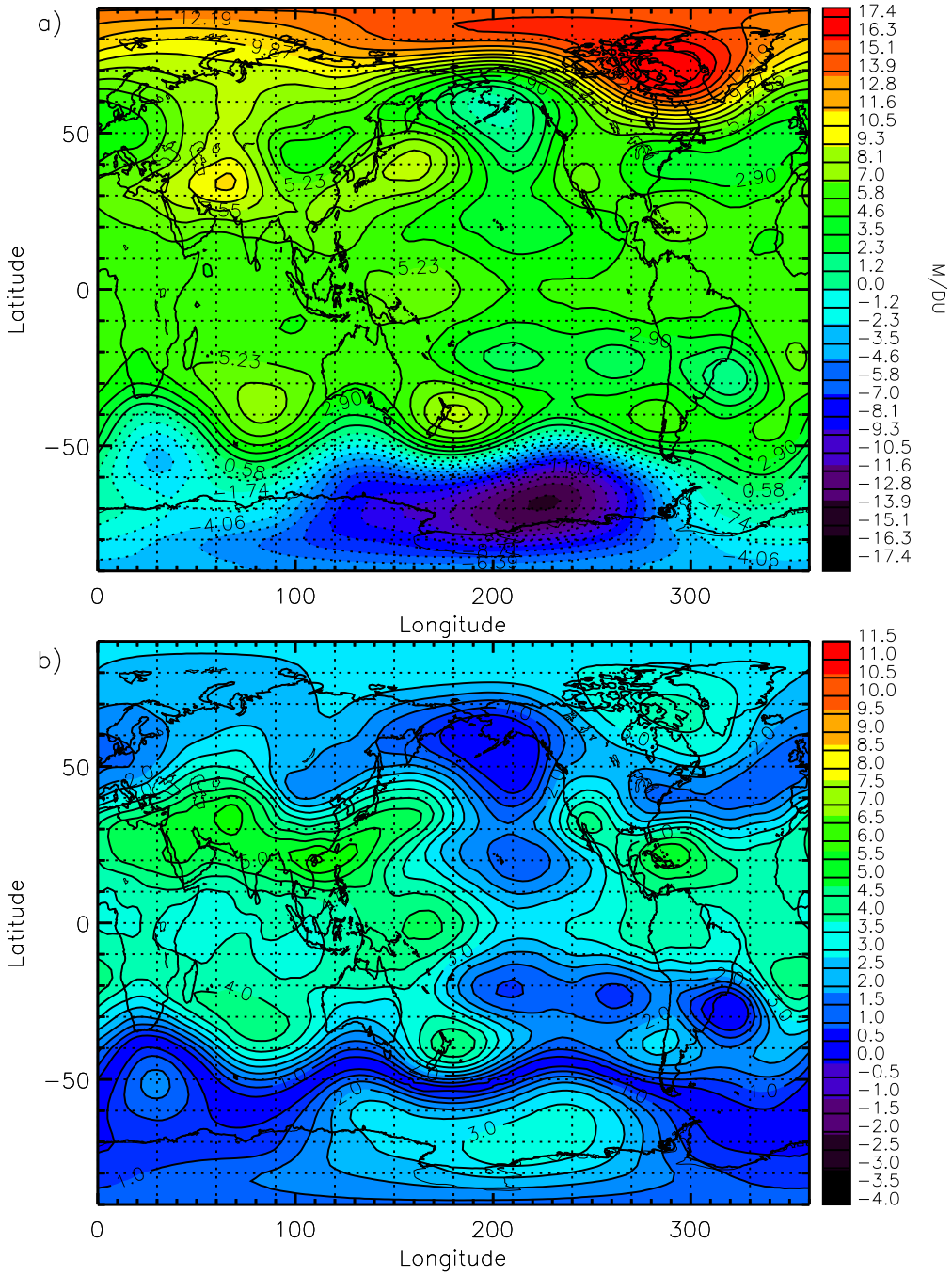

Figure 4.11: **(a)** Regression coefficient for the regression of the M270 decadal component (RCs 9+10) onto the NCEP 100 hPa geopotential height. **(b)** t-statistic associated with the regression coefficient.

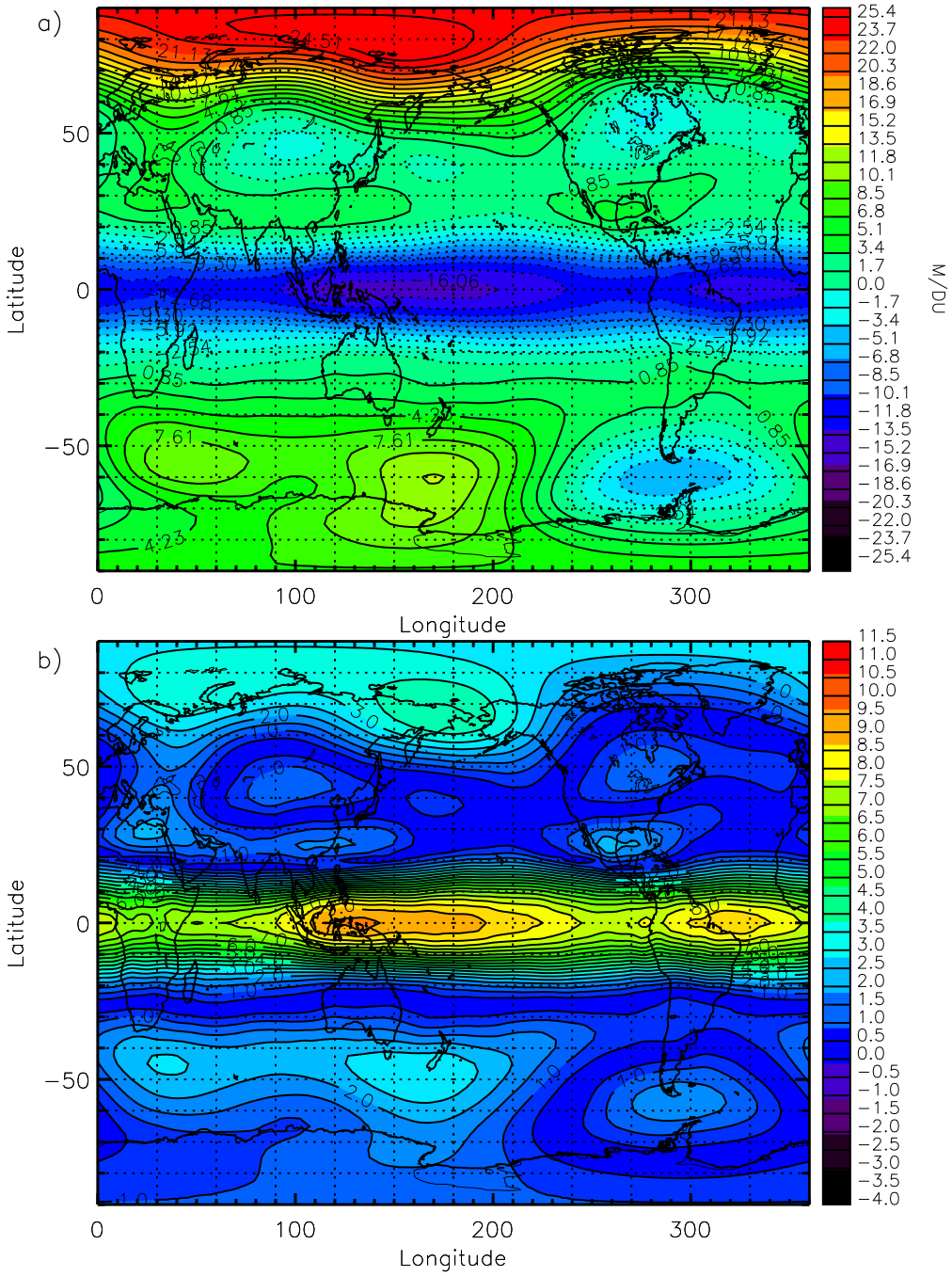

Figure 4.12: **(a)** Regression coefficient for the regression of the M270 QBO component (RCs 11+12) onto the NCEP 30 hPa geopotential height. **(b)** t-statistic associated with the regression coefficient.

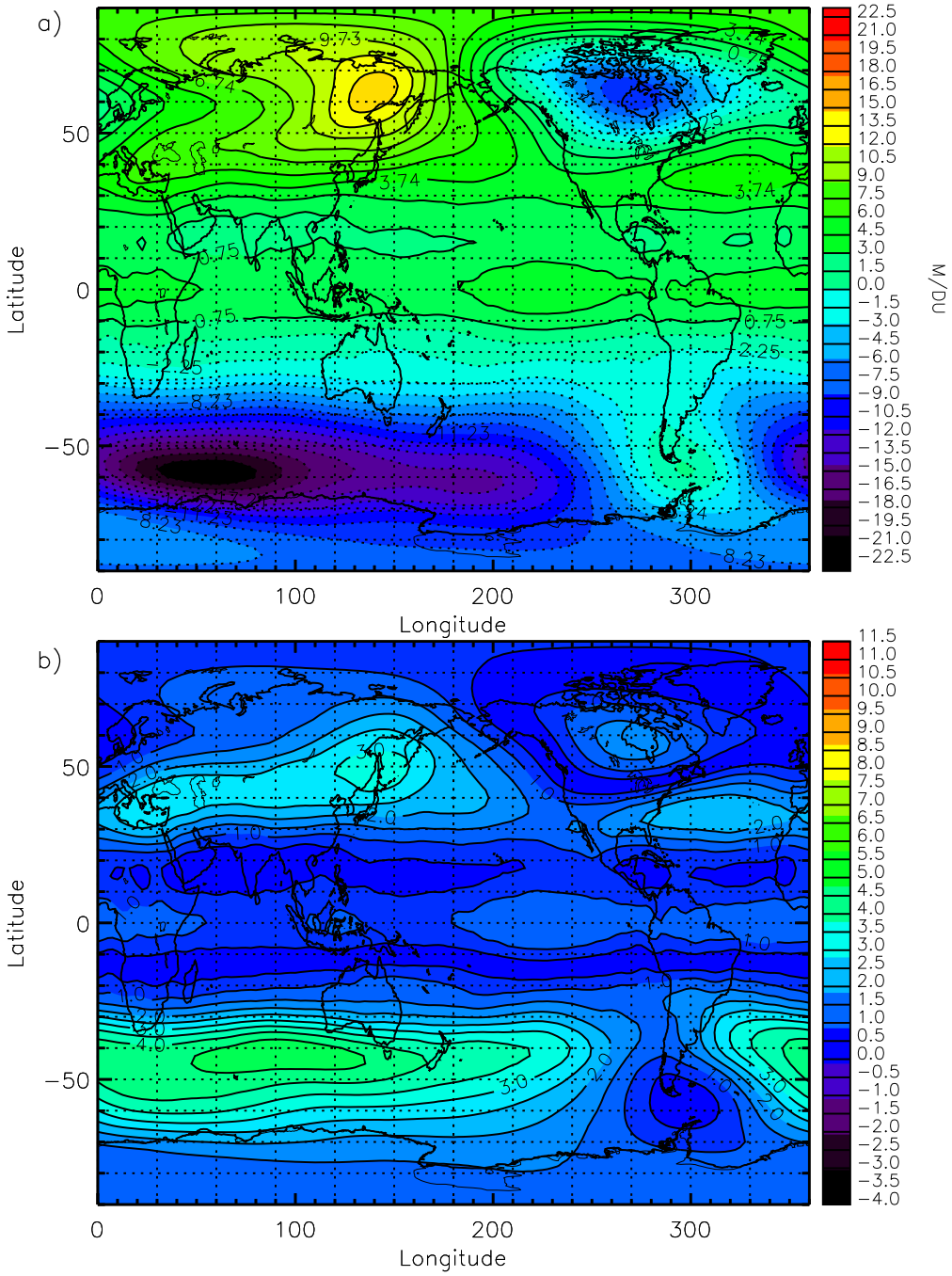

Figure 4.13: **(a)** Regression coefficient for the regression of the M270 QBO-AB component (RCs 13+14) onto the NCEP 30 hPa geopotential height. **(b)** t-statistic associated with the regression coefficient.

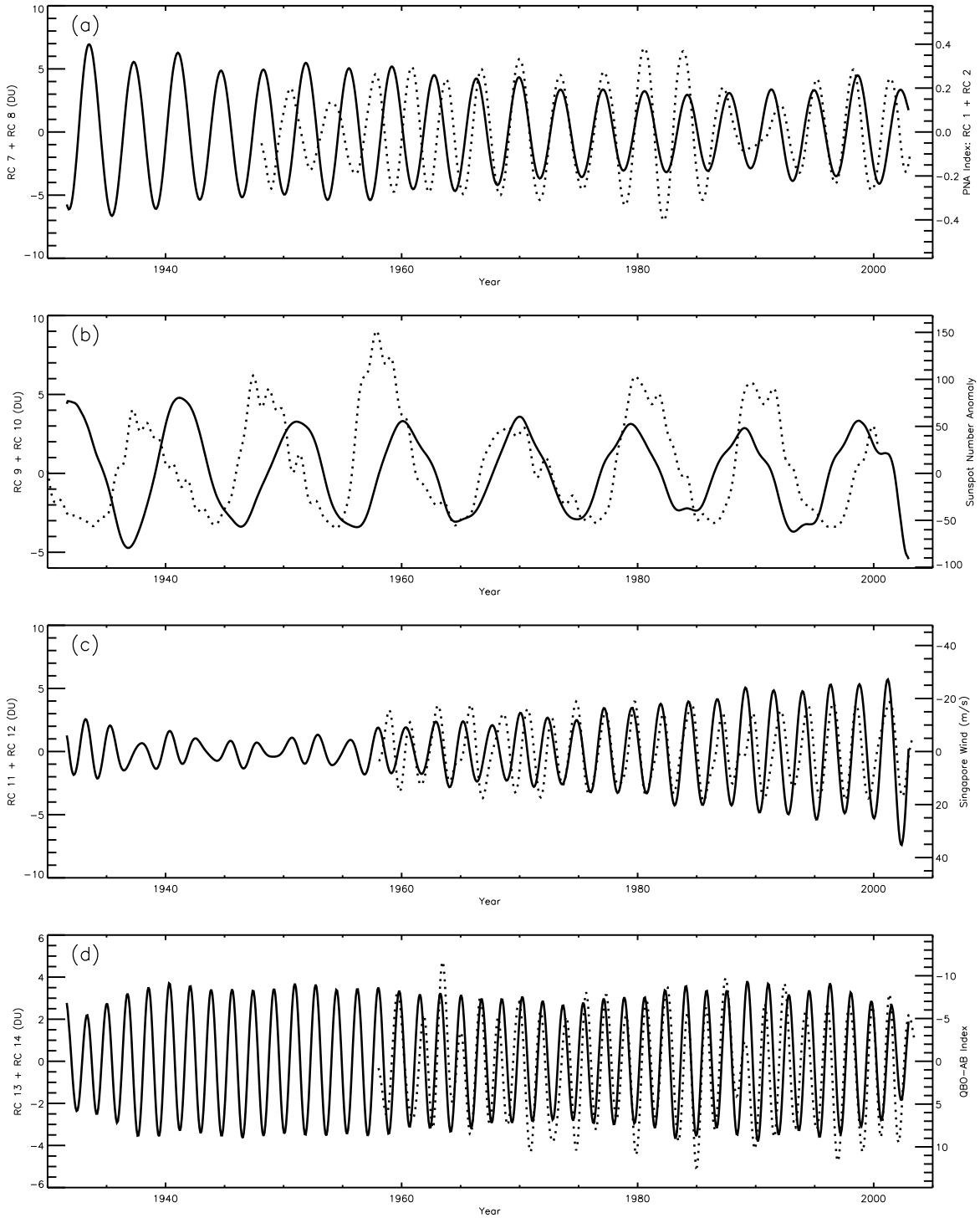

Figure 4.14: Comparison of various reconstructed IAV oscillations (solid curves), based on pairs of M270 EOFs, to appropriate indices (dotted). (a) M270 3.5-year oscillation (RCs 7+8) and leading oscillation of a SSA analysis of the PNA, (b) M270 decadal oscillation (RCs 9+10) and anomalous sunspot number, (c) M270 QBO oscillation and the 30 hPa Singapore wind, (d) M270 QBO-AB oscillation and a QBO-AB index.

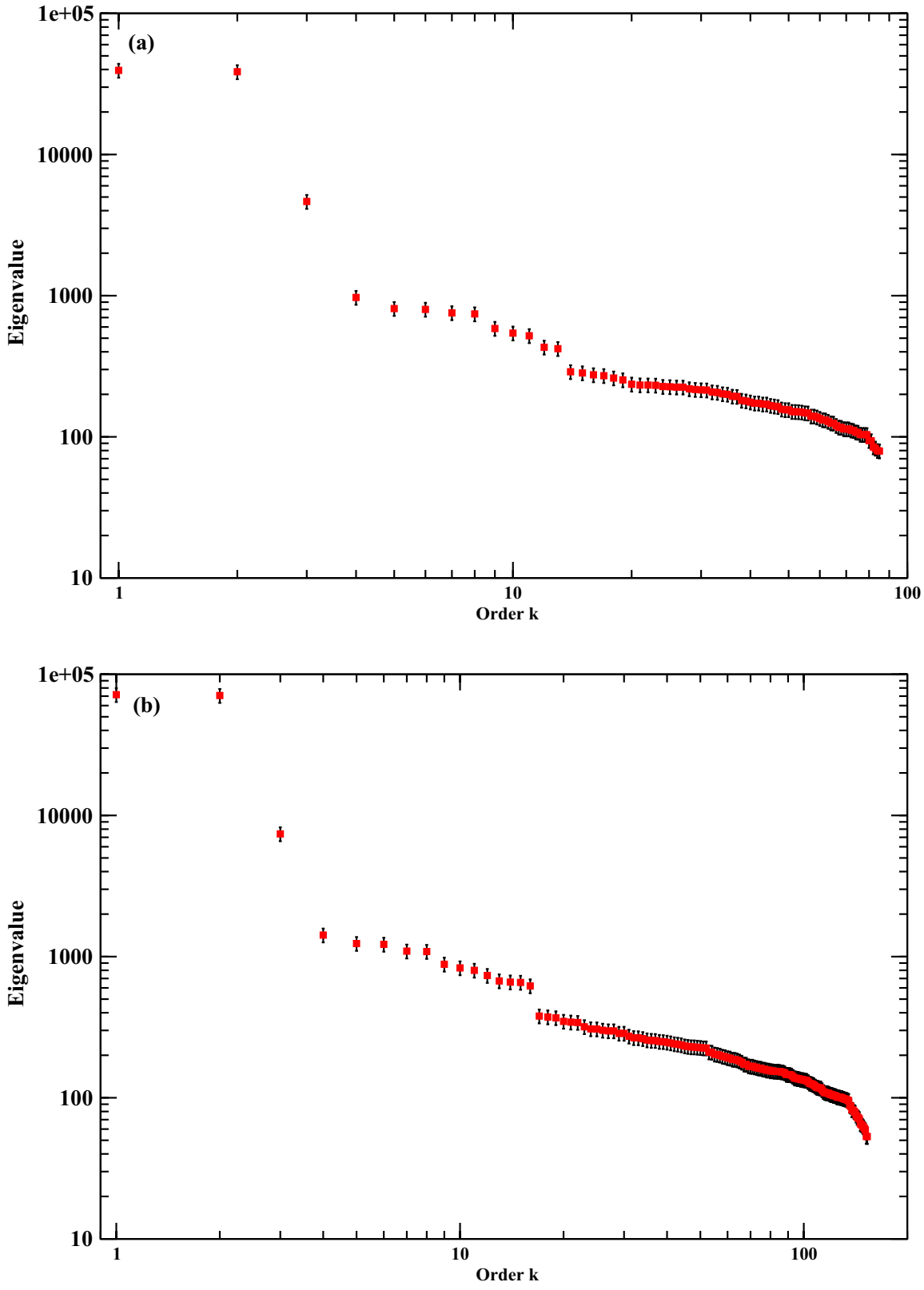

Figure 4.15: Eigenvalue spectra for M155 and M85 SSA analyses of ATCO. (a) M155 (b) M85.

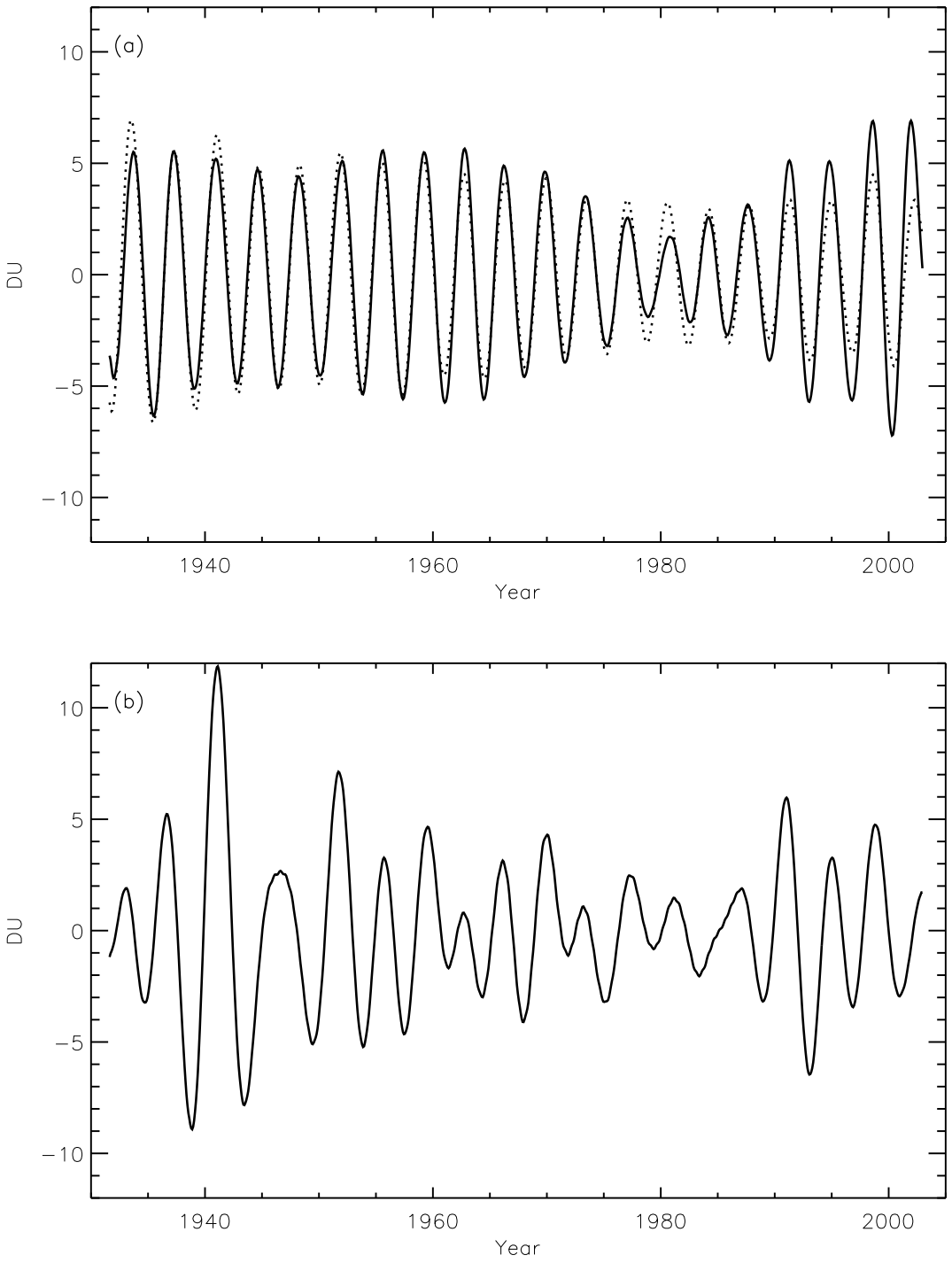

Figure 4.16: Comparison of the 3.5-year oscillations found in SSA analyses of ATCO for various window lengths. **(a)** sum of paired RCs (7,8) from the M155 (solid) and M270 (dotted) analyses. **(b)** sum of paired RCs (5,6) from the M85 analysis.

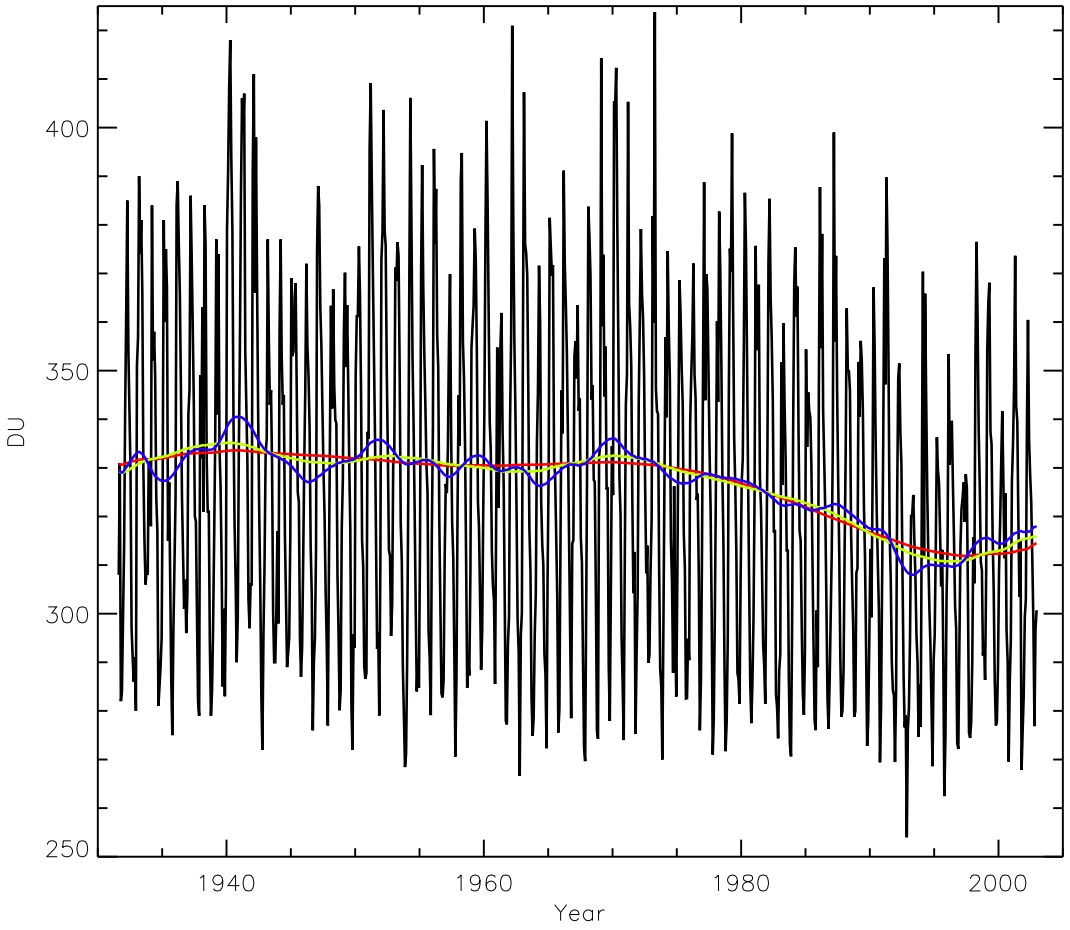

Figure 4.17: Comparison of the trends found in SSA analyses of ATCO for various window lengths plotted against the original ATCO (black line): $M = 270$ (red), 155 (green), and 85 (blue).

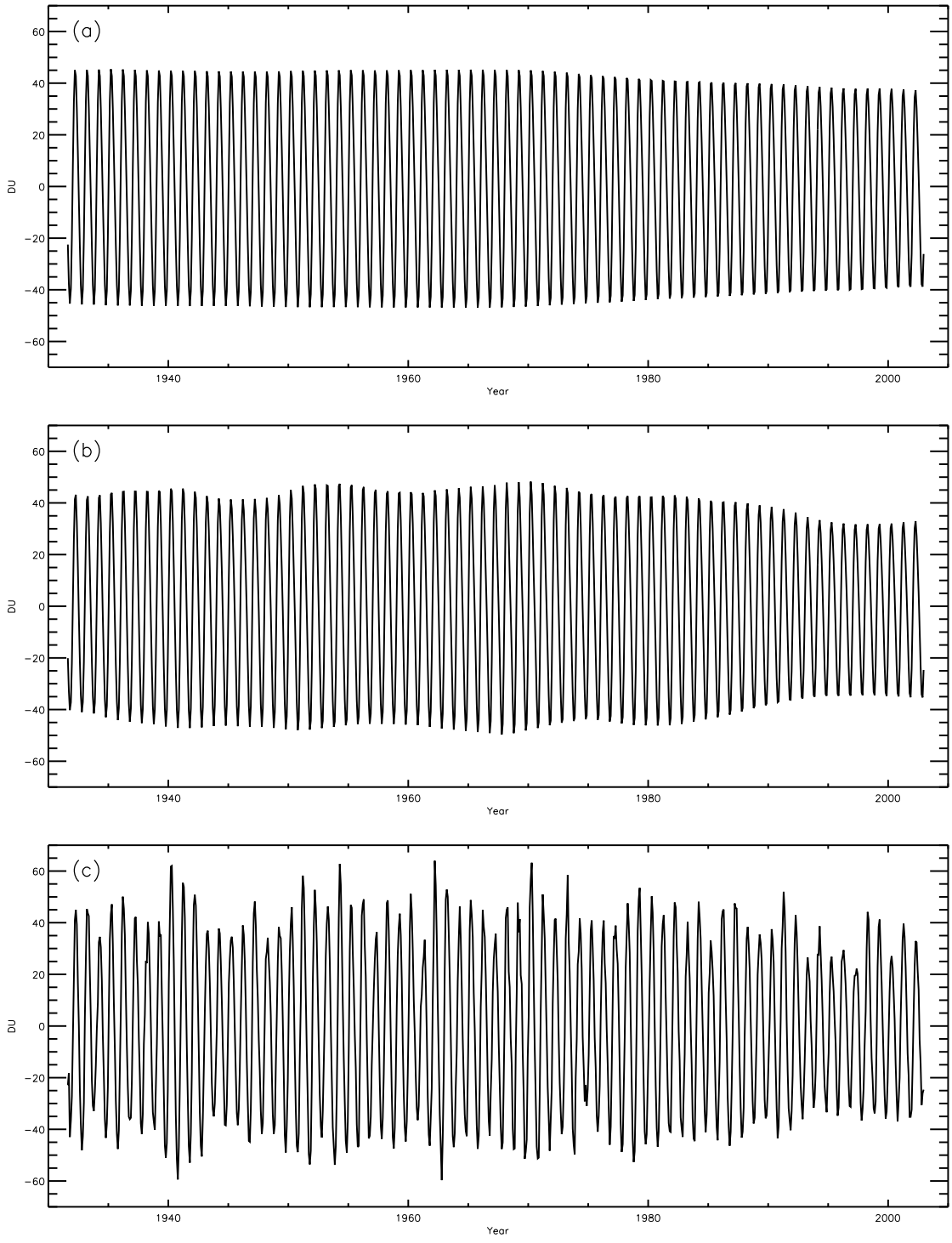

Figure 4.18: Comparison of the annual cycle found in SSA analyses of ATCO for various window lengths **(a)** $M = 270$, **(b)** $M = 85$, **(c)** $M = 12$.

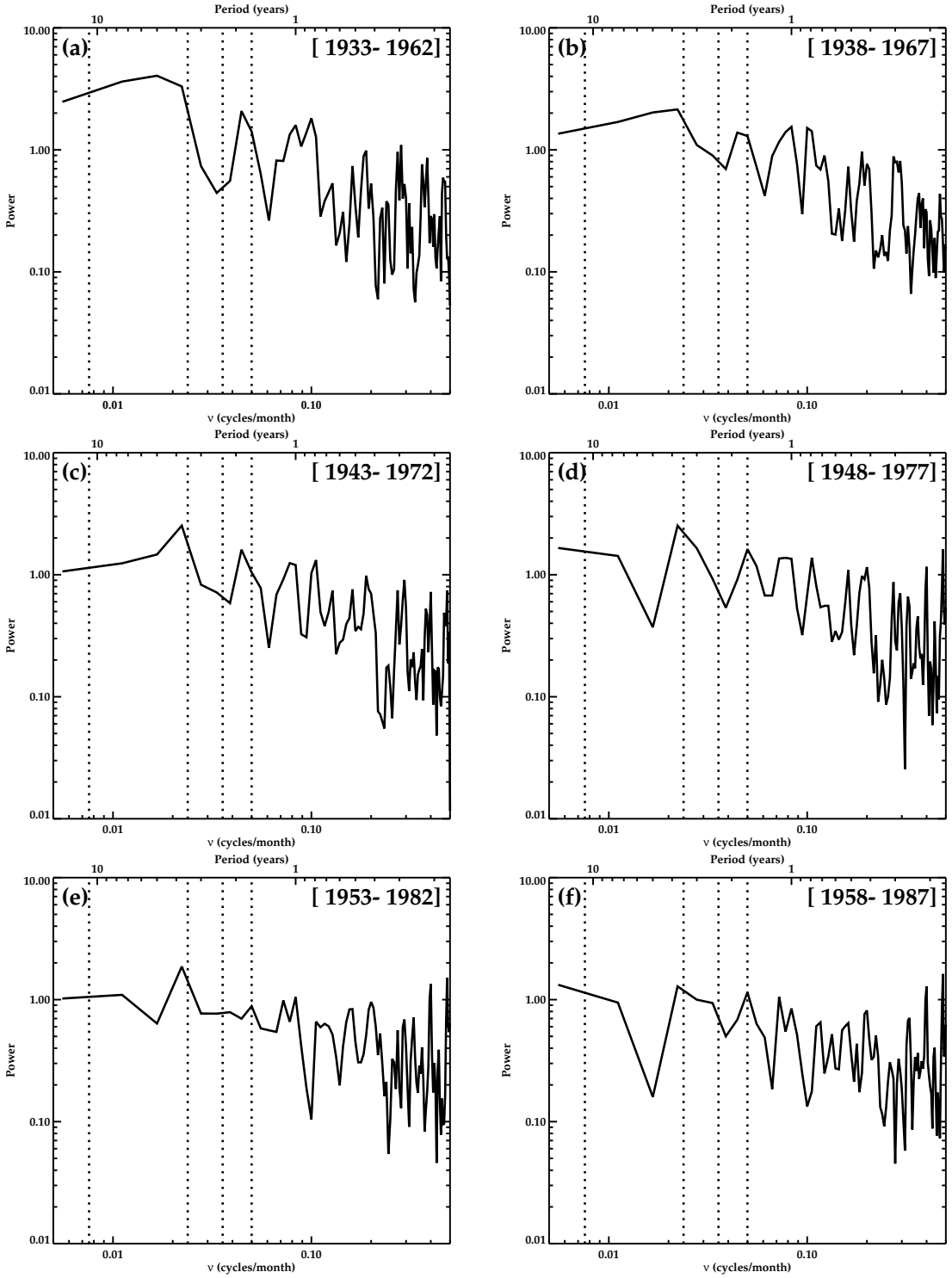

Figure 4.19: Power spectral estimates of 30 year segments of the deseasonalized, detrended ATCO. Segments begin every 5 years staring in 1933. Vertical dotted lines mark periods of 11 years, 3.5 years, 28 months and 20 months.

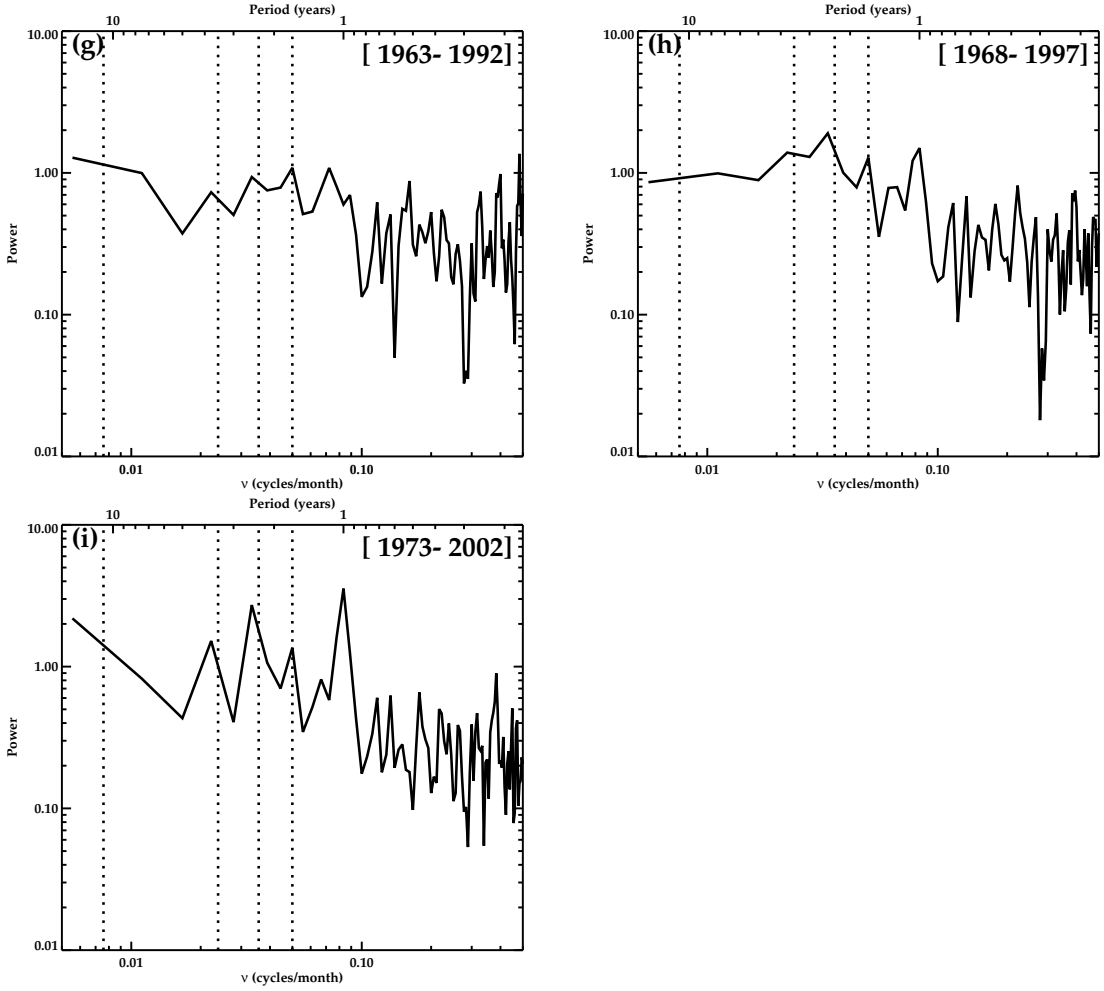

Figure 4.19 cont.

Chapter 5

The Sensitivity of Tropospheric Methane to the Interannual Variability in Stratospheric Ozone

5.1 Introduction

The most important mechanism for removing methane from the atmosphere is reaction with tropospheric OH radicals (*Khalil et al.*, 1993)

$$CH_4 + OH \rightarrow CH_3 + H_2O \tag{5.1}$$

The primary source of OH is the UV photolysis of tropospheric ozone to give electronically excited oxygen atoms. A small fraction of these excited atoms then react with water to produce the OH radical. This source of OH is described by *Levy* (1972) and *Thompson* (1992)

$$O_3 + h\nu \rightarrow O\left(^1D\right) + O_2 \tag{5.2}$$

$$O\left(^1D\right) + H_2O \rightarrow 2OH \tag{5.3}$$

where $h\nu$ is a near-UV photon. As oxidation by OH is the main loss mechanism for tropospheric methane it follows that any perturbation to the abundance of OH will affect the abundance of methane. Any modulation of the UV flux to the troposphere will affect the abundance of OH (*Liu and Trainer*, 1988) which will in turn modulate the concentration of methane via reactions (5.1), (5.2) and (5.3). The primary source of UV fluctuations on interannual time scales is fluctuations in the ozone column abundance.

For small perturbations, these effects may be approximated by the linear relations

$$\frac{[OH]'}{[OH]_0} = -\alpha_{OH}\frac{\Omega'}{\Omega_0} \tag{5.4a}$$

$$\frac{[CH_4]'}{[CH_4]_0} = -\alpha_{CH_4}\frac{\Omega'}{\Omega_0} \tag{5.4b}$$

where α is the sensitivity of a given species to changes in the ozone column abundance. Ω_0 and Ω' are, respectively, the reference level and the perturbation from the reference level of ozone, with similar definitions for reference levels and perturbations of the concentrations of CH_4 and OH. The minus sign follows the convention in the literature (*Fuglestvedt et al.*, 1994; *Granier and Shine*, 1999). We expect α_{CH_4} to be negative, since the oscillations in methane are positively correlated with the oscillations in ozone. A value for α_{CH_4} can be calculated from a comparison of the observations of the fluctuations in the methane signal to those in the ozone signal. Note that the α so determined is based on the methane's relatively short response time to

the ozone oscillations and is therefore fundamentally different from the α's obtained from studies using models run until a steady state is achieved (*Bekki et al.*, 1994; *Fuglestvedt et al.*, 1994; *Granier et al.*, 1996; *van Dop and Krol*, 1996). However, the empirically determined α can, with appropriate modifications, still be used to calibrate the behavior of the modeling studies. This is explored in more detail in the next section and in the Discussion.

While the sensitivity will be determined empirically, a simple model can be used to help interpret the results. Changes in methane concentration can be modeled by the equation

$$\frac{d\left[\mathrm{CH_4}\right]}{dt} = P - k\left[\mathrm{OH}\right]\left[\mathrm{CH_4}\right] \tag{5.5}$$

where P is the production of methane and k is the rate coefficient for destruction of methane by OH. P and k are assumed to be constants. The methane concentration can be written as $[\mathrm{CH_4}] = [\mathrm{CH_4}]_0 + [\mathrm{CH_4}]'$ and the OH concentration as $[\mathrm{OH}] = [\mathrm{OH}]_0 + [\mathrm{OH}]'$, where a zero subscript represents the time-invariant mean and a prime represents the deviation from the mean. Equation (5.5) can now be expanded

$$\begin{aligned}\frac{d\left[\mathrm{CH_4}\right]'}{dt} = P &- k\left[\mathrm{OH}\right]_0\left[\mathrm{CH_4}\right]_0 - k\left[\mathrm{OH}\right]_0\left[\mathrm{CH_4}\right]' \\ &- k\left[\mathrm{OH}\right]'\left[\mathrm{CH_4}\right]_0 - k\left[\mathrm{OH}\right]'\left[\mathrm{CH_4}\right]'\end{aligned} \tag{5.6}$$

The first two terms on the right-hand side of (5.6) cancel since the steady state solution of (5.5) gives $P - k\left[\mathrm{OH}\right]_0\left[\mathrm{CH_4}\right]_0 = 0$. The last term is second order in the perturbation and can be neglected for small perturbations. Dividing the remaining

terms in (5.6) by $[CH_4]_0$ leaves the linearized model

$$\frac{dy}{dt} = -\frac{y}{\tau} - \frac{F(t)}{\tau} \tag{5.7}$$

where $y = [CH_4]' / [CH_4]_0$ is the fractional deviation from the mean methane concentration and $F = [OH]' / [OH]_0$ is the fractional deviation of the OH concentration. $\tau = 1/k[OH]_0$ is the mean lifetime of methane in the troposphere. This analysis can be expanded to a time-dependent source, $P(t)$, by detrending the chemical time series and assuming that $P(t)$ balances the trends removed. Since the lifetime of OH in the atmosphere is extremely short, the perturbations in OH should very closely track the perturbations in O_3. For small perturbations, the forcing term in Equation (5.7) can be represented as

$$F(t) = \kappa \frac{\Omega'}{\Omega_0} \tag{5.8}$$

where, as before, Ω represents the total column abundance of ozone.

5.2 Sensitivity to Interannual Fluctuations

We have carried out an empirical study of the sensitivity of the methane to interannual fluctuations in ozone column abundance. The ozone dataset we used was one of the Merged Ozone Datasets (MOD), which combine the monthly mean column abundances collected by the Total Ozone Mapping Spectrometer (TOMS) instruments on Nimbus-7, Meteor-3 and Earth Probe with the total ozone measurements collected by the Solar Backscatter Ultraviolet (SBUV / SBUV2) instruments on Nimbus 7, NOAA

9 and NOAA 11 (*McPeters et al.*, 1996; *Bojkov and Hudson*, 1999). We used version 1, all stations, of the combined dataset (SBUV+TOMS), as described in the NASA website: http://hyperion.gsfc.nasa.gov/Analysis/merged. The methane data we used were monthly means of surface methane measurements made from samples collected at fixed sites in the National Oceanic and Atmospheric Administration-Climate Monitoring and Diagnostics Laboratory (NOAA-CMDL) Global Cooperative Air Sampling Network (*Dlugokencky et al.*, 1997). These samples are taken at approximately weekly intervals.

We restricted our analysis to data at mid latitudes in the southern hemisphere. In the northern hemisphere, fluctuations in the methane production by the terrestrial biosphere and by anthropogenic sources obscure the weak signal in the data. In the tropics, CH_4 is transported from midlatitudes by the convergence of surface winds near the equator, introducing additional fluctuations other than those caused by stratospheric O_3. In our analysis, we used the Cape Grim (CGO) (40°41′S, 144°41′E) site from the NOAA-CMDL methane dataset. Of the southern sites, CGO is the only one with a long continuous record that is also remote from known sources of methane. For ozone, we used the [40°S, 45°S] latitude band of the TOMS ozone dataset. We had ozone data for the months from Nov. 1978 to Mar. 1999, but we had methane data only for the months from Apr. 1984 to Dec. 1998. Therefore our calculation of the sensitivity was done using the latter time domain where we had data for both ozone and methane.

Both datasets were quadratically detrended and their seasonal cycles were then

removed. Missing months were interpolated using cubic splines. Further filtering was done spectrally to isolate fluctuations with periods between 15 and 60 months. The spectral filter was a convolution of stepfunctions with Hanning windows chosen to get a full signal from periods inside the (15, 60) month interval and no signal from periods outside of the (12.5, 92) month interval (*Press et al.*, 1992, chap. 13). The frequency filtering was done to remove those periods for which the changes in the UV flux to the troposphere are not simply the result of changes in stratospheric ozone. For the seasonal cycle (and shorter periods) the fluctuations in UV insolation are large, of roughly the same order as the mean values. The reason for removing the longer period fluctuations was to eliminate the solar cycle. The solar cycle manifests itself both as a change in the UV insolation to the top of the atmosphere and an associated change in stratospheric ozone which in turn leads to a UV screening effect which works in the opposite sense to the change in UV insolation. In both of these regimes, the signal from the stratospheric ozone could be obscured by the fluctuations in UV insolation. Figures 5.1 and 5.2 show the detrended, deseasonalized data, both filtered and unfiltered, and the associated spectra for ozone and methane, respectively.

From the spectrum in Figure 5.1b, we can see that the dominant features of the ozone signal are two structures with periods of approximately 29 and 20 months. The 29 month period corresponds to the quasi-biennial oscillation (QBO) of the stratosphere. The QBO is a quasi-periodic reversal in equatorial winds above the tropopause (*Reed et al.*, 1961; *Veryard and Ebdon*, 1961). The presence of the signal in stratospheric ozone is well documented (*Angell and Korshover*, 1964, 1973; *Tung*

and Yang, 1994a). The QBO accounts for about 10% of total ozone variance. The 20 month signal is a beat frequency occurring from interactions between the QBO and annual fluctuations (*Tung and Yang*, 1994a). Its frequency is the difference combination of the annual and QBO frequencies: $f_{beat} = f_{annual} - f_{QBO} = 1/12 - 1/29 \simeq 1/20$ months^{-1}.

To determine the sensitivity, it is necessary to determine the delay of the methane response to the ozone forcing. We can estimate the delay directly from the data by calculating the cross correlation of the two datasets (truncated to their common time domain) for a range of lag times. The lag associated with the maximum correlation is the estimate of the delay. Figure 5.3a shows that the delay is approximately 6 months. We can use our simple model, Equation (5.7), to investigate this empirically determined value for the delay. If the forcing for this model is an oscillatory signal dominated by a single frequency and the lifetime, τ, is much longer than the period of the forcing, we expect the delay to be a quarter of the forcing period. This is derived in detail in Section A.3 of the Appendix. From Figure 5.1b, we see that the period with the largest magnitude is the QBO, $\sim$29 months. If the only dominant frequency in the forcing was that of the QBO, Equation (A.9) shows that the delay would be $\sim$7 months. On the other hand, if the only dominant frequency was that of the QBO-annual beat, with its $\sim$20 month period, we would expect a delay of $\sim$5 months. Since the ozone forcing is actually dominated by both the QBO and the QBO-annual beat, we expect a delay somewhere between these two values. This is clearly consistent with our empirically determined value of 6 months. The details of determining the

delay for a signal consisting of the superposition of multiple periodic signals are examined in Section A.4 of the Appendix. If we estimate the delay using Equation (A.16) for the two dominant frequencies of the ozone forcing, we recover a delay of ∼6 months. This is illustrated in Figure 5.3b which shows that the smallest positive root of $G(L) \equiv \cos(\omega_1 L) + \delta_2 \cos(\omega_2 L)$ is $L \simeq 6$. The frequencies, $\omega_1 \simeq 2\pi/29$ months^{-1} and $\omega_2 \simeq 2\pi/20$ months^{-1}, and amplitude ratio, $\delta_2 \simeq 1.0/1.1$, were determined from the filtered ozone spectrum shown in Figure 5.1b.

Once the appropriate delay of 6 months was determined, we created a paired dataset consisting of the filtered ozone data for the interval from Oct. 1983 to Jun. 1998 and the filtered methane data for the interval from Apr. 1984 to Dec. 1998. The sensitivity was then calculated by performing a least squares linear fit to the paired data, with α equal to the slope of the linear fit. Figure 5.4 displays the paired dataset and the linear fit. The results of the sensitivity calculations are given in Table 5.1. As expected from the definition of α, Equation (5.4b), the line from the linear fit passes close to the origin. The rather wide spread of the data will be discussed below. To get a very rough idea of the accuracy of α calculation, we have redone the calculation on a partition of the full time series. The values of α (and the intercept) for data between 1984 and 1991 and for data between 1992 and 1998 are determined and shown in Table 5.1 and Figure 5.4.

5.3 Simulating Interannual Fluctuations

To gain further insight into the effect of variability in stratospheric O_3 on tropospheric CH_4 and to test the previously determined value for the sensitivity α, Equation (5.7) was integrated for the period from Nov. 1978 to Mar. 1999. The forcing used was

$$F(t) = -\alpha_{CH_4}\omega\tau\frac{\Omega'}{\Omega_0} \tag{5.9}$$

where Ω'/Ω_0 is the filtered ozone data described in the previous section and shown in Figure 5.1a. The relationship between the sensitivity and the multiplicative factor for the forcing, $\kappa \simeq -\alpha_{CH_4}\omega\tau$, can be seen in Equation (A.10). The change in sign is caused by the change from negative forcing by the hydroxyl radical to positive forcing by ozone. Values for the sensitivity, $\alpha_{CH_4} = -0.038$, and the QBO frequency, $\omega = 2\pi/29$ months^{-1}, were determined in the previous section. An estimate of 10 years has been used for τ, the lifetime of methane (*Spivakovsky et al.*, 1990; *Prinn et al.*, 1992; *Michelsen et al.*, 1994). The initial condition was set to zero and a fourth order Runge-Kutta method was used for the integration (*Press et al.*, 1992, chap. 16).

Figure 5.5a shows the observed (filtered) ozone fluctuations in comparison to the observed (filtered) methane fluctuations. The ozone data has been multiplied by the sensitivity, α_{CH_4}, and has been shifted forward by 6 months to account for the delay in the methane response. Figure 5.5b shows the resulting simulated methane response in comparison to the observed (filtered) methane data. The ozone signal and

the simulation clearly capture much, but not all, of the variability of the methane signal. In particular, the phases of the oscillations are in reasonable agreement. The disparities between these curves will be discussed below. Correlations between the datasets have been calculated and are shown in Table 5.2. Corresponding statistical significances were determined by the Fisher-Z test. The necessary estimate of the number of degrees of freedom was found by using the first zero of the autocorrelation to estimate the spacing between independent data points (*Harrison and Larkin*, 1997).

5.4 Discussion

We can compare the estimate of α_{CH_4} from our empirical study to estimates of α_{OH} and α_{CH_4} from various modeling studies (*Bekki et al.*, 1994; *Fuglestvedt et al.*, 1994; *Granier et al.*, 1996; *van Dop and Krol*, 1996). Table 5.3, derived from Table 10.3 of (*Granier and Shine*, 1999), summarizes some of these results. But there exists a fundamental difference between our time-dependent calculations and the steady-state ones performed in the modeling studies. Our calculations are based on the relatively short term response, on the order of months, to oscillatory forcing. The calculations from modeling studies are based on the long term response to a shift in the overall ozone level, i.e. to a constant forcing. The derivations in Sections A.2 and A.3 of the Appendix explore this difference for a simple linear system. For a species with a short lifetime, such as OH, Equations (A.5) and (A.8) demonstrate that the estimates of the sensitivity will not strongly depend upon whether the forcing is constant or oscillatory (assuming that forcing period, $2\pi/\omega$, is much longer than the lifetime, τ).

However, for a long-lifetime species such as CH_4, a comparison of Equations (A.5) and (A.10) demonstrates that the sensitivity measurement depends strongly on the type (and frequency) of the forcing. We can compare our empirical calculation of α_{CH_4} to the α_{CH_4} from Table 5.3 by including a multiplicative factor of $\omega\tau$. This also serves as a rough comparison of the empirical α_{CH_4} to the α_{OH}'s from Table 5.3. From Equations (5.4a), (5.4b), (A.8) and (A.10), we can estimate the ratio

$$\frac{\alpha_{CH_4}}{\alpha_{OH}} \simeq -\frac{1}{\omega\tau} \tag{5.10}$$

Using $\alpha_{CH_4} \simeq -0.038 \pm 0.009$, $\omega = 2\pi/29$ months^{-1}, and $\tau = 10$ years, we get $\alpha_{CH_4}\omega\tau \simeq -0.98 \pm 0.23$. These values are consistent with the values from the modeling studies.

While the high significances of our correlations give us confidence that part of the methane signal is responding to the ozone forcing, the relatively low values of these correlations demonstrate that other processes have a strong effect on the methane on these time scales. The square of the correlation (the coefficient of determination or R^2) measures the amount of the variability in methane signal caused by the fluctuations in the ozone forcing. The R^2 values for our correlations, shown in Table 5.2, demonstrate that more than half of the methane variability is due to other causes. This is also evident in methane spectrum, Figure 5.2b, where the QBO and the QBO-annual beat frequencies are clearly not the dominant features. Other possible causes for the methane variability include source fluctuations and tropospheric dynamics. Signals from these other causes partially obscure the response to the ozone forcing

and contribute to the spread of the data used in the α calculation, Figure 5.4, and to the disparities seen in the comparisons shown in Figure 5.5.

We must also consider the possibility that there may exist alternative sources for our measured correlations. A process may be forcing both the ozone and methane directly, although it would need to affect the ozone approximately 6 months prior to the methane to explain the lag at which the maximum correlation occurs. One such alternative is that the QBO in the stratosphere may be directly creating a tropospheric QBO signal through dynamical processes. To explore this possibility, we examined the tropospheric CO_2 record from the CGO and MLO (Mauna Loa) sites. Since we detected no significant QBO signal in these records, we can rule out this hypothesis.

The signals we analyzed in this paper are very small, on the order of 0.1% for methane and 1.0% for ozone, over a few years. It is a tribute to the CMDL and TOMS programs that such high quality calibrations are maintained over decadal time periods. Obviously, this analysis can be greatly improved with a longer record in the future.

Table 5.1: **Calculated sensitivity, α_{CH_4}, of the methane response to ozone fluctuations.** The sensitivity is estimated by the slope of the linear fit to the paired ozone and methane data, as shown in Figure 5.4. Values are shown for the entire time domain and for a partition of the time domain. Values for the intercepts of the linear fits are also given.

Years	**Alpha**	**Intercept**
$1984 - 1998$	-0.038	3.4×10^{-5}
$1984 - 1991$	-0.029	-1.0×10^{-4}
$1992 - 1998$	-0.047	1.6×10^{-4}

Table 5.2: **Correlations between the methane observations, $(CH_4)_d$, and the ozone observations, O_3, and the simulated methane response, $(CH_4)_s$.** The coefficient of determination (R^2), associated Fisher Z significance and estimated degrees of freedom are also shown.

Datasets	**Years**	**Corr.**	$\mathbf{R^2}$	**Sig.(%)**	**D.o.F**
$O_3 - (CH_4)_d$	$1984 - 1998$	0.65	0.43	99.99	26
$(CH_4)_s - (CH_4)_d$	$1984 - 1998$	0.53	0.29	99.6	23

Table 5.3: **Sensitivity, α_X, of tropospheric chemical species X to stratospheric ozone changes for the period 1979–1994.** The values reported here correspond to the relative change in global tropospheric annual average levels in X (%) resulting from a 1% decrease in total column ozone; the assumed scenarios are discussed in the cited publications. The type of model used is indicated in parentheses. Note that the values of Granier *et al.* (1996) correspond to the 1990–1994 period. The calculations indicated as Granier-1997 correspond to the 1979–1994 period and have been obtained using an updated version of the model used by Granier *et al.* (1996).

References	**X = OH**	**X = CH_4**
Bekki *et al.* (1994) (2D)	0.86	N/A
Fuglestvedt *et al.* (1994) (2D)	0.99	-0.79
Granier *et al.* (1996) (3D)	0.82	N/A
Granier-1997 (3D JPL94)	0.70	N/A
Granier-1997 (3D JPL97)	0.74	N/A
Our result: $\alpha_{CH_4}\omega\tau$		-0.98

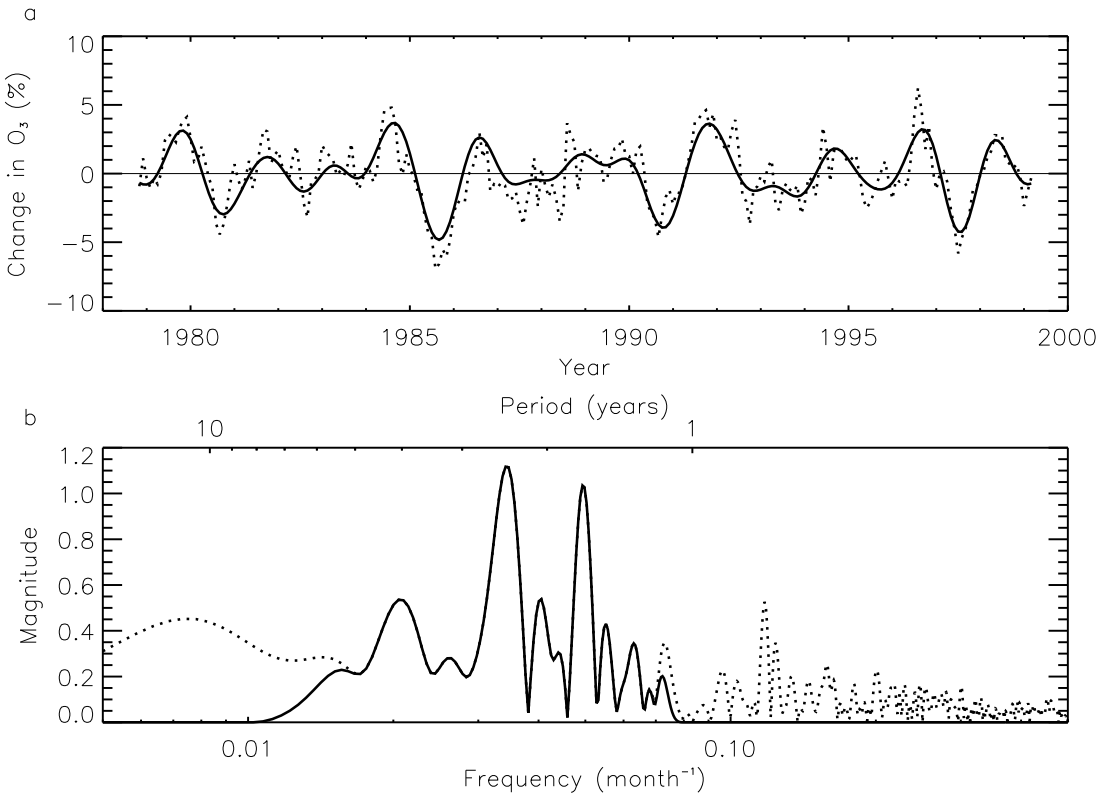

Figure 5.1: (a) Fractional change in ozone column abundance from the merged SBUV/TOMS dataset. (b) Spectrum of the ozone data. The solid line is the filtered data or spectrum and the dotted line is the unfiltered data or spectrum.

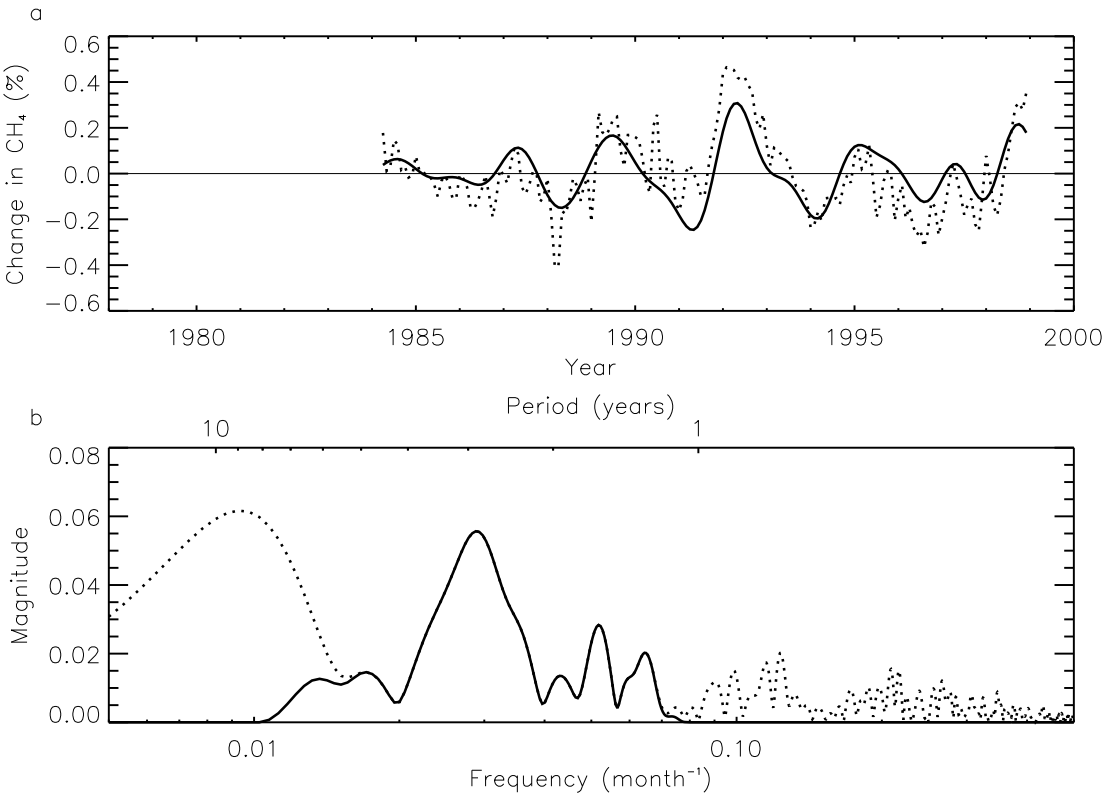

Figure 5.2: **(a)** Fractional change in methane abundance from the NOAA-CMDL flask monthly means database. **(b)** Spectrum of the methane data. The solid line is the filtered data or spectrum and the dotted line is the unfiltered data or spectrum.

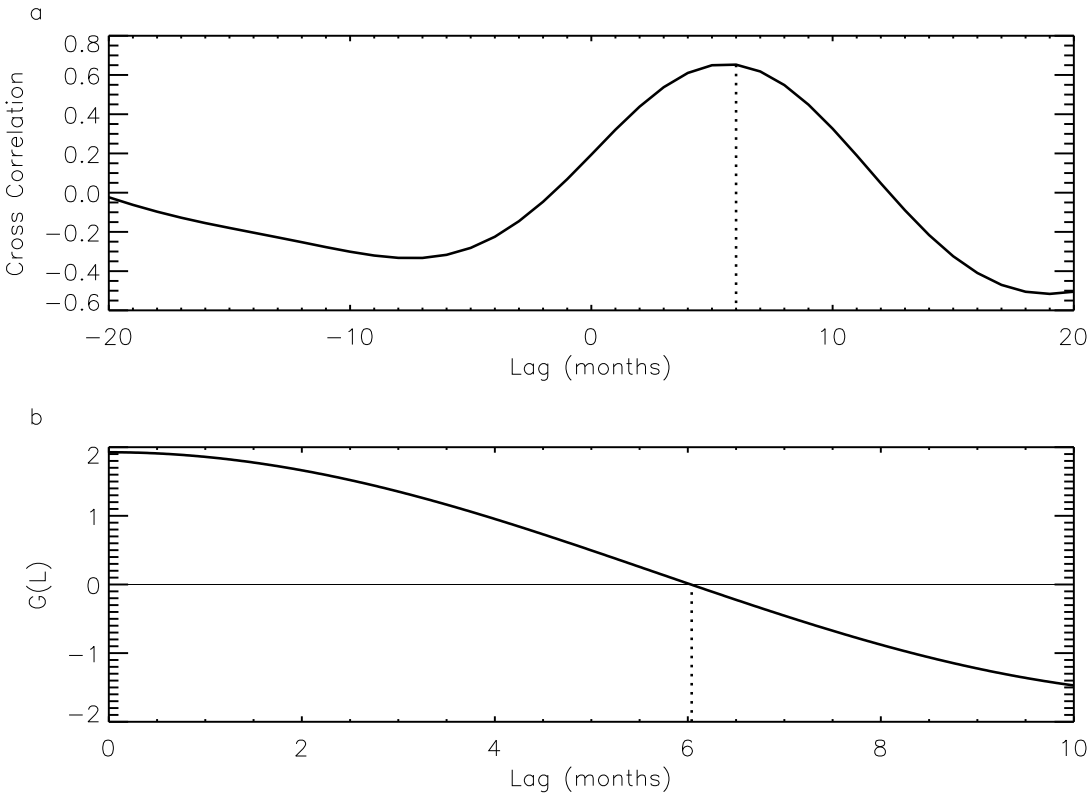

Figure 5.3: Estimates of the delay of the methane response to the ozone forcing. **(a)** Cross correlation of the changes in ozone and methane abundances for the 1984–1998 period. The delay can be estimated by the lag corresponding to the maximum cross correlation. **(b)** Plot of $G(L)$ from Equation (A.16). The delay can be estimated by the lag corresponding to the first positive root.

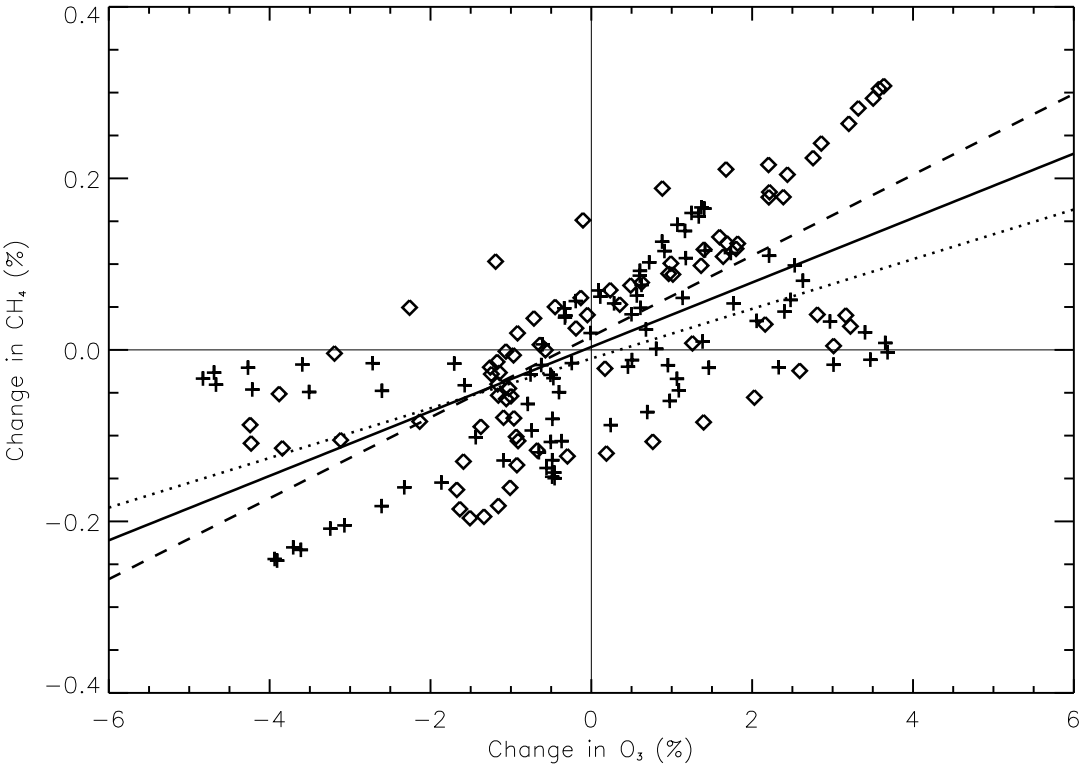

Figure 5.4: Paired ozone-methane changes (with a 6 month delay). The sensitivity, α_{CH_4}, is the slope of the least squares linear fit (solid line) to the paired data. Data between Apr. 1984 and Dec. 1991 are denoted by +'s. Data between Jan. 1992 and Dec. 1998 are denoted by $\diamond$'s. Least square linear fits are shown for the data prior to 1992 (dotted line) and the data for 1992 on (dashed line).

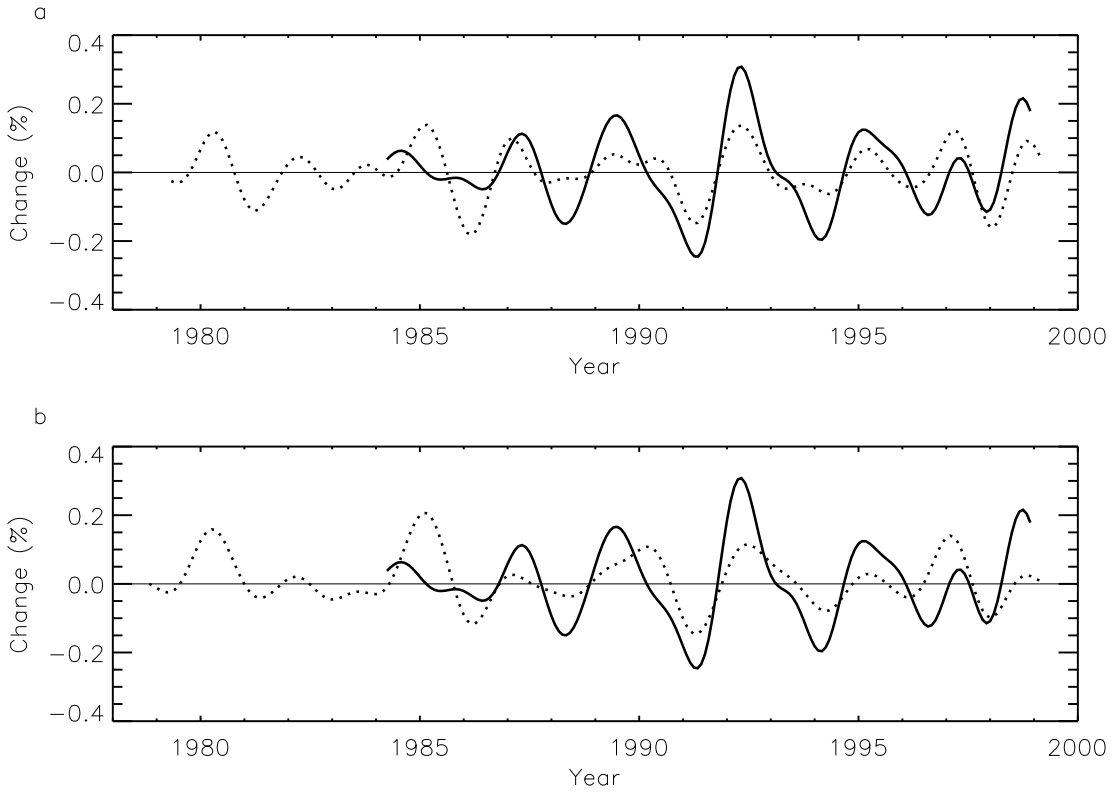

Figure 5.5: **(a)** Comparison of the filtered methane data (solid line) to filtered ozone data (dotted line). The ozone data has been shifted up 6 months and its amplitude has been multiplied by the sensitivity, α_{CH_4}. **(b)** Comparison of the filtered methane data to the simulated methane response (dotted line).

Appendix A

Response of the Methane Evolution Equation to Various Forcings

Our model is the first-order ODE

$$\frac{dy}{dt} = -\frac{1}{\tau}y - \frac{1}{\tau}F(t) \tag{A.1}$$

The general solution, given an initial condition $y(0)$ at time $t = 0$, is

$$y(t) = y(0)\, e^{-t/\tau} - \frac{1}{\tau}\int_0^t \exp\left[-\frac{1}{\tau}(t - t')\right] F(t')\, dt' \tag{A.2}$$

A.1 Impulse Response

If we assume that the forcing in Equation A.1 is an instantaneous impulse at some time t_0,*i.e.,* $F(t) = \kappa\delta(t - t_0)$, then the solution A.2 becomes

$$y(t) = \begin{cases} y(0)\, e^{-t/\tau} & \text{for} \quad 0 < t < t_0 \\ y(0)\, e^{-t/\tau} - \frac{\kappa}{\tau} \exp\left[-\frac{1}{\tau}(t - t_0)\right] & \text{for} \quad t > t_0 \end{cases} \tag{A.3}$$

Therefore, the solution responds immediately to the impulse forcing, then slowly decays back to $y = 0$. The speed of the decay is controlled by the lifetime, τ.

A.2 Constant Forcing

If we assume that the forcing in Equation (A.1) is constant,*i.e.,* $F(t) = \kappa f(t) = \kappa f_0$, the solution (A.2) becomes

$$y(t) = [y(0) + \kappa f_0]\, e^{-t/\tau} - \kappa f_0 \tag{A.4}$$

Ignoring the transient terms, the sensitivity of the response to constant forcing can be estimated by

$$\alpha \simeq -\frac{\|y(t)\|}{f_0} \simeq \kappa \tag{A.5}$$

Note that this result is independent of the lifetime, τ, of the responding species.

A.3 Single Period Oscillatory Forcing

If we assume that the forcing in Equation (A.1) is proportional to a sinusoidal forcing,*i.e.,* $F(t) = \kappa f(t) = \kappa f_0 \cos(\omega t)$, and define $\tan\phi = \omega\tau$, the solution (A.2) becomes

$$y(t) = \left[y(0) + \frac{\kappa f_0 \cos(\phi)}{\sqrt{1+\omega^2\tau^2}}\right] e^{-t/\tau} - \frac{\kappa}{\sqrt{1+\omega^2\tau^2}} f_0 \cos(\omega t - \phi) \tag{A.6}$$

If we assume $\omega\tau \ll 1$, we get $\phi = \arctan(\omega\tau) \to 0$ and $\sqrt{1+\omega^2\tau^2} \simeq 1$. Ignoring the transient term, the solution (A.6) becomes

$$y(t) \simeq -\kappa f_0 \cos(\omega t) \simeq -\kappa f(t) \tag{A.7}$$

So, the solution closely tracks the forcing. The sensitivity of the response of a short lifetime species to oscillatory forcing is estimated by

$$\alpha = -\frac{\|y(t)\|}{\|f(t)\|} = \frac{\kappa}{\sqrt{1+\omega^2\tau^2}} \simeq \kappa \tag{A.8}$$

If we assume $\omega\tau \gg 1$, we get $\phi = \arctan(\omega\tau) \simeq \pi/2$ and $\sqrt{1+\omega^2\tau^2} \simeq \omega\tau$. Now the nontransient solution (A.6) becomes

$$\begin{aligned} y(t) &\simeq -\frac{\kappa}{\sqrt{1+\omega^2\tau^2}} f_0 \cos\left(\omega t - \frac{\pi}{2}\right) \\ &\simeq -\frac{\kappa}{\omega\tau} f\left(t - \frac{T}{4}\right) \end{aligned} \tag{A.9}$$

where $T = 2\pi/\omega$ is the period of the forcing. So, for a long lifetime species, we get a response which lags the forcing by a quarter period. Furthermore, the sensitivity to oscillatory forcing can be estimated by

$$\alpha = -\frac{\|y(t)\|}{\|f(t)\|} = \frac{\kappa}{\sqrt{1+\omega^2\tau^2}} \simeq \frac{\kappa}{\omega\tau} \tag{A.10}$$

A.4 Multiple Period Oscillatory Forcing

For a more realistic forcing for Equation (A.1), we can consider the superposition of multiple sinusoidal terms $F(t) = \kappa \sum_i f_i \cos(\omega_i t)$. Then, ignoring the transient terms, we get the solution

$$y(t) = -\kappa \sum_i \frac{f_i}{\omega_i \tau} \cos\left(\omega_i t - \frac{\pi}{2}\right) \tag{A.11}$$

When comparing datasets, the delay of the response to the forcing can be determined by finding the lag associated with the maximum (or minimum, if anticorrelated) cross correlation between the two datasets. It would therefore be illuminating to examine the cross correlation of the above idealized case. Note that here, the solution and

forcing are anticorrelated. The cross correlation for the time interval $[0, T]$ is

$$\begin{aligned} C(y, F; L, T) &= \int_0^T y(t+L) F(t)\, dt \\ &= \kappa \sum_i \sum_{j \neq i} \frac{f_i f_j}{\omega_j \tau} \left[\frac{\cos\left[(\omega_j - \omega_i) T + \omega_j L\right] - \cos(\omega_j L)}{2(\omega_j - \omega_i)} \right. \\ &\qquad \left. + \frac{\cos\left[(\omega_j + \omega_i) T + \omega_j L\right] - \cos(\omega_j L)}{2(\omega_j + \omega_i)} \right] \\ &\quad - \kappa \sum_i \frac{f_i^2}{\omega_i \tau} \left[\frac{T}{2} \sin(\omega_i L) - \frac{\cos(2\omega_i T + \omega_i L) - \cos(\omega_i L)}{4\omega_i} \right] \end{aligned} \tag{A.12}$$

We can greatly simplify this expression by letting T be the product of all possible periods in (A.12),

$$T = \prod_{i,j} (T_{ij+})(T_{ij-}), \qquad T_{ij\pm} = \frac{2\pi}{\omega_j \pm \omega_i} \tag{A.13}$$

leaving

$$C(y, F; L, T) = -\frac{\kappa T}{2} \sum_i \frac{f_i^2}{\omega_i \tau} \sin(\omega_i L) \tag{A.14}$$

The lag associated with the maximum anticorrelation occurs at the minimum of $C(y, F; L, T)$ with respect to L.

For a single forcing frequency, ω_1, the first minimum for positive lag, L, occurs when

$$\omega_1 L = \frac{\pi}{2} \tag{A.15}$$

So the response lags the forcing by a quarter period as expected.

For two or more forcing frequencies, sorted by decreasing amplitude, the extrema

occur at the roots of

$$G(L) \equiv \cos(\omega_1 L) + \sum_{i>1} \delta_i^2 \cos(\omega_i L) \tag{A.16}$$

where $\delta_i = F_i/F_1 < 1$. If $\delta_i \ll 1$ for all $i > 1$, then this approximates the single frequency case with $\omega_i L = \pi/2 \pm \varepsilon$, $\varepsilon \ll 1$. In general, as the δ_i's grow, so will ε.

Bibliography

Andrews, D. G., J. R. Holton, and C. B. Leovy, *Middle Atmosphere Dynamics*, International Geophysics Series, Academic Press, San Diego, 1987.

Angell, J. K., and J. Korshover, Quasi-biennial variations in temperature, total ozone, and tropopause height, *J. Atmos. Sci.*, *21*(5), 479–492, 1964.

Angell, J. K., and J. Korshover, Quasi-biennial and long-term fluctuations in total ozone, *Mon. Weather Rev.*, *101*(5), 426–443, 1973.

Austin, J., J. Knight, and N. Butchart, Three-dimensional chemical model simulations of the ozone layer: 1979-2015, *Q. J. R. Meteorol. Soc.*, *126*(565), 1533–1556, 2000.

Baldwin, M. P., et al., The quasi-biennial oscillation, *Rev. Geophys.*, *39*(2), 179–229, 2001.

Bartels, J., D. Peters, and G. Schmitz, Climatological Ertel's potential-vorticity flux and mean meridional circulation in the extratropical troposphere – lower stratosphere, *Ann. Geophys.-Atmos. Hydrospheres Space Sci.*, *16*(2), 250–265, 1998.

Bekki, S., K. S. Law, and J. A. Pyle, Effect of ozone depletion on atmospheric CH_4 and CO concentrations, *Nature*, *371*(6498), 595–597, 1994.

Bojkov, R., and R. Hudson, Ozone variability and trends, *Tech. Rep. 44*, World Meteorological Organization: Global Ozone Research and Monitoring Project, 1999.

Brasseur, G. P., J. J. Orlando, and G. S. Tindall (Eds.), *Atmospheric Chemistry and Global Change*, Oxford University Press, New York, 1999.

Brönnimann, S., J. Luterbacher, C. Schmutz, H. Wanner, and J. Staehelin, Variability of total ozone at Arosa, Switzerland, since 1931 related to atmospheric circulation indices, *Geophys. Res. Lett.*, *27*(15), 2213–2216, 2000.

Brönnimann, S., J. Luterbacher, J. Staehelin, and T. M. Svenby, An extreme anomaly in stratospheric ozone over Europe in 1940–1942, *Geophys. Res. Lett.*, *31*, art. no. L08,101, 2004.

Burg, J. P., Maximum entropy spectral analysis, in *Modern Spectrum Analysis*, edited by D. G. Childers, p. 334, IEEE Press, New York, 1978.

Camp, C. D., M. S. Roulston, A. F. C. Haldemann, and Y. L. Yung, The sensitivity of tropospheric methane to the interannual variability in stratospheric ozone, *Chemosphere — Global Change Science*, *3*, 147–156, 2001.

Camp, C. D., M. S. Roulston, and Y. L. Yung, Temporal and spatial patterns of the interannual variability of total ozone in the tropics, *J. Geophys. Res.*, *108*(D20), art. no. 4643, 2003.

Chandra, S., and R. D. McPeters, The solar-cycle variation of ozone in the strato-

sphere inferred from NIMBUS-7 and NOAA-11 satellites, *J. Geophys. Res.*, *99*(D10), 20,665–20,671, 1994.

DeMore, W. B., S. P. Sander, D. M. Golden, R. F. Hampson, M. J. Kurylo, C. J. Howard, A. R. Ravishankara, C. E. Kolb, and M. J. Molina, Chemical kinetics and photochemical data for use in stratospheric modeling, *Tech. Rep. Evaluation No. 12, JPL Pub. 97-4*, Jet Propulsion Laboratory, 1997.

Devore, J. L., *Probability and Statistics for Engineering and the Sciences*, 1st ed., Brooks/Cole, Monterey, Calif., 1982.

Dlugokencky, E. J., P. M. Lang, K. A. Masarie, and L. P. Steele, Atmospheric methane mixing ratios—the NOAA/CMDL Global Cooperative Air Sampling Network, 1983-1993, *Tech. rep.*, Carbon Dioxide Information Analysis Center, 1997.

Fleming, E., C. Jackman, J. Rosenfield, and D. Considine, Two-dimensional model simulations of the QBO in ozone and tracers in the tropical stratosphere, *J. Geophys. Res.*, *107*, 4665, 2002.

Fuglestvedt, J. S., J. E. Jonson, and I. S. A. Isaksen, Effects of reductions in stratospheric ozone on tropospheric chemistry through changes in photolysis rates, *Tellus Ser. B-Chem. Phys. Meteorol.*, *46*(3), 172–192, 1994.

Fusco, A. C., and M. L. Salby, Interannual variations of total ozone and their relationship to variations of planetary wave activity, *J. Clim.*, *12*(6), 1619–1629, 1999.

Ghil, M., and A. W. Robertson, Solving problems with GCMs: General circulation

models and their role in the climate modeling hierarchy, in *General Circulation Model Development: Past, Present and Future*, edited by D. Randall, pp. 285–325, Academic Press, San Diego, 2000.

Ghil, M., et al., Advanced spectral methods for climatic time series, *Rev. Geophys.*, *40*(1), art. no. 1003, 2002.

Goody, R. M., and Y. L. Yung, *Atmospheric Radiation: Theoretical Basis*, 2nd ed., Oxford University Press, New York, 1989.

Granier, C., and K. P. Shine, Climate effects of ozone and halocarbon changes, *Tech. Rep. 44*, World Meteorological Organization: Global Ozone Research and Monitoring Project, 1999.

Granier, C., J. F. Mller, S. Madronich, and G. P. Brasseur, Possible causes for the 1990-1993 decrease in the global tropospheric CO abundances: A three-dimensional sensitivity study, *Atmos. Environ.*, *30*(10-11), 1673–1682, 1996.

Hadjinicolaou, P., A. Jrrar, J. A. Pyle, and L. Bishop, The dynamically driven long-term trend in stratospheric ozone over northern middle latitudes, *Q. J. R. Meteorol. Soc.*, *128*(583), 1393–1412, 2002.

Harrison, D. E., and N. K. Larkin, Darwin sea level pressure, 1876-1996: Evidence for climate change?, *Geophys. Res. Lett.*, *24*(14), 1779–1782, 1997.

Hasebe, F., Quasi-biennial oscillations of ozone and diabatic circulation in the equatorial stratosphere, *J. Atmos. Sci.*, *51*(5), 729–745, 1994.

Held, I. M., and T. Schneider, The surface branch of the zonally averaged mass transport circulation in the troposphere, *J. Atmos. Sci.*, *56*(11), 1688–1697, 1999.

Herman, J. R., R. McPeters, R. Stolarski, D. Larko, and R. Hudson, Global average ozone change from November 1978 to May 1990, *J. Geophys. Res.*, *96*(D9), 17,297–17,305, 1991.

Holton, J. R., P. H. Haynes, M. E. McIntyre, A. R. Douglass, R. B. Rood, and L. Pfister, Stratosphere-troposphere exchange, *Rev. Geophys.*, *33*(4), 403–439, 1995.

Hood, L. L., The solar cycle variation of total ozone: Dynamical forcing in the lower stratosphere, *J. Geophys. Res.*, *102*(D1), 1355–1370, 1997.

Hood, L. L., J. P. McCormack, and K. Labitzke, An investigation of dynamical contributions to midlatitude ozone trends in winter, *J. Geophys. Res.*, *102*(11D), 13,079–13,093, 1997.

Huesmann, A. S., and M. H. Hitchman, The stratospheric quasi-biennial oscillation in the NCEP reanalyses: Climatological structures, *J. Geophys. Res.*, *106*(D11), 11,859–11,874, 2001.

Huesmann, A. S., and M. H. Hitchman, The 1978 shift in the NCEP reanalysis stratospheric quasi-biennial oscillation, *Geophys. Res. Lett.*, *30*(2), art. no. 1048, 2003.

Jiang, N., J. D. Neelin, and M. Ghil, Quasi-quadrennial and quasi-biennial variability in the equatorial Pacific, *Clim. Dyn.*, *12*(2), 101–112, 1995.

Jiang, X., C. D. Camp, R. L. Shia, D. Noone, C. Walker, and Y. L. Yung, Qbo and qbo-annual beat in the tropical total column ozone: A two-dimensional model simulation, *J. Geophy. Res.*, doi:10.129/2003JD004377, 2004, in press.

Johnson, D. R., The forcing and maintenance of global monsoonal circulations—an isentropic analysis, *Adv. Geophys.*, *31*, 43–316, 1989.

Jones, D. B. A., H. R. Schneider, and M. B. McElroy, Effects of the quasi-biennial oscillation on the zonally averaged transport of tracers, *J. Geophys. Res.*, *103*(D10), 11,235–11,249, 1998.

Juckes, M. N., I. N. James, and M. Blackburn, The influence of Antarctica on the momentum budget of the southern extratropics, *Q. J. R. Meteorol. Soc.*, *120*(518), 1017–1044, 1994.

Kalnay, E., et al., The NCEP/NCAR 40-year reanalysis project, *Bull. Amer. Meteorol. Soc.*, *77*(3), 437–471, 1996.

Kayano, M. T., Principal modes of the total ozone on the Southern Oscillation timescale and related temperature variations, *J. Geophys. Res.*, *102*(D22), 25,797–25,806, 1997.

Khalil, M. A. K., M. J. Shearer, and R. Rasmussen, Methane sinks and distribution, in *NATO Advanced Research Workshop: Atmospheric Methane—Sources, Sinks, Distributions, and Role in Global Change.*, *NATO ASI Series, Series I, Global Environmental Change*, vol. 13, edited by M. A. K. Khalil, Springer-Verlag, New

York, in cooperation with NATO Scientific Affairs Division, conference held at Mount Hood near Portland, OR, 1993.

Kinnersley, J. S., and K. K. Tung, Mechanisms for the extratropical QBO in circulation and ozone, *J. Atmos. Sci.*, *56*(12), 1942–1962, 1999.

Kistler, R., et al., The NCEP-NCAR 50-year reanalysis: Monthly means CD-ROM and documentation, *Bull. Amer. Meteorol. Soc.*, *82*(2), 247–267, 2001.

Ko, M. K. W., K. K. Tung, D. K. Weisenstein, and N. D. Sze, A zonal mean model of stratospheric tracer transport in isentropic coordinates—numerical simulations for nitrous oxide and nitric acid, *J. Geophys. Res.*, *90*(ND1), 2313–2329, 1985.

Levy, H., Photochemistry of lower troposphere, *Planet Space Sci.*, *20*(6), 919–935, 1972.

Liu, S. C., and M. Trainer, Responses of the tropospheric ozone and odd hydrogen radicals to column ozone change, *J. Atmos. Chem.*, *6*(3), 221–233, 1988.

Malhman, J. D., D. G. Andrews, D. L. Hartmann, T. Matsuno, and R. G. Murgatroyd, Transport of trace constituents in the stratosphere, in *Dynamics of the Middle Atmosphere*, edited by J. R. Holton and T. Matsuno, pp. 387–416, Terra Scientific, 1984.

Marquardt, C., Die tropische QBO und dynamische Prozesse in der Stratosphäre, Ph.D., Freie Univ. Berlin, 1997.

Marquardt, C., and B. Naujokat, An update of the equatorial QBO and its variability, in *1st SPARC Gen. Assemb., TD-No. 814*, vol. 1, pp. 87–90, World Meteorological Association, Melbourne, Australia, 1997.

McElroy, M. B., S. C. Wofsy, J. E. Penner, and McConnel.Jc, Atmospheric ozone—possible impact of stratospheric aviation, *J. Atmos. Sci.*, *31*(1), 287–303, 1974.

McPeters, R., et al., NIMBUS-7 Total Ozone Mapping Spectrometer (TOMS) data products user's guide, *Tech. rep.*, NASA, 1996.

Michelsen, H. A., R. J. Salawitch, P. O. Wennberg, and J. G. Anderson, Production of $O(^1D)$ from photolysis of O_3, *Geophys. Res. Lett.*, *21*(20), 2227–2230, 1994.

Morgan, C. G., M. Allen, M. C. Liang, R. L. Shia, G. A. Blake, and Y. L. Yung, Isotopic fractionation of nitrous oxide in the stratosphere: Comparison between model and observations, *J. Geophys. Res.*, *109*(D4), art. no. D04,305, 2004.

Naujokat, B., An update of the observed quasi-biennial oscillation of the stratospheric winds over the tropics, *J. Atmos. Sci.*, *43*(17), 1873–1877, 1986.

Pawson, S., and M. Fiorino, A comparison of reanalyses in the tropical stratosphere. Part 1: Thermal structure and the annual cycle, *Clim. Dyn.*, *14*(9), 631–644, 1998a.

Pawson, S., and M. Fiorino, A comparison of reanalyses in the tropical stratosphere. Part 2: The quasi biennial oscillation, *Clim. Dyn.*, *14*(9), 645–658, 1998b.

Pawson, S., and M. Fiorino, A comparison of reanalyses in the tropical stratosphere. Part 3: Inclusion of the pre-satellite data era, *Clim. Dyn.*, *15*(4), 241–250, 1999.

Plumb, R. A., and R. C. Bell, A model of the quasi-biennial oscillation on an equatorial beta-plane, *Q. J. R. Meteorol. Soc.*, *108*(456), 335–352, 1982.

Politowicz, P. A., and M. H. Hitchman, Exploring the effects of forcing quasi-biennial oscillations in a two-dimensional model, *J. Geophys. Res.*, *102*(D14), 16,481–16,497, 1997.

Prather, M. J., Numerical advection by conservation of 2nd-order moments, *J. Geophys. Res.*, *91*(D6), 6671–6681, 1986.

Preisendorfer, R., *Principal Component Analysis in Meteorology and Oceanography*, 1st ed., Elsevier Sci., New York, 1988.

Press, W., S. Teukolsky, W. Vetterling, and B. Flannery, *Numerical Recipes in Fortran 77: The Art of Scientific Computing*, 2nd ed., Cambridge Univ. Press, New York, 1992.

Prinn, R., et al., Global average concentration and trend for hydroxyl radicals deduced from ALE-GAGE trichloroethane (methyl chloroform) data for 1978-1990, *J. Geophys. Res.*, *97*(D2), 2445–2461, 1992.

Randel, W. J., and J. B. Cobb, Coherent variations of monthly mean total ozone and lower stratospheric temperature, *J. Geophys. Res.*, *99*(D3), 5433–5448, 1994.

Randel, W. J., F. Wu, R. Swinbank, J. Nash, and A. O'Neill, Global QBO circulation derived from UKMO stratospheric analyses, *J. Atmos. Sci.*, *56*(4), 457–474, 1999.

Randel, W. J., F. Wu, and D. J. Gaffen, Interannual variability of the tropical tropopause derived from radiosonde data and NCEP reanalyses, *J. Geophys. Res.*, *105*(D12), 15,509–15,523, 2000.

Reed, R. J., W. J. Campbell, L. A. Rasmussen, and D. G. Rogers, Evidence of downward-propagating annual wind reversal in the equatorial stratosphere, *J. Geophys. Res.*, *66*, 813–818, 1961.

Salby, M., and P. Callaghan, Connection between the solar cycle and the QBO: The missing link, *J. Clim.*, *13*(14), 2652–2662, 2000.

Salby, M. L., and P. F. Callaghan, Fluctuations of total ozone and their relationship to stratospheric air motions, *J. Geophys. Res.*, *98*(D2), 2715–2727, 1993.

Shia, R. L., Y. L. Yung, M. Allen, R. W. Zurek, and D. Crisp, Sensitivity study of advection and diffusion coefficients in a 2-dimensional stratospheric model using excess C_{14} data, *J. Geophys. Res.*, *94*(D15), 18,467–18,484, 1989.

Shia, R. L., Y. L. Ha, J. S. Wen, and Y. L. Yung, 2-dimensional atmospheric transport and chemistry model—numerical experiments with a new advection algorithm, *J. Geophys. Res.*, *95*(D6), 7467–7483, 1990.

Shindell, D., D. Rind, N. Balachandran, J. Lean, and P. Lonergan, Solar cycle variability, ozone, and climate, *Science*, *284*(5412), 305–308, 1999.

Shiotani, M., Annual, quasi-biennial, and El-Niño-Southern Oscillation (ENSO) time-

scale variations in equatorial total ozone, *J. Geophys. Res.*, *97*(D7), 7625–7633, 1992.

Spivakovsky, C. M., R. Yevich, J. A. Logan, S. C. Wofsy, M. B. McElroy, and M. J. Prather, Tropospheric OH in a 3-dimensional chemical tracer model—an assessment based on observations of CH_3CCl_3, *J. Geophys. Res.*, *95*(D11), 18,441–18,471, 1990.

Staehelin, J., R. Kegel, and N. R. P. Harris, Trend analysis of the homogenized total ozone series of Arosa (Switzerland), 1926-1996, *J. Geophys. Res.-Atmos.*, *103*(D7), 8389–8399, 1998a.

Staehelin, J., A. Renaud, J. Bader, R. McPeters, P. Viatte, B. Hoegger, V. Bugnion, M. Giroud, and H. Schill, Total ozone series at Arosa (Switzerland): Homogenization and data comparison, *J. Geophys. Res.-Atmos.*, *103*(D5), 5827–5841, 1998b.

Stephenson, D. B., and J. F. Royer, Low-frequency variability of Total Ozone Mapping Spectrometer and general circulation model total ozone stationary waves associated with the El-Niño Southern Oscillation for the period 1979-1988, *J. Geophys. Res.*, *100*(D4), 7337–7346, 1995.

Stevermer, A., and E. C. Weatherhead, Detecting recovery in vertically-resolved ozone records, *Tech. Rep. A11C-04*, American Geophysical Union, 2001.

Summers, M. E., D. E. Siskind, J. T. Bacmeister, R. R. Conway, S. E. Zasadil, and D. F. Strobel, Seasonal variation of middle atmospheric CH_4 and H_2O with a new chemical-dynamical model, *J. Geophys. Res.*, *102*(D3), 3503–3526, 1997.

Thompson, A. M., The oxidizing capacity of the earth's atmosphere—probable past and future changes, *Science*, *256*(5060), 1157–1165, 1992.

Thompson, D. W. J., and J. M. Wallace, Annular modes in the extratropical circulation. Part I: Month- to-month variability, *J. Clim.*, *13*(5), 1000–1016, 2000.

Tung, K. K., Modeling of tracer transport in the middle atmosphere, in *Dynamics of the Middle Atmosphere*, edited by J. R. Holton and T. Matsuno, pp. 417–444, Terra Scientific, 1984.

Tung, K. K., Nongeostrophic theory of zonally averaged circulation. 1. Formulation, *J. Atmos. Sci.*, *43*(22), 2600–2618, 1986.

Tung, K. K., and H. Yang, Global QBO in circulation and ozone. 1. Reexamination of observational evidence, *J. Atmos. Sci.*, *51*(19), 2699–2707, 1994a.

Tung, K. K., and H. Yang, Global QBO in circulation and ozone. 2. A simple mechanistic model, *J. Atmos. Sci.*, *51*(19), 2708–2721, 1994b.

van Dop, H., and M. Krol, Changing trends in tropospheric methane and carbon monoxide: A sensitivity analysis of the OH radical, *J. Atmos. Chem.*, *25*(3), 271–288, 1996.

Vautard, R., P. Yiou, and M. Ghil, Singular-spectrum analysis—a toolkit for short, noisy chaotic signals, *Physica D*, *58*(1-4), 95–126, 1992.

Veryard, R. G., and R. A. Ebdon, Fluctuations in tropical stratospheric winds, *Meteorol. Mag.*, *90*, 125–143, 1961.

WMO, Scientific assessment of ozone depletion: 1998, *Tech. Rep. 44*, World Meteorological Organization: Global Ozone Research and Monitoring Project, 1999.

WMO, Scientific assessment of ozone depletion: 2002, *Tech. Rep. 47*, World Meteorological Organization: Global Ozone Research and Monitoring Project, 2003.

Yang, H., K. K. Tung, and E. Olaguer, Nongeostrophic theory of zonally averaged circulation. 2. Eliassen-Palm flux divergence and isentropic mixing coefficient, *J. Atmos. Sci.*, *47*(2), 215–241, 1990.